**NUREG/????**
**ORNL/TM-2005/???**

# Fracture Analysis of Vessels – Oak Ridge – Elastic-Plastic, FAVOR$^{EP}$, v05.1, Computer Code: Theory and Implementation of Algorithms, Methods, and Correlations

Prepared by
P. T. Williams, T. L. Dickson, S. Yin, and B. R. Bass

**Oak Ridge National Laboratory**

**Prepared for**
**U.S. Nuclear Regulatory Commission**

**NUREG/????**
**ORNL/TM-2005/???**

# Fracture Analysis of Vessels – Oak Ridge – Elastic-Plastic, FAVOR$^{EP}$, v05.1, Computer Code: Theory and Implementation of Algorithms, Methods, and Correlations

**Manuscript Completed: October 2005**
**Date Published:**

Prepared by

P. T. Williams, T. L. Dickson, S. Yin, and B. R. Bass

**Oak Ridge National Laboratory**
**Managed by UT-Battelle, LLC**
**Oak Ridge National Laboratory**
**Oak Ridge, TN 37831-8063**

**Prepared for**
**Division of Engineering Technology**
**Office of Nuclear Regulatory Research**
**U.S. Nuclear Regulatory Commission**
**Washington, DC 20555-0001**
**NRC Job Code Y6533**

# FRACTURE ANALYSIS OF VESSELS – OAK RIDGE – Elastic-Plastic, FAVOR$^{EP}$, v05.1, Computer Code:

# THEORY AND IMPLEMENTATION OF ALGORITHMS, METHODS, AND CORRELATIONS

P. T. Williams, T. L. Dickson, S. Yin, and B. R. Bass

---

## Abstract

The current approach to RPV integrity assessment is exemplified by the methodology implemented in the FAVOR computer code. The FAVOR code executes probabilistic defect assessments of RPVs using linear-elastic stress analysis methods and conventional, high-constraint fracture toughness data. Advanced fracture mechanics methodologies under recent development introduce nonlinear material response, elastic-plastic fracture toughness with applicable adjustments for constraint variations, and probabilistic effects on fracture toughness data through the procedures codified in ASTM E-1921 (test method for determination of the reference temperature $T_0$ in ferritic steels). The development of an updated FAVOR code that incorporates these advanced techniques will have much ex-tended applicability to RPV assessments that reflect modern fracture mechanics technology.

Updated computational methodologies have been developed through interactions between experts in the relevant disciplines of thermal hydraulics, probabilistic risk assessment, materials embrittlement, fracture mechanics, and inspection (flaw characterization). Contributors to the development of these methodologies include the NRC staff, their contractors, and representatives from the nuclear industry. These updated methodologies will be integrated into the **F**racture **A**nalysis of **V**essels – **O**ak **R**idge – **E**lastic-**P**lastic (FAVOR$^{EP}$, v05.1) computer code developed for the NRC by the Heavy Section Steel Technology (HSST) program at Oak Ridge National Laboratory (ORNL). Intended to document the technical bases for the assumptions, algorithms, methods, and correlations in the development of FAVOR$^{EP}$, v05.1, this report is one of a series of software quality assurance documentation deliverables being prepared according to the guidance provided in IEEE Std. 730.1-1995, *IEEE Guide for Software Quality Assurance Planning* and IEEE Std.1016-1998, *IEEE Recommended Practice for Software Design Descriptions.* Additional documents in this series include (1) *FAVOR$^{EP}$, v05.1, Computer Code: Software Requirements Specification*, (2) *FAVOR$^{EP}$, v05.1, Computer Code: Software Design Description,* and (3) *FAVOR$^{EP}$, v05.1, Computer Code: User's Guide*.

# CONTENTS

Page

Abstract ..... ii

Acronyms ..... v

ACKNOWLEDGMENTS ..... x

1 . Introduction ..... 1

2 . Pressurized Thermal Shock Events ..... 5

2.1 Historical Review ..... 5
2.2 Current NRC Regulatory Approach to PTS ..... 6
2.3 Contributions of Large-Scale Experiments to the Technical Basis for PTS Assessment ..... 7

3 . Structure and Organization of the FAVOR$^{EP}$ Code ..... 10

3.1 FAVOR$^{EP}$ – Computational Modules and Data Streams ..... 10
3.2 FAVOR$^{EP}$ Load Module (FAVLoad) ..... 11
3.2.1 Thermal-Hydraulic Transient Definitions ..... 11
3.2.2 Required Vessel Geometry and Thermo-Elastic Property Data ..... 12
3.2.3 Deterministic Analyses ..... 12
3.2.4 Flaw Categories Used in FAVOR$^{EP}$ ..... 13
3.3 FAVOR$^{EP}$ PFM Module (FAVPFM) ..... 14
3.3.1 FAVPFM$^{EP}$ Flowchart ..... 16
3.3.2 Beltline Configurations and Region Discretization ..... 18
3.3.3 Treatment of the Fusion-Line Along Welds ..... 20
3.3.4 Constraint-Loss Effects ..... 22
3.3.5 Warm Prestressing ..... 26
3.3.6 Probability Distributions ..... 31
3.3.7 Truncation Protocol ..... 36
3.3.8 Conditional Probability of Initiation (*CPI*) ..... 36
3.3.9 Post-Initiation Flaw Geometries and Orientations ..... 41
3.3.10 Conditional Probability of Failure (*CPF*) by Through-Wall Cracking ..... 43
3.3.11 Multiple Flaws ..... 44
3.3.12 Ductile-Tearing Models in FAVOR$^{EP}$ ..... 44
3.3.12.1 Ductile-Tearing Model No. 1 (implemented in FAVOR, v05.1) ..... 49
3.3.12.2 Ductile-Tearing Model No. 2 (implemented in FAVOR, v03.1) ..... 51
3.3.13 Initiation-Growth-Arrest (*IGA*) Submodel ..... 56
3.3.14 Ductile-Tearing Submodel ..... 67
3.3.15 Ductile Tearing as an Initiating Event ..... 70
3.4 FAVOR$^{EP}$ Post Module – FAVPost$^{EP}$ ..... 71

4 . Probabilistic Fracture Mechanics ..... 73

4.1 Deterministic Analyses ..... 73
4.1.1 Thermal Analysis ..... 74
4.1.2 Stress Analysis ..... 77
4.1.3 Linear-Elastic Fracture Mechanics (LEFM) ..... 80
4.1.3.1 Mode I Stress-Intensity Factors ..... 80
4.1.3.2 Inner Surface-Breaking Flaw Models –Semi-Elliptic and Infinite Length 81
4.1.3.3 Embedded-Flaw Driving-Force Model for $K_I$ ..... 87

4.1.3.4 Elastic $T_{stress}$ Models ..... 91
4.1.3.5 Inclusion of Residual Stresses in Welds ..... 102
4.1.3.6 Inclusion of Crack-Face Pressure Loading for Surface-Breaking Flaws ..... 104
4.2 Sampled LEFM Material and Correlative Properties ..... 105
4.2.1 Reference Nil-Ductility Transition Temperature, $RT_{NDT}$ ..... 105
4.2.2 Radiation Embrittlement ..... 105
4.2.3 Fast-Neutron Fluence Attenuation and Sampling Distribution ..... 109
4.2.4 ORNL 99/27 $K_{Ic}$ and $K_{Ia}$ Databases ..... 109
4.2.5 Index Temperature $RT_{NDT}$ – Uncertainty Classification and Quantification 115
4.2.6 Index Temperature $RT_{Arrest}$ – Uncertainty Classification and Quantification 120
4.2.7 Plane-Strain Static Cleavage Initiation Toughness – $K_{Ic}$ ..... 124
4.2.8 Plane-Strain Crack Arrest Toughness – $K_{Ia}$ ..... 126
4.2.9 Material Chemistry –Sampling Protocols ..... 129
4.3 NRC RVID2 Database ..... 134
4.4 Discrete Flaw Density and Size Distributions ..... 134
4.5 Summary of Sampling Distributions and Protocols ..... 138
5 . Summary and Conclusions ..... 145
References ..... 146
Appendix A – Background and Antecedents of FAVOR$^{EP}$, v05.1 ..... 157
Appendix B – Stress-Intensity Factor Influence Coefficients ..... 162
Appendix C – Listings of $K_{Ic}$ And $K_{Ia}$ Extended Databases ..... 176
Appendix D – Summary of RVID2 Data for Use in FAVOR Calculations ..... 188
Appendix E – Statistical Point-Estimation Techniques for Weibull Distributions ..... 191
Appendix F – Development of Stochastic Models for $\Delta RT_{epistemic}$ and $\Delta RT_{arrest}$ ..... 194

## Acronyms

| | |
|---|---|
| ASME | American Society of Mechanical Engineers |
| ASTM | American Society for Testing and Materials |
| BNL | Brookhaven National Laboratory |
| CCA | compact crack-arrest test specimen |
| C(T) | compact tension fracture-toughness test specimen |
| CDF | cumulative distribution function |
| CPI | conditional probability of initiation |
| CPF | conditional probability of failure (as indicated by through-wall cracking) |
| CRP | copper-rich precipitate |
| CVN | Charpy V-Notch test specimen |
| DTE | differential-thermal expansion |
| EFPY | effective full-power years |
| EPFM | elastic-plastic fracture mechanics |
| EPRI | Electric Power Research Institute |
| EOL | end-of-licensing |
| FAVOREP | Fracture Analysis of Vessels – Oak Ridge |
| FEM | finite-element method |
| HAZ | heat-affected zone |
| HSST | Heavy Section Steel Technology Program |
| IPTS | Integrated Pressurized Thermal Shock Program |
| LEFM | linear-elastic fracture mechanics |
| LOCA | loss-of-coolant accident |
| NESC | Network for Evaluating Structural Components |
| NIST | National Institute for Standards and Technology |
| NRC | United States Nuclear Regulatory Commission |
| ORNL | Oak Ridge National Laboratory |
| PDF | probability density function |
| PFM | probabilistic fracture mechanics |
| PNNL | Pacific Northwest National Laboratory |
| PRA | Probabilistic Risk Assessment |
| PTS | pressurized thermal shock |
| PWHT | post-weld heat treatment |
| PWR | pressurized water reactor |
| RCW | recirculating cooling water |
| RG1.99 | NRC Regulatory Guide 1.99, Revision 2, ref. [12] |
| RG1.154 | NRC Regulatory Guide 1.154, ref. [11] |
| RPV | reactor pressure vessel |
| RVID | Reactor Vessel Integrity Database, Version 2, ref. [156] |
| SIFIC | stress-intensity influence coefficients |
| SMD | stable matrix defect |
| 10CFR50.61 | Title 10 of the *Code of Federal Regulations*, Part 50, Section 50.61, ref. [10] |
| TMI | Three-Mile-Island nuclear reactor |
| T-E | thermo-elastic |
| T-H | thermal-hydraulic |
| UMD | unstable matrix defect |
| WOL | wedge-open loading test specimen for fracture toughness |
| WPS | warm prestressing |

## LIST OF TABLES

**Table** **Page**

**1.1 Large-Scale PTS Experiments and Performing Organizations ....9**
**3.1. Illustration of Computational Procedure to Determine *CPI* and *CPF* for a Postulated Flaw (Warm Prestress Not Included)....39**
**3.2. Applied Flaw Orientations by Major Region....41**
**3.3. Sources for Ductile-Tearing Data [27, 28, , , , 137]....45**
**3.4. Chemical Composition of Materials Used in the Ductile-Tearing Model Development .45**
**3.5. Summary of Ductile-Tearing Data Used in the Model Development ....45**
**3.5. (cont.) Summary of Ductile-Tearing Data Used in the Ductile-Tearing Model Development ....46**
**4.1. Summary of ORNL 99/27 $K_{Ic}$ Extended Database....113**
**4.2. Summary of $K_{Ia}$ Extended Database....113**
**4.3. Chemistry and Heat Treatment of Principal Materials: ORNL 99/27 Database ....114**
**4.4. Materials Used from the ORNL 99/27 $K_{Ic}$ Extended Database ....117**
**4.5. Values of Lower-Bounding Reference Temperature ....118**
**4.6. ORNL 99/27 $K_{Ia}$ Database – Reference-Transition Temperatures ....122**
**B1. Influence Coefficients for Inside Axial and Circumferential Semi-elliptic Surface Flaws: $R/t = 10$ and $a/t = 0.01$....163**
**B2. Influence Coefficients for Inside Axial and Circumferential Semi-elliptic Surface Flaws: $R/t = 10$ and $a/t = 0.0184$....164**
**B3. Influence Coefficients for Inside Axial and Circumferential Semi-elliptic Surface Flaws: $R/t = 10$ and $a/t = 0.05$....165**
**B4. Influence Coefficients for Inside Axial and Circumferential Semi-elliptic Surface Flaws: $R/t = 10$ and $a/t = 0.075$....166**
**B5. Influence Coefficients for Inside Axial and Circumferential Semi-elliptic Surface Flaws: $R/t = 10$ and $a/t = 0.1$....167**
**B6. Influence Coefficients for Inside Axial and Circumferential Semi-elliptic Surface Flaws: $R/t = 10$ and $a/t = 0.2$....168**
**B7. Influence Coefficients for Inside Axial and Circumferential Semi-elliptic Surface Flaws: $R/t = 10$ and $a/t = 0.3$....169**
**B8. Influence Coefficients for Inside Axial Semi-elliptic Surface Flaws: $R/t = 10$ and $a/t = 0.5$....170**
**B9. Influence Coefficients for Inside Circumferential Semi-elliptic Surface Flaws: $R/t = 10$ and $a/t = 0.5$....171**
**B10. Influence Coefficients for Inside Axial Infinite-Length Surface Flaws, $R/t = 10$ ....172**
**B10. (continued) Influence Coefficients for Inside Axial Infinite-Length Surface Flaws, $R/t = 10$ ....173**
**B11. Influence Coefficients for Inside Circumferential 360 Degree Surface Flaws, $R/t = 10$174**
**B11. (continued) Influence Coefficients for Inside Circumferential 360 Degree Surface Flaws, $R/t = 10$....175**
**C1. Static Initiation Toughness $K_{Ic}$ Extended Database....177**
**C2. Crack Arrest Toughness $K_{Ia}$ ORNL 99/27 Database....183**
**C3. Crack Arrest Toughness $K_{Ia}$ Extended $K_{Ia}$ Database – Large Specimen Data....186**
**F1. $\Delta RT_{epistemic}$ Ranked Data with Order-Statistic Estimates of $P$....195**
**F2. ODRPACK Results of ODR Analysis of $\Delta RT_{epistemic}$ Model Equation ....199**
**F2. ODRPACK Results of ODR Analysis of $\Delta RT_{epistemic}$ Model Equation (continued)....200**
**F3. Data Used in the Development of the $\Delta RT_{arrest}$ Model ....205**
**F4. ODRPACK Results of ODR Analysis of $\Delta RT_{arrest}$ Model Equation ....206**
**F4. ODRPACK Results of ODR Analysis of $\Delta RT_{arrest}$ Model Equation (continued)....207**
**F4. ODRPACK Results of ODR Analysis of $\Delta RT_{arrest}$ Model Equation (continued)....208**

# LIST OF FIGURES

**Figure** **Page**

**1.1 The beltline region of the reactor pressure vessel wall extends from approximately one foot above the active reactor core to one foot below the core (adapted from []). .....2**
**3.1. FAVOR$^{EP}$ data streams flow through three modules: (1) FAVLoad, (2) FAVPFM, and (3) FAVPost.....10**
**3.2. The FAVOR$^{EP}$ load generator module FAVLoad performs deterministic analyses for a range of thermal-hydraulic transients.....11**
**3.3. Flaw models in FAVOR$^{EP}$ include infinite-length surface breaking flaws, finite-length semi-elliptic surface flaws (with aspect ratios $L$ / $a$ = 2, 6, and 10), and fully elliptic embedded flaws. All flaw models can be oriented in either the axial or circumferential directions. .....13**
**3.4. The FAVPFM$^{EP}$ module takes output from FAVLoad$^{EP}$ and user-supplied data on flaw distributions and embrittlement of the RPV beltline and generates PFMI and PFMF arrays.....15**
**3.5. Flow chart for improved PFM model implemented in FAVPFM$^{EP}$ showing the four primary nested loops – (1) *RPV Trial Loop*, (2) *Flaw Loop*, (3) *Transient Loop*, and (4) *Time Loop*. Note: ++ notation indicates increment index by 1, e.g., $i$++ means $i$=$i$+1.17**
**3.6. Fabrication configurations of PWR beltline shells (adapted from [4]): (a) rolled-plate construction with axial and circumferential welds and (b) ring-forging construction with circumferential welds only.....19**
**3.7. FAVOR$^{EP}$ uses a discretization of the RPV beltline region to resolve the variation in radiation damage in terms of plate, axial weld, and circumferential weld major regions which are further discretized into multiple subregions. .....21**
**3.8. Fitted surface functions for $n$ = 5 (a) and (b) $\alpha\left(E/\sigma_y, m\right)$ and (c) and (d) $k\left(E/\sigma_y, m\right)$. 25**
**3.9. Fitted surface functions for $n$ = 20 (a) and (b) $\alpha\left(E/\sigma_y, m\right)$ and (c) and (d) $k\left(E/\sigma_y, m\right)$.25**
**3.10. Example of warm prestressing: (a) loading history with pressure applied to the inner surface and the temperature at the crack tip, (b) load path for a flaw showing two WPS regions. (*cpi* is the instantaneous conditional probability of initiation). .....30**
**3.11. Example probability density functions for (a) normal and logistic and (b) uniform, Weibull, and lognormal continuous distributions. .....35**
**3.12. Interaction of the applied $K_I$ time history and the Weibull $K_{Ic}$ statistical model for a postulated flaw.....38**
**3.13. The parameter $cpi(\tau)_{(i,j,k)}$ is the instantaneous conditional probability of initiation (*cleavage fracture*) obtained from the Weibull $K_{Ic}$ cumulative distribution function. $CPI_{(i,j,k)}$ is the maximum value of $cpi(\tau)_{(i,j,k)}$. (Note: $i$ = transient index, $j$ = RPV trial index, and $k$ = flaw index) .....40**
**3.14. $\Delta cpi(\tau^n)_{(i,j,k)}$ is the increase in $cpi(\tau^n)_{(i,j,k)}$ that occurs during each discrete time step. When the maximum value of $cpi(\tau^n)_{(i,j,k)}$ is reached, negative values of $\Delta cpi(\tau^n)_{(i,j,k)}$ are set to zero. (Note: $i$ = transient index, $j$ = RPV trial index, and $k$ = flaw index).....40**
**3.15. At the time of initiation, the three categories of flaws are transformed into infinite-length flaws: (a) Category 1 semi-elliptic surface-breaking circumferential flaws become 360 degree circumferential flaws, (b) and (c) Category 2 and 3 embedded flaws become inifinite-length axial or 360 degree circumferential flaws at the same depth. Category 1 flaws are only oriented in the circumferential direction.....42**
**3.16. Given a $J_R$ curve in power-law model form and current flow stress, $\sigma_f$, the initiation toughness, $J_{Ic}$, and local tearing modulus, $T_R$, are uniquely defined (see ASTM E-1820 [87]). .....48**
**3.17. Flowchart for PFM model – the Initiation-Growth-Arrest (*IGA*) submodel can be viewed as a Monte Carlo model nested within the larger PFM Monte Carlo model. For a**

given flaw, the *IGA* submodel is called after the *CPI* for the current transient has been calculated. Note: ++ notation indicates increment index by 1; e.g., *i*++ means *i*=*i*+1. ....57
Fig 3.18. (a) Flow chart for Initiation-Growth-Arrest Submodel – The *IGA Propagation* submodel is only called for flaws with increasing *CPIs*. The weld-layering scheme is also shown for *Initiation-Growth-Arrest* Model. No through-wall resampling is carried out for plates or forgings. ....58
3.18. (continued) (b) *IGA Propagation* submodel to test for Stable Arrest (no failure) and Vessel Failure. ....59
3.18 (continued) (c) *Unstable-Ductile-Tearing* submodel to test for either stable tearing to a new flaw position, *a**, or unstable ductile tearing that fails the vessel. ....60
3.19. An example Category 2 flaw (a) initiates, (b) expands into an infinite-length flaw, (c) advances to new weld layer and resamples chemistry content to calculate new $RT_{NDT}$, (d) continues growth until either failure by net-section plastic collapse of remaining ligament or stable crack arrest. The potential for arrest and subsequent re-initiation is also modeled. ....61
3.20. *IGA Propagation* submodel mesh used to estimate $dJ_{applied}$ / d*a* using a second-order central finite-difference ratio. ....70
3.21. The FAVOR$^{EP}$ post-processor FAVPost$^{EP}$ combines the distributions of conditional probabilities of initiation and failure calculated by FAVPFM$^{EP}$ with initiating frequency distributions for all of the transients under study to create distributions of frequencies of RPV fracture and failure. ....72
4.1. Isoparametric mapping from parameter space to axisymmetric $\mathbb{R}^1$ Euclidean space using three-node quadratic basis functions. ....75
4.2. One-dimensional axisymmetric finite-element model used in FAVOR$^{EP}$ to calculate both temperature and stress histories through the wall of an RPV. ....76
4.3. Influence coefficients, *K**, have been calculated for finite semi-elliptic flaws with aspect ratios $L / a = 2$, 6, and 10 for $R_i / t = 10$. ....83
4.4. Crack-surface loading cases for determining finite 3D flaw influence coefficients: (a) uniform unit load, (b) linear load, (c) quadratic load, and (d) cubic load. ....84
4.5. Influence coefficients have been computed for both infinite axial and 360-degree circumferential flaws. ....86
4.6. Superposition allows the use of an equivalent problem to compute the stress intensity factor. ....86
4.7. Influence coefficients, *K**, represent stress intensity factor per unit load applied to the crack face. ....87
4.8. Geometry and nomenclature used in embedded-flaw model. ....89
4.9. Resolution of computed nonlinear stress profile into the linear superposition of effective membrane and bending stresses. ....89
4.10 Comparison of benchmark ABAQUS solutions against FAVOR$^{EP}$ for a PTS transient: (a) $K_I$ driving force and (b) *T*-stress. ....94
4.11 Normalized reference *T*-stresses, $V_n$, for (a) axial infinite and (b) 360-degree circumferential inner surface-breaking flaws as a function of relative flaw depth, *a/t*. $R_{inner} / t = 10$ for a cylindrical RPV. ....97
Fig.4.12 *T*-stress influence coefficients, $D_n$, for (a) axial infinite and (b) 360-degree circumferential inner surface-breaking flaws as a function of relative flaw depth, *a/t*. $R_{inner} / t = 10$ for a cylindrical RPV. ....97
4.13 Comparison of benchmark ABAQUS solutions against FAVOR$^{EP}$ for a PTS transient: (a) $K_I$ driving force and (b) *T*-stress. ....98
4.14 Comparison between ABAQUS, v6.5, (symbols) and FAVOR$^{EP}$, v05.1, (curves) ($K_I$,$T_{stress}$) embedded flaw solutions: (a) and (b) pure mechanical (increasing internal pressure) loading on flaw model e-A3, (c) and (d) combined mechanical and thermal loading on flaw models e-A1 to e-A4 (Oconee thermal hydraulic transient 109), (e) and (f) combined mechanical and thermal loading on flaw models e-C1 to e-C3 (Oconee thermal hydraulic transient 109), (g) and (h) predominantly thermal loading on flaw

**models e-A1 to e-A4 (Beaver Valley thermal hydraulic transient 007) – RPV inner radius = 90 in., $t_{wall}$ = 9 in., and $t_{clad}$ = 0.25 in., aspect ratio = $L/2a$. .....101**
**4.15. Weld residual stress through-thickness distribution developed for use in RPV integrity analyses.....103**
**4.16. Relationship between the change in the fracture-toughness index temperature ($\Delta T_0 \approx \Delta RT_{NDT}$) change in the 30 ft-lbf CVN transition temperature ($\Delta T_{30}$) for welds and plates/forgings produced by irradiation. The difference in the best-fit slopes is statistically significant (from [129]). .....108**
**4.17. ORNL 99/27 $K_{Ic}$ database including modified ASME $K_{Ic}$ curve that served as a lower-bounding reference curve in the development of a new transition index temperature. .111**
**4.18. $K_{Ia}$ databases (a) ORNL 99/27 $K_{Ia}$ database and (b) Extended $K_{Ia}$ database. .....112**
**4.19. Cumulative distribution function of the observed difference in $RT_{NDT\ 0}$ and $T_o$ (with a size of 1T) using data in the ORNL 99/27 database. 116**
**4.20 Cumulative distribution function of the difference (designated as $\Delta RT_{epistemic}$) between $RT_{NDT0}$ and a new lower-bounding reference index designated $RT_{LB}$. .....116**
**4.21The $\Delta RT_{LB}$ for HSST Plate 02. The lower-bounding transition reference temperature, $RT_{LB}$, was developed from 18 materials in the ORNL 99/27 database, where for each material $RT_{LB} = RT_{NDT0} - \Delta RT_{LB}$ .....117**
**4.22Comparison of cumulative distribution functions developed for $RT_{NDT0}$-$T_0$ and $RT_{NDT0}$-$RT_{LB}$ . .....119**
**4.23 Lognormal distribution of $\Delta RT_{ARREST} = T_{K_{Ia}} - T_0$ as a function of $T_0$ .....122**
**4.24 Lognormal probability densities for $\Delta RT_{Arrest}$ as function of $T_0$. .....122**
**4.25 Proposed adjustment to $RT_{LB}$ arises from observed offset between $\Delta RT_{LB}$ CDF and $RT_{NDT} - T_0$ CDF at median ($P$ = 0.5). .....123**
**4.26 Weibull statistical distribution for plane-strain cleavage initiation fracture toughness, $K_{Ic}$, with prescribed validity bounds. The ORNL 99/27 $K_{Ic}$ database was used in the construction of the model. .....125**
**4.27 Lognormal statistical distribution for plane-strain crack arrest fracture toughness, $K_{Ia}$, constructed using the (a) Model 1: ORNL 99/27 $K_{Ia}$ database normalized by the arrest reference temperature, $RT_{Arrest}$ and (b) Model 2: Extended $K_{Ia}$ database normalized by the arrest reference temperature, $RT_{Arrest}$. .....127**
**4.28 Weld fusion area definitions for (a) axial-weld subregion elements and (b) circumferential subregion elements. .....136**
**4.28 (continued) (c) Plate subregion element. .....137**
**A1. Depiction of the development history of the FAVOR$^{EP}$ code.....159**
**F1. Comparison of the initial Weibull model, $W_0$, for $\Delta RT_{epistemic}$ with the ODR model: (a) probability density functions and (b) cumulative distribution functions. .....211**
**F2. Comparison of ODR Weibull model, $W_{ODR}$, for $\Delta RT_{epistemic}$ with the models for Case 1 ($W_1$) and Case 2 ($W_2$): (a) probability density functions and (b) cumulative distribution functions. .....212**
**F3. Comparison of initial model in FAVOR$^{EP}$, $W_0$, with Case 2, $W_2$. .....213**
**F4. Comparison of ODR model, $W_{ODR}$, with Case 2, $W_2$. .....214**
**F5. Data used to develop the lognormal statistical model for $\Delta RT_{arrest}$ as a function of $T_0$ .215**
**F6. Model developed from ODR analysis of log-transformed data. .....216**
**F7. Variance of ODR model compared to final model. .....217**
**F8. Comparison of ODR model with final model. .....218**

## ACKNOWLEDGMENTS

The development of the new methodologies and models incorporated into FAVOR$^{EP}$, v05.1, has been the result of a long and fruitful collaboration with many colleagues. The contributions of the NRC staff including Dr. L. Abramson, D. Bessette, Dr. N. Chokshi, Dr. E. Hackett, D. Jackson, W. Jones, D. Kalinousky, Dr. M. Kirk, Dr. S. Malik, M. Mayfield, T. Santos, Dr. N. Siu, and R. Woods are gratefully acknowledged. The new approaches to conditional probability of initiation and failure and the treatment of multiple flaws were developed in collaboration with Professors M. Modarres, A. Mosleh, and Dr. F. Li of the University of Maryland Center for Technology Risk Studies. The new flaw-characterization distributions were developed by D. Jackson of the NRC and Drs. F. Simonen, S. Doctor, and G. Schuster at Pacific Northwest National Laboratory, and the new detailed fluence maps were developed by W. Jones and T. Santos of the NRC and Dr. J. Carew of Brookhaven National Laboratory. Dr. K. Bowman of the Computer Science and Mathematics Division at Oak Ridge National Laboratory (ORNL) developed the statistical procedures that were applied in the development of the Weibull fracture-toughness model for FAVOR$^{EP}$. Drs. M. Sokolov and S. K. Iskander of the Metals and Ceramics Division at ORNL carried out the survey of fracture-toughness data that produced the ORNL 99/27 extended fracture-toughness database. Dr. B. R. Bass, head of the Heavy Section Steel Technology Program at ORNL, provided the survey of fracture-arrest data from the Large-Specimen experiments carried out in the 1980s. Drs. E. Eason and J. Wright of Modeling and Computing Services, Boulder, Colorado and Prof. G. R. Odette of the University of California at Santa Barbara developed the new irradiation-shift model implemented in FAVOR$^{EP}$, v05.1. In addition to developing the ductile-tearing model implemented in this version of FAVOR$^{EP}$, Dr. M. Kirk of the NRC led a Working Group in the development of the new fracture-toughness models in FAVOR$^{EP}$. Other members of this Working Group included, in addition to the authors, Dr. R. K. Nanstad and J. G. Merkle of the Metals and Ceramics Division at ORNL, Professor Modarres and Dr. F. Li of the University of Maryland Center for Technology Risk Studies, Dr. M. Natishan of PEAI, and Dr. B. R. Bass. J. G. Merkle with Dr. Nanstad developed the lower-bounding reference temperature approach that was adopted in the uncertainty analysis of the reference-nil-ductility transition temperature. Several conversations with Prof. R. Dodds of the University of Illinois, Prof. K. Wallin of VTT, Finland, and Dr. C. Faidy of Electricité de France were most helpful in the course of this effort. There were also contributions from many members of the nuclear industry.

# 1. Introduction

The **F**racture **A**nalysis of **V**essels – **O**ak **R**idge – **E**lastic-**P**lastic (FAVOR$^{EP}$, v05.1) computer program has been developed to perform a risk-informed probabilistic analysis of the structural integrity of a nuclear reactor pressure vessel (RPV) when subjected to an overcooling event. The focus of this analysis is the *beltline* region of the RPV wall as shown in Fig. 1.1. *Overcooling events*, where the temperature of the coolant in contact with the inner surface of the RPV wall rapidly decreases with time, produce temporally dependent temperature gradients that induce biaxial stress states varying in magnitude through the vessel wall. Near the inner surface and through most of the wall thickness, the stresses are tensile, thus generating Mode I opening driving forces that can act on possible surface-breaking or embedded flaws. If the internal pressure of the coolant is sufficiently high, then the combined thermal plus mechanical loading results in a transient condition known as a pressurized-thermal shock (PTS) event.

In 1999, Dickson et al. [1] illustrated that the application of fracture-related technology developed since the derivation of the current pressurized-thermal-shock (PTS) regulations (established in the early-mid 1980s) had the potential for providing a technical basis for a re-evaluation of the current PTS regulations. Based on these results, the U.S. Nuclear Regulatory Commission (NRC) began the *PTS Re-evaluation Project* to establish a technical basis rule within the framework established by modern probabilistic risk assessment techniques and advances in the technologies associated with the physics of PTS events. An updated computational methodology has been developed over the last four years through research and interactions among experts in the relevant disciplines of thermal-hydraulics, probabilistic risk assessment (PRA), materials embrittlement, probabilistic fracture mechanics (PFM), and inspection (flaw characterization). This updated methodology has been implemented in the **F**racture **A**nalysis of **V**essels – **O**ak **R**idge – **E**lastic-**P**lastic (FAVOR$^{EP}$, v05.1) computer code developed for the NRC by the Heavy Section Steel Technology (HSST) program at Oak Ridge National Laboratory (ORNL).

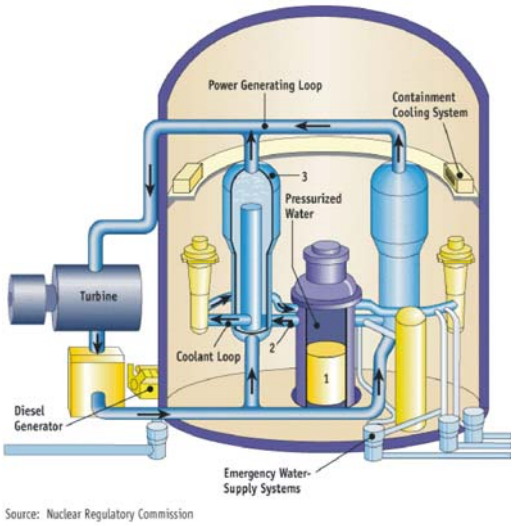


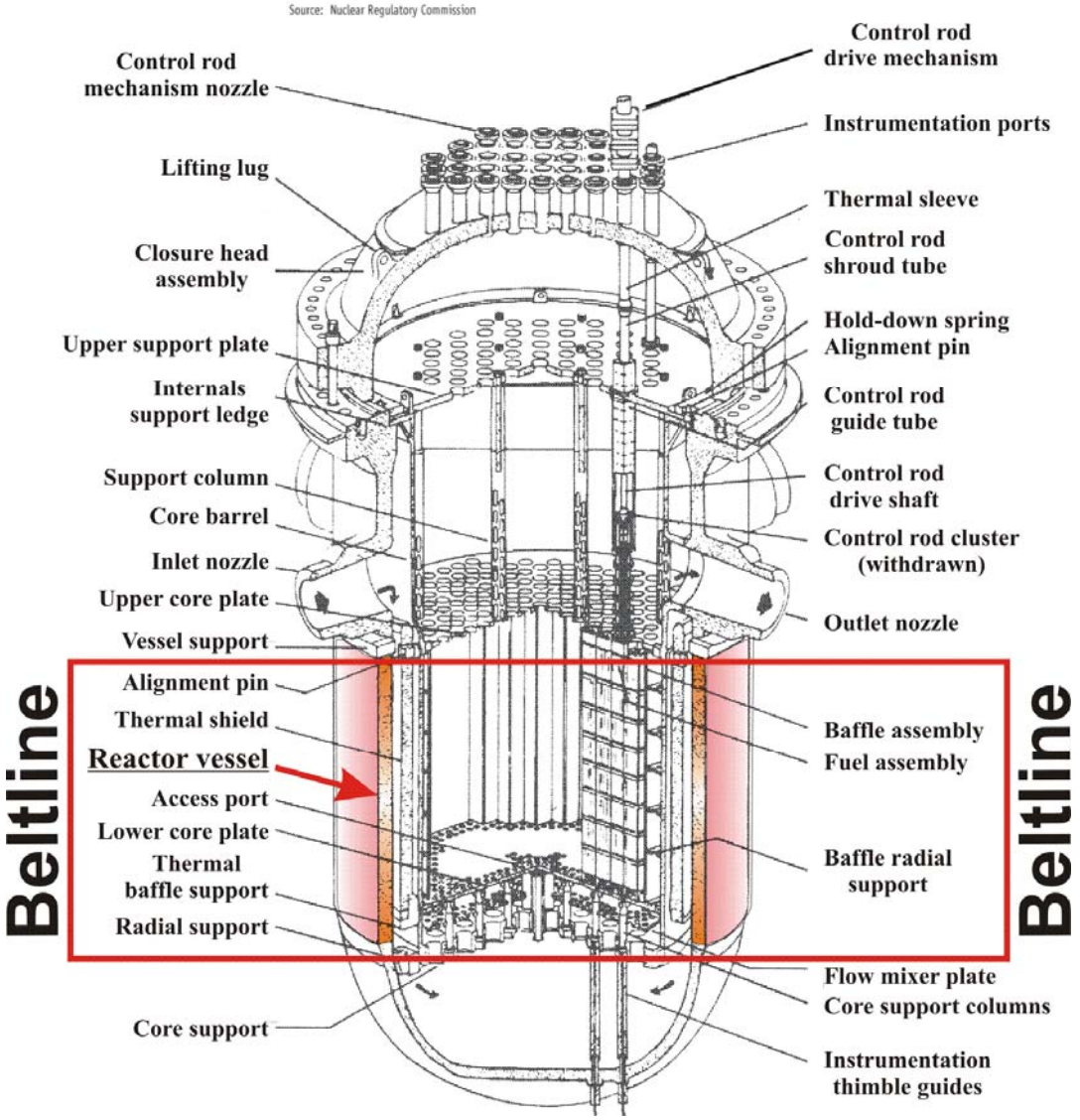


**Fig. 1.1 The beltline region of the reactor pressure vessel wall extends from approximately one foot above the active reactor core to one foot below the core (adapted from [2]).**

This baseline release of the new FAVOR$^{EP}$ (version-control code v05.1) implements the results of the preparatory phase of the PTS Re-evaluation Project in an improved PFM model for calculating the conditional probability of crack initiation (by plane-strain cleavage initiation) and the conditional probability of vessel failure (by through-wall cracking). Although the analysis of PTS has been the primary motivation in the development of FAVOR$^{EP}$, it should also be noted that the problem class for which FAVOR$^{EP}$ is applicable encompasses a broad range of events that include normal operational transients (such as start-up and shut-down) as well as additional upset conditions beyond PTS. Essentially any event in which the reactor pressure vessel (RPV) wall is exposed to time-varying thermal-hydraulic boundary conditions could be an appropriate candidate for a FAVOR$^{EP}$ analysis of the vessel's structural integrity.

In support of the PTS Re-evaluation Project, the following advanced technologies and new capabilities have been incorporated into FAVOR$^{EP}$, v05.1:

- **the ability to incorporate detailed flaw-characterization distributions from NRC research (with Pacific Northwest National Laboratory, PNNL),**
- **the ability to incorporate detailed neutron fluence regions – detailed fluence maps from Brookhaven National Laboratory, BNL,**
- **the ability to incorporate the effects of constraint loss, including approximations for plasticity, through the use of a simplified scaling model based a two-parameter ( $K_I$, $T_{stress}$ ) characterization of cleavage initiation,**
- **the ability to incorporate warm-prestressing effects into the analysis,**
- **the ability to include temperature-dependencies in the thermo-elastic properties of base and cladding,**
- **the ability to include crack-face pressure loading for surface-breaking flaws,**
- **a new ductile-fracture model simulating stable and unstable ductile tearing,**
- **a new embrittlement correlation,**
- **the ability to include multiple transients in one execution of FAVOR$^{EP}$,**
- **input from the Reactor Vessel Integrity Database, Revision 2, (RVID2) of relevant RPV material properties,**
- **fracture-toughness models based on extended databases and improved statistical distributions,**
- **a variable failure criterion, i.e., how far must a flaw propagate into the RPV wall for the vessel simulation to be considered as "failed" ?**
- **semi-elliptic surface-breaking and embedded-flaw models,**
- **through-wall weld residual stresses, and an**
- **improved PFM methodology that incorporates modern PRA procedures for the classification and propagation of input uncertainties and the characterization of output uncertainties as statistical distributions.**

Chapter 2 of this report provides a short historical perspective for viewing the pressurized-thermal-shock problem, including a summary of events leading to the current regulations. This chapter is followed by a full description of the analytical models employed in the FAVOR$^{EP}$ code, described in Chapters 3 and 4. In that presentation, particular emphasis is given to the new features of the code that were highlighted above. A summary and conclusions are given in Chapter 5. Appendix A gives a summary of the development history of FAVOR$^{EP}$ and its antecedents. Appendix B presents the database of stress-intensity-factor influence coefficients that has been implemented in FAVOR$^{EP}$ for its surface-breaking flaw models. The database of plane-strain static initiation fracture toughness, $K_{Ic}$, and plane-strain crack arrest, $K_{Ia}$, properties for pressure vessel steels is given in Appendix C. This fracture-toughness database was used in the construction of the statistical models for crack initiation and arrest that are implemented in FAVOR$^{EP}$. Appendix D presents a summary of RVID2 data to be used in FAVOR$^{EP}$ analyses for the PTS Re-evaluation Project. The point-estimation techniques used in the development of the Weibull cumulative distribution functions that estimate the epistemic uncertainty in the fracture initiation and arrest reference temperatures are given in Appendix E. The development of the sampling protocols for the epistemic uncertainties in two important reference temperatures is given in Appendix F.

# 2. Pressurized Thermal Shock Events

Overcooling events, where the temperature of the coolant in contact with the inner surface of the reactor pressure vessel (RPV) wall rapidly decreases with time, produce temporally dependent temperature gradients that induce biaxial stress states varying in magnitude through the vessel wall. Near the inner surface and through most of the wall thickness the stresses are tensile, thus presenting Mode I opening driving forces that can act on possible surface-breaking or embedded flaws. The combined thermal plus mechanical loading results in a transient condition known as a pressurized thermal shock (PTS) event.

Concern with PTS results from the combined effects of (1) simultaneous pressure and thermal-shock loadings, (2) embrittlement of the vessel material due to cumulative irradiation exposure over the operating history of the vessel, and (3) the possible existence of crack-like defects at the inner surface of or embedded within the RPV heavy-section wall. The decrease in vessel temperature associated with a thermal shock also reduces the fracture toughness of the vessel material and introduces the possibility of flaw propagation. Inner surface-breaking flaws and embedded flaws near the inner surface are particularly vulnerable, because at the inner surface the temperature is at its minimum and the stress and radiation-induced embrittlement are at their maximum.

## 2.1 Historical Review

The designers of the first pressurized-water reactor (PWR) vessels in the late 1950s and early 1960s were cognizant of PTS as a reactor vessel integrity issue where nonductile fracture was evaluated as a part of the design basis using a transition-temperature approach [3]. Continued concerns about vessel failure due to overcooling events motivated a number of advances in fracture mechanics technology in the late 1960s and the 1970s. Before the late 1970s, it was postulated that the most severe thermal shock challenging a PWR vessel would occur during a large-break loss-of-coolant accident (LOCA), where room-temperature emergency core-cooling water would flood the reactor vessel within a few minutes, rapidly cooling the wall and inducing tensile thermal stresses near the inner surface of the vessel [4]. However, the addition of pressure loading to the thermal loading was not typically considered, since it was expected that during a large-break LOCA the system would remain at low pressure. Two events in the late 1970s served to raise the concern of PTS to a higher priority in the 1980s, and this concern continues to the present.

In 1978, the occurrence of a non-LOCA event at the Rancho Seco Nuclear Power Plant in California showed that during some types of overcooling transients, the rapid cooldown could be accompanied by repressurization of the primary recirculating-cooling-water (RCW) system, compounding the effects of the thermal stresses. The Three-Mile-Island (TMI) incident in 1979, which also involved a cooldown event at high RCW system pressure, drew additional attention to the impact of operator action and control system effects on transient temperature and pressure characteristics for PTS events [3].

Following these two events, the U.S. Nuclear Regulatory Commission (NRC) designated PTS as an unresolved safety issue (A-49). Questions also arose concerning the mixing (or lack of mixing) of cold safety injection water with reactor coolant in the vessel, leading to an amplification of the PTS effect. In late 1980, the NRC issued NUREG 0737-Item II.K.2.13, which required that the operators of all PWRs and all applicants for licenses evaluate reactor vessel integrity following a small-break LOCA as part of the TMI action plan [5]. Additional potential transients were added in March of 1981. At the end of 1981, the nuclear power industry submitted its response to NUREG 0737 to the NRC. These submittals were based primarily on deterministic analyses using conservative thermal-hydraulic and fracture-mechanics models of postulated design-basis transients and the temperature and pressure time-histories from some of the PTS events that had actually been experienced in operating PWR plants [3]. On the basis of these analyses, the NRC concluded that no event having a significant probability of occurring could cause a PWR vessel to fail at that time or within the next few years. However, the NRC continued to be concerned that other events with more limiting transient characteristics in combination with the impact of operator action and control system effects were not being addressed. As a result, greater emphasis was placed on Probabilistic Risk Assessment (PRA) combined with thermal-hydraulic (T-H) analysis and probabilistic fracture mechanics (PFM) as primary vessel-integrity assessment tools.

## 2.2 Current NRC Regulatory Approach to PTS

During the 1980s, in an effort to establish generic limiting values of vessel embrittlement, the NRC funded the Integrated Pressurized Thermal Shock (IPTS) Program [4, 6, 7] which developed a comprehensive probabilistic approach to risk assessment. Current regulatory requirements are based on the resulting *risk-informed* probabilistic methodology. In the early 1980s, extensive analyses were performed by the NRC and others to estimate the likelihood of vessel failure due to PTS events in PWRs. Though a large number of parameters governing vessel failure were identified, the single most significant parameter was a correlative index of the material that also serves as a measure of embrittlement. This material index is the reference nil-ductility transition temperature, $RT_{NDT}$. The NRC staff and others performed analyses of PTS risks on a conservative and generic basis to bound

the risk of vessel failure for any PWR reactor. The NRC staff approach to the selection of the $RT_{NDT}$ screening criteria is described in SECY-82-465 [8]. Reference [9] is a short review of the derivation of the PTS *screening criteria* from both deterministic and probabilistic fracture mechanics considerations. The analyses discussed in SECY-82-465 led to the establishment of the *PTS rule* [10], promulgated in Title 10 of the *Code of Federal Regulations*, Chapter I, Part 50, Section 50.61 (10CFR50.61), and the issuance of NRC Regulatory Guide 1.154 (RG1.154) [11].

The *PTS rule* specifies *screening criteria* in the form of limiting irradiated values of $RT_{NDT}$ (designated by the rule as $RT_{PTS}$) of 270 °F for axially oriented welds, plates, and forgings and 300 °F for circumferentially oriented welds. The PTS rule also prescribes a method to estimate $RT_{PTS}$ for materials in an RPV in Regulatory Guide 1.99, Revision 2 [12]. For nuclear power plants to operate beyond the time that they exceed the screening criteria, the licensees must submit a plant-specific safety analysis to the NRC three years before the screening limit is anticipated to be reached. Regulatory Guide 1.154 recommends the content and format for these plant-specific integrated PTS analyses with the objective of calculating an estimate for the frequency of vessel failure caused by PTS events. RG1.154 also presents the *primary PTS acceptance criterion* for acceptable failure risk to be a mean frequency of less than $5\times10^{-6}$ vessel failures per year.

## 2.3 Contributions of Large-Scale Experiments to the Technical Basis for PTS Assessment

A number of large-scale experiments conducted internationally over the past 30 years have contributed significantly to a better understanding of the factors influencing the behavior of RPVs subjected to postulated PTS scenarios [13]. These experiments, several of which are summarized in Table 1.1, reflect different objectives that range from studies of "separate effects" to others that integrate several features into a single experiment. In Table 1.1, the experiments are organized in terms of four specimen groups: (1) pressure-vessel specimens, (2) cylindrical specimens, (3) plate specimens, and (4) beam specimens. The actual test specimens were fabricated from prototypical RPV steels, including plate, forgings, and weld product forms. Some of the specimens included prototypical cladding, and others used steels that had been heat-treated or were fabricated with a special chemistry to simulate near-end-of-licensing (degraded properties) conditions.

In recent years, these large-scale experiments have provided a catalyst in western Europe and the United States for intensive international collaboration and for the formation of multinational networks to assess and extend RPV/PTS technology. Project FALSIRE [14-17] was initiated in 1989 through support provided by governmental agencies within Germany and the U. S., under sponsorship of the OECD/Nuclear Energy Agency. Within FALSIRE, researchers from a large number of international organizations used selected large-scale experiments to evaluate levels of conservatism in RPV

integrity assessment methodologies. In 1993, the Joint Research Centre of the European Commission launched the Network for Evaluating Structural Components (NESC) to study the entire process of RPV integrity assessment. The NESC projects brought together a large number of leading international research organizations to evaluate all aspects of the assessment process (i.e., fracture methodologies, material properties characterization, inspection trials, and experimental techniques) through a large-scale PTS spinning cylinder experiment [18, 36]. Issues receiving special attention in the NESC experiment included (1) effects of constraint, (2) effects of cladding and HAZ regions, and (3) behavior of sub-clad flaws under simulated PTS loading.

The large-scale experimental database and extensive body of associated analytical interpretations have provided support for the technical basis that underpins various elements of the fracture models implemented in the FAVOR$^{EP}$ code. In particular, these results have contributed significantly to confirming the applicability of fracture methodologies to cleavage fracture events in RPV steels, including crack initiation and crack arrest. References [14-18, 36] (and references given therein) provide comprehensive evaluations of RPV integrity assessment methodologies applied to a broad selection of experiments.

Within the HSST Program, the large-scale experiments are contributing to a framework for future integration of advanced fracture techniques into RPV integrity assessment methodology. These advanced techniques provide a sharp contrast to the current approach to RPV integrity assessment as exemplified by the methodology implemented in the FAVOR$^{EP}$ code (described herein). The FAVOR$^{EP}$ code executes probabilistic defect assessments of RPVs using (1) linear-elastic stress analysis methods and (2) conventional, high-constraint fracture-toughness data. The advanced fracture-mechanics methodologies currently under development depart from the latter approach in three major components: (1) stress analyses of cracked regions to include plasticity, (2) constraint adjustments to material toughness values for shallow surface and embedded flaws, and (3) probabilistic descriptions of material fracture toughness in the transition temperature region consistent with the methodologies embodied by ASTM Standard E-1921 (i.e., the Master Curve). Development of an updated analytical tool incorporating these advanced techniques and providing extended applicability to RPV integrity assessments is envisioned for the near future.

**Table 1.1 Large-Scale PTS Experiments and Performing Organizations**

| ID No. | Experiment Title | Research Organization | Country | Refs. |
|---|---|---|---|---|
| **Tests with Pressurized Vessels** | | | | |
| ITV 1-8 | Intermediate Test Vessels | Oak Ridge National Laboratory | USA | 19-25 |
| PTSE-1 | Pressurized Thermal Shock Experiments | Oak Ridge National Laboratory | USA | 26 |
| PTSE-2 | Pressurized Thermal Shock Experiments | Oak Ridge National Laboratory | USA | 27 |
| PTS I/6 | Pressurized Thermal Shock Experiment I/6 | Central Research Institute for Structural Materials (CRISM) | Russia | 28, 29 |
| **Tests with Cylindrical Specimens** | | | | |
| NKS-3 | Thermal Shock Experiment 3 | Materialprüfungsanstalt (MPA) | Germany | 30 |
| NKS-4 | Thermal Shock Experiment 4 | Materialprüfungsanstalt (MPA) | Germany | 30 |
| NKS-5 | Thermal Shock Experiment 5 | Materialprüfungsanstalt (MPA) | Germany | 31 |
| NKS-6 | Thermal Shock Experiment 6 | Materialprüfungsanstalt (MPA) | Germany | 29, 31 |
| SC-1 | Spinning Cylinder PTS Experiment 1 | AEA Technology | UK | 32 |
| SC-2 | Spinning Cylinder PTS Experiment 2 | AEA Technology | UK | 32 |
| SC-4 | Spinning Cylinder PTS Experiment 4 | AEA Technology | UK | 33 |
| TSE-6 | Thermal Shock Cylinders (Cylinder with Short Flaws) | Oak Ridge National Laboratory (ORNL) | USA | 34 |
| TSE-7 | Thermal Shock Cylinders (Clad Cylinder) | Oak Ridge National Laboratory (ORNL) | USA | 35 |
| TSE-8 | Thermal Shock Cylinders (Clad Cylinder) | Oak Ridge National Laboratory (ORNL) | USA | 35 |
| NESC-1 | NESC-1 Spinning Cylinder PTS Experiment | Network for Evaluating Steel Components (NESC) | International Network | 36 |
| **Tests with Plate Specimens** | | | | |
| PTS Step B | Wide-Plate PTS Step B Experiment | Japan Power and Engineering Inspection Corporation (JAPEIC) | Japan | 37 |
| WP-1 & 2 | Wide-Plate Crack Arrest Tests of A533B and LUS Steels | Oak Ridge National Laboratory (ORNL) | USA | 38, 39 |
| GP-1 | Wide Plate Test | Materialprüfungsanstalt (MPA) | Germany | 40 |
| **Tests with Beam Specimens** | | | | |
| DD-2 & DSR-3 | Clad-beam experiments | Electricité de France (EdF) | France | 29, 41 |
| SE(B) RPV Steel | Full-Thickness Clad Beam Experiments | National Institute of Standards and Testing (NIST) and ORNL | USA | 42, 43 |
| CB | Cruciform Beam (CB) Experiments | Oak Ridge National Laboratory (ORNL) | USA | 44 |

# 3. Structure and Organization of the FAVOR$^{EP}$ Code

## 3.1 FAVOR$^{EP}$ – Computational Modules and Data Streams

As shown in Fig. 3.1, FAVOR$^{EP}$ is composed of three computational modules: (1) a deterministic load generator (**FAVLoad$^{EP}$**), (2) a Monte Carlo PFM module (**FAVPFM$^{EP}$**), and (3) a post-processor (**FAVPost$^{EP}$**). Figure 3.1 also indicates the nature of the data streams that flow through these modules.

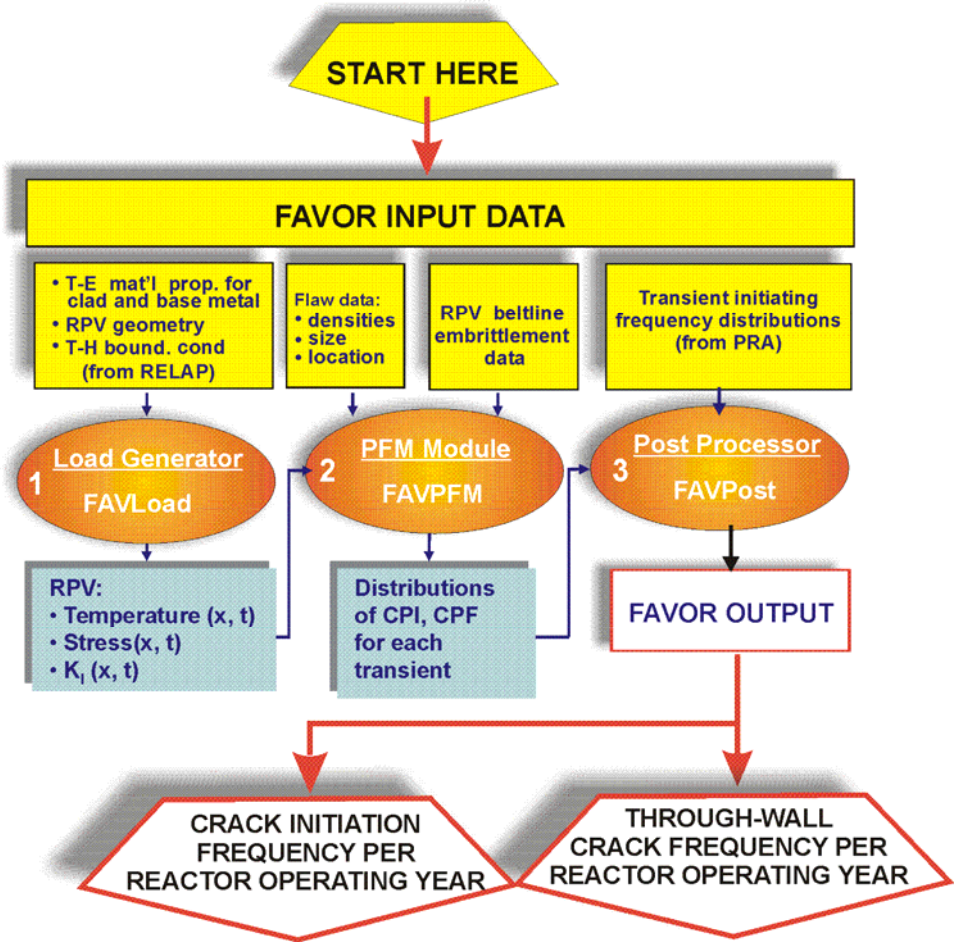


**Fig. 3.1. FAVOR$^{EP}$ data streams flow through three modules: (1) FAVLoad, (2) FAVPFM, and (3) FAVPost.**

The formats of the required user-input data files are discussed in detail in the companion report *FAVOR$^{EP}$ (v05.1): User's Guide* [45].

## 3.2 FAVOR$^{EP}$ Load Module (FAVLoad)

The functional structure of the FAVOR$^{EP}$ load module, FAVLoad$^{EP}$, is shown in Fig. 3.2, where multiple thermal-hydraulic transients are defined in the input data. The number of transients that can be analyzed in a single execution of FAVLoad$^{EP}$ is dependent upon the memory capacity of the computer being used for the analysis. For each transient, deterministic calculations are performed to produce a load-definition input file for FAVPFM$^{EP}$. These load-definition files include time-dependent through-wall temperature profiles, through-wall circumferential and axial stress profiles, and stress-intensity factors for a range of axially and circumferentially oriented inner surface-breaking flaw geometries (both infinite- and finite-length).

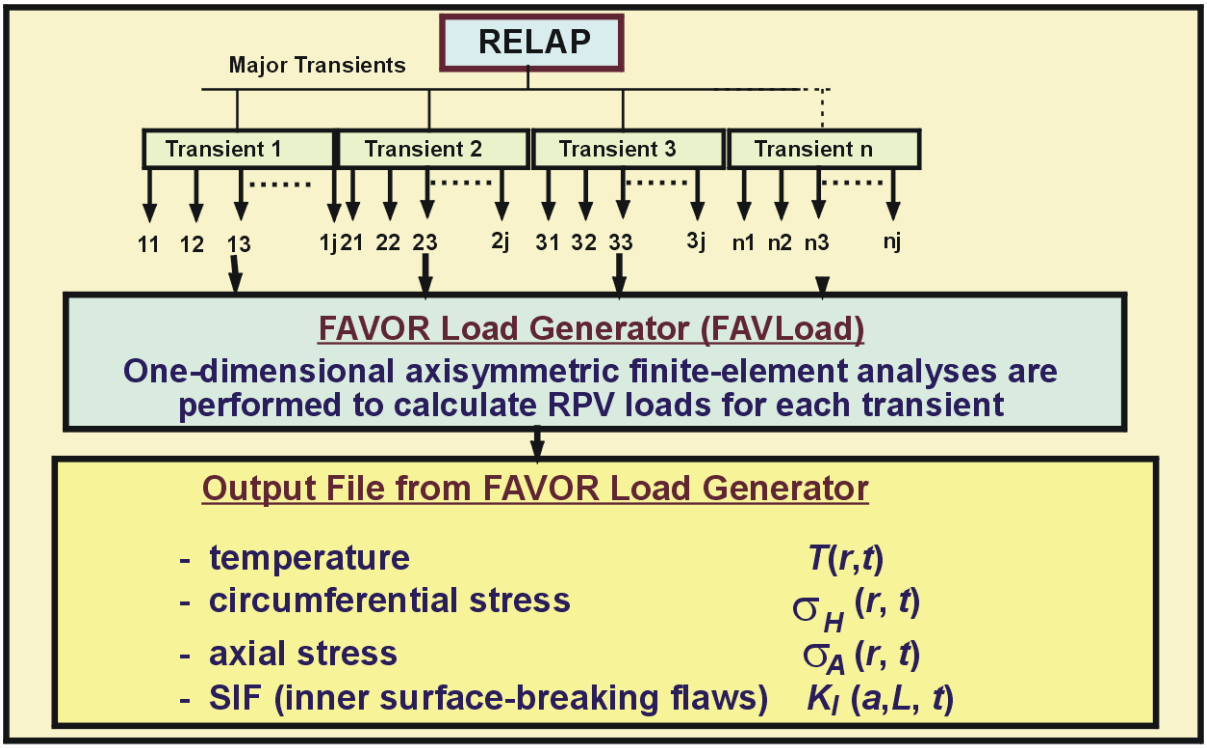


**Fig. 3.2. The FAVOR$^{EP}$ load generator module FAVLoad performs deterministic analyses for a range of thermal-hydraulic transients.**

### 3.2.1 Thermal-Hydraulic Transient Definitions

The thermal-hydraulic (T-H) definitions required by FAVLoad$^{EP}$ are supplied by the user in the form of digitized tables of bulk coolant temperature, convective heat-transfer coefficient, and internal pressure, all as functions of elapsed time for the transient. Time-history data pairs can be input for each of the three variables, allowing a very detailed definition of the thermal-hydraulic loading imposed on the RPV internal wall. An option is also available to specify a stylized exponentially decaying coolant temperature-time history.

### 3.2.2 Required Vessel Geometry and Thermo-Elastic Property Data

The FAVLoad$^{EP}$ module requires fundamental vessel geometry data, including the vessel's inner radius, wall thickness, and cladding thickness. Temperature-dependent thermo-elastic properties are also input for the cladding and base materials. These geometric descriptions and property data for the RPV are treated as fixed parameters in all subsequent analyses.

### 3.2.3 Deterministic Analyses

Finite-element analyses are carried out on a one-dimensional axisymmetric model of the vessel wall. The transient heat conduction equation with temperature-dependent properties is solved for the combined cladding and base materials to produce time-varying temperature profiles through the wall. The finite-element stress analysis calculates radial displacements and then, through strain-displacement and linear-elastic stress-strain relationships, time-varying axial and hoop stress profiles are also calculated. These stresses include the effects of thermal and mechanical loading (internal pressure applied to the inner vessel surface and exposed crack face) along with the option of superimposed weld-residual stress profiles developed by the HSST program. The stress discontinuity at the clad-base interface is also captured by the finite-element stress model. Through the specification of a selected stress-free temperature by the user, the effects of an initial thermal-differential expansion between the cladding and base materials can also be included in the quasi-static load path. The finite-element thermal and stress models use the same quadratic elements and graded-mesh discretization.

The finite-element method (FEM), together with the very detailed definition of the thermal-hydraulic boundary conditions, provides the capability to generate accurate thermal, stress, and applied stress-intensity factor, $K_I$, solutions. The application of FEM in this way allows the resolution of complex thermal-hydraulic transients that exhibit discontinuities in the boundary condition time-histories, e.g., transients with late repressurizations.

Time-dependent stress-intensity factors for infinite-length and finite-length (semi-elliptic) surface-breaking flaws are calculated for a range of flaw depths, sizes, and aspect ratios. Due to its generality, the embedded-flaw model was implemented in the FAVPFM$^{EP}$ module, rather than FAVLoad$^{EP}$. The details of these deterministic analyses are given in Chapter 4. See Fig. 3.3 for a summary of the flaw models available in FAVOR$^{EP}$.

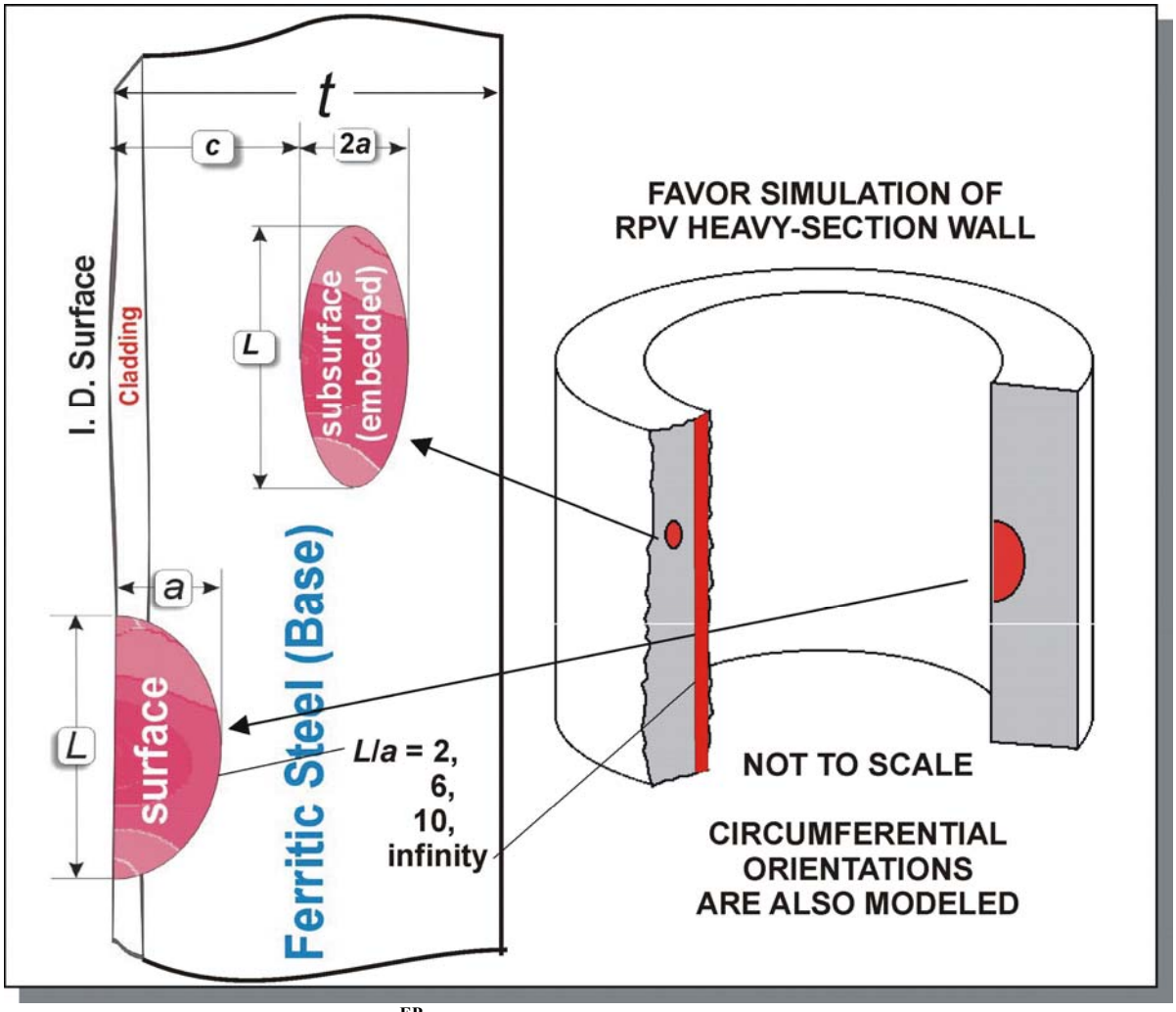


**Fig. 3.3. Flaw models in FAVOR$^{EP}$ include infinite-length surface breaking flaws, finite-length semi-elliptic surface flaws (with aspect ratios $L$ / $a$ = 2, 6, and 10), and fully elliptic embedded flaws. All flaw models can be oriented in either the axial or circumferential directions.**

### 3.2.4 Flaw Categories Used in FAVOR$^{EP}$

As indicated in Fig. 3.3, three categories of flaws are available in FAVOR$^{EP}$:

- **Category 1 – surface-breaking flaws**

  infinite length – aspect ratio $L/a = \infty$
  semi-elliptic – aspect ratio $L/a = 2$
  semi-elliptic – aspect ratio $L/a = 6$
  semi-elliptic – aspect ratio $L/a = 10$

- **Category 2 – embedded flaws – fully elliptic geometry with inner crack tip located between the clad/base interface and 1/8$t$ from the inner surface ($t$ = thickness of the RPV wall)**

- **Category 3 – embedded flaws – fully elliptic geometry with inner crack tip located between 1/8$t$ and 3/8$t$ from the inner surface**

## 3.3 FAVOR$^{EP}$ PFM Module (FAVPFM)

The FAVOR$^{EP}$ PFM model is based on the Monte Carlo technique, where deterministic fracture analyses are performed on a large number of stochastically generated RPV *trials* or *realizations*. Each vessel realization can be considered a perturbation of the *uncertain* condition of the specific RPV under analysis. The condition of the RPV is considered uncertain in the sense that a number of the vessel's properties along with the postulated flaw population have uncertainties associated with them. These input uncertainties are described by statistical distributions. The RPV trials propagate the input uncertainties with their interactions through the model, thereby determining the probabilities of crack initiation and through-wall cracking for a set of postulated PTS events at a selected time in the vessel's operating history. The improved PFM model also provides estimates of the uncertainties in its outputs in terms of discrete statistical distributions. By repeating the RPV trials a large number of times, the output values constitute a random sample from the probability distribution over the output induced by the combined probability distributions over the several input variables [46].

The assumed fracture mechanism is stress-controlled cleavage initiation (in the lower-transition-temperature region of the vessel material) modeled under the assumptions of linear-elastic fracture mechanics (LEFM). The failure mechanism by through-wall cracking is the prediction of sufficient flaw growth either (1) to produce a net-section plastic collapse of the remaining ligament or (2) to advance the crack tip through a user-specified fraction of the wall thickness. Flaw growth can be due to either cleavage propagation or stable ductile tearing. In addition, if the conditions for unstable ductile tearing are satisfied, then vessel failure by through-wall cracking is assumed to occur.

The Monte Carlo method involves sampling from appropriate probability distributions to simulate many possible combinations of flaw geometry and RPV material embrittlement subjected to transient loading conditions. The PFM analysis is performed for the beltline of the RPV, usually assumed to extend from one foot below the reactor core to one foot above the reactor core. The RPV beltline can be divided into *major regions* such as axial welds, circumferential welds, and plates or forgings that may have their own embrittlement-sensitive chemistries. The major regions may be further discretized into *subregions* to accommodate detailed neutron fluence maps that can include significant details regarding azimuthal and axial variations in neutron fluence. The general data streams that flow through the FAVPFM$^{EP}$ module are depicted in Fig. 3.4.

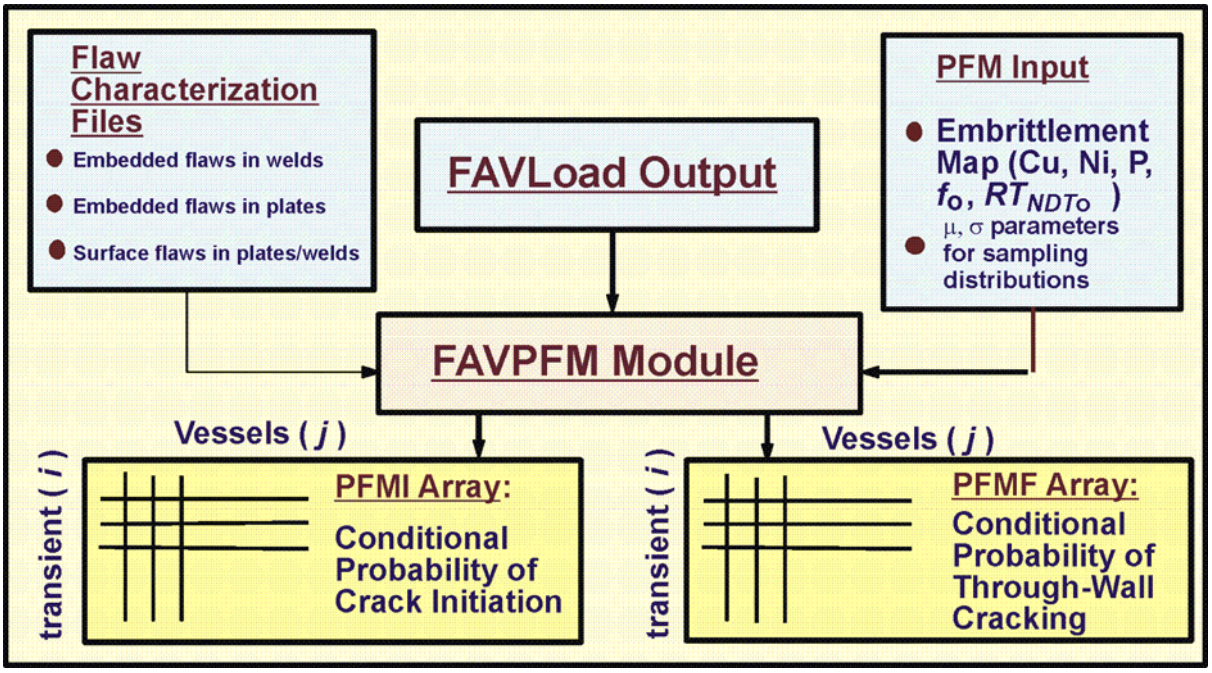


**Fig. 3.4. The FAVPFM$^{EP}$ module takes output from FAVLoad$^{EP}$ and user-supplied data on flaw distributions and embrittlement of the RPV beltline and generates PFMI and PFMF arrays.**

As shown in Fig. 3.4, the FAVPFM$^{EP}$ module requires, as input, load-definition data from FAVLoad$^{EP}$ and user-supplied data on flaw distributions and embrittlement of the RPV beltline. FAVPFM$^{EP}$ then generates two matrices: (1) the conditional probability of crack initiation (PFMI) matrix and (2) conditional probability of through-wall cracking (PFMF) matrix. The ($i$, $j$)th entry in each array contains the results of the PFM analysis for the $j$th vessel simulation subjected to the $i$th transient.

Current PTS regulations are based on analyses from PFM models that produced a Bernoulli sequence of boolean results for cleavage fracture initiation and RPV failure by through-wall cracking; i.e., the outcome for each RPV trial in the Monte Carlo analysis was either crack initiation or no crack initiation and either failure or no failure. The conditional probability of initiation, $P(I|E)$, was calculated simply by dividing the number of RPV trials predicted to experience cleavage fracture by the total number of trials. Similarly, the conditional probability of failure, $P(F|E)$, was calculated by dividing the number of RPV trials predicted to fail by the total number of trials. The final results were discrete values for $P(I|E)$ and $P(F|E)$, without any quantification of the uncertainty in the solution. The improved PFM model in the new FAVPFM$^{EP}$ (v05.1) module provides for the calculation of discrete probability *distributions* of RPV fracture and failure along with the estimation of uncertainties in the results. In this improved PFM model, values for the conditional probability of

initiation ( $0 \le CPI \le 1$ ) and conditional probability of failure ( $0 \le CPF \le 1$ ) by through-wall cracking are calculated for each flaw subjected to each transient.

### 3.3.1 FAVPFM$^{EP}$ Flowchart

Figure 3.5 is a flowchart illustrating the essential elements of the nested-loop structure of the PFM Monte Carlo model – (1) *RPV Trial Loop*, (2) *Flaw Loop*, (3) *Transient Loop*, and (4) *Time-integration Loop*. The outermost *RPV Trial Loop* is indexed for each RPV trial included in the analysis, where the number of RPV trials is specified by the user in the FAVPFM$^{\mathbf{EP}}$ input stream. Since each RPV trial can be postulated to contain multiple flaws, the next innermost loop (the *Flaw Loop*) is indexed for the number of flaws for this trial. Each postulated flaw is positioned (through sampling) in a particular RPV beltline subregion having its own distinguishing embrittlement-related parameters. Next, the flaw geometry (depth, length, aspect ratio, and location within the RPV wall) is determined by sampling from appropriate distributions derived from expert judgment [47] and non-destructive and destructive examinations [48-50] of RPV steels. Each of the embrittlement-related parameters [nickel (an alloying element), copper and phosphorus (contaminants), neutron fluence, and an estimate of the *epistemic* and *aleatory* uncertainties in the unirradiated $RT_{NDT0}$] are sampled from appropriate distributions.[1] The neutron fluence is attenuated to the crack-tip location, and a value for the irradiated reference index, $RT_{NDT}$ (serving as a quantitative estimate of radiation damage), is calculated.

A deterministic fracture analysis is then performed on the current flaw for each of the postulated PTS transients; thus, the deterministic component of the analysis involves two inner nested loops – a *Transient Loop* and a *Time-integration Loop*. The temporal relationship between the applied Mode I stress intensity factor ($K_I$) and the static cleavage fracture initiation toughness ($K_{Ic}$) at the crack tip is calculated at discrete transient time steps. The fracture-toughness, $K_{Ic}$, statistical model is a function of the normalized temperature, $T(\tau) - RT_{NDT}$, where $T(\tau)$ is the time-dependent temperature at the crack tip. Analysis results are used to calculate the conditional probability of crack initiation ($CPI$)[2], i.e., the probability that pre-existing fabrication flaws will initiate in cleavage fracture. Also, the PFM model calculates the conditional probability of failure ($CPF$)[2] by through-wall cracking, i.e., the probability that an initiated flaw will propagate through the RPV wall. These probabilities are conditional in the sense that the transients are assumed to occur. In the treatment of multiple flaws to be discussed in Sect. 3.3.12, the values of *CPI* and *CPF* calculated for individual flaws become the

[1] The details of the protocols and statistical distributions for all sampled parameters are given in Chapter 4.

[2] The notations of *CPI* and *CPF* are used here rather than the older $P(I|E)$ and $P(F|E)$ notations in order to highlight the fact that a new PFM methodology is being applied.

*statistically independent marginal* probabilities used in the construction of the joint conditional probabilities of initiation and failure.

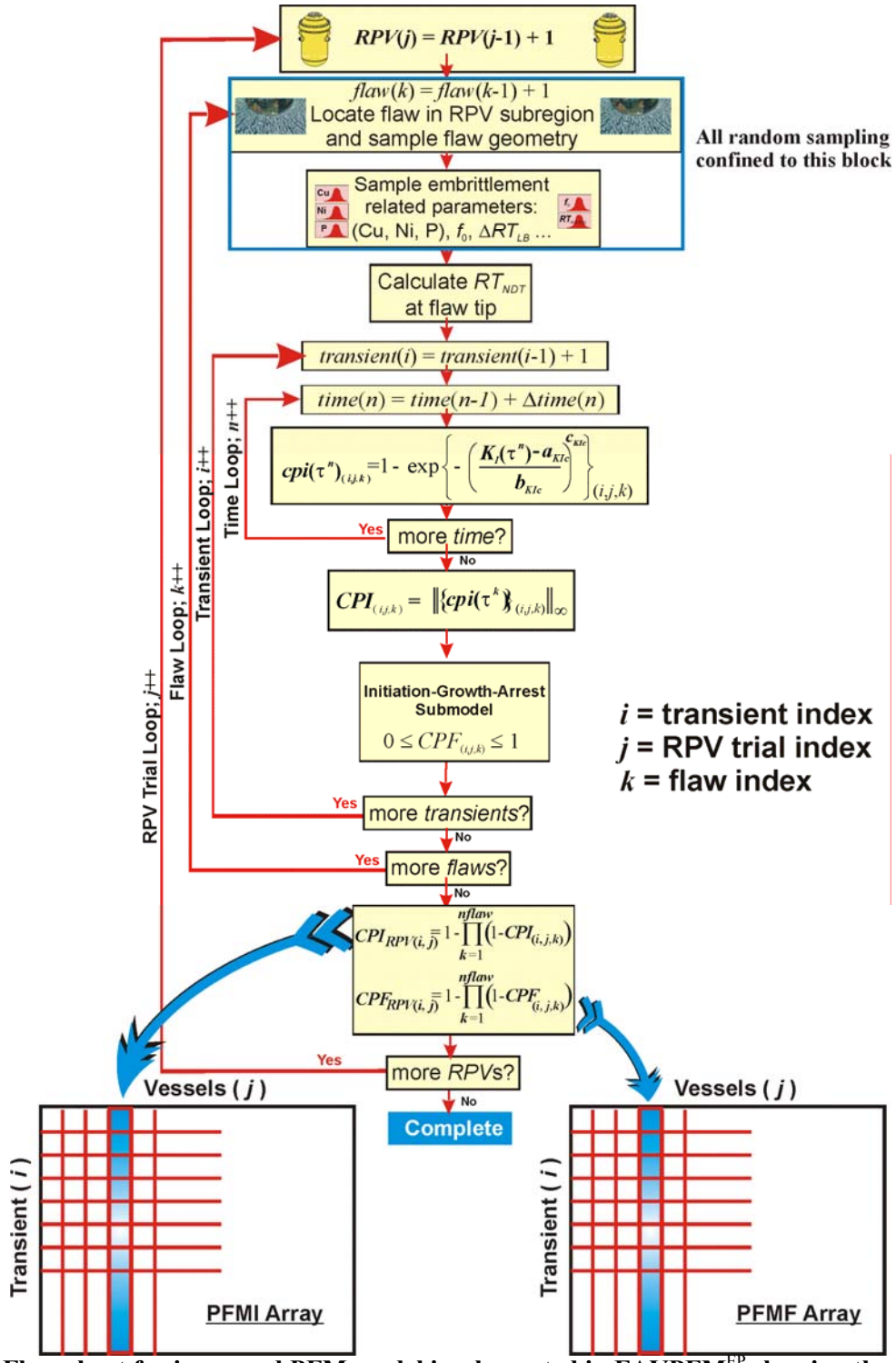


**Fig. 3.5. Flow chart for improved PFM model implemented in FAVPFM$^{EP}$ showing the four primary nested loops – (1) *RPV Trial Loop*, (2) *Flaw Loop*, (3) *Transient Loop*, and (4) *Time Loop*. Note: ++ notation indicates increment index by 1, e.g., *i*++ means *i*=*i*+1.**

Great care was taken in the construction of the nested-loop structure shown in Fig. 3.5 to preclude the introduction of a bias in the results due to the arbitrary ordering of the transients. In other words, for a given RPV trial, flaw, and transient, the same value of *CPI* and *CPF* will be calculated irrespective of the position of the transient (or the number of transients) in the load-definition transient stack. This objective was accomplished by confining all random sampling to the *sampling block* located at the point of entry into the flaw loop. Any sampling required in the crack *Initiation-Growth-Arrest* submodel[3] draws from sets of random number sequences derived in the sampling block. These set-aside random number sequences remain fixed for the current flaw and are reset to the start of the sequence as each transient is incremented in the *Transient Loop*. New random number sequences are constructed (resampled) for each increment in the *Flaw Loop*. The above approach involves an implementation of a variance reduction technique called *common random numbers* (CRN) which, in the terminology of classical experimental design, is a form of *blocking*. CRN has also been called *correlated sampling* or *matched streams* in some statistical simulation contexts [51].

### 3.3.2 Beltline Configurations and Region Discretization

The FAVOR$^{EP}$ code provides the capability to model the variation of radiation damage in the *beltline region* of an RPV with as much detail as the analyst considers necessary. In this section, a description of the beltline region is given, focusing on those aspects that are relevant to a FAVOR$^{EP}$ PFM analysis.

The beltline region of an RPV is fabricated using either forged-ring segments or rolled-plate segments [4]. The vessels are typically constructed of a specialty pressure vessel ferritic steel (e.g., A533-B, Class 1 plate or A508, Class 2 forging) as the base material. The heavy-section steel wall is lined with an internal cladding of austenitic stainless steel. Vessels made with forgings have only circumferential welds, and plate-type vessels have both circumferential welds and axial welds, as shown in Fig. 3.6. Therefore, beltline shells of a plate-type vessel contain three *major region* categories to model: (1) axial welds, (2) circumferential welds, and (3) plate segments. Only that portion of a weld that is within the axial bounds of the core need be considered, because the fast-neutron flux (and thus the radiation damage) experiences a steep attenuation beyond the fuel region. The extended surface length of an axially oriented flaw in a plate segment is also limited by the height of the core but not by the height of the shell course; therefore, the surface length of axial flaws in plate segments can be greater than those in axial welds [4]. Circumferential flaws in circumferential welds can be assumed to be limited by the full 360-degree arc-length of the weld. Due to the fabrication procedures for

[3] As will be discussed in Chapter 4, resampling of weld chemistry is required in the through-wall crack growth protocol as the crack front advances into a different weld layer.

applying the cladding on the inner surface of the vessel, FAVOR$^{EP}$ assumes all pre-existing surface-breaking flaws (in plate or weld subregions) are circumferential flaws. Embedded flaws can be either axially or circumferentially oriented.

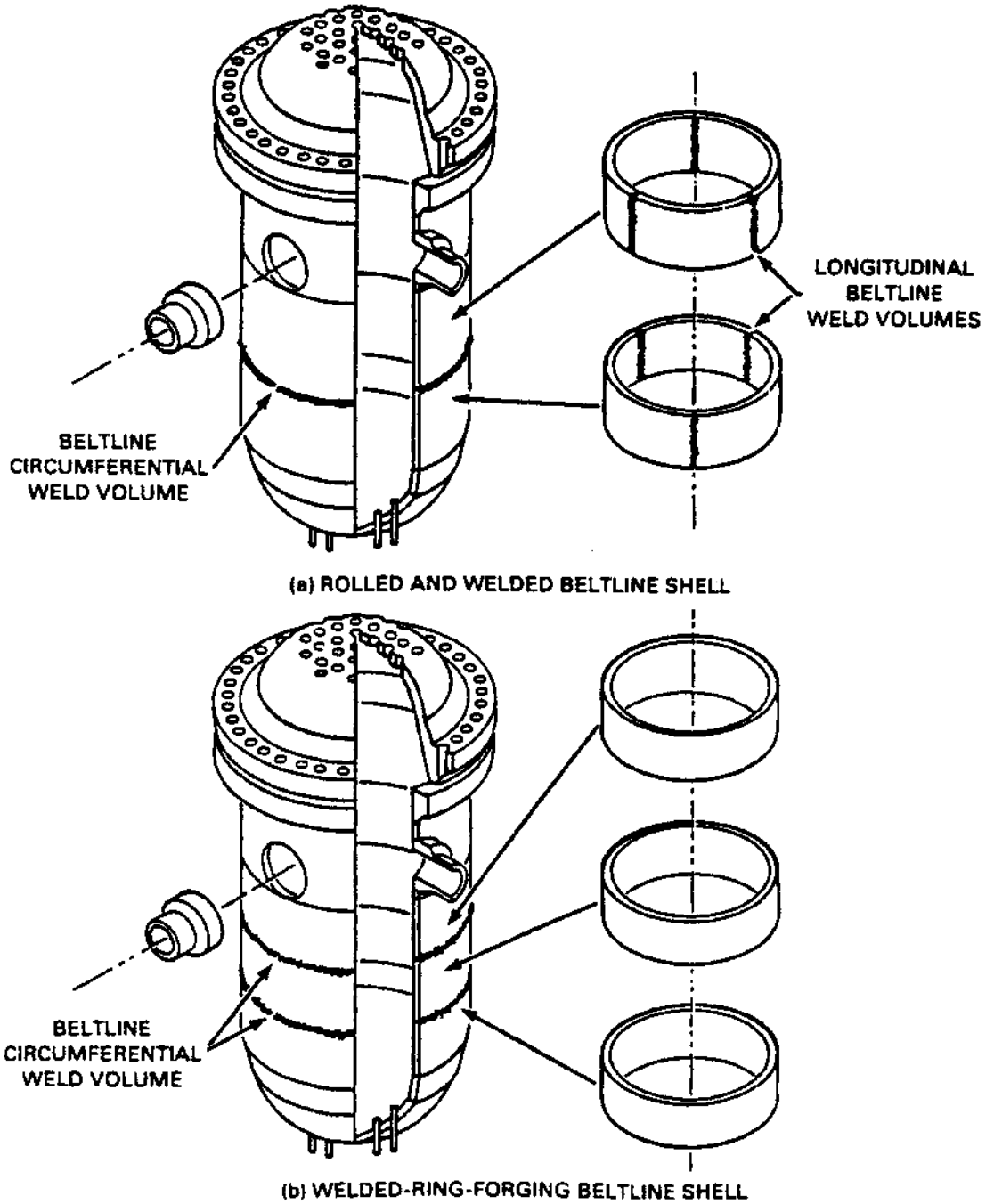


**Fig. 3.6. Fabrication configurations of PWR beltline shells (adapted from [3]): (a) rolled-plate construction with axial and circumferential welds and (b) ring-forging construction with circumferential welds only.**

Given the above considerations, the beltline region in FAVOR$^{EP}$ is defined as that portion of the RPV shell (including plate segments and welds) that extends from one foot below the bottom of the active core to one foot above the core. It is this region of the RPV wall that is explicitly modeled in FAVOR$^{EP}$. As will be discussed in later sections, the assumption applied in the crack *Initiation-Growth-Arrest* submodel is that all finite-length flaws (both surface-breaking and embedded) instantly upon initiation become infinite-length flaws at depths corresponding to the locations of their outer crack tips at the time of initiation. This assumption that there is lateral extension of finite flaws before they extend through the vessel wall is supported by experimental observations made during large-scale PTS experiments (discussed in Chapter 2) conducted at ORNL in the 1980s.

Figure 3.7 shows a typical rollout section of the beltline region. The user is required to discretize (subdivide) the beltline into several major regions that contain plates (or forgings), axial welds, and circumferential welds. These major regions are further discretized into subregions for greater resolution of the variation in radiation-induced embrittlement. An embrittlement-distribution map is defined in the input data for FAVPFM$^{\mathbf{EP}}$ using these major region and subregion definitions.

### 3.3.3 Treatment of the Fusion-Line Along Welds

The discretization and organization of major regions and subregions in the beltline includes a special treatment of weld *fusion lines* These fusion lines can be visualized as approximate boundaries between the weld subregion and its neighboring plate or forging subregions. FAVOR$^{EP}$ checks for the possibility that the plate subregions adjacent to a weld subregion could have a higher degree of radiation-induced embrittlement than the weld. The irradiated value of $RT_{NDT}$ for the weld subregion of interest is compared to the corresponding values of the adjacent (i.e., nearest-neighbor) plate subregions. Each weld subregion will have at most two adjacent plate subregions. The embrittlement-related properties of the most limiting (either the weld or the adjacent plate subregion with the highest value of irradiated $RT_{NDT}$) material are used when evaluating the fracture toughness of the weld subregion. These embrittlement-related properties include the unirradiated value of $\widehat{RT}_{NDT0}$, the fast-neutron fluence, $\widehat{f}_0$, product form, and chemistry content, $\widehat{Cu}$, $\widehat{Ni}$, and $\widehat{P}$ wt %, as discussed in Steps 3 and 4 and Eqs. (146) and (147) of Sect. 4.5. Flaw type and pre- and post-initiation orientation (see Sect. 3.3.10 and Table 3) of flaws are not transferred from a dominant plate subregion to a weld subregion.

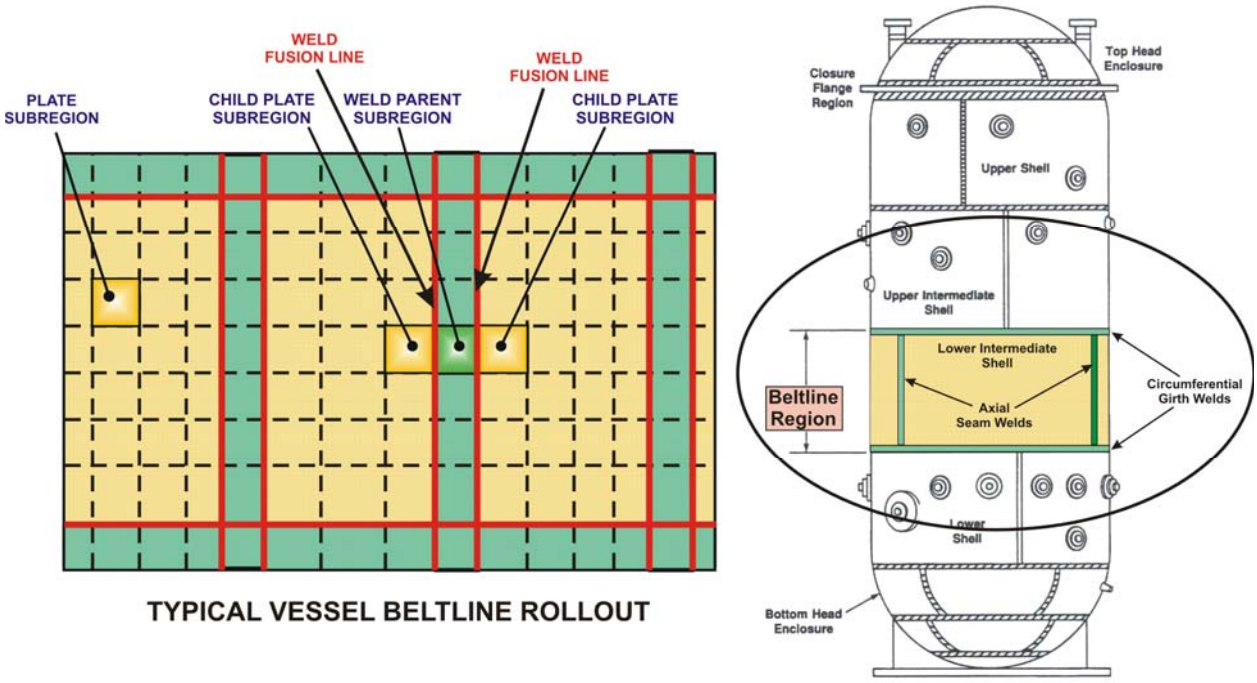


**Fig. 3.7. FAVOR$^{EP}$ uses a discretization of the RPV beltline region to resolve the variation in radiation damage in terms of plate, axial weld, and circumferential weld major regions which are further discretized into multiple subregions.**

For the Ductile Tearing Model No. 2, implemented in FAVOR$^{EP}$, v03.1 (see the discussion in Sect. 3.3.13), a second *weld-fusion-line dependency structure* is created based on the irradiated upper-shelf energy, *USE*. This weld-fusion-line dependency structure for sampling ductile-tearing properties is independent of the embrittlement-related dependency structure discussed above. For Ductile-tearing Model No. 2, the ductile-tearing-related properties of the most limiting (either the weld or the adjacent plate subregion with the lowest value of irradiated *USE*) material are used when evaluating ductile-tearing of a flaw located in the weld subregion. As with the embrittlement-related weld-fusion-line treatment, the flaw type and pre- and post-initiation orientation of flaws are not transferred from a dominant plate subregion to a weld subregion. Ductile-Tearing Model No. 1, implemented in FAVOR$^{EP}$, v05.1, this second weld-fusion-line dependency structure for sampling ductile-tearing properties is not required.

For those conditions in which plate embrittlement properties are used to characterize the weld subregion fracture toughness, the weld chemistry re-sampling protocols continue to be applied.

### 3.3.4 Constraint-Loss Effects

A scaling function has been implemented into FAVOR$^{EP}$ to approximate the effects of constraint loss for the flaws and loading conditions that are analyzed in the code.

Gao and Dodds [52] developed a simplified procedure using a Modified Boundary Layer (MBL) model to create a scaling function for constraint loss that incorporates elastic-plastic properties, an elastic constraint parameter called the *T*-stress, $T_{str}$, and the Weibull stress shape parameter, *m*. This scaling function, $\Im$, expresses the ratio of the small scale yielding (SSY) fracture toughness, $K_{Jc}^{T_{str}=0}$, and an expected MBL fracture toughness with non-zero *T*-stress, $K_{Jc}^{T_{str}\neq 0}$, based on an enforced equality of Weibull stresses. Equality of Weibull stresses establishes an equivalence of the probability of cleavage initiation. The scaling function in [52] has the following definition and functional dependencies:

$$\frac{K_{Jc}^{T_{str}\neq 0}}{K_{Jc}^{T_{str}=0}} \equiv \Im\left(n, E/\sigma_0, \nu; T_{str}/\sigma_0; m\right) \tag{1}$$

where the elastic properties are Young's elastic modulus, *E*, and Poisson's ratio, $\nu$, and the plastic properties are $\sigma_0$, equal to the proportional limit, and *n,* a strain-hardening exponent corresponding to the following power-law model:

$$\begin{aligned} \frac{\varepsilon}{\varepsilon_0} &= \frac{\sigma}{\sigma_0} \quad ;\ \varepsilon \le \varepsilon_0 \ \text{ linear-elastic deformation} \\ \frac{\varepsilon}{\varepsilon_0} &= \left(\frac{\sigma}{\sigma_0}\right)^n \quad ;\ \varepsilon > \varepsilon_0 \ \text{ plastic deformation} \end{aligned} \tag{2}$$

where $\varepsilon_0 = \sigma_0 / E$. An additional size correction factor of the form $\left(\frac{B_{1T}}{B_{xT}}\right)^{1/4}$ can then be applied to account for flaw lengths not equal to 1T ($B_{1T}$ = 25 mm).

Gao and Dodds [52] curve-fitted the results of a series of finite-element solutions using the following approximate fitting function:

$$\Im\left(n, E/\sigma_0, \nu; T_{str}/\sigma_0; m\right) = 1 + \sum_{i=1}^{4}\left[\sum_{j=0}^{4} b_{ij}\left(n, E/\sigma_0, \nu\right) m^j\right]\left(\frac{T_{str}}{\sigma_0}\right)^i \tag{3}$$

$$\text{for } 5 \le m \le 20,\ -0.9 \le T_{str}/\sigma_0 \le 0.6,\ n = 5, 7.5, 10, \text{ and } 20; \text{ and } E/\sigma_0 = f(n)$$

Sherry et al. [53] both verified and extended the work of Gao and Dodds [52] by developing a large number of additional solutions to provide a better resolution of the dependence on elastic-plastic

properties and Weibull modulus, *m*. A different functional form was used in [53] to curve-fit the finite-element solutions:

$$\begin{aligned} \Im &= 1 \qquad && T_{str}/\sigma_y \geq 0 \\ \Im &= 1+\alpha\left(-\frac{T_{str}}{\sigma_y}\right)^{\kappa} && T_{str}/\sigma_y < 0 \end{aligned} \tag{4}$$

where $\alpha$ and *k* are fitting parameters and $\sigma_y$ is the yield stress at 0.2% plastic strain. An extensive set of lookup tables for $\alpha\left(E/\sigma_y, m, n\right)$ and $\kappa\left(E/\sigma_y, m, n\right)$ are provided in [53] that cover the ranges of $100 \leq E/\sigma_y \leq 750$, $5 \leq m \leq 20$, and $5 \leq n \leq 20$.

To facilitate interpolation within these tables for implementation into FAVOR$^{EP}$, the HSST Program at ORNL developed surface fits for all of the $(\alpha, \kappa)$ data in Table 2 of [53]. The functional form used in the surface fitting was a bivariate Chebyshev series polynomial. The Chebyshev series, consisting of a sum of sequential terms, is a type of orthogonal polynomial defined from -1 to +1.

The input *X* and *Y* values must first be scaled such that the *X* and *Y* ranges are mapped to the required $-1 < (X, Y) < +1$ range. In addition, the specific bivariate Chebyshev series polynomial selected for surface fitting performs a log transformation of either the *X* or *Y* values to improve the fidelity of the fitting. For example, at *n* = 20 the scaling of the surface function $\alpha\left(E/\sigma_y, m \mid n = 20\right)$ is:

$$\begin{aligned} x &= \min\left\{\max\left[\left(\frac{\ln(E/\sigma_y) - 5.298317366548037}{0.6931471805599453}\right), -1\right], +1\right\} \;;\; 100 \leq E/\sigma_y \leq 400 \\ y &= \min\left\{\max\left[\left(\frac{m - 12.5}{7.5}\right), -1\right], +1\right\} \;;\; 5 \leq m \leq 20 \end{aligned} \tag{5}$$

An order *n* Chebyshev polynomial *of the first kind* can be defined using Rodrigues' formula

$$\begin{aligned} T_n(x) &= \frac{\sqrt{1-x^2}}{(-1)^n(2n-1)(2n-3)\ldots 1}\ \frac{d^n}{dx^n}\left(1-x^2\right)^{n-\frac{1}{2}} \\ &\text{or} \\ T_n(x) &= \cos\left(n\cos^{-1}(x)\right) \end{aligned} \tag{6}$$

As an example, a value for $\alpha\left(E/\sigma_y, m \mid n\right)$ using a 10$^{th}$ order bivariate Chebyshev series polynomial is calculated by

$$\alpha\left(E/\sigma_y, m \mid n\right) =$$

$$\begin{aligned} z(x,y) = {} & c_1 + c_2T_2(x) + c_3T_1(y) + c_4T_2(x) + c_5T_1(x)T_1(y) + c_6T_2(y) + c_7T_3(x) + c_8T_2(x)T_1(y) + c_9T_1(x)T_2(y) + \\ & c_{10}T_3(y) + c_{11}T_4(x) + c_{12}T_3(x)T_1(y) + c_{13}T_2(x)T_2(y) + c_{14}T_1(x)T_3(y) + c_{15}T_4(y) + c_{16}T_5(x) + c_{17}T_4(x)T_1(y) + \\ & c_{18}T_3(x)T_2(y) + c_{19}T_2(x)T_3(y) + c_{20}T_1(x)T_4(y) + c_{21}T_5(y) + c_{22}T_6(x) + c_{23}T_5(x)T_1(y) + c_{24}T_4(x)T_2(y) + \\ & c_{25}T_3(x)T_3(y) + c_{26}T_2(x)T_4(y) + c_{27}T_1(x)T_5(y) + c_{28}T_6(y) + c_{29}T_7(x) + c_{30}T_6(x)T_1(y) + \\ & c_{31}T_5(x)T_2(y) + c_{32}T_4(x)T_3(y) + c_{33}T_3(x)T_4(y) + c_{34}T_2(x)T_5(y) + c_{35}T_1(x)T_6(y) + c_{36}T_7(y) + \\ & c_{37}T_8(x) + c_{38}T_7(x)T_1(y) + c_{39}T_6(x)T_2(y) + c_{40}T_5(x)T_3(y) + c_{41}T_4(x)T_4(y) + c_{42}T_3(x)T_5(y) + \\ & c_{43}T_2(x)T_6(y) + c_{44}T_1(x)T_7(y) + c_{45}T_8(y) + c_{46}T_9(x) + c_{47}T_8(x)T_1(y) + c_{48}T_7(x)T_2(y) + \\ & c_{49}T_6(x)T_3(y) + c_{50}T_5(x)T_4(y) + c_{51}T_4(x)T_5(y) + c_{52}T_3(x)T_6(y) + c_{53}T_2(x)T_7(y) + c_{54}T_1(x)T_8(y) + \\ & c_{55}T_9(y) + c_{56}T_{10}(x) + c_{57}T_9(x)T_1(y) + c_{58}T_8(x)T_2(y) + c_{59}T_7(x)T_3(y) + c_{60}T_6(x)T_4(y) + \\ & c_{61}T_5(x)T_5(y) + c_{62}T_4(x)T_6(y) + c_{63}T_3(x)T_7(y) + c_{64}T_2(x)T_8(y) + c_{65}T_1(x)T_9(y) + c_{66}T_{10}(y) \end{aligned} \tag{7}$$

where the 66 parameters, $c_i$ , required to complete the surface fit are calculated using TableCurve 3D [54], version 3.0. Surface functions for each of the 16 values of $n$ ($n = 5, 6, 7 \ldots 20$) in [53] for $\alpha\left(E/\sigma_y, m \mid n\right)$ and $\kappa\left(E/\sigma_y, m \mid n\right)$ are fitted giving a total of 32 surface functions that have been implemented into FAVOR$^{EP}$.

Figure 3.8 presents the surface function fits for $\alpha\left(E/\sigma_y, m \mid n = 5\right)$ and $\kappa\left(E/\sigma_y, m \mid n = 5\right)$. Figures 3.8a and 3.8c show the data available from the lookup tables given in [53]. The *Interpolate to Uniform Grid* option in TableCurve 3D was used to enhance the resolution of the surface definition by carrying out exact interpolations (i.e., the interpolations produce surfaces that pass exactly through the original data) of the data to increase the size of the dataset. The algorithm employed for this purpose was the Renka I [55, 56] triangulation procedure. Figures 3.8b and 3.8d present the final fitted surfaces with their enhanced interpolated datasets. The fitted surfaces for $n = 20$ are shown in Fig. 3.9.

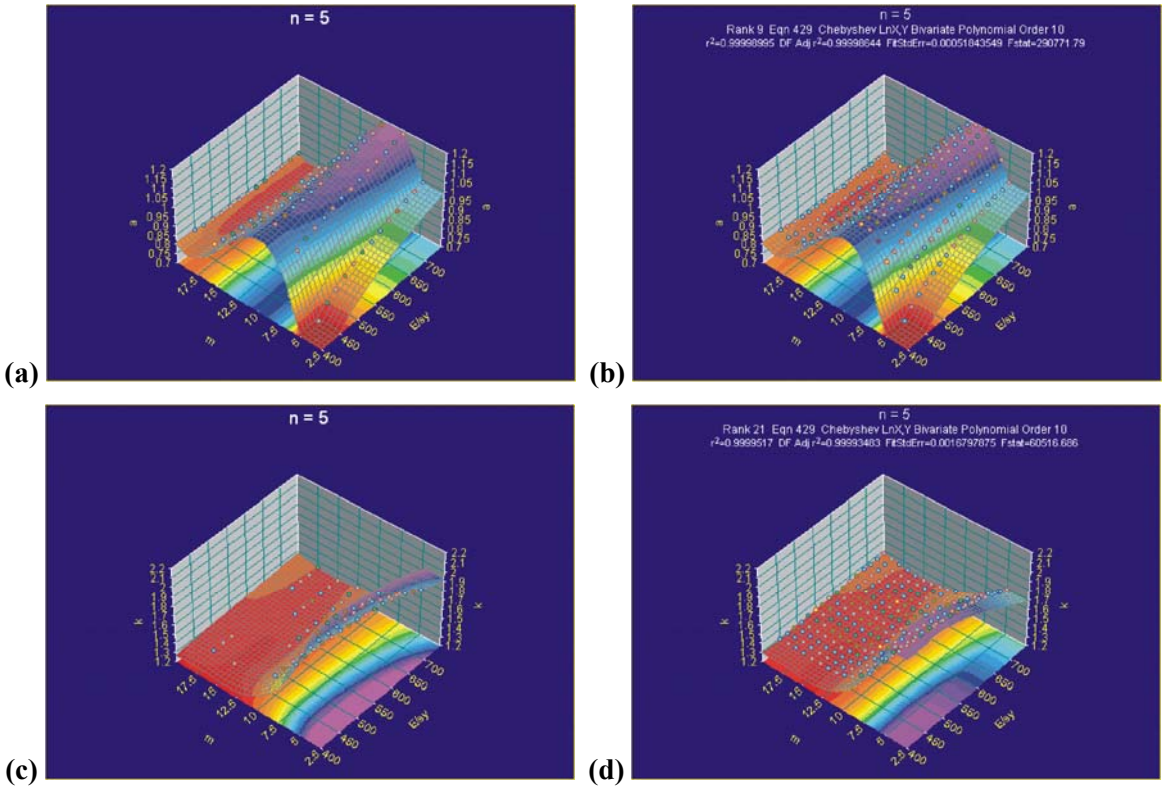


**Fig. 3.8. Fitted surface functions for *n* = 5 (a) and (b) $\alpha\left(E/\sigma_y, m\right)$ and (c) and (d) $k\left(E/\sigma_y, m\right)$.**

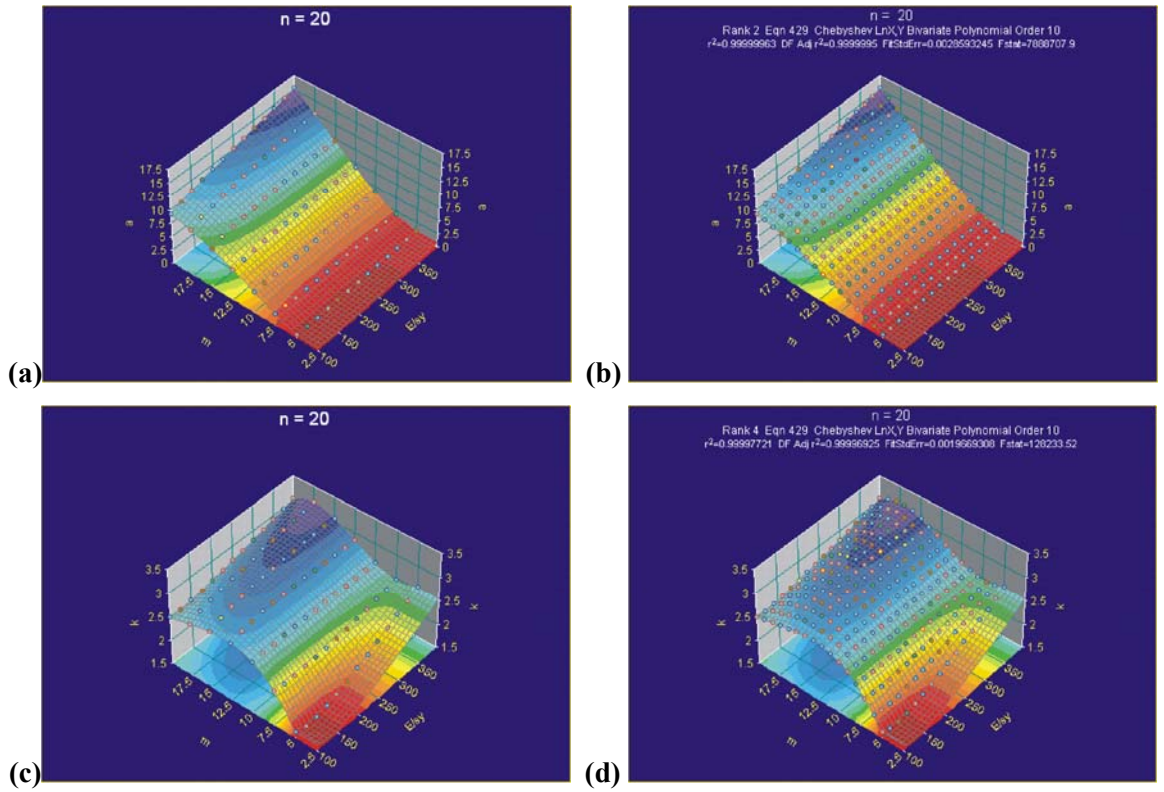


**Fig. 3.9. Fitted surface functions for *n* = 20 (a) and (b) $\alpha\left(E/\sigma_y, m\right)$ and (c) and (d) $k\left(E/\sigma_y, m\right)$.**

### 3.3.5 Plastic-Flow Properties Model – Temperature and Radiation Damage Effects

Based on the results of research described in refs.[57-60] and the recommendations in ref. [61], a plastic-flow properties model has been developed for FAVOR$^{EP}$ to include the effects of temperature and radiation damage on the engineering 0.2% offset yield strength and ultimate strength for RPV ferritic steels. This model then treats the flow stress (required for the remaining-ligament instability model in FAVOR$^{EP}$) as the average of the yield and ultimate stresses.

**Temperature Dependency for 0.2% Offset Yield Strength**

The temperature dependency for the 0.2% offset engineering yield strength is modeled by the following form:

$$\sigma_{yield}(T) = \sigma_{yield(ref)}(T_{ref}) + \Delta\sigma_{yield}(T, T_{ref}) \tag{8}$$

where the temperature-dependent shift in yield strength for bcc metals is derived from the Zerilli-Armstrong [58] constitutive relation

$$\Delta\sigma_{yield}(T, Tref) = C_1\left\{\exp\left[-T\left(C_2 + C_3\ln(\dot{\varepsilon})\right)\right] - \exp\left[-T_{ref}\left(C_2 + C_3\ln(\dot{\varepsilon})\right)\right]\right\} \quad [\text{MPa}] \tag{9}$$

$$C_1 = 1033 \text{ MPa} \qquad C_2 = 0.00698 \text{ K}^{-1}$$
$$C_3 = 0.000415 \text{ K}^{-1} \qquad \dot{\varepsilon} = 0.0004 \text{ sec}^{-2}$$

In the above equation, $T$, in [K], is the temperature of interest, and $T_{ref}$, also in [K], is the reference temperature corresponding to a (typically room temperature) reference value for tensile yield strength, $\sigma_{yield(ref)}$, in [MPa].

**Radiation Damage Effects on Yield Strength**

Kirk and Natishan [59] demonstrated that a product-form-dependent relationship exists between the Charpy CVN transition shift model for $\Delta T_{30}$ and the increase in the room-temperature yield strength produced by irradiation. This linear relation has the form:

$$\Delta\sigma_{yield(rad)}\left(\Delta T_{30}\right) = \gamma \times \Delta T_{30} \text{ [MPa]} \tag{10}$$

where $\Delta T_{30}$ is in $[°\text{C}]$ and the product-form dependent $\gamma$ is (from Fig. 5.2 in [59])

$$\gamma\left[\frac{\text{MPa}}{°\text{C}}\right] = \begin{cases} 1.45 \text{ welds} \\ 1.67 \text{ plates} \\ 2.04 \text{ forgings} \end{cases}$$

Kirk and Natishan [59] note that the value of $\gamma$ estimated for forgings is based a small sample size and should be used with caution. The $\Delta T_{30}$ model in FAVOR$^{EP}$ is from ref. [62].

The temperature and radiation-damage dependent model for yield strength is therefore

$$\sigma_{yield}(T, T_{ref}, \Delta T_{30}) = \sigma_{yield(ref)}(T_{ref}) + \Delta\sigma_{yield}(T, T_{ref}) + \Delta\sigma_{yield(rad)}(\Delta T_{30}) \tag{11}$$

**Ultimate Strength Correlated with Yield Strength**

Using data obtained from a surveillance and pre-construction database maintained by EPRI [63] combined with additional data taken from research studies reported in the open literature [57], Natishan et al. [60] observed that a consistent relationship exists between the ultimate tensile strength and yield strength of U.S. RPV steels and their weldments, irrespective of their irradiation condition. This linear relation takes the following form:

$$\sigma_{ult}(T) = 114 + (1.03 \times \sigma_{yield}(T)) \quad [\text{MPa}] \tag{12}$$

**Proposed Plastic Flow-Properties Model**

In summary, the proposed plastic flow-properties model implemented in FAVOR$^{EP}$ for the yield, ultimate, and flow strengths is

$$\begin{aligned}
\sigma_{yield}(T, T_{ref}, \Delta T_{30}) &= \sigma_{yield(ref)}(T_{ref}) + \Delta\sigma_{yield}(T, T_{ref}) + \Delta\sigma_{yield(rad)}(\Delta T_{30}) \quad [\text{MPa}] \\
\sigma_{ult}(T, T_{ref}, \Delta T_{30}) &= 114 + (1.03 \times \sigma_{yield}(T, T_{ref}, \Delta T_{30})) \quad [\text{MPa}] \\
\sigma_{flow}(T, T_{ref}, \Delta T_{30}) &= \frac{(\sigma_{yield}(T, T_{ref}, \Delta T_{30}) + \sigma_{ult}(T, T_{ref}, \Delta T_{30}))}{2} \quad [\text{MPa}]
\end{aligned} \tag{13}$$

The plastic-flow properties model requires as input data a reference 0.2% offset yield strength, $\sigma_{yield(ref)}$, and its associated reference temperature, $T_{ref}$. The other parameters required by the model are already calculated internally by FAVOR$^{EP}$.

### 3.3.6 Warm Prestressing

Experimental evidence for the warm prestressing (WPS) effect in ferritic steels was first reported almost 40 years ago [64]. Since then, this phenomena has been the subject of extensive research; e.g., see [65-74]. The technical basis for the inclusion of warm prestressing effects in FAVOR$^{EP}$ is presented in detail in [75]. The following is a summary of the discussion in [75].

The WPS phenomena can be characterized as an increase in the apparent fracture toughness of a ferritic steel after first being "prestressed" at an elevated temperature. Three mechanisms have been identified [65, 69, 73] to produce the WPS phenomena:

1. Preloading at an elevated temperature *work-hardens the material ahead of the crack tip*. The increase in yield strength with decreasing temperature "immobilizes" the dislocations in the plastic zone [67,68]. Consequently, an increase in applied load is needed for additional plastic flow (a prerequisite for fracture) to occur at the lower temperature.
2. Preloading at an elevated temperature *blunts the crack tip*, reducing the geometric stress concentration making subsequent fracture more difficult.
3. Unloading after or during cooling from the elevated WPS temperature down to a reduced temperature *produces residual compressive stresses ahead of the crack tip*. The load applied at the reduced temperature must first overcome these compressive stresses before the loading can produce additional material damage and possibly fracture. The residual compressive stresses associated with the unloaded initial plastic zone can be viewed as protecting the crack tip, since higher applied loads are required to achieve a given level of crack driving force compared to the condition before preloading [71].

Heretofore, probabilistic fracture mechanics calculations performed in the United States have typically not included the WPS phenomena as a part of the PFM model. This omission was based on the following considerations:

1. Thermal-hydraulic (TH) transients were often represented as smooth temporal variations of both pressure and coolant temperature; however, data taken from operating nuclear power plants demonstrate that actual overcooling events are not necessarily so well behaved. This non-smoothness of these fundamental mechanical and thermal loads created the possibility that, due to short-duration time-dependent fluctuations of pressure and/or coolant temperature, the criteria for WPS might be satisfied by the idealized transient but not satisfied by the real transient.
2. Previous PRA models of human reliability (HR) were typically not sufficiently sophisticated to capture the potential for plant operators to repressurize the primary coolant system as part of their response to an RPV-integrity challenge. Since such a repressurization would largely nullify the benefit of WPS, it was viewed as nonconservative to account for WPS within a model that may also ignore the potentially deleterious effects of operator actions.

FAVOR$^{EP}$, v05.1, addresses both of these concerns by allowing as input data (1) more realistic and detailed representations of the postulated PTS transients and (2) more sophisticated PRA/HR models that explicitly consider both acts of omission and commission on the part of plant operators.

The FAVOR$^{EP}$ WPS-modeling option implements the *conservative WPS principle* first proposed by McGowan [66]. This principle states that for cleavage crack initiation to be possible the following criteria must be met: (1) the applied-$K_I$ at the crack tip must exceed some minimum value of $K_{Ic}$ and (2) the applied-$K_I$ must be increasing with time (i.e., $dK_I / d\tau > 0$) when the load path first enters the finite $K_{Ic}$ probability space. Equivalently, a flaw is assumed by FAVOR$^{EP}$ to be in a state of WPS when either of the two following conditions are met:

1. the time-rate-of-change of the applied-$K_I$ is nonpositive ( $dK_I / d\tau \le 0$ ), or
2. the applied $K_I$ is less than the maximum $K_I$ experienced by the flaw up to the current time in the transient, where this $K_{I(max)}$ must be greater than the current value of $K_{Ic(\min)}$ as defined by the location parameter of the statistical model (to be discussed in Sect. 3.3.9) for cleavage-fracture initiation.

Figures 3.10a and b present an example of a PTS transient (Fig. 3.10a) applied to a flaw with its resulting load path (Fig. 3.10b). At Point 1 in Fig. 3.10b, the load path for the flaw enters finite $K_{Ic}$ probability space, and, shortly thereafter, $dK_I / d\tau$ becomes negative. The flaw is in a state of WPS from Point 1 to Point 2. At Point 2, the applied-$K_I$ at the crack tip exceeds the current $K_{I(max)}$ (established at Point 1).

Along the load path between Points 2 and 3, the flaw is no longer in a state of WPS and has a finite probability of crack initiation. At Point 3, a new $K_{I(max)}$ is established, and, since $dK_I / d\tau \le 0$ or $K_I < K_{I(max)}$ for the remainder of the load path, the flaw returns to and remains in a state of WPS. While the WPS condition is in effect, the instantaneous conditional probability of initiation, $cpi(\tau)$, for the flaw is set to zero, even though the applied $K_I$ of the flaw is within the finite $K_{Ic}$ probability space ($K_I > K_{Ic(min)}$). To assess the impact of including WPS in the analysis, WPS has been implemented in FAVOR$^{EP}$ as a user-set option, thus allowing cases to be run with and without WPS effects.

If the WPS option is activated, the applied $K_I$ of an arrested flaw must also be greater than the previous maximum $K_I$ (of the arrested flaw geometry since the time of the arrest) for the flaw to reinitiate.

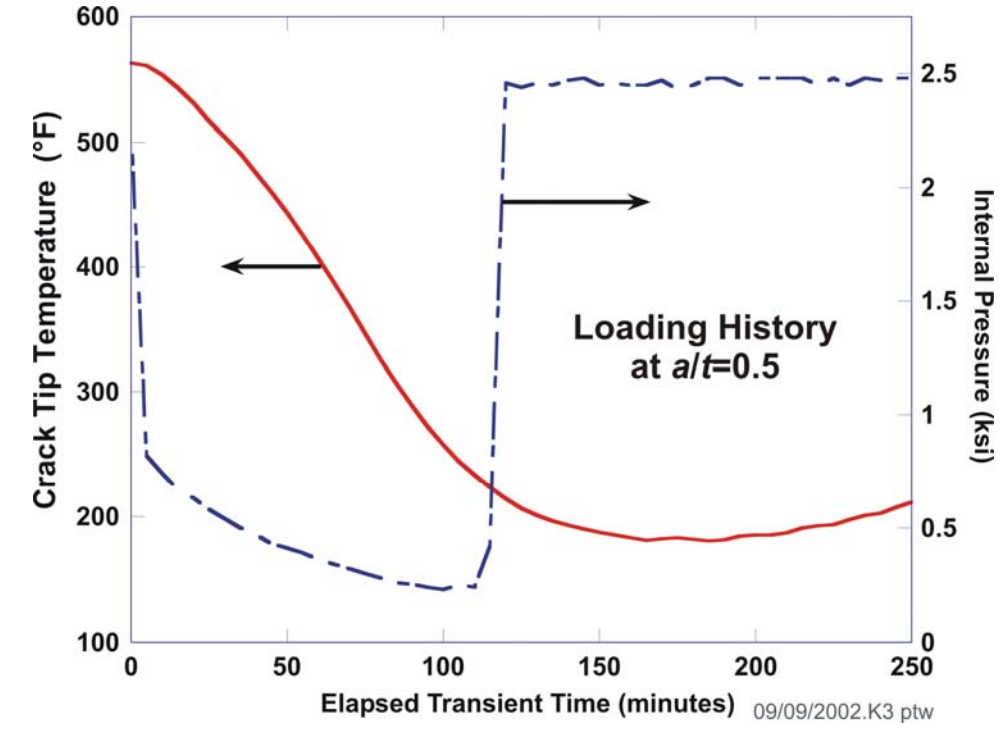


(a)

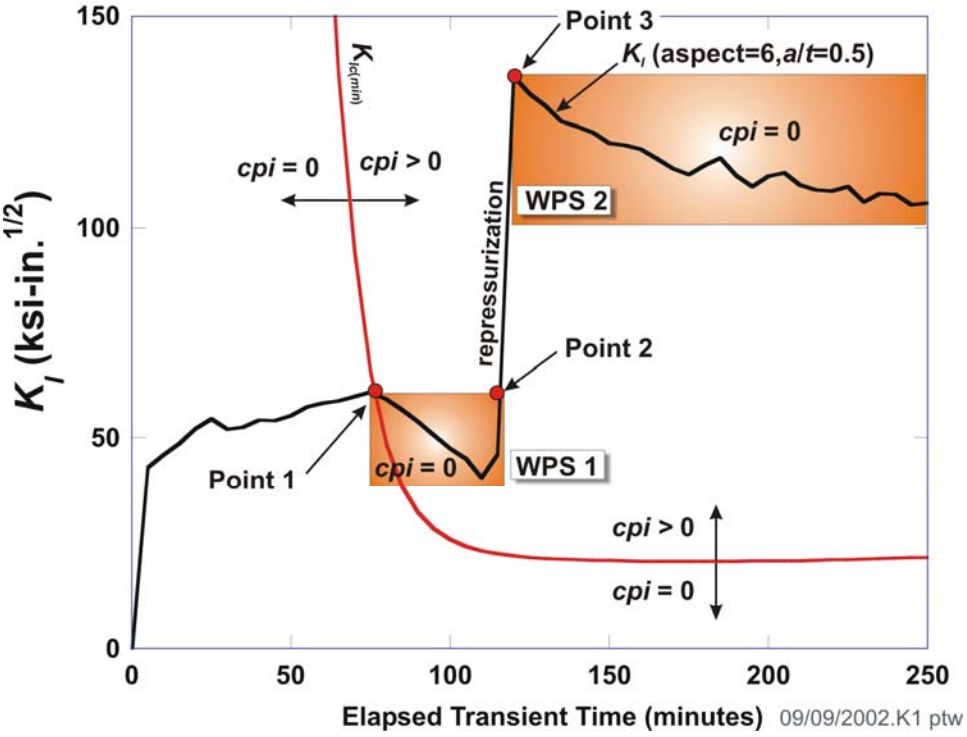


(b)

**Fig. 3.10. Example of warm prestressing: (a) loading history with pressure applied to the inner surface and the temperature at the crack tip, (b) load path for a flaw showing two WPS regions. (*cpi* is the instantaneous conditional probability of initiation).**

### 3.3.7 Probability Distributions

The sampled variables used in FAVPFM[EP] are drawn from a range of specified statistical distributions. The following presents general information about these distributions including, the form of their probability density function (PDF), cumulative distribution function (CDF), first and second moments, and sampling methods used in FAVOR[EP]. The notation $X_i \leftarrow N(\mu,\sigma)$ signifies that a random variate is drawn as a sample from a population described by the specified distribution. In this example, the population is described by a two-parameter normal distribution with mean, $\mu$, and standard deviation, $\sigma$. Other distributions applied in FAVOR[EP] include the standard *uniform* distribution for a unit open interval, *U*(0,1); the two-parameter *lognormal* distribution, $\Lambda(\mu_{\log},\sigma_{\log})$; the three-parameter *Weibull* distribution, *W*(*a*,*b*,*c*); and the two-parameter *logistic* distribution, $L(\alpha,\beta)$.

A standard uniform distribution on the interval *U*(0,1) is the starting point for all of the transformation methods that draw random variates from nonuniform continuous distributions. A uniform distribution is defined by the following:

**Uniform Distribution** – *U*(*a*,*b*)

PDF:
$$f_U(x \mid a,b) = \begin{cases} 0 & ; \quad x < a \\ \dfrac{1}{b-a}; & a \le x \le b \\ 0 & ; \quad x > b \end{cases}$$

CDF:
$$\Pr(X \le x) = F_U(x \mid a,b) = \begin{cases} 0 & ; \quad x < a \\ \dfrac{x-a}{b-a}; & a \le x \le b \\ 1 & ; \quad x > b \end{cases}$$

**Moments**:

Mean
$$\mu = \frac{a+b}{2}$$

Variance
$$\sigma^2 = \frac{(b-a)^2}{12}$$

**Sampling from a two-parameter Uniform Distribution:** $U_i \leftarrow U(0,1)$

Sampling from a standard uniform distribution, $U(0,1)$, is accomplished computationally with a *Random Number Generator* (RNG). A portable random number generator [76-78], written in Fortran, has been implemented and tested in FAVOR$^{EP}$. This portable generator, based on a composite of two multiplicative linear congruential generators using 32 bit integer arithmetic, has a reported theoretical minimum period of $2.3\times10^{18}$. This implementation was successfully tested by the HSST Program at ORNL for statistical randomness using the NIST *Statistical Test Suite for Random and Pseudorandom Number Generators* [79].

**Normal Distribution** – $N(\mu,\sigma)$

PDF: $$f_N(x\,|\,\mu,\sigma)=\frac{1}{\sigma\sqrt{2\pi}}\exp\left[-\frac{(x-\mu)^2}{2\sigma^2}\right];\quad -\infty<x<+\infty$$

CDF: $$\Pr(X\le x)=\Phi(z)=\frac{1}{\sqrt{2\pi}}\int_{-\infty}^{z}\exp\left(-\frac{\xi^2}{2}\right)d\xi\ ;\quad z=\frac{x-\mu}{\sigma};\quad -\infty<x<+\infty$$

**Moments:**

Mean $\mu$

Variance $\sigma^2$

**Sampling from a two-parameter Normal Distribution:** $X_i \leftarrow N(\mu,\sigma)$

Earlier versions of FAVOR used the Box-Müller *Transformation Method* [80-82] to sample from a standard normal distribution, $N(0,1)$. Beginning with FAVOR, v04.1, the more computationally efficient Forsythe's method (as extended by Ahrens and Dieter [83]) for sampling from a standard normal distribution has been implemented. The sampled standard normal deviate, $Z_i$, is then scaled to the required random normal deviate with mean, $\mu$, and standard deviation, $\sigma$, by.

$$\begin{aligned} Z_i &\leftarrow N(0,1) \\ X_i &= Z_i\sigma+\mu \end{aligned} \qquad (14)$$

The extended Forsythe's method is computationally very efficient; however, one problem with the method is that there is no direct connection between the standard normal deviate and its associated *p-value* in the normal cumulative distribution function. When this relationship between the *p-value* and the deviate is required, an alternative method for expressing the inverse of a standard normal

CDF (also known as a percentile function) is applied in FAVOR$^{EP}$. The following rational function [84] represents an accurate approximation of the standard normal percentile function:

$$x = \begin{cases} p & \text{for } p < \frac{1}{2} \\ 1-p & \text{for } p \geq \frac{1}{2} \end{cases}$$
$$y = \sqrt{-2\ln(x)} \qquad (15)$$
$$Z_p = \text{sgn}\left(p - \frac{1}{2}\right)\left(y + \frac{a_0 + a_1 y + a_2 y^2 + a_3 y^3 + a_4 y^4}{b_0 + b_1 y + b_2 y^2 + b_3 y^3 + b_4 y^4}\right)$$

where

$$\text{sgn}(x) = \begin{cases} -1 & \text{if } x < 0 \\ +1 & \text{if } x \geq 0 \end{cases}$$

and the coefficients of the rational function are:

$a_0 = $ -0.3222324310880000 $\quad b_0 = 0.0993484626060$
$a_1 = $ -1.0000000000000000 $\quad b_1 = 0.5885815704950$
$a_2 = $ -0.3422420885470000 $\quad b_2 = 0.5311034623660$
$a_3 = $ -0.0204231210245000 $\quad b_3 = 0.1035377528500$
$a_4 = $ -0.0000453642210148 $\quad b_4 = 0.0038560700634$

The standard normal deviate is then scaled to obtain the required quantile

$$X_p = Z_p \sigma + \mu \qquad (16)$$

**Lognormal Distribution** $-\Lambda\left(\mu_{\log}, \sigma_{\log}\right)$

PDF:
$$f_\Lambda(x \mid \mu_{\log}, \sigma_{\log}) = \begin{cases} 0 & ; \quad x \leq 0 \\ \frac{1}{\sigma_{\log} x \sqrt{2\pi}} \exp\left[-\frac{\left(\ln x - \mu_{\log}\right)^2}{2\sigma_{\log}^2}\right] & ; \quad 0 < x < \infty \end{cases}$$

CDF:
$$\Pr(X \leq x) = \Phi(z) = \begin{cases} 0 & ; \quad x \leq 0 \\ \frac{1}{\sqrt{2\pi}} \int_{-\infty}^{z} \exp\left(-\frac{\xi^2}{2}\right) d\xi \; ; \; z = \frac{\ln x - \mu_{\log}}{\sigma_{\log}}, & 0 < x < \infty \end{cases}$$

**Moments:**

Mean
$$\mu = \exp\left(\mu_{\log} + \frac{\sigma_{\log}^2}{2}\right)$$

Variance $\sigma^2 = \omega(\omega-1)\exp(2\mu_{\log}); \quad \omega = \exp(\sigma^2_{\log})$

**Sampling from a two-parameter Lognormal Distribution:** $X_i \leftarrow \Lambda(\mu_{\log}, \sigma_{\log})$

The log-transformed deviate is sampled from a normal distribution with mean equal to the lognormal mean, $\mu_{\log}$, and standard deviation equal to the lognormal standard deviation, $\sigma_{\log}$. The log-transformed deviate is then converted into the required random deviate by the exponential function.

$$\begin{aligned} Y_i &\leftarrow N(\mu_{\log}, \sigma_{\log}) \\ X_i &= \exp(Y_i) \end{aligned} \tag{17}$$

**Weibull Distribution** – $W(a,b,c)$

($a$ = location parameter, $b$ = scale parameter, $c$ = shape parameter)

PDF: $$f_w(x|a,b,c) = \begin{cases} 0 \quad ; & x \le a \\ \dfrac{c}{b} y^{c-1} \exp\left(-y^c\right); & (y = (x-a)/b, x > a,\ b,c > 0) \end{cases}$$

CDF: $$\Pr(X \le x) = F_w(x \mid a,b,c) = \begin{cases} 0 \quad ; & x \le a \\ 1 - \exp\left[-y^c\right]; & (y = (x-a)/b, x > a,\ b,c > 0) \end{cases}$$

**Moments:**

Mean $$\mu = a + b\,\Gamma\left(1 + \frac{1}{c}\right)$$

Variance $$\sigma^2 = b^2\left[\Gamma\left(1 + \frac{2}{c}\right) - \Gamma^2\left(1 + \frac{1}{c}\right)\right]$$

where $\Gamma(x)$ is Euler's gamma function.

**Sampling from a three-parameter Weibull Distribution:** $X_i \leftarrow W(a,b,c)$

A random number is drawn from a uniform distribution on the open interval (0,1) and then transformed to a Weibull variate with the Weibull percentile function.

$$\begin{aligned} U_i &\leftarrow U(0,1) \\ X_i &= a + b\left[-\ln(1-U_i)\right]^{1/c} \end{aligned} \tag{18}$$

**Logistic Distribution** – $L(\alpha,\beta)$

PDF: $$f_L(x\,|\,\alpha,\beta)=\frac{z}{\beta(1+z)^2};\quad z=\exp\left[-\left(\frac{x-\alpha}{\beta}\right)\right],\quad -\infty<x<\infty$$

CDF: $$\Pr(X\le x)=F_L(x\,|\,\alpha,\beta)=\frac{1}{1+z};\quad z=\exp\left[-\left(\frac{x-\alpha}{\beta}\right)\right],\quad -\infty<x<\infty$$

**Moments:**

Mean $$\mu=\alpha$$

Variance $$\sigma^2=\frac{\pi^2\beta^2}{3}$$

**Sampling from a two-parameter Logistic Distribution** $X_i \leftarrow L(\alpha,\beta)$

A random number is drawn from a uniform distribution on the open interval (0,1) and then transformed to a logistic variate by the logistic percentile function.

$$\begin{aligned} U_i &\leftarrow U(0,1) \\ X_i &= \alpha-\beta\ln\left(\frac{1}{U_i}-1\right) \end{aligned} \tag{19}$$

Figure 3.11 gives examples of PDFs for each of these continuous probability distributions.

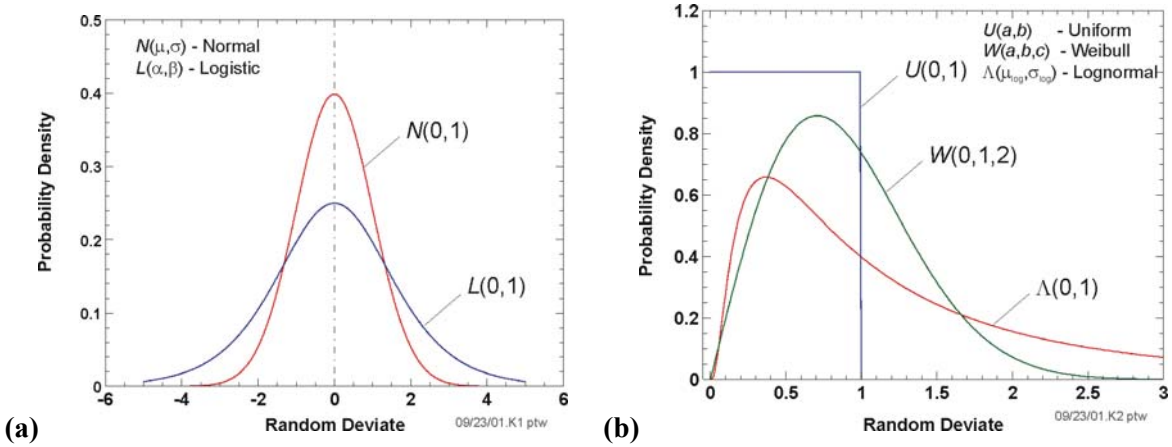


**Fig. 3.11. Example probability density functions for (a) normal and logistic and (b) uniform, Weibull, and lognormal continuous distributions.**

### 3.3.8 Truncation Protocol

When sampling physical variables from statistical distributions, it is sometimes necessary to truncate the distribution to preclude the sampling of nonphysical values. When truncation is required in FAVOR$^{EP}$, the truncation bounds, either symmetric or one-sided, are explicitly stated in the sampling protocols presented in Chapters 3 and 4. The truncation rule applied in FAVOR$^{EP}$ requires a sampled variable that exceeds its truncation bounds to be replaced by the boundary value. This exception-handling protocol ensures that the integrated area under the truncated probability density function remains equal to unity; however, the shape of the resulting sampled density distribution will have a step-function rise at the truncated boundaries.

### 3.3.9 Conditional Probability of Initiation (*CPI*)

As discussed above, a deterministic fracture analysis is performed by stepping through discrete transient time steps to examine the temporal relationship between the applied Mode I stress intensity factor ($K_I$) and the static cleavage fracture initiation toughness ($K_{Ic}$) at the crack tip. The computational model for quantification of fracture-toughness uncertainty has been improved (relative to the models used in the 1980s to derive the current PTS regulations) in three ways: (1) the $K_{Ic}$ and $K_{Ia}$ databases were extended by 84 and 62 data values, respectively, relative to the databases in the EPRI NP-719-SR[4] report [85]; (2) the statistical representations for $K_{Ic}$ and $K_{Ia}$ were derived through the application of rigorous mathematical procedures; and (3) a method for estimating the *epistemic* uncertainty in the transition-reference temperature was developed. Bowman and Williams [86] provide details regarding the extended database and mathematical procedures employed in the derivation of a Weibull distribution for fracture-toughness data. Listings of the extended ORNL 99/27 $K_{Ic}$ and $K_{Ia}$ database are given in Appendix C. A Weibull distribution, in which the parameters were calculated by the *Method of Moments* point-estimation technique, forms the basis for the new statistical model of $K_{Ic}$. For the Weibull distribution, there are three parameters to estimate: the location parameter, $a$, of the random variate; the scale parameter, $b$, of the random variate; and the shape parameter, $c$. The Weibull probability density, $f_W$, is given by:

$$f_w(x|a,b,c) = \begin{cases} 0 \quad ; & x \le a \\ \dfrac{c}{b} y^{c-1} \exp\left(-y^c\right); & (y = (x-a)/b, x > a,\ b, c > 0) \end{cases} \tag{20}$$

where the parameters of the $K_{Ic}$ distribution are a function of $\widehat{\Delta T}_{RELATIVE}$ :

[4] The fracture-toughness database given in EPRI NP-719-SR (1978) [85] served as the technical basis for the statistical $K_{Ic}$ / $K_{Ia}$ distributions used in the IPTS studies of the 1980s.

$$\begin{aligned} a_{K_{Ic}}(\widehat{\Delta T}_{RELATIVE}) &= 19.35 + 8.335\exp\left[0.02254(\widehat{\Delta T}_{RELATIVE})\right] \ [\text{ksi}\sqrt{\text{in.}}] \\ b_{K_{Ic}}(\widehat{\Delta T}_{RELATIVE}) &= 15.61 + 50.132\exp\left[0.008(\widehat{\Delta T}_{RELATIVE})\right] \ [\text{ksi}\sqrt{\text{in.}}] \\ c_{K_{Ic}} &= 4 \end{aligned} \tag{21}$$

where $\widehat{\Delta T}_{RELATIVE} = (T(t) - \widehat{RT_{NDT}})$ in °F. The curve, "$\widehat{X}$", above a variable indicates that it is a randomly sampled value. The details of the development of Eq. (21) will be given in Chapter 4 along with a discussion of the sampling methods for $\widehat{RT_{NDT}}$.

For each postulated flaw, a deterministic fracture analysis is performed by stepping through the transient time history for each transient. At each time step, $\tau^n$, for the *i*th transient and *j*th RPV trial, an instantaneous $cpi(\tau^n)_{(i,j,k)}$ is calculated for the *k*th flaw from the Weibull $K_{Ic}$ cumulative distribution function at time, $\tau$, to determine the fractional part (or fractile) of the distribution that corresponds to the applied $K_I(\tau^n)_{(i,j,k)}$:

$$\Pr\left(K_{Ic} \le K_I(\tau^n)_{(i,j,k)}\right) = cpi(\tau)_{(i,j,k)} = \begin{cases} 0 \ ; & K_I(\tau^n)_{(i,j,k)} \le a_{K_{Ic}} \\ 1 - \exp\left\{-\left[\dfrac{K_I(\tau^n)_{(i,j,k)} - a_{K_{Ic}}}{b_{K_{Ic}}}\right]^{c_{K_{Ic}}}\right\} \ ; & K_I(\tau^n)_{(i,j,k)} > a_{K_{Ic}} \end{cases} \tag{22}$$

Here, $cpi(\tau^n)_{(i,j,k)}$ is the instantaneous conditional probability of initiation at the crack tip at time $\tau^n$. Figure 3.12 illustrates the interaction of the applied $K_I$ time history and the Weibull $K_{Ic}$ distribution for an example case, in which an embedded flaw 0.67-in. in depth, 4.0-in. in length, with the inner crack tip located 0.5-in. from the inner surface, is subjected to a severe PTS transient. The $RT_{NDT}$ of the RPV material is 270 °F. A Weibull distribution, as a lower-bounded continuous statistical distribution, has a lower limit (referred to as the *location parameter,* $a_{K_{Ic}}$) such that any value of $K_I$ below the location parameter has a zero probability of initiation. As described in Fig. 3.12, the applied $K_I$ must be greater than the local value of $a_{K_{Ic}}$ before $cpi > 0$. The region designated as $cpi > 0$ in the figure represents the finite probability $K_{Ic}$ initiation space, and outside of this region $cpi = 0$.

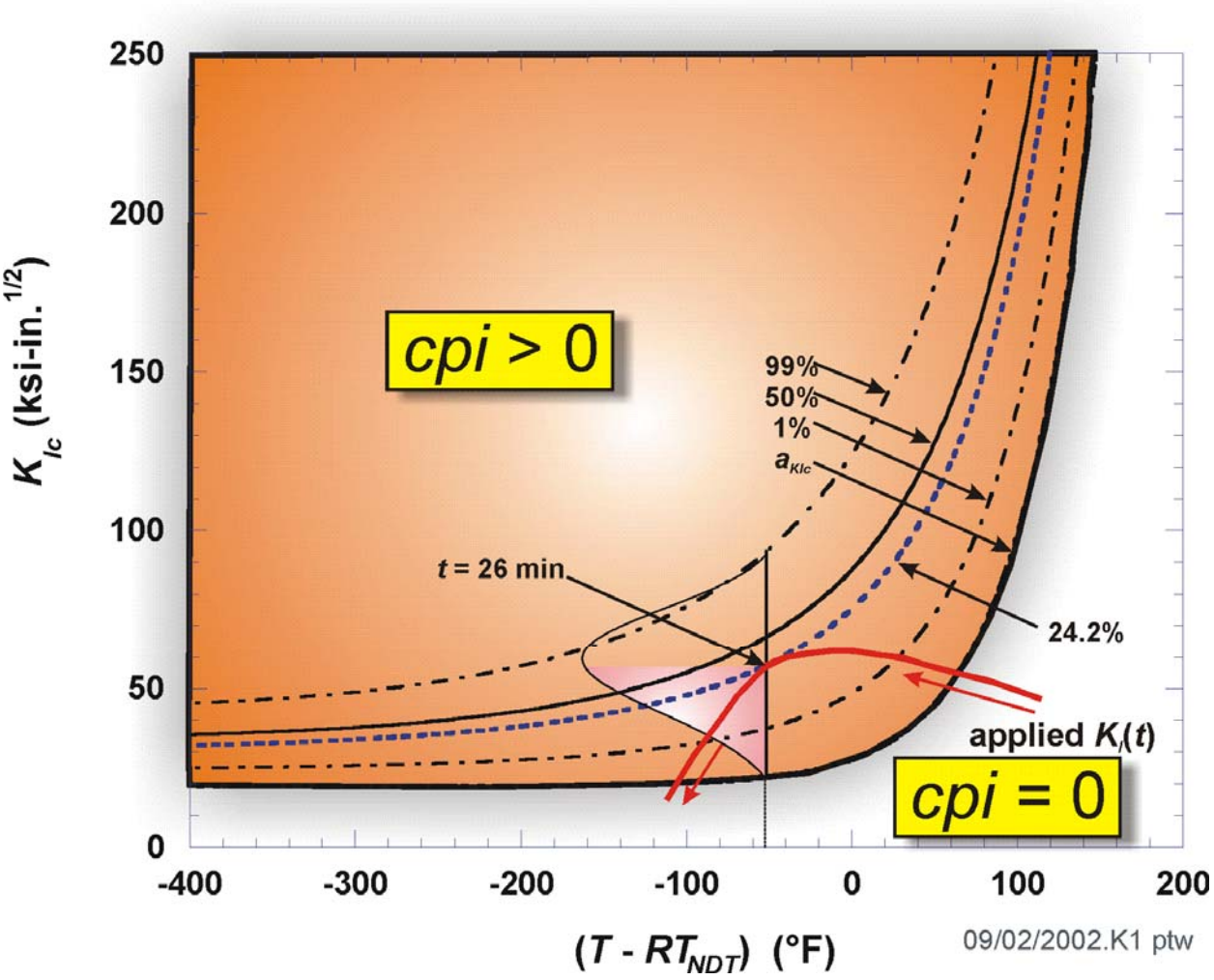


**Fig. 3.12. Interaction of the applied $K_I$ time history and the Weibull $K_{Ic}$ statistical model for a postulated flaw.**

**Table 3.1. Illustration of Computational Procedure to Determine *CPI* and *CPF* for a Postulated Flaw (Warm Prestress Not Included)**

| | | | | $K_{Ic}$ Weibull Parameters | | | | | | | | |
|---|---|---|---|---|---|---|---|---|---|---|---|---|
| Time($\tau^n$) (min) | $T(\tau^n)$ (°F) | $RT_{NDT}$ (°F) | $T(\tau^n)$-$RT_{NDT}$ (°F) | $a$ (ksi√in) | $b$ (ksi√in) | $c$ (-) | $K_I(\tau^n)$ (ksi√in) | $cpi(\tau^n)$ (-) | $\Delta cpi(\tau^n)$ (-) | $P(F\|I)$ (-) | $\Delta cpf(\tau^n)$ (-) | $cpf(\tau^n)$ (-) |
| 8 | 360.68 | 270.0 | 90.68 | 83.70 | 119.16 | 4 | 50.90 | 0 | 0 | 0 | 0 | 0 |
| 10 | 328.28 | 270.0 | 58.28 | 50.35 | 95.52 | 4 | 55.70 | 9.82E-06 | 9.82E-06 | 0 | 0 | 0 |
| 12 | 302.18 | 270.0 | 32.18 | 36.57 | 80.46 | 4 | 59.20 | 6.24E-03 | 6.23E-03 | 0.20 | 0.0012 | 0.0012 |
| 14 | 281.48 | 270.0 | 11.48 | 30.15 | 70.56 | 4 | 61.00 | 3.59E-02 | 2.96E-02 | 0.25 | 0.0074 | 0.0087 |
| 16 | 264.74 | 270.0 | -5.26 | 26.75 | 63.68 | 4 | 61.80 | 8.77E-02 | 5.18E-02 | 0.30 | 0.0155 | 0.0242 |
| 18 | 251.24 | 270.0 | -18.76 | 24.81 | 58.76 | 4 | 61.70 | 1.44E-01 | 5.62E-02 | 0.40 | 0.0225 | 0.0467 |
| 20 | 240.44 | 270.0 | -29.56 | 23.63 | 55.18 | 4 | 61.10 | 1.91E-01 | 4.76E-02 | 0.50 | 0.0238 | 0.0705 |
| 22 | 231.62 | 270.0 | -38.38 | 22.86 | 52.49 | 4 | 60.10 | 2.24E-01 | 3.24E-02 | 0.60 | 0.0194 | 0.0899 |
| 24 | 224.24 | 270.0 | -45.76 | 22.32 | 50.37 | 4 | 58.80 | 2.40E-01 | 1.66E-02 | 0.70 | 0.0116 | 0.1015 |
| 26 | 218.12 | 270.0 | -51.88 | 21.94 | 48.71 | 4 | 57.30 | 2.42E-01 | 2.04E-03 | 0.80 | 0.0016 | 0.1031 |

Notes:
$cpi(\tau^n)$ – instantaneous conditional probability of initiation
$\Delta cpi(\tau^n)$ – incremental change in instantaneous conditional probability of initiation
$P(F|I)$ - the number of flaws that propagated through the wall thickness divided by the total number of initiated flaws
$\Delta cpf(\tau^n) = P(F|I) \times \Delta cpi(t^n)$
$cpf(\tau^n)$ = instantaneous conditional probability of failure by through-wall cracking
*CPI* = *sup*-norm[5] of the vector $\{cpi(\tau^n)\}$
*CPF* = *sup*-norm of the vector $\{cpf(\tau^n)\}$
The transient index, *i*, RPV trial index, *j*, and flaw index, *k*, are implied.

Table 3.1 summarizes results of the PFM model for the postulated flaw. The transient index, *i*, RPV trial index, *j*, and flaw index, *k*, are implied for all variables. The column headed $cpi(\tau^n)$ is the instantaneous value of the conditional probability of initiation determined from Eq. (22) (see Fig. 3.13). The next column headed $\Delta cpi\ (\tau^n)$ is the increase in $cpi(\tau^n)$ that occurred during the discrete time step, $\Delta\tau^n$, as illustrated in Fig. 3.14. The current value of $CPI_{(i,j,k)}$ is

$$CPI_{(i,j,k)} = \left\| \left\{ cpi(\tau^m) \right\}_{(i,j,k)} \right\|_\infty \quad \text{for } 1 \le m \le n \tag{23}$$

For the example flaw in Table 3.1, *CPI* = 0.242 occurs at a transient time of 26 minutes. The last three columns in Table 3.1 are used in the determination of the conditional probability of vessel failure, *CPF*, by through-wall cracking, as will be discussed below.

[5] the *sup*-norm is the maximum-valued element (in absolute value) in the vector

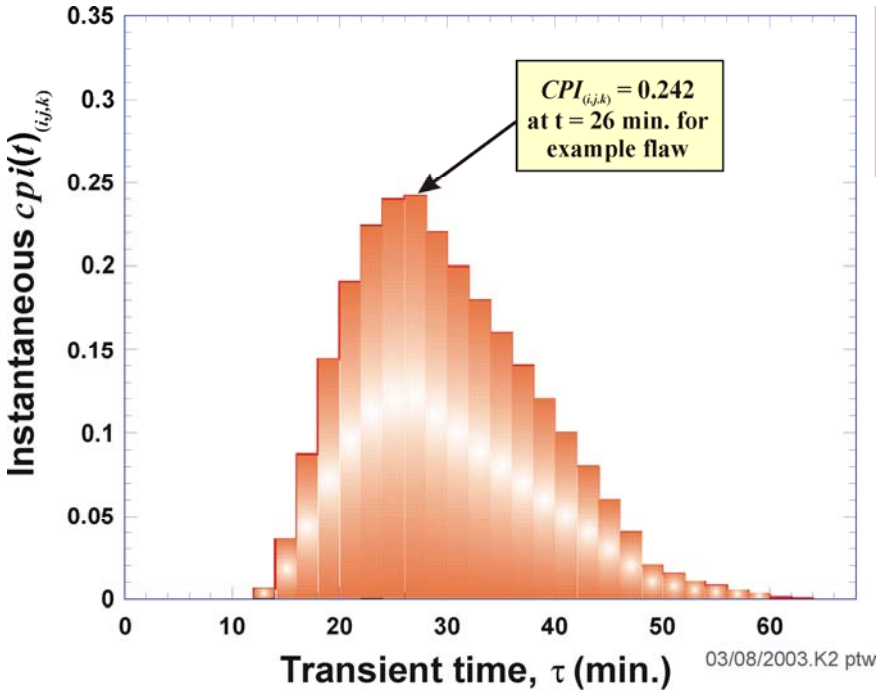


**Fig. 3.13. The parameter $cpi(\tau)_{(i,j,k)}$ is the instantaneous conditional probability of initiation (*cleavage fracture*) obtained from the Weibull $K_{Ic}$ cumulative distribution function. $CPI_{(i,j,k)}$ is the maximum value of $cpi(\tau)_{(i,j,k)}$. (Note: $i$ = transient index, $j$ = RPV trial index, and $k$ = flaw index)**

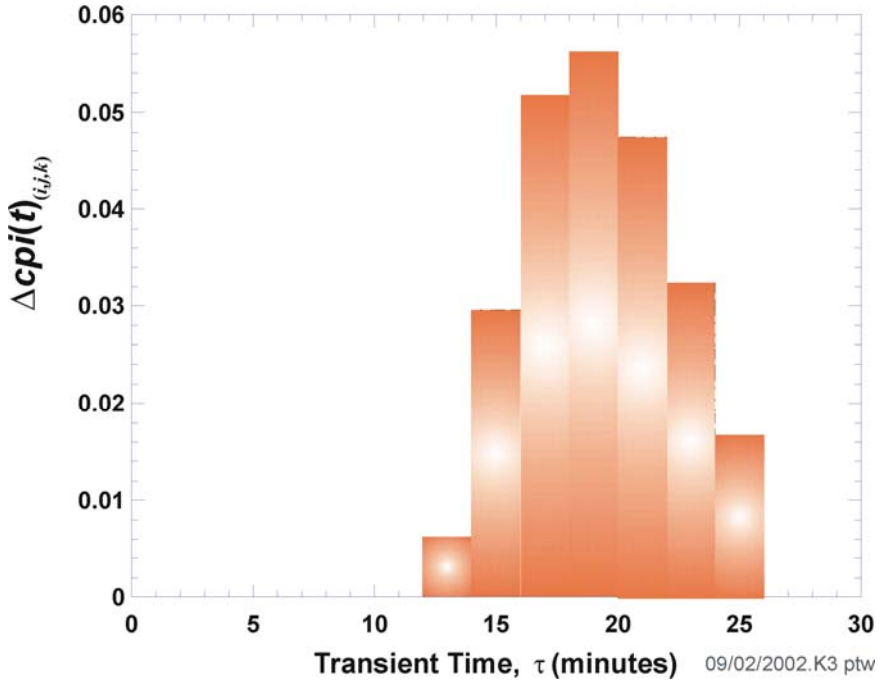


**Fig. 3.14. $\Delta cpi(\tau^n)_{(i,j,k)}$ is the increase in $cpi(\tau^n)_{(i,j,k)}$ that occurs during each discrete time step. When the maximum value of $cpi(\tau^n)_{(i,j,k)}$ is reached, negative values of $\Delta cpi(\tau^n)_{(i,j,k)}$ are set to zero. (Note: $i$ = transient index, $j$ = RPV trial index, and $k$ = flaw index)**

### 3.3.10 Post-Initiation Flaw Geometries and Orientations

A flaw that initiates in cleavage fracture is assumed to become an infinite-length inner surface-breaking flaw, regardless of its original geometry (see Fig. 3.15). This assumption is consistent with the results of large-scale fracture experiments in which flaws, initiated in cleavage fracture, were observed to extend in length before propagating through the wall thickness [87]. For example, a circumferentially oriented semi-elliptic surface-breaking flaw ½-inch in depth is assumed to become a ½-inch deep 360-degree circumferential flaw. An embedded flaw ½-inch in depth with its inner crack tip located at ½-inch from the RPV inner surface becomes a 1-inch deep infinite-length flaw, since it is assumed that an initiated embedded flaw first propagates through the clad, thus becoming an infinite-length surface-breaking flaw before advancing into the vessel wall.

All surface-breaking semi-elliptic flaws in FAVOR$^{EP}$ are assumed to be pre-existing fabrication flaws that are circumferentially oriented; see Table 3.2. This restriction is based on the assumption that Category 1 flaws were created during vessel fabrication, as the austenitic stainless-steel cladding was being applied to the inner surface of the vessel. This assumption introduces a preferred orientation for these flaws. Embedded flaws may be oriented either axially or circumferentially. Upon initiation, the transformed infinite-length flaws retain the orientation of the parent initiating flaw.

**Table 3.2. Applied Flaw Orientations by Major Region**

| Major Region | Flaw Category 1 | Flaw Category 2 | Flaw Category 3 |
|---|---|---|---|
| axial weld | circumferential | axial | axial |
| circumferential weld | circumferential | circumferential | circumferential |
| plate/forging | circumferential | axial/circumferential* | axial/circumferential* |

Flaw Category 1 – surface-breaking flaw

Flaw Category 2 – embedded flaw in the base material between the clad/base interface and $\frac{1}{8}t$

Flaw Category 3 – embedded flaw in the base material between $\frac{1}{8}t$ and $\frac{3}{8}t$

*Flaw Categories 2 and 3 in plates/forgings are equally divided between axial and circumferential orientations

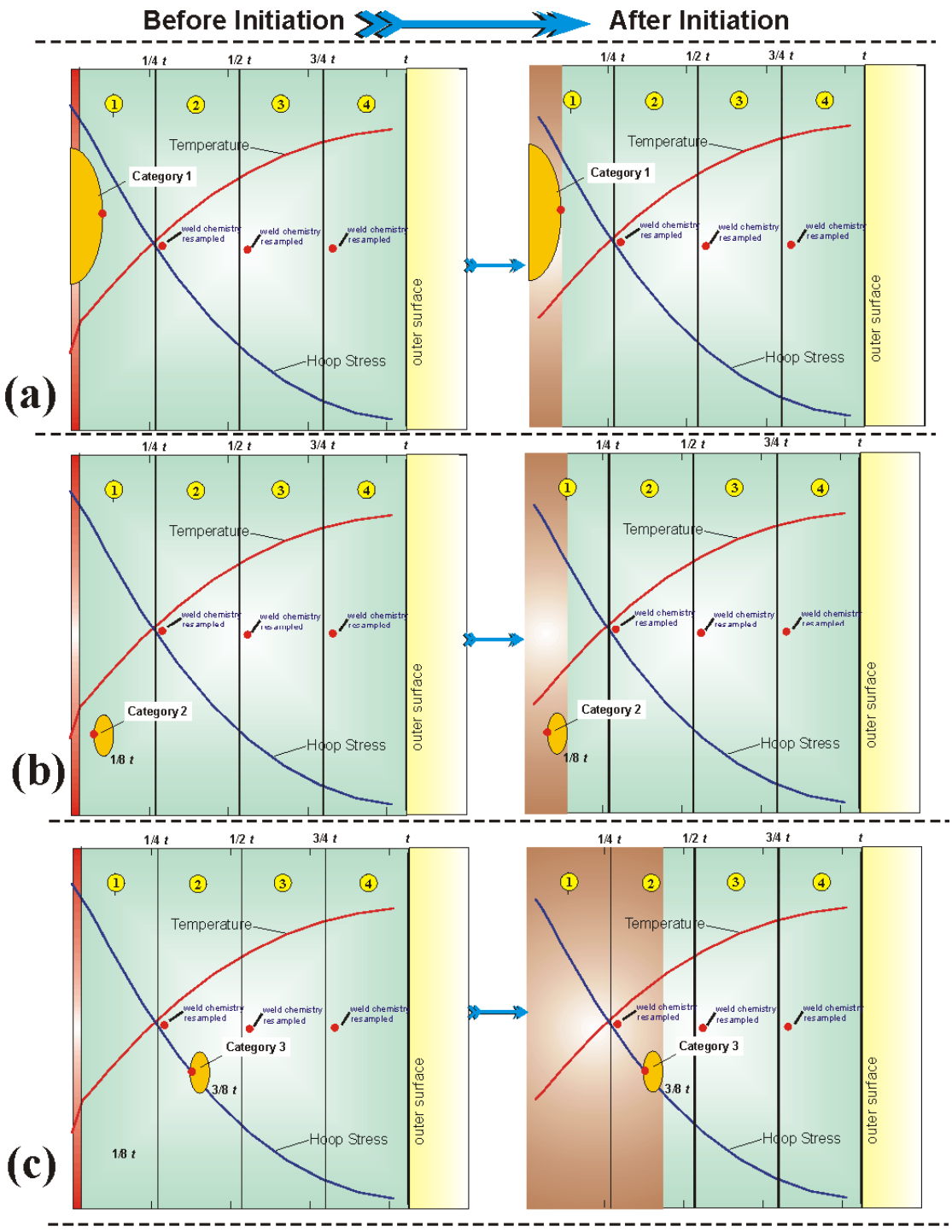


**Fig. 3.15. At the time of initiation, the three categories of flaws are transformed into infinite-length flaws: (a) Category 1 semi-elliptic surface-breaking circumferential flaws become 360 degree circumferential flaws, (b) and (c) Category 2 and 3 embedded flaws become inifinite-length axial or 360 degree circumferential flaws at the same depth. Category 1 flaws are only oriented in the circumferential direction.**

### 3.3.11 Conditional Probability of Failure (*CPF*) by Through-Wall Cracking

A flaw that has initiated in cleavage fracture has two possible outcomes for the time remaining in the transient. The newly-formed infinite-length flaw either propagates through the entire wall thickness causing RPV failure by through-wall cracking, or it experiences a stable arrest at some location in the wall. In either case, the advancement of the crack tip through the RPV wall may involve a sequence of *initiation* / *arrest* / *re-initiation* events as discussed in the following section. In the discussion in this section, the transient index, *i*, RPV trial index, *j*, and flaw index, *k*, are implied for all variables. They have been left off to simplify the notation.

Table 3.1 summarizes the calculation of RPV failure in the improved PFM model. The column headed $P(F \mid I)$ is the conditional probability of failure given initiation; $P(F \mid I)$ is equal to the fraction of initiated flaws that propagate through the wall thickness causing RPV failure. At the current time, $\tau^n$, the increment in the conditional probability of failure, $\Delta cpf(\tau^n)$, is the product of $P(F \mid I)$ and $\Delta cpi(\tau^n)$. The instantaneous value of the conditional probability of failure at time $\tau^n$, $cpf(\tau^n)$, is therefore

$$cpf(\tau^n) = \sum_{m=1}^{n_{\max}} P(F \mid I) \times \Delta cpi(\tau^m) = \sum_{m=1}^{n_{\max}} \Delta cpf(\tau^m) \tag{24}$$

where $n_{\max}$ is the time step at which the current value of *CPI* occurred, i.e., the time at which the maximum value of $cpi(\tau)$ occurred.

The fraction of flaws that would fail the RPV is determined (at each time step for each flaw) by performing a Monte Carlo analysis of through-wall propagation of the infinite-length flaw. In each analysis, the infinite-length flaw is incrementally propagated through the RPV wall until it either fails the RPV or experiences a stable arrest. In each analysis, a $K_{Ia}$ curve is sampled from the lognormal $K_{Ia}$ distribution (to be discussed). The applied $K_I$ for the growing infinite-length flaw is compared to $K_{Ia}$ as the flaw propagates through the wall. If crack arrest does not occur ($K_I \geq K_{Ia}$), the crack tip advances another small increment, and again a check is made for arrest. If the crack does arrest ($K_I \leq K_{Ia}$), the simulation continues stepping through the transient time history checking for re-initiation of the arrested flaw. At the end of the Monte Carlo analysis, $P(F|I)$ is simply the number of flaws (that initiated at time $\tau^n$) that propagated through the wall thickness causing RPV failure, divided by the total number of simulated flaws. See Sect. 3.3.14 for details of the Initiation-Growth-Arrest (*IGA*) submodel.

The *sup*-norm of the vector $\{cpf(\tau^n)\}$, *CPF*, occurs at the same time step as the *CPI*. In Table 3.1, for the example flaw, *CPF* is 0.103 and occurs at a transient elapsed time of 26 minutes.

### 3.3.12 Multiple Flaws

The technical basis for the treatment of multiple flaws in the beltline region of an RPV is given in [88,89]. For each *j*th RPV trial and *i*th transient, the process described above is repeated for all postulated flaws, resulting in an array of values of $CPI_{(i,j,k)}$, for each *k*th flaw, where the value of $CPI_{(i,j,k)}$ is the *sup*-norm of the vector $\{cpi(\tau^n)_{(i,j,k)}\}$ (0.242 for the example in Table 3.1).

If $CPI_{(i,j,1)}$ is the *probability of initiation* of a flaw in an RPV trial that contains a single flaw, then $(1\text{-}CPI_{(i,j,1)})$ is the *probability of non-initiation*. If $CPI_{(i,j,1)}$ and $CPI_{(i,j,2)}$ are the *marginal* probabilities of initiation of two flaws in an RPV trial that contains two flaws, then $(1\text{-}CPI_{(i,j,1)})\times\ (1\text{-}CPI_{(i,j,2)})$ is the total probability of non-initiation, i.e., the joint probability that neither of the two flaws will fracture. This can be generalized to an RPV simulation with *nflaw* flaws, so that the total joint probability that none of the flaws will initiate is:

$$\left\{\begin{matrix}\text{Conditional probability} \\ \text{of non-initiation}\end{matrix}\right\}_{(i,j)} = \prod_{k=1}^{nflaw}(1-CPI_{(i,j,k)}) = (1-CPI_{(i,j,1)})(1-CPI_{(i,j,2)})\ldots(1-CPI_{(i,j,nflaw)}) \tag{25}$$

Therefore, for the *i*th transient and *j*th RPV trial with *nflaw* flaws, the total probability that at *least one of the flaws* will fracture is just the complement of Eq. (25):

$$CPI_{RPV(i,j)} = 1 - \prod_{k=1}^{nflaw}(1-CPI_{(i,j,k)}) = 1-\left[\left(1-CPI_{(i,j,1)}\right)(1-CPI_{(i,j,2)})\ldots(1-CPI_{(i,j,nflaw)})\right] \tag{26}$$

The method described here for combining the values of *CPI* for multiple flaws in an RPV is also used for combining the values of *nonfailure* to produce *CPFs* for multiple flaws.

### 3.3.13 Ductile-Tearing Models in FAVOR$^{EP}$

Two ductile-tearing models have been implemented into FAVOR$^{EP}$. Ductile-Tearing Model No. 1, implemented in the FAVOR, v05.1, is the recommended model to estimate the effects of ductile tearing in the *Initiation-Growth-Arrest* model. Ductile-Tearing Model No. 2 was implemented in FAVOR, v03.1, and is retained in the current release for the purposes of backward compatibility with previous analyses carried out using FAVOR, v03.1.

Ductile-tearing property data were obtained from the PTSE-1 [26] and PTSE-2 [27] studies carried out in the late 1980s along with additional data collected in [94-96] and applied in the model development. A summary of the major materials and data sources is presented in Table 3.3 along with the chemistry composition and relevant ductile-tearing properties in Tables 3.4 and 3.5.

**Table 3.3. Sources for Ductile-Tearing Data [26, 27, 90, 91, 92, 143]**

| Materials | Reference |
|---|---|
| 61-67W | NUREG/CR-3506 |
| Midland Weld | NUREG/CR-5736 |
| P02, 68-71W | NUREG/CR-4880 |
| PTSE-1 Post Test | NUREG/CR-4106 |
| PTSE-2 Post Test | NUREG/CR-4888 |
| W8A & W9A | NUREG/CR-5492 |

**Table 3.4. Chemical Composition of Materials Used in the Ductile-Tearing Model Development**

| HSST | Weld Flux | Chemistry Composition (wt %) | | | | | | | | | |
|---|---|---|---|---|---|---|---|---|---|---|---|
| ID | Lot ID | C | Mn | P | S | Si | Cr | Ni | Mo | Cu | V |
| Plate 02 | (-) | 0.230 | 1.550 | 0.009 | 0.014 | 0.200 | 0.040 | 0.670 | 0.530 | 0.140 | 0.003 |
| Midland Beltine | Linde 80 | 0.083 | 1.607 | 0.017 | 0.006 | 0.622 | 0.100 | 0.574 | 0.410 | 0.256 | 0.006 |
| Midland Nozzle | Linde 80 | 0.083 | 1.604 | 0.016 | 0.007 | 0.605 | 0.110 | 0.574 | 0.390 | 0.290 | 0.008 |
| W8A | Linde 80 | 0.083 | 1.330 | 0.011 | 0.016 | 0.770 | 0.120 | 0.590 | 0.470 | 0.390 | 0.003 |
| W9A | Linde 0091 | 0.190 | 1.240 | 0.010 | 0.008 | 0.230 | 0.100 | 0.700 | 0.490 | 0.390 | |
| 68W | Linde 0091 | 0.150 | 1.380 | 0.008 | 0.009 | 0.160 | 0.040 | 0.130 | 0.600 | 0.040 | 0.007 |
| 69W | Linde 0091 | 0.140 | 1.190 | 0.010 | 0.009 | 0.190 | 0.090 | 0.100 | 0.540 | 0.120 | 0.005 |
| 70W | Linde 0124 | 0.100 | 1.480 | 0.011 | 0.011 | 0.440 | 0.130 | 0.630 | 0.470 | 0.056 | 0.004 |
| 71W | Linde 80 | 0.120 | 1.580 | 0.011 | 0.011 | 0.540 | 0.120 | 0.630 | 0.450 | 0.046 | 0.005 |
| 61W | Linde 80 btwn A533B | 0.090 | 1.480 | 0.020 | 0.014 | 0.570 | 0.160 | 0.630 | 0.370 | 0.280 | 0.005 |
| 62W | Linde 80 btwn A508 | 0.083 | 1.510 | 0.160 | 0.007 | 0.590 | 0.120 | 0.537 | 0.377 | 0.210 | 0.010 |
| 63W | Linde 80 btwn A508 | 0.098 | 1.650 | 0.016 | 0.011 | 0.630 | 0.095 | 0.685 | 0.427 | 0.299 | 0.011 |
| 64W | Linde 80 btwn A508 | 0.085 | 1.590 | 0.014 | 0.015 | 0.520 | 0.092 | 0.660 | 0.420 | 0.350 | 0.007 |
| 65W | Linde 80 btwn A508 | 0.080 | 1.450 | 0.015 | 0.015 | 0.480 | 0.088 | 0.597 | 0.385 | 0.215 | 0.006 |
| 66W | Linde 80 btwn A508 | 0.092 | 1.630 | 0.018 | 0.009 | 0.540 | 0.105 | 0.595 | 0.400 | 0.420 | 0.009 |
| 67W | Linde 80 btwn A508 | 0.082 | 1.440 | 0.011 | 0.012 | 0.500 | 0.089 | 0.590 | 0.390 | 0.265 | 0.007 |

**Table 3.5. Summary of Ductile-Tearing Data Used in the Model Development**

| Material | Size | Fluence | Temp. | $J_{Ic}$ | Avg. $T_R$ | Avg. USE | Material | Size | Fluence | Temp. | $J_{Ic}$ | Avg. $T_R$ | Avg. USE | Material | Size | Fluence | Temp. | $J_{Ic}$ | Avg. $T_R$ | Avg. USE |
|---|---|---|---|---|---|---|---|---|---|---|---|---|---|---|---|---|---|---|---|---|
| ID | | $10^{19}$ n/cm$^2$ | (°C) | (kJ/m$^2$) | (-) | (ft-lbf) | ID | | $10^{19}$ n/cm$^2$ | (°C) | (kJ/m$^2$) | (-) | (ft-lbf) | ID | | $10^{19}$ n/cm$^2$ | (°C) | (kJ/m$^2$) | (-) | (ft-lbf) |
| 61W | 0.8 | 0 | 75 | 142.3 | 89 | 62 | 64W | 0.5 | 0.582 | 177 | 119.1 | 36 | 75 | Mid-Belt | NA | 0 | 21 | 167.4 | 71 | 65 |
| 61W | 0.5 | 0 | 75 | 143.4 | 106 | 62 | 64W | 4 | 0.66 | 200 | 78.7 | 50 | 75 | Mid-Belt | NA | 0 | 21 | 116.4 | 84 | 65 |
| 61W | 0.8 | 0 | 121 | 123.9 | 74 | 62 | 64W | 4 | 0.64 | 200 | 94.9 | 49 | 75 | Mid-Belt | NA | 0 | 21 | 131.4 | 76 | 65 |
| 61W | 0.5 | 0 | 121 | 130.6 | 90 | 62 | 64W | 1.6 | 0.623 | 200 | 57.3 | 46 | 75 | Mid-Belt | NA | 0 | 21 | 164.7 | 70 | 65 |
| 61W | 4 | 0 | 200 | 97.4 | 100 | 62 | 64W | 1.6 | 0.671 | 200 | 80.2 | 50 | 75 | Mid-Belt | NA | 0 | 150 | 133.4 | 41 | 65 |
| 61W | 4 | 0 | 200 | 128.1 | 72 | 62 | 64W | 0.8 | 0.773 | 200 | 101.9 | 31 | 75 | Mid-Belt | NA | 0 | 150 | 125.1 | 44 | 65 |
| 61W | 1.6 | 0 | 200 | 78.3 | 70 | 62 | 64W | 0.5 | 0.672 | 200 | 99.4 | 23 | 75 | Mid-Belt | NA | 0 | 150 | 141.1 | 60 | 65 |
| 61W | 0.8 | 0 | 200 | 89.5 | 52 | 62 | 64W | 0.8 | 0.773 | 288 | 46 | 15 | 75 | Mid-Belt | NA | 0 | 288 | 86.4 | 32 | 65 |
| 61W | 0.5 | 0 | 200 | 89.1 | 66 | 62 | 64W | 0.5 | 0.672 | 288 | 66.3 | 18 | 75 | Mid-Belt | NA | 0 | 288 | 103.3 | 33 | 65 |
| 61W | 1.6 | 0 | 288 | 57.7 | 68 | 62 | 65W | 1.6 | 0 | 132 | 123.4 | 120 | 108 | Mid-Nozz | NA | 0 | 21 | 126.6 | 47 | 64 |
| 61W | 0.8 | 0 | 288 | 66.1 | 47 | 62 | 65W | 0.8 | 0 | 132 | 147.2 | 97 | 108 | Mid-Nozz | NA | 0 | 21 | 113.0 | 57 | 64 |
| 61W | 0.5 | 0 | 288 | 75 | 53 | 62 | 65W | 0.5 | 0 | 132 | 118.5 | 130 | 108 | Mid-Nozz | NA | 0 | 150 | 102.8 | 39 | 64 |
| 61W | 0.5 | 0 | 288 | 76.5 | 53 | 62 | 65W | 4 | 0 | 177 | 80.4 | 138 | 108 | Mid-Nozz | NA | 0 | 150 | 89.9 | 43 | 64 |
| 61W | 0.8 | 1.1 | 121 | 103.1 | 51 | 52 | 65W | 0.8 | 0 | 177 | 117.6 | 76 | 108 | Mid-Nozz | NA | 0 | 288 | 69.1 | 32 | 64 |
| 61W | 1.6 | 1.3 | 121 | 83 | 41 | 52 | 65W | 0.5 | 0 | 177 | 114.8 | 102 | 108 | Mid-Nozz | NA | 0 | 288 | 64.5 | 39 | 64 |
| 61W | 0.5 | 1.6 | 121 | 76.4 | 22 | 52 | 65W | 4 | 0 | 200 | 69.3 | 114 | 108 | Mid-Nozz | NA | 0 | 288 | 64.3 | 37 | 64 |
| 61W | 0.5 | 1 | 200 | 96.4 | 60 | 52 | 65W | 1.6 | 0 | 200 | 104.1 | 72 | 108 | Plate 02 | NA | 0 | 50 | 117.3 | 197 | 105 |
| 61W | 4 | 1.1 | 200 | 52.4 | 38 | 52 | 65W | 0.8 | 0 | 200 | 128.9 | 84 | 108 | Plate 02 | NA | 0 | 50 | 189.9 | 164 | 105 |
| 61W | 1.6 | 1.2 | 200 | 63.6 | 31 | 52 | 65W | 0.5 | 0 | 200 | 94.8 | 111 | 108 | Plate 02 | NA | 0 | 50 | 191.8 | 154 | 105 |
| 61W | 0.8 | 1.2 | 200 | 69.5 | 44 | 52 | 65W | 4 | 0 | 288 | 120.1 | 73 | 108 | Plate 02 | NA | 0 | 50 | 205.1 | 141 | 105 |
| 61W | 4 | 1.4 | 200 | 61.3 | 30 | 52 | 65W | 1.6 | 0 | 288 | 71.9 | 73 | 108 | Plate 02 | NA | 0 | 50 | 218.9 | 153 | 105 |
| 61W | 0.8 | 1.1 | 288 | 46.4 | 15 | 52 | 65W | 1.6 | 0 | 288 | 74.2 | 69 | 108 | Plate 02 | NA | 0 | 121 | 111.0 | 156 | 105 |
| 61W | 0.5 | 1.4 | 288 | 44.6 | 17 | 52 | 65W | 0.8 | 0 | 288 | 73.5 | 56 | 108 | Plate 02 | NA | 0 | 121 | 137.1 | 178 | 105 |
| 62W | 0.5 | 0 | 75 | 121.7 | 119 | 93 | 65W | 0.5 | 0 | 288 | 83.8 | 69 | 108 | Plate 02 | NA | 0 | 121 | 161.7 | 147 | 105 |
| 62W | 1.6 | 0 | 149 | 114.5 | 124 | 93 | 65W | 1.6 | 0.67 | 132 | 106.2 | 77 | 72 | Plate 02 | NA | 0 | 121 | 168.3 | 133 | 105 |
| 62W | 0.8 | 0 | 149 | 150.1 | 139 | 93 | 65W | 0.8 | 0.744 | 132 | 113.6 | 54 | 72 | Plate 02 | NA | 0 | 121 | 171.4 | 138 | 105 |
| 62W | 0.5 | 0 | 149 | 91.4 | 99 | 93 | 65W | 0.5 | 0.767 | 132 | 110.3 | 48 | 72 | Plate 02 | NA | 0 | 204 | 132.1 | 118 | 105 |
| 62W | 4 | 0 | 177 | 107.6 | 154 | 93 | 65W | 4 | 0.74 | 177 | 53.1 | 89 | 72 | Plate 02 | NA | 0 | 204 | 134.7 | 99 | 105 |
| 62W | 0.8 | 0 | 177 | 160.3 | 115 | 93 | 65W | 0.8 | 0.744 | 177 | 104.8 | 45 | 72 | Plate 02 | NA | 0 | 204 | 139.2 | 115 | 105 |
| 62W | 0.5 | 0 | 177 | 101 | 94 | 93 | 65W | 0.5 | 0.629 | 177 | 114.7 | 47 | 72 | Plate 02 | NA | 0 | 204 | 140.4 | 113 | 105 |
| 62W | 4 | 0 | 200 | 145.5 | 140 | 93 | 65W | 4 | 0.61 | 200 | 85.6 | 61 | 72 | Plate 02 | NA | 0 | 204 | 181.0 | 100 | 105 |
| 62W | 1.6 | 0 | 200 | 154.4 | 117 | 93 | 65W | 1.6 | 0.62 | 200 | 70.4 | 56 | 72 | Plate 02 | NA | 0 | 288 | 111.8 | 81 | 105 |
| 62W | 1.6 | 0 | 200 | 128.7 | 133 | 93 | 65W | 0.8 | 0.756 | 200 | 91.5 | 41 | 72 | Plate 02 | NA | 0 | 288 | 112.1 | 73 | 105 |
| 62W | 0.8 | 0 | 200 | 150.8 | 99 | 93 | 65W | 0.5 | 0.629 | 200 | 107 | 54 | 72 | Plate 02 | NA | 0 | 288 | 118.1 | 92 | 105 |
| 62W | 0.5 | 0 | 200 | 78.4 | 83 | 93 | 65W | 0.8 | 0.756 | 288 | 41 | 23 | 72 | Plate 02 | NA | 0 | 288 | 121.9 | 73 | 105 |
| 62W | 0.5 | 0 | 200 | 113.8 | 87 | 93 | 65W | 0.5 | 0.767 | 288 | 43.9 | 32 | 72 | Plate 02 | NA | 0 | 288 | 132.6 | 89 | 105 |
| 62W | 4 | 0 | 288 | 87.3 | 112 | 93 | 66W | 0.5 | 0 | 100 | 94.4 | 41 | 76 | 68W | NA | 0 | 23 | 160.1 | 219 | 147 |
| 62W | 1.6 | 0 | 288 | 101 | 118 | 93 | 66W | 1.6 | 0 | 200 | 67 | 55 | 76 | 68W | NA | 0 | 121 | 151.1 | 204 | 147 |
| 62W | 0.8 | 0 | 288 | 93.8 | 59 | 93 | 66W | 0.8 | 0 | 200 | 103.6 | 50 | 76 | 68W | NA | 0 | 121 | 196.9 | 204 | 147 |
| 62W | 0.5 | 0 | 288 | 83.6 | 59 | 93 | 66W | 0.5 | 0 | 200 | 73 | 42 | 76 | 68W | NA | 0 | 200 | 223.5 | 111 | 147 |
| 62W | 0.5 | 0 | 288 | 85 | 84 | 93 | 66W | 0.8 | 0 | 288 | 73.8 | 40 | 76 | 68W | NA | 0 | 288 | 121.3 | 132 | 147 |

## Table 3.5. (cont.) Summary of Ductile-Tearing Data Used in the Ductile-Tearing Model Development

| Material ID | Size | Fluence $10^{19}$ n/cm$^2$ | Temp. (°C) | $J_{Ic}$ (kJ/m$^2$) | Avg. $T_R$ (-) | Avg. USE (ft-lbf) |
|---|---|---|---|---|---|---|
| 62W | 1.6 | 1.4 | 149 | 118.3 | 60 | 80 |
| 62W | 0.8 | 1.3 | 149 | 118.7 | 91 | 80 |
| 62W | 0.5 | 1.6 | 149 | 96.2 | 32 | 80 |
| 62W | 0.5 | 1.3 | 176 | 94.1 | 50 | 80 |
| 62W | 4 | 1.4 | 177 | 105.9 | 62 | 80 |
| 62W | 0.8 | 1.5 | 177 | 127.4 | 45 | 80 |
| 62W | 0.5 | 0.8 | 177 | 95.9 | 34 | 80 |
| 62W | 4 | 1.5 | 200 | 90 | 62 | 80 |
| 62W | 1.6 | 1.6 | 200 | 85 | 52 | 80 |
| 62W | 0.8 | 1.3 | 200 | 115.9 | 69 | 80 |
| 62W | 0.5 | 1 | 200 | 63.3 | 29 | 80 |
| 62W | 0.8 | 1.5 | 288 | 60.9 | 24 | 80 |
| 62W | 0.5 | 1.5 | 288 | 61.9 | 24 | 80 |
| 63W | 1.6 | 0 | 100 | 118 | 120 | 87 |
| 63W | 0.8 | 0 | 100 | 141.2 | 95 | 87 |
| 63W | 0.5 | 0 | 100 | 131.1 | 86 | 87 |
| 63W | 4 | 0 | 171 | 148.4 | 100 | 87 |
| 63W | 1.6 | 0 | 171 | 103.5 | 97 | 87 |
| 63W | 0.8 | 0 | 171 | 112.4 | 77 | 87 |
| 63W | 0.5 | 0 | 171 | 113.2 | 88 | 87 |
| 63W | 4 | 0 | 200 | 77.7 | 113 | 87 |
| 63W | 1.6 | 0 | 200 | 79.6 | 94 | 87 |
| 63W | 0.8 | 0 | 200 | 120.3 | 69 | 87 |
| 63W | 0.5 | 0 | 200 | 89.2 | 70 | 87 |
| 63W | 0.5 | 0 | 200 | 98.4 | 80 | 87 |
| 63W | 4 | 0 | 288 | 88.4 | 62 | 87 |
| 63W | 1.6 | 0 | 288 | 122.4 | 64 | 87 |
| 63W | 0.8 | 0 | 288 | 66.8 | 57 | 87 |
| 63W | 0.5 | 0 | 288 | 59.1 | 55 | 87 |
| 63W | 0.5 | 0 | 288 | 66.7 | 52 | 87 |
| 63W | 0.5 | 1.1 | 149 | 68.4 | 43 | 68 |
| 63W | 1.6 | 1.3 | 171 | 79.2 | 49 | 68 |
| 63W | 0.8 | 1.1 | 171 | 89.7 | 32 | 68 |
| 63W | 0.5 | 1.3 | 171 | 78.9 | 27 | 68 |
| 63W | 4 | 1.25 | 200 | 72.7 | 16 | 68 |
| 63W | 1.6 | 1.4 | 200 | 62.2 | 29 | 68 |
| 63W | 0.8 | 1.1 | 200 | 75.8 | 33 | 68 |
| 63W | 0.5 | 0.9 | 200 | 77 | 49 | 68 |
| 63W | 0.5 | 1 | 204 | 56.3 | 42 | 68 |
| 63W | 0.8 | 1.4 | 288 | 42.7 | 19 | 68 |
| 63W | 0.5 | 1.2 | 288 | 51.5 | 23 | 68 |
| 64W | 1.6 | 0 | 100 | 105.7 | 148 | 100 |
| 64W | 0.8 | 0 | 100 | 160.4 | 105 | 100 |
| 64W | 0.5 | 0 | 100 | 116 | 89 | 100 |
| 64W | 4 | 0 | 177 | 117.4 | 146 | 100 |
| 64W | 1.6 | 0 | 177 | 134.6 | 103 | 100 |
| 64W | 0.8 | 0 | 177 | 114.9 | 83 | 100 |
| 64W | 0.5 | 0 | 177 | 125 | 73 | 100 |
| 64W | 4 | 0 | 200 | 161.4 | 96 | 100 |
| 64W | 1.6 | 0 | 200 | 67.8 | 97 | 100 |
| 64W | 0.8 | 0 | 200 | 118.8 | 76 | 100 |
| 64W | 0.5 | 0 | 200 | 115.8 | 54 | 100 |
| 64W | 4 | 0 | 288 | 85.5 | 96 | 100 |
| 64W | 1.6 | 0 | 288 | 76.6 | 83 | 100 |
| 64W | 0.8 | 0 | 288 | 75.9 | 54 | 100 |
| 64W | 0.5 | 0 | 288 | 74.2 | 44 | 100 |
| 64W | 0.8 | 0.773 | 177 | 92.9 | 37 | 75 |
| 66W | 0.5 | 0 | 288 | 61.9 | 25 | 76 |
| 66W | 1.6 | 0.854 | 200 | 68.4 | 31 | 58 |
| 66W | 1.6 | 0.944 | 200 | 66.4 | 29 | 58 |
| 66W | 0.8 | 1.022 | 200 | 75.2 | 22 | 58 |
| 66W | 0.5 | 0.896 | 200 | 67.4 | 18 | 58 |
| 66W | 0.8 | 1.03 | 288 | 42.8 | 17 | 58 |
| 66W | 0.5 | 0.896 | 288 | 51.6 | 16 | 58 |
| 67W | 1.6 | 0 | 100 | 130.4 | 164 | 103 |
| 67W | 0.8 | 0 | 100 | 166.5 | 112 | 103 |
| 67W | 0.5 | 0 | 100 | 132.8 | 98 | 103 |
| 67W | 4 | 0 | 200 | 97.4 | 121 | 103 |
| 67W | 1.6 | 0 | 200 | 84.1 | 116 | 103 |
| 67W | 0.8 | 0 | 200 | 118 | 85 | 103 |
| 67W | 0.5 | 0 | 200 | 102.1 | 76 | 103 |
| 67W | 0.5 | 0 | 200 | 92 | 69 | 103 |
| 67W | 4 | 0 | 288 | 97.9 | 58 | 103 |
| 67W | 1.6 | 0 | 288 | 63.4 | 83 | 103 |
| 67W | 0.8 | 0 | 288 | 82.6 | 56 | 103 |
| 67W | 0.5 | 0 | 288 | 80 | 51 | 103 |
| 67W | 4 | 0.86 | 200 | 67.3 | 45 | 73 |
| 67W | 4 | 0.96 | 200 | 56.7 | 57 | 73 |
| 67W | 0.8 | 1.022 | 200 | 76.3 | 45 | 73 |
| 67W | 0.5 | 0.834 | 200 | 92.2 | 32 | 73 |
| 67W | 0.8 | 1.03 | 288 | 58.6 | 23 | 73 |
| 67W | 0.5 | 0.617 | 288 | 80 | 24 | 73 |
| W8A | 1 | 0 | 0 | 104.4 | 72 | 58 |
| W8A | 1 | 0 | 75 | 94.4 | 81 | 58 |
| W8A | 1 | 0 | 200 | 79.7 | 57 | 58 |
| W8A | 1 | 0 | 288 | 58.6 | 34 | 58 |
| W8A | 1 | 2.1 | 125 | 69.9 | 16 | 36 |
| W8A | 1 | 2.1 | 200 | 54.1 | 14 | 36 |
| W8A | 1 | 2.1 | 288 | 38.6 | 9 | 36 |
| W8A | 1 | 1.5 | 30 | 80.8 | 54 | 40 |
| W8A | 1 | 1.5 | 75 | 84.6 | 28 | 40 |
| W8A | 1 | 1.5 | 200 | 60 | 17 | 40 |
| W8A | 1 | 1.5 | 200 | 57.4 | 18 | 40 |
| W8A | 1 | 1.5 | 288 | 41.6 | 11 | 40 |
| W9A | 1 | 0 | -40 | 207.4 | NA | 115 |
| W9A | 1 | 0 | 0 | 255 | 173 | 115 |
| W9A | 1 | 0 | 75 | 195.9 | 170 | 115 |
| W9A | 1 | 0 | 200 | 147.9 | 130 | 115 |
| W9A | 1 | 0 | 288 | 92.9 | 120 | 115 |
| W9A | 1 | 0 | 288 | 116 | 97 | 115 |
| W9A | 1 | 2.1 | 75 | 156.2 | 42 | 74 |
| W9A | 1 | 2.1 | 200 | 124.1 | 37 | 74 |
| W9A | 1 | 2.1 | 200 | 147.7 | 40 | 74 |
| W9A | 1 | 2.1 | 288 | 81.5 | 31 | 74 |
| W9A | 1 | 1.5 | 75 | 167.7 | 52 | 84 |
| W9A | 1 | 1.5 | 200 | 146.4 | 46 | 84 |
| W9A | 1 | 1.5 | 200 | 127.2 | 47 | 84 |
| W9A | 1 | 1.5 | 288 | 96.1 | 36 | 84 |
| PTSE-2 | NA | 0 | 100 | 64 | 120 | 46.4 |
| PTSE-2 | NA | 0 | 100 | 55.6 | 145 | 46.4 |
| PTSE-2 | NA | 0 | 175 | 58.3 | 106 | 46.4 |
| PTSE-2 | NA | 0 | 175 | 68.4 | 105 | 46.4 |
| PTSE-2 | NA | 0 | 250 | 52.8 | 67 | 46.4 |
| PTSE-2 | NA | 0 | 250 | 52.2 | 61 | 46.4 |
| 68W | NA | 0 | 288 | 190.7 | 138 | 147 |
| 69W | NA | 0 | 50 | 143.0 | 87 | 147 |
| 69W | NA | 0 | 50 | 147.9 | 80 | 147 |
| 69W | NA | 0 | 50 | 163.7 | 70 | 147 |
| 69W | NA | 0 | 121 | 139.5 | 89 | 147 |
| 69W | NA | 0 | 121 | 141.7 | 93 | 147 |
| 69W | NA | 0 | 121 | 142.7 | 82 | 147 |
| 69W | NA | 0 | 121 | 158.9 | 88 | 147 |
| 69W | NA | 0 | 200 | 174.5 | 54 | 147 |
| 69W | NA | 0 | 204 | 98.9 | 76 | 147 |
| 69W | NA | 0 | 204 | 117.5 | 61 | 147 |
| 69W | NA | 0 | 288 | 89.7 | 56 | 147 |
| 69W | NA | 0 | 288 | 94.1 | 49 | 147 |
| 69W | NA | 0 | 288 | 103.8 | 56 | 147 |
| 69W | NA | 0 | 288 | 129.4 | 56 | 147 |
| 70W | NA | 0 | 50 | 106.2 | 188 | 74 |
| 70W | NA | 0 | 50 | 177.8 | 163 | 74 |
| 70W | NA | 0 | 121 | 127.5 | 159 | 74 |
| 70W | NA | 0 | 121 | 131.1 | 148 | 74 |
| 70W | NA | 0 | 121 | 142.8 | 140 | 74 |
| 70W | NA | 0 | 204 | 103.3 | 108 | 74 |
| 70W | NA | 0 | 204 | 112.0 | 133 | 74 |
| 70W | NA | 0 | 204 | 121.0 | 110 | 74 |
| 70W | NA | 0 | 288 | 89.0 | 79 | 74 |
| 70W | NA | 0 | 288 | 105.6 | 93 | 74 |
| 70W | NA | 0 | 288 | 106.2 | 88 | 74 |
| 71W | NA | 0 | 30 | 128.0 | 186 | 81 |
| 71W | NA | 0 | 50 | 97.9 | 144 | 81 |
| 71W | NA | 0 | 50 | 121.0 | 98 | 81 |
| 71W | NA | 0 | 121 | 110.8 | 153 | 81 |
| 71W | NA | 0 | 121 | 126.7 | 105 | 81 |
| 71W | NA | 0 | 121 | 131.0 | 155 | 81 |
| 71W | NA | 0 | 204 | 77.6 | 66 | 81 |
| 71W | NA | 0 | 204 | 84.7 | 87 | 81 |
| 71W | NA | 0 | 204 | 115.4 | 90 | 81 |
| 71W | NA | 0 | 288 | 64.5 | 72 | 81 |
| 71W | NA | 0 | 288 | 77.4 | 71 | 81 |
| 71W | NA | 0 | 288 | 80.2 | 61 | 81 |

In conjunction with the ductile-tearing model development, a revised fracture arrest toughness stochastic model has also been implemented in FAVOR$^{EP}$. A discussion of this new arrest model is given in Sect. 4.2.8.

One of the constraints in developing a ductile-tearing model for FAVOR$^{EP}$ is that the required material properties should currently be available for the four plants being studied in the PTS Re-evaluation project. The relevant information available from RVID2 [156] includes Cu, Ni, and P content; the upper-shelf Charpy V-notch (CVN) energy, *USE*; and the unirradiated flow stress of the RPV steels. Consequently, all ductile fracture toughness properties used in FAVOR$^{EP}$ need to be derived from this information.

The following models are required:

- a model for the variation of ductile crack initiation toughness, $J_{Ic}$ , with temperature and irradiation, and
- a model for the variation of ductile-tearing resistance as a function of temperature, irradiation, and accumulated ductile tearing, $\Delta a$ .

These two models are connected in that they both can be derived from a $J_R$ curve, expressed in a power-law model form by:

$$J_R = C(\Delta a^m) \tag{27}$$

where the tearing resistance is characterized by the material's local tearing modulus, $T_R$, defined by

$$T_R = \left(\frac{E}{\sigma_f^2}\right)\left(\frac{dJ_R}{da}\right) = \left(\frac{E}{\sigma_f^2}\right) \times m \times C \times \Delta a^{(m-1)} \tag{28}$$

Given the elastic modulus, $E$, and sampled irradiated flow stress, $\sigma_f$ , the remaining three variables required by the ductile-tearing model are $J_{Ic}$, $C$, and $m$, where all three are a function of temperature and level of irradiation damage.

Applying the definition of $J_{Ic}$ in ASTM E-1820 [93], estimates of two of the variables allows the calculation of the third. In Fig. 3.16, the ductile-tearing initiation toughness, $J_{Ic}$ , is defined in ASTM E-1820 as the intersection of the $J_R$ curve with a 0.2 mm offset blunting line given by

$$J_{(0.2\text{ mm offset})} = 2\sigma_f(\Delta a - \Delta a_0) \tag{29}$$

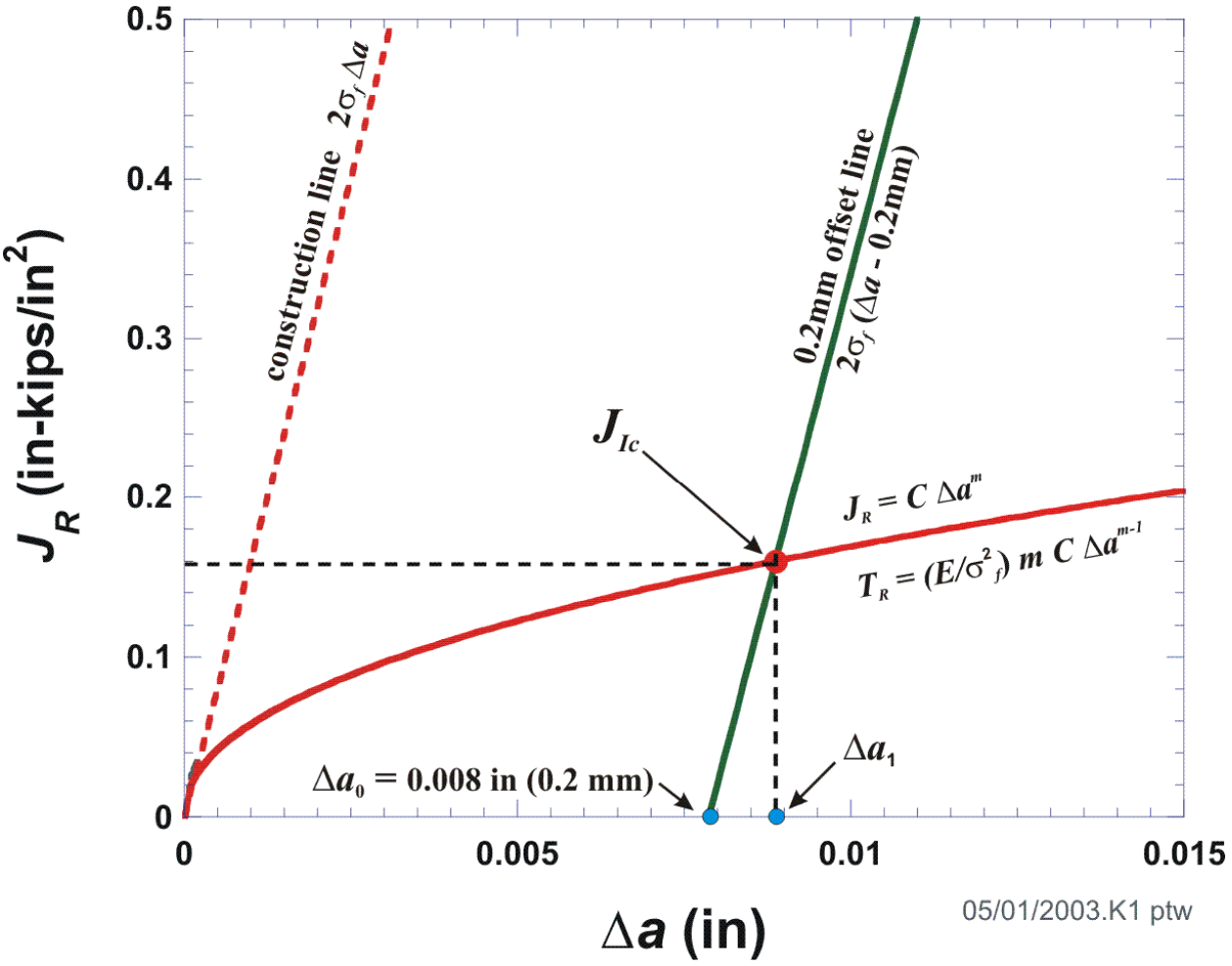


**Fig. 3.16. Given a $J_R$ curve in power-law model form and current flow stress, $\sigma_f$, the initiation toughness, $J_{Ic}$, and local tearing modulus, $T_R$, are uniquely defined (see ASTM E-1820 [93]).**

where the prescribed offset is $\Delta a_0 = 0.2$ mm (0.008 in). Therefore, with an estimate of $J_{Ic}$ and the power-law exponent, $m$, the power-law coefficient, $C$, is

$$J_{Ic} = C\Delta a^m \Rightarrow C = \frac{J_{Ic}}{\Delta a^m}$$

$$J_{Ic} = 2\sigma_f(\Delta a - \Delta a_0) \Rightarrow \Delta a = \frac{J_{Ic}}{2\sigma_f} + \Delta a_0 \qquad (30)$$

$$\therefore \quad C = \frac{J_{Ic}}{\left(\frac{J_{Ic}}{2\sigma_f} + \Delta a_0\right)^m}$$

The local tearing modulus then follows from Eq. (28). The focus of model development was, therefore, placed on providing methods of estimating the initiation fracture toughness, $J_{Ic}$, and the power-law exponent, $m$, as a function of temperature and irradiation damage.

#### 3.3.13.1 Ductile-Tearing Model No. 1 (implemented in FAVOR, v05.1)

The recommended Ductile-Tearing Model No. 1 was developed from the research described in [94,95]. The following is a summary of the model described in these references.

A model of ferritic steel toughness that accounts for fracture mode transition behavior, upper shelf behavior, and the interaction between these two different fracture modes can be constructed based on Wallin's Master Curve [151], the relationship between the upper-shelf temperature, $T_{US}$, the Master Curve reference temperature, $T_0$, and the upper-shelf Master Curve. Using these relationships it is possible, as described below, to estimate the complete variation of initiation fracture toughness, $J_{Ic}$, with temperature in both the transition regime and on the upper shelf based only on an estimate of $T_0$.

The following sampling protocols are taken from [95]:

Step 1. – Estimate a Value for $T_0$

Given a sampled value of $\widehat{RT}_{NDT0}\left[°\mathrm{F}\right]$ and an adjustment for the effects of irradiation damage, $\widehat{\Delta RT}_{NDT}\left(r,\ldots\right)$, an estimate for $T_0$ (for a reference size of 1T) can be sampled using Eq. (115) (see Sect. 4.2.5)

$$\widehat{T}_0 = \frac{\left\langle \widehat{RT}_{NDT-DT} + 27.82 - \left\{ 122.4 \left[ \left( -\ln(1-P_{T_0}) \right)^{\frac{1}{2.25}} \right] \right\} \right\rangle - 32}{1.8} \quad \left[°\mathrm{C}\right] \tag{31}$$

Where $\widehat{RT}_{NDT-DT}\left(r,\ldots\right) = \widehat{RT}_{NDT0} + \widehat{\Delta RT}_{NDT}\left(r,\ldots\right)$, (see Eq. (117)) with $\widehat{RT}_{NDT0}$ equal to the sampled unirradiated value of $RT_{NDT,}$ $\widehat{\Delta RT}_{NDT}\left(r,\ldots\right)$ equal to the shift due to radiation embrittlement, and $P_{T_0} = \Phi$ is the fractile drawn for the epistemic uncertainty in $RT_{NDT}$ in Eq. (116).

Step 2. – Estimate a Value for the Upper-Shelf Temperature, $T_{US}$

From the relationship developed in [95], an estimate for the upper-shelf temperature associated with this sampled value for $T_0$ can be calculated from

$$\widehat{T_{US}} = 50.1 + \left(0.794\,\widehat{T_0}\right) \quad [°\text{C}] \tag{32}$$

Step 3. – Calculate a Value for $J_C$ Using the Master Curve at $T_{US}$

Using a plane strain conversion from $K_{Jc}$ to $J_c$, we have, from the Master Curve model [151]

$$J_{c(med)} = \frac{1000\left\{30 + 70\exp\left[0.019\left(T_{US} - T_0\right)\right]\right\}^2\left(1-\nu^2\right)}{E} \quad \left[\frac{\text{kJ}}{\text{m}^2}\right]$$

where (33)

$$E = 207200 - \left(57.1\,T_{US}\right) \ \left[\text{MPa}\right] \text{ and } \nu = 0.3$$

Step 4. – Calculate an Estimate for $\Delta J_{Ic}$ at $T_{US}$

Using the relationship derived in [95] to characterize the temperature dependence of $J_{Ic}$

$$\Delta J_{Ic} = J_{Ic}^{meas} - J_{Ic}^{288°\text{C}} = 2.09\left\{C_1\exp\left[-C_2\left(T_{US}+273.15\right) + C_3\left(T_{US}+273.15\right)\ln\left(\dot{\varepsilon}\right)\right] - \sigma_{ref}\right\}$$

$$\text{where} \quad C_1 = 1033 \text{ MPa}, \quad C_2 = 0.00698 \text{ K}^{-1}, \quad C_3 = 0.000415 \text{ K}^{-1}, \quad \dot{\varepsilon} = 0.0004 \text{ sec}^{-1}, \quad \sigma_{ref} = 3.3318 \text{ MPa} \tag{34}$$

Step 5. – Calculate an Estimated Mean and Standard Deviation for the Aleatory Uncertainty in $J_{Ic}$

At a given wall temperature, $T_{wall}(R,t)$ $[°\text{C}]$, an estimated mean value for $J_{Ic}$ can now be estimated by

$$\overline{J_{Ic}} = J_{c(med)} - \Delta J_{Ic} + 2.09\left\{C_1\exp\left[-C_2\left(T_{wall}+273.15\right) + C_3\left(T_{wall}+273.15\right)\ln\left(\dot{\varepsilon}\right)\right] - \sigma_{ref}\right\} \quad \left[\frac{\text{kJ}}{\text{m}^2}\right] \tag{35}$$

Where an estimate for the standard deviation is given in [95] by

$$\sigma_{J_{Ic}} = 62.023\exp\left(-0.0048\,T_{wall}\right) \quad \left[\frac{\text{kJ}}{\text{m}^2}\right] \tag{36}$$

Step 6. – Sample a Value for $J_{Ic}$ from a Normal Distribution

The aleatory uncertainty in $J_{Ic}$ is now estimated by sampling from the following normal distribution

$$\widehat{J}_{Ic} \leftarrow N\left(\overline{J_{Ic}}, \sigma_{J_{Ic}}\right) \quad \left[\frac{\text{kJ}}{\text{m}^2}\right] \tag{37}$$

where the sampled value is truncated at $\overline{J_{Ic}} - 2\sigma_{J_{Ic}} \le \widehat{J_{Ic}} \le \overline{J_{Ic}} + 2\sigma_{J_{Ic}}$ using the truncation protocol of Sect. 3.3.8.

Step 7. – Calculate an Estimate for the Power-Law Exponent, *m*, and Coefficient, *C*

The mean value of the *J-R* curve exponent *m* (as in $J_R = C\left(\Delta a^m\right)$) is estimated based on the sampled value of $J_{Ic}$ and the local value of the wall temperature, $T_{wall}(R,t)$, from the following equation (developed from the data given in [95])

$$\begin{gathered} \overline{m} = a + b\exp\left(\frac{T_{wall}\left[^{\circ}\mathrm{C}\right]}{d}\right) + c\left(\widehat{J_{Ic}}\left[\mathrm{kJ/m^2}\right]\right)^3 \\ a = 0.1117 \quad c = 5.8701\times 10^{-09} \\ b = 0.4696 \qquad d = -758.19 \\ \sigma_{\text{std-error}} = 0.08425 \\ R^2 = 0.2992 \end{gathered} \tag{38}$$

The *J-R* curve exponent *m* with aleatory uncertainty can then be sampled from the following normal distribution:

$$\widehat{m} \leftarrow N(\overline{m}, 0.08425) \tag{39}$$

The *J-R* curve coefficient, *C*, then follows from

$$\widehat{C} = \frac{\widehat{J_{Ic\,(\text{at } T_{wall})}}}{\left(\dfrac{\widehat{J_{Ic\,(\text{at } T_{wall})}}}{2\widehat{\sigma_f}} + \Delta a_0\right)^{\widehat{m}}} \tag{40}$$

where $\widehat{\sigma_f}$ is the sampled flow stress and $\Delta a_0 = 0.2$ mm.

### 3.3.13.2 Ductile-Tearing Model No. 2 (implemented in FAVOR, v03.1)

Pursuant to the proposal in [96], a preliminary ductile-tearing model was developed and implemented into FAVOR, v03.1, for a scoping study of the effects of tearing resistance associated with RPV materials.

#### 3.3.13.2.1 Upper-Shelf Irradiation Effects Model

The following discussion is taken from [96]:

To date, efforts to trend the effects of irradiation damage on RPV steels have focused predominantly on predicting the joint effects of radiation (as quantified by the fast-neutron fluence, energy > 1 MEv)

and chemical composition on the energy absorbed by a Charpy V-notch (CVN) specimen on the upper shelf (i.e., the upper shelf energy, or *USE*). This focus occurs because CVN specimens are placed into surveillance capsules that are used to assess the effect of irradiation damage on the RPV steel. It should be emphasized that the *USE* is ***not*** the initiation fracture toughness ($J_{Ic}$) or the tearing modulus ($T_R$) information needed by FAVOR$^{EP}$ to assess the probability of through-wall cracking of the RPV arising from a PTS event. Nevertheless, without significant additional research the only way to predict the effect of irradiation on $J_{Ic}$ and $T_R$ is to first predict the effect of irradiation on *USE* and then correlate $J_{Ic}$ and $T_R$ with *USE*.

In 1998, Eason, Wright, and Odette [97, 98] proposed the following relation between *USE*, chemical composition, and fluence based on the *USE* data available from domestic nuclear RPV surveillance programs at that time (692 data records) (NUREG/CR-6551) [98]. This model is given by the following equation

$$USE_{(i)} = A + 0.0570 \cdot USE_{(u)}^{1.456} - \left[17.5 \cdot f\left(Cu\right) \cdot \left(1 + 1.17 Ni^{0.8894}\right) + 305P\right]\left(\frac{\phi t}{10^{19}}\right)^{0.2223} \quad \text{[ft-lbf]} \qquad (41)$$

where $USE_u$ is the unirradiated upper-shelf energy in ft-lbf; *Cu*, *Ni*, and *P* are the copper, nickel, and phosphorous content in wt %; $\phi t$ is the fast-neutron fluence in neutrons/cm$^2$; *A* is a product-form constant; and *f*(*Cu*) is a function of copper content defined as

$$A = \begin{cases} 55.4 & \text{for welds} \\ 61.0 & \text{for plates} \\ 66.3 & \text{for forgings} \end{cases}$$

$$f\left(Cu\right) = \frac{1}{2} + \frac{1}{2}\tanh\left[\frac{Cu - 0.138}{0.0846}\right]$$

Reference [96] proposes the following method to simulate upper-shelf energies and address uncertainties in $USE_{(u)}$:

Step 1. Input a best-estimate value for the unirradiated upper-shelf energy for a given major region in the FAVOR$^{EP}$ embrittlement map of the beltline. Treat this value as the mean of a normal distribution of $USE_{(u)}$ values, $\mu_{USE_{(u)}}$ .

Step 2. At this value of $\mu_{USE_{(u)}}$, sample a value for the standard deviation from a normal distribution given by

$$\begin{aligned} \sigma_{USE_{(u)}(mean)} &= 4.3296 - 0.0857\mu_{USE_{(u)}} + 0.0012\mu_{USE_{(u)}}^2 \\ \widehat{\sigma}_{USE_{(u)}} &\leftarrow N(\sigma_{USE_{(u)}(mean)}, 2.2789) \end{aligned} \qquad (42)$$

Step 3. Sample a value for the unirradiated upper-shelf energy, $\widehat{USE_{(u)}}$, from the following normal distribution

$$\widehat{USE_{(u)}} \leftarrow N(\mu_{USE_{(u)}}, \widehat{\sigma}_{USE_{(u)}}) \tag{43}$$

Step 4. The irradiated value for the upper-shelf energy is then estimated from Eq. (41), or, applying sampling notation:

$$\widehat{USE}_{(i)} = A + 0.0570 \cdot \widehat{USE}_{(u)}^{1.456} - \left[17.5 \cdot f\left(\widehat{Cu}\right) \cdot \left(1 + 1.17\widehat{Ni}^{0.8894}\right) + 305\widehat{P}\right]\left(\frac{\widehat{\phi t}}{10^{19}}\right)^{0.2223} \quad \text{[ft-lbf]} \tag{44}$$

where the chemistry and attenuated fluence have been previously sampled.

3.3.13.2.2 Model for Initiation Ductile Fracture Toughness, $J_{Ic}$

The sampling protocol for $J_{Ic}$ developed in [96] is as follows:

Step 1. Determine a value of $\widehat{USE}_{(u)}$ using the sampling protocol outlined in Sect. 3.3.13.2.1 and Eqs. (42) and (43).

Step 2. Apply this sampled value of $\widehat{USE}_{(u)}$ along with sampled values of $\widehat{Cu}$, $\widehat{Ni}$, $\widehat{P}$ and $\widehat{\phi t}$ to estimate a value of $\widehat{USE}_{(i)}$ using Eq. (44).

Step 3. Convert this estimate of $\widehat{USE}_{(i)}$ value to a value of $\widehat{K}_{J_{Ic}(i)(\text{at } 550°\text{F})}$ at 550°F using the mean curve established in [96], where the uncertainty in $\widehat{K}_{J_{Ic}(i)(\text{at } 550°\text{F})}$ is ***not*** sampled,

$$\widehat{K}_{J_{Ic}(i)(\text{at } 550°\text{F})} = 70.855 + \left(0.5784 \times \widehat{USE}_{(i)}\right) \ [\text{ksi}\sqrt{\text{in}}] \tag{45}$$

Step 4. Convert the $\widehat{K}_{J_{Ic}(i)(\text{at } 550°\text{F})}$ value to a $\widehat{K}_{J_{Ic}(i)(\text{at } T_{wall})}$ value at the wall temperature of interest using the mean curve from [96]:

$$\widehat{\Delta K}_{J_{Ic}} = K_{J_{Ic}(\text{at } T_{wall})} - \widehat{K}_{J_{Ic}(\text{at } 550°\text{F})} =$$
$$= 1.35\left\{1033 \cdot \exp\left[\begin{array}{c} 0.000415\left(\frac{T_{wall} + 459.69}{1.8}\right) \cdot \ln\left(0.0004\right) \\ -0.00698\left(\frac{T_{wall} + 459.69}{1.8}\right) \end{array}\right] - \sigma_{ref}\right\} \ [\text{ksi}\sqrt{\text{in}}] \tag{46}$$

where $\sigma_{ref}$ is

$$\sigma_{ref} = 1033 \cdot \exp\left[\begin{array}{c} 0.000415\left(\frac{550 + 459.69}{1.8}\right) \cdot \ln\left(0.0004\right) \\ -0.00698\left(\frac{550 + 459.69}{1.8}\right) \end{array}\right] = 3.331798 \tag{47}$$

and $T_{wall}$ is the wall temperature at the crack tip in °F. Therefore

$$\widehat{K}_{J_{Ic}(\text{at } T_{wall})} = \widehat{K}_{J_{Ic}(\text{at } 550°\text{F})} + \widehat{\Delta K}_{J_{Ic}} \qquad [\text{ksi}\sqrt{\text{in}}] \tag{48}$$

The required sampled value of $J_{Ic}$ follows from the plane strain conversion

$$\widehat{J}_{Ic(\text{at } T_{wall})} = \left(\frac{1-\nu^2}{E}\right)\widehat{K}^2_{J_{Ic}(\text{at } T_{wall})} \quad [\text{in-kips/in}^2] \tag{49}$$

3.3.13.2.3 Model for Normalized Average Tearing Resistance, $T_{mat}$ , and $J_R$ Curve Power-Law Exponent, $m$

In the analysis of ductile-tearing data in [96], the exponent, $m$, of the $J_R$ power-law curve (see Eq. (27)) has been correlated with the material's estimated value for the average tearing modulus, $T_{mat}$ , which is the normalized linear slope of all the $J$-$\Delta a$ data between the 0.15 and 1.5 mm exclusion lines in the ASTM E-1820 determination of $J_{Ic}$.

The sampling protocol for estimating a value for $T_{mat}$ is the following:

Step 1. Determine a value of $\widehat{USE}_{(u)}$ using the sampling protocol outlined in Sect. 3.3.13.2.1 and Eqs. (42) and (43).

Step 2. Apply this sampled value of $\widehat{USE}_{(u)}$ along with sampled values of $\widehat{Cu}$ , $\widehat{Ni}$ , $\widehat{P}$ and $\widehat{\phi t}$ to estimate a value of $\widehat{USE}_{(i)}$ using Eq. (44).

Step 3. Convert this estimate of $\widehat{USE}_{(i)}$ value to a value of $\widehat{T}_{mat(i)(\text{at } 550°\text{F})}$ at 550 °F using the mean curve established in [96], where the uncertainty in $\widehat{T}_{mat(i)(\text{at } 550°\text{F})}$ is ***not*** sampled

$$\widehat{T}_{mat(i)(\text{at } 550°\text{F})} = 3.9389 + \left(0.5721 \times \widehat{USE}_{(i)}\right) \tag{50}$$

Step 4. Convert the $\widehat{T}_{mat(i)(\text{at } 550°\text{F})}$ value to a $\widehat{T}_{mat(i)(\text{at } T_{wall})}$ value at the wall temperature of interest using the mean curve from [96]:

$$\widehat{\Delta T}_{mat} = T_{mat(i)(\text{at } T_{wall})} - \widehat{T}_{mat(i)(\text{at } 550°\text{F})} =$$
$$= 1.38\left\{1033 \cdot \exp\left[\begin{array}{c} 0.000415\left(\frac{T_{wall}+459.69}{1.8}\right)\cdot \ln\left(0.0004\right) \\ -0.00698\left(\frac{T_{wall}+459.69}{1.8}\right) \end{array}\right] - \sigma_{ref}\right\} \quad [-] \tag{51}$$

where $\sigma_{ref}$ is

$$\sigma_{ref} = 1033 \cdot \exp\left[\begin{array}{c} 0.000415\left(\frac{550+459.69}{1.8}\right)\cdot \ln\left(0.0004\right) \\ -0.00698\left(\frac{550+459.69}{1.8}\right) \end{array}\right] = 3.331798 \tag{52}$$

and $T_{wall}$ is the wall temperature at the crack tip in °F. Therefore

$$\widehat{T}_{mat(i)(\text{at } T_{wall})} = \widehat{T}_{mat(i)(\text{at } 550°\text{F})} + \widehat{\Delta T}_{mat} \quad [-] \tag{53}$$

Step 5. Calculate an estimated value of the $J_R$ power-law exponent, $m$, using the correlation developed in [96], where the uncertainty in $\widehat{m}$ is not sampled.

$$\widehat{m} = 0.3214 + \left(0.0019 \times \widehat{T}_{mat(i)}\right) \tag{54}$$

Step 6. Calculate a value for the $J_R$ power-law coefficient, $C$, from the definition of $J_{Ic}$ in ASTM E-1820

$$\widehat{C} = \frac{\widehat{J}_{Ic(i)(\text{at } T_{wall})}}{\left(\frac{\widehat{J}_{Ic(i)(\text{at } T_{wall})}}{2\widehat{\sigma}_f} + \Delta a_0\right)^{\widehat{m}}} \tag{55}$$

where $\Delta a_0 = 0.2$ mm (0.008 in) and $\widehat{\sigma_f}$ is the sampled flow stress.

### 3.3.14 Initiation-Growth-Arrest (*IGA*) Submodel

As shown in Fig. 3.17, after the value of *CPI* has been calculated for the current flaw and transient, the conditional probability of vessel failure, *CPF*, by through-wall cracking is determined by the flaw Initiation-Growth-Arrest (*IGA*) submodel. The *IGA* submodel may be viewed as a small Monte Carlo model nested within the larger PFM Monte Carlo model. The following steps in the *IGA* submodel are shown in Fig. 3.18a:

Step G1. The *IGA* submodel is entered from the *PFM* model with a given flaw and transient. The *IGA* trial counter, *NTRIAL*, is initialized to zero. The pointer to the vector holding the random number sequence containing the values of $P_f$ [6] is reset to 1. Each transient for this flaw will start with the same random number sequence for internal sampling; however, each flaw has a different vector of random numbers. Go to Step G2.

Step G2. The *NTRIAL* counter is incremented; the time-step counter *NSTEP* is initialized to zero; and a random number $P_f$ is drawn from a uniform distribution on the open interval (0,1). Go to Step G3.

Step G3. The time-step counter is incremented up to the time step corresponding to when CPI occurred; time advances to the next time step. Go to Step G4.

Step G4. For the given flaw, subjected to the current transient, the change in *cpi* with respect to time is checked. If $\mathrm{d}cpi/dt > 0$, then the flaw becomes a candidate for propagation through the wall. (This submodel will be described in detail in the following.) If $\mathrm{d}cpi/\mathrm{d}t \le 0$, then control branches to Step G8.

Step G5. The *IGA Propagation* submodel is entered for this flaw, providing the submodel with the current time step, flaw depth, and value of $P_f$. Go to Step G6.

Step G6. Control returns from the *IGA Propagation* submodel with the fate of the flaw, either a vessel failure or a stable arrest (no failure). If a vessel failure occurred, control is transferred to Step G7. If a stable arrest occurred, control is transferred to Step G8.

Step G7. The vessel failure counter, *NFAIL*(*NSTEP*), for this time step is incremented. Go to Step G8.

Step G8. If the transient has completed, i.e., $NSTEP > NSTEP_{CPI}$, branch to Step G9. If the transient is not finished, cycle to Step G3. Note that $NSTEP_{CPI} = NSTEP$ at which $cpi(t) = \|cpi(t)\|_\infty = CPI$.

[6] The value of $P_f$ represents the percentile used in sampling $\widehat{\Delta RT}_{ARREST}$ (see Step 11 in Sect. 4.5) and $\widehat{K_{Ia}}$ (see Step 15 in Sect. 4.5) in Step P6 and in sampling $\widehat{K_{Ic}}$ in Step P8 of the *IGA Propagation Submodel*, and is used to ensure that the calculated initiation and failure probabilities are not affected by the order in which transients are analyzed. The *IGA Propagation Submodel* is an embedded Monte Carlo model that is repeated a user-set number of times using a different value of $P_f$ each time. See the discussion in the final paragraph of Sect. 3.3.1.

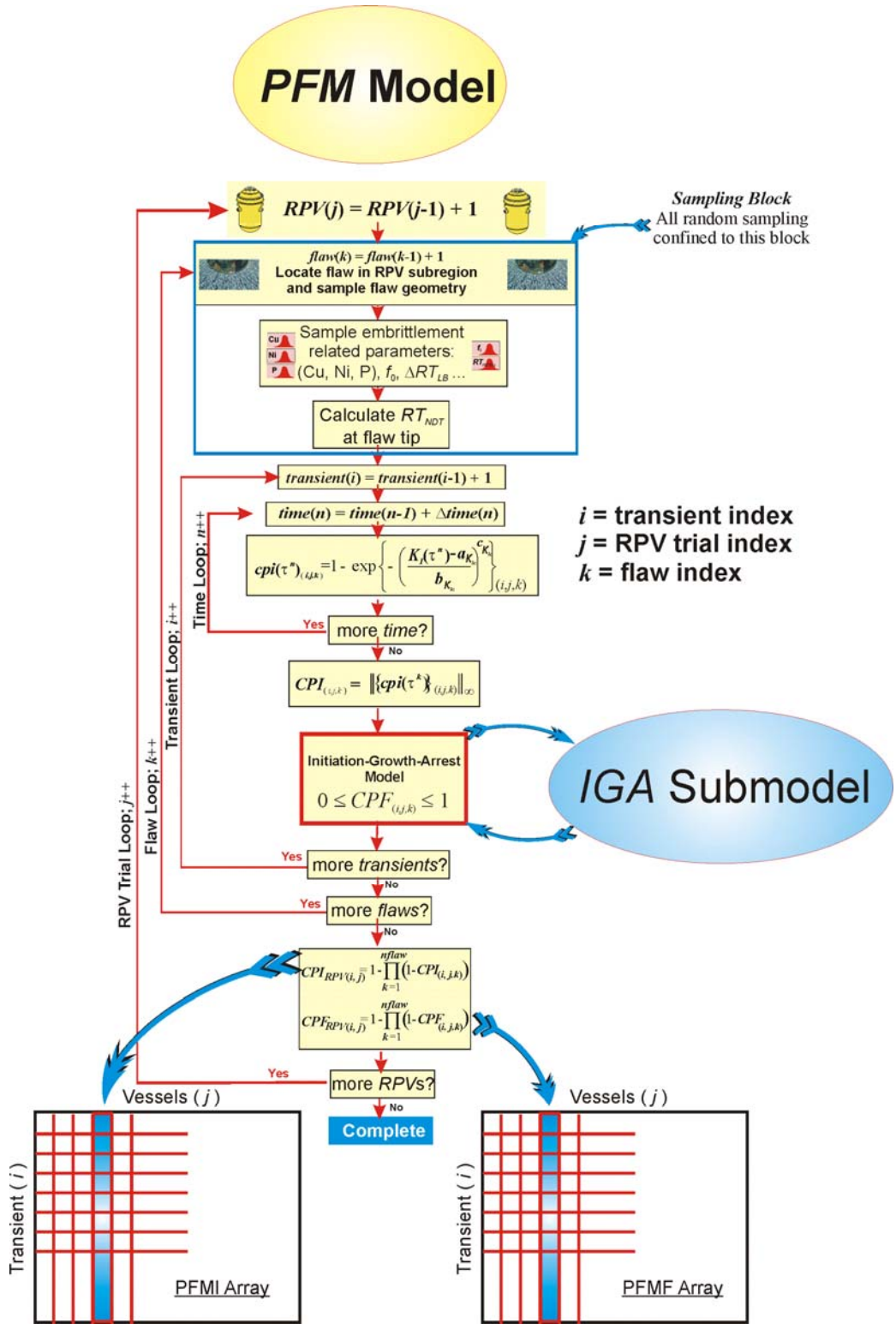


**Fig. 3.17. Flowchart for PFM model – the Initiation-Growth-Arrest (*IGA*) submodel can be viewed as a Monte Carlo model nested within the larger PFM Monte Carlo model. For a given flaw, the *IGA* submodel is called after the *CPI* for the current transient has been calculated. Note: ++ notation indicates increment index by 1; e.g., *i*++ means *i*=*i*+1.**

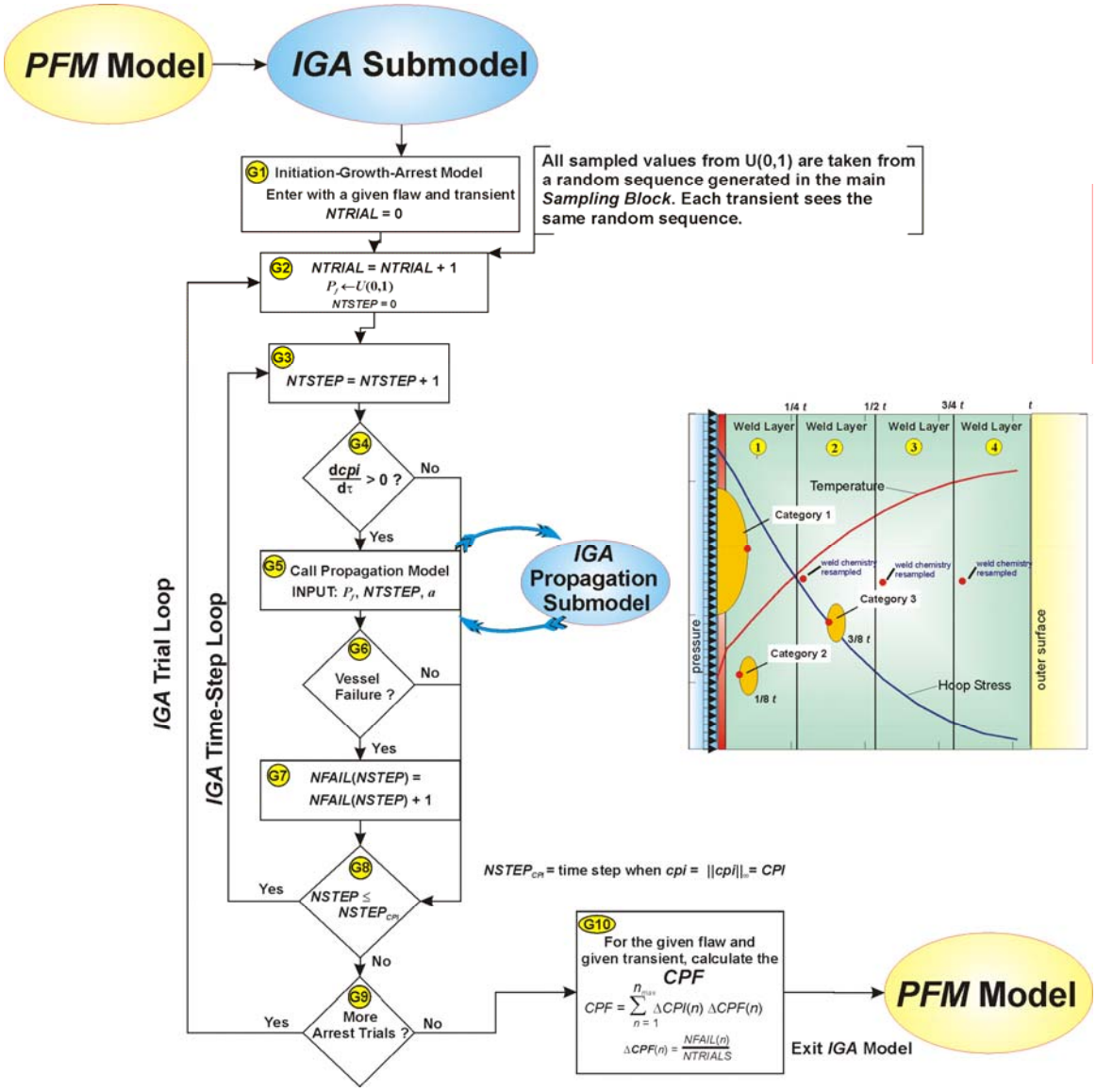


(a)

**Fig 3.18. (a) Flow chart for Initiation-Growth-Arrest Submodel – The *IGA Propagation* submodel is only called for flaws with increasing *CPIs*. The weld-layering scheme is also shown for *Initiation-Growth-Arrest* Model. No through-wall resampling is carried out for plates or forgings.**

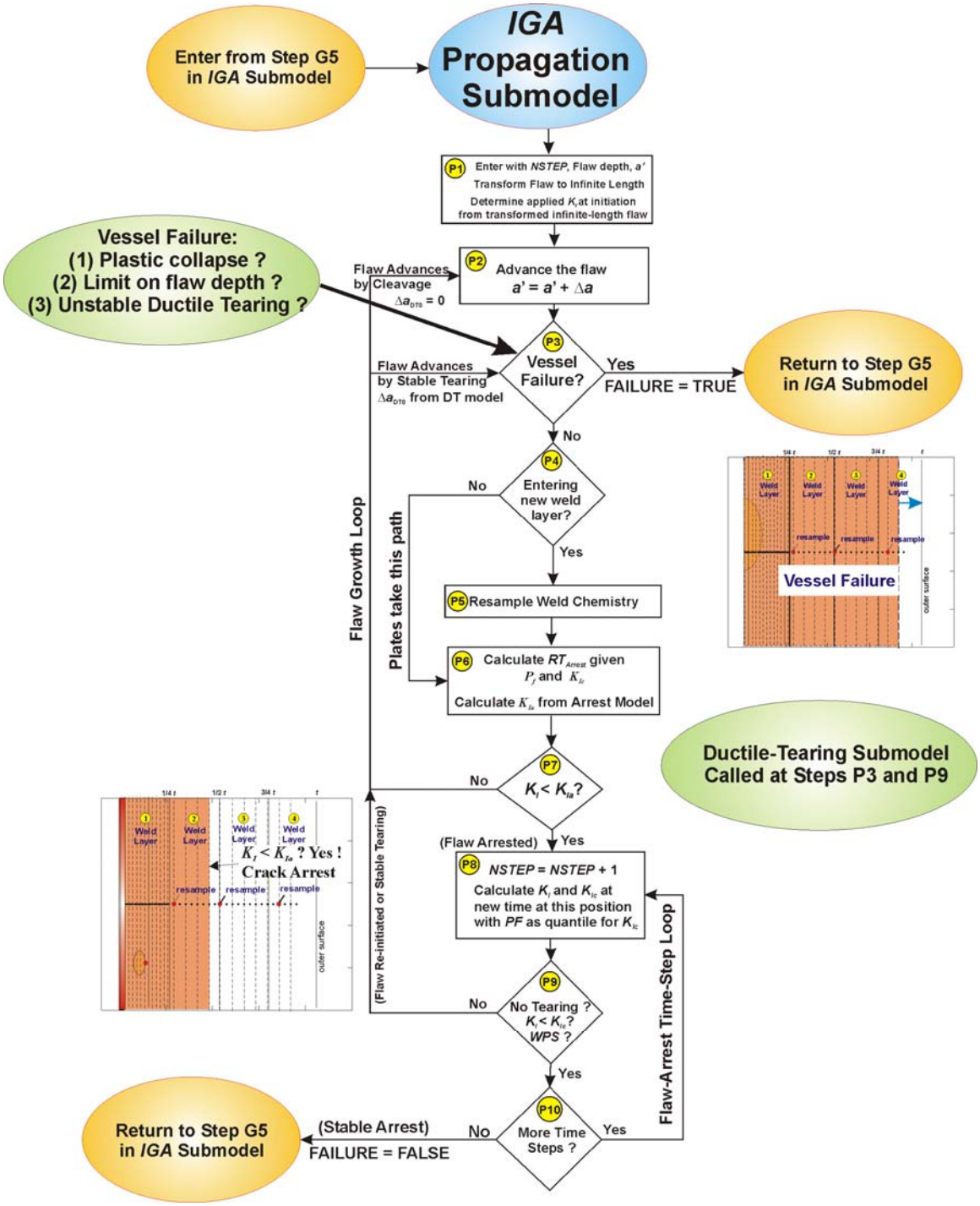


**(b)**

**Fig. 3.18. (continued) (b) *IGA Propagation* submodel to test for Stable Arrest (no failure) and Vessel Failure.**

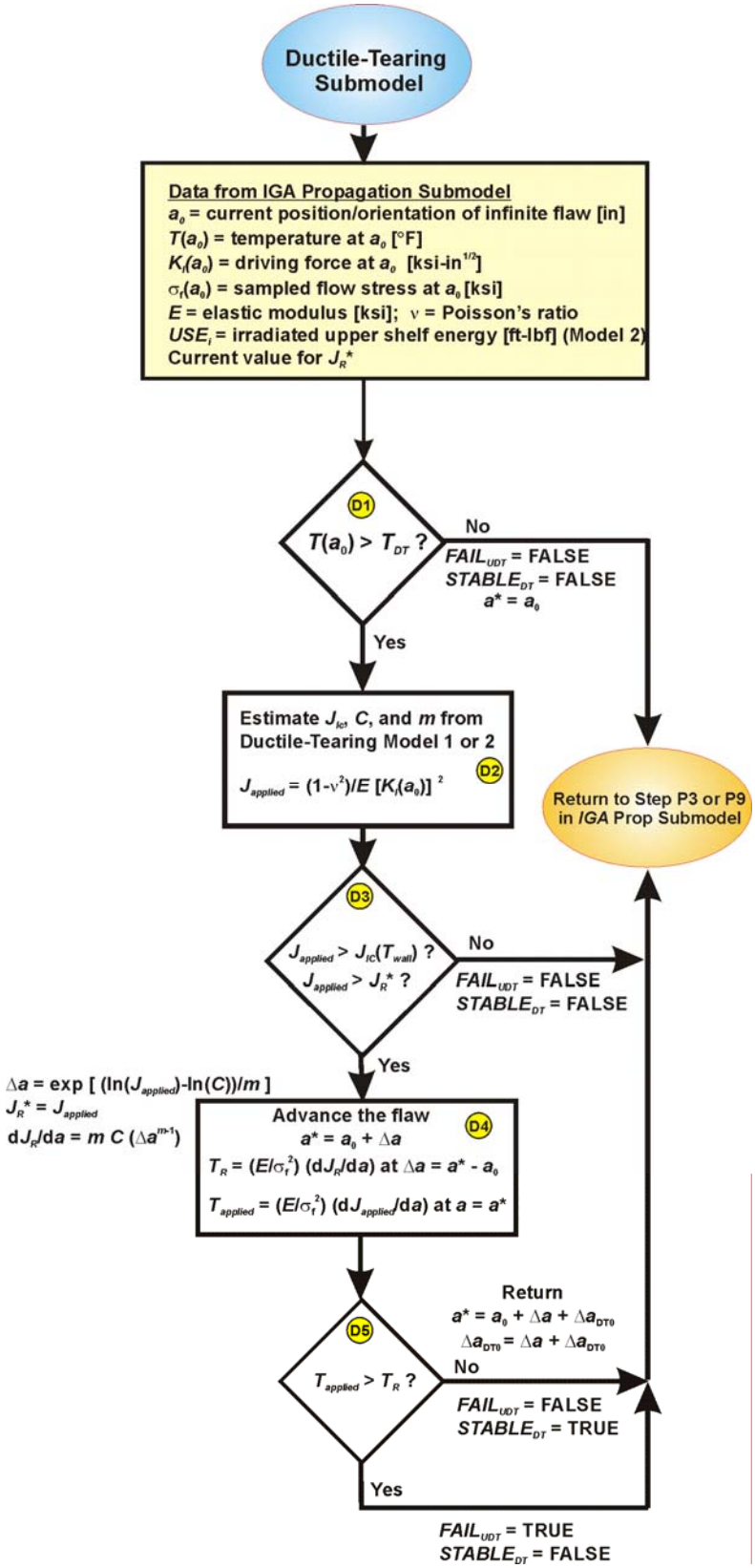


(c)

**Fig. 3.18 (continued) (c) *Unstable-Ductile-Tearing* submodel to test for either stable tearing to a new flaw position, *a**, or unstable ductile tearing that fails the vessel.**

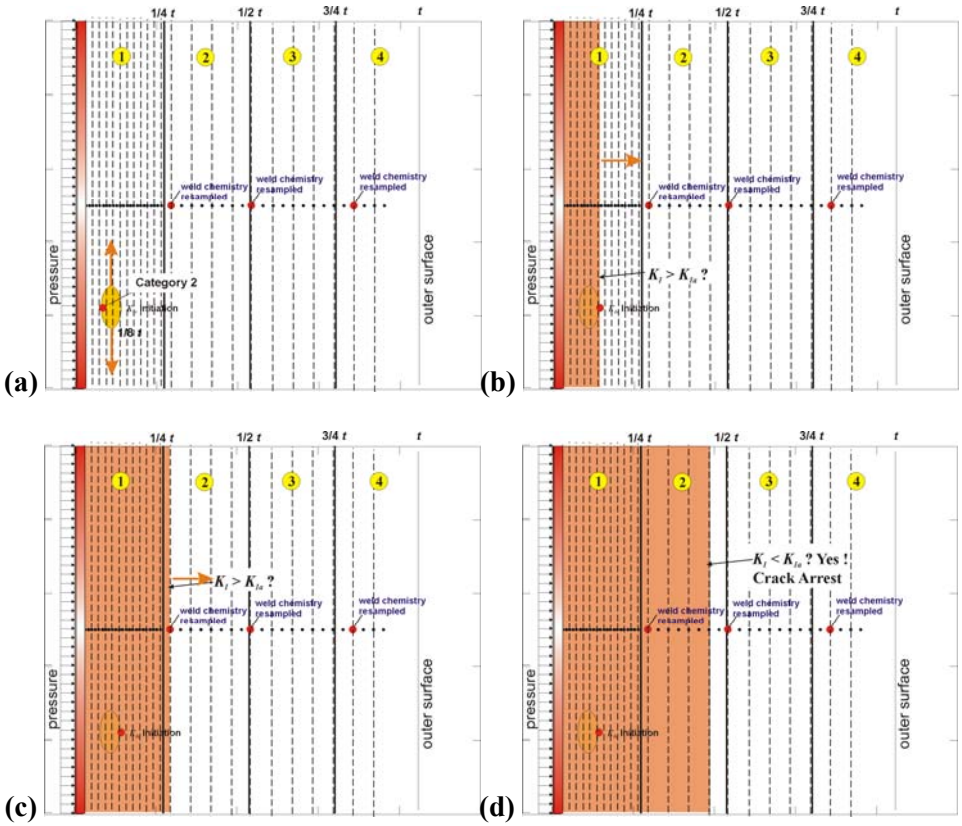


**Fig. 3.19. An example Category 2 flaw (a) initiates, (b) expands into an infinite-length flaw, (c) advances to new weld layer and resamples chemistry content to calculate new $RT_{NDT}$, (d) continues growth until either failure by net-section plastic collapse of remaining ligament or stable crack arrest. The potential for arrest and subsequent re-initiation is also modeled.**

Step G9. A check is made to see if the required number of trials has been completed. If there are more *NTRIALS* to be run, control is transferred to Step G2. If the *IGA* submodel has completed its sample trials for the current transient, then control is transferred to Step G10.

Step G10. The $CPF_{(i,j,k)}$ for the *i*th transient, and *j*th RPV trial, and *k*th flaw is calculated by the following:

$$CPF_{(i,j,k)} = \sum_{m=1}^{NSTEP_{CPI}} \Delta cpi(t^m)_{(i,j,k)} P(F \mid I)^m$$
$$P(F \mid I)^m = \frac{NFAIL(m)}{NTRIALS} \tag{56}$$

where $NSTEP_{CPI}$ is the time step at which the value of $CPI_{(i,j,k)}$ was calculated for this *i*th transient, *j*th RPV trial, and *k*th flaw.

Steps G2 through G9 are repeated *NTRIAL* cycles through the *IGA* submodel.

Figure 3.18b presents the control structure of the *IGA Propagation* submodel. This submodel proceeds in the following manner:

*IGA Propagation Submodel*

Step P1. Enter the submodel with the initiating time step, *NSTEP*, and the flaw depth. Transform the Category 1, 2, or 3 flaw into its corresponding infinite-length flaw, and calculate the applied stress-intensity factor, $K_I$, for the transformed flaw at this time and designate it $K_{I\text{-}initiation}$. This value of $K_I$ will be higher than the $K_I$ for the finite-flaw at initiation. Go to Step P2.

Step P2. Advance the infinite-length flaw to its next position in the *IGA* mesh (see Fig. 3.19). Proceed to Step P3.

Step P3. Check for vessel failure by through-wall cracking. At this new flaw depth and current time, calculate the current sampled estimate for the flow stress of the material. The current sampled value of $\widehat{\Delta T_{30}}$ (to be discussed in Chapter 4) is also used to estimate the effects of irradiation on the unirradiated flow stress, $\sigma_{flow(u)}$. After each resampling of $\widehat{\Delta T_{30}}$, the flow stress will have been adjusted by the following relation:

$$\widehat{\sigma_{flow}} = \sigma_{flow(u)} + \gamma\widehat{\Delta T_{30}} \text{ where } \gamma = \begin{cases} 0.112 \text{ ksi/°F for welds} \\ 0.131 \text{ ksi/°F for plates} \end{cases}$$

This sampled value of $\widehat{\sigma_{flow}}$ is then used in the vessel-failure test against the pressure-induced membrane stress in the remaining ligament, checking for net-section plastic collapse. The membrane stress is equal to

$$\sigma_m(t) = \frac{p_i(\tau)\left(R_i + a\right)}{\beta\left(R_o - R_i - a\right)}; \quad \beta = \begin{cases} 1 & \text{hoop stress} \\ 2 & \text{axial stress} \end{cases}$$

where $p_i(\tau)$ is the time-dependent internal pressure, $R_i$ and $R_o$ are the inner and outer vessel radii, respectively, and $a$ is the current flaw depth.

For the initial entry into the *IGA Propagation* submodel, the flaw is growing due to a cleavage initiation; therefore, the ductile-tearing model will not be applied until the flaw has experienced its first arrest event. After the flaw has arrested, the ductile-tearing model is called at this point to check for unstable ductile tearing. This check for unstable tearing is made only if the flaw has re-initiated in ductile tearing. If the flaw has re-initiated as a cleavage event, the ductile-tearing submodel is not called. If the conditions for unstable ductile tearing are encountered, the logical variable FAIL_UDT is set to TRUE in the ductile-tearing submodel and returned to the IGA Propagation Submodel.

The vessel failure criterion is

if REINITIATED_BY_DUCTILE_TEARING is TRUE then

$$\text{if} \left\{ \begin{array}{c} \sigma_m > \widehat{\sigma_{flow}} \\ \text{or} \\ FAIL\_UDT \text{ is TRUE} \\ \text{or} \\ \left( \dfrac{a}{R_o - R_i} \right) > FAILCR \end{array} \right\} \text{then}$$

vessel failure = TRUE during ductile tearing

return to Step G5 in *IGA* Model

$$\text{elseif} \left\{ \begin{array}{c} \sigma_m > \widehat{\sigma_{flow}} \\ or \\ \left( \dfrac{a}{R_o - R_i} \right) > FAILCR \end{array} \right\} \text{then}$$

vessel failure = TRUE during flaw growth by cleavage

return to Step G5 in *IGA* Model

else

vessel failure = FALSE

proceed to Step P4

where $0.25 \le FAILCR \le 0.95$ is a user-supplied failure criterion.

Step P4. If the material is a plate or forging product form, proceed directly to Step P6. If the material is a weld, check to see if the flaw has advanced into a new weld layer. Weld subregions are sectioned into through-wall quadrants to simulate, in an approximate manner, multiple weld layers. As the flaw advances from one weld-layer quadrant into the next, the weld chemistry will be resampled with the attenuated fluence. If the flaw has just advanced into a new weld layer, go to Step P5. If not, then proceed to Step P6.

Step P5. Resample the weld chemistry (Cu, Ni, and P) using the sampling distributions given in Chapter 4. Update the irradiation shift, $\widehat{\Delta RT_{NDT}}$, and the irradiated value of the upper shelf energy, $\widehat{USE_{(i)}}$, using the resampled weld chemistry. If the weld-layer-resampling option is turned on and the flaw has just entered layer 2, 3, or 4, then resample for a new value of $P_f$ to replace the value of $P_f$ sampled in Step G2 of the *IGA* submodel. The random iterate $P_f$ is drawn from a uniform distribution on the open interval $U(0,1)$.

Step P6. Using the current chemistry content and current value of $P_f$, recalculate the arrest reference temperature. The details are given in Chapter 4; however, the equations are given here for completeness. Calculate the epistemic uncertainty in the arrest reference temperature by Eqs. (145) and (151) given in Sect. 4.5.

$$\widehat{\Delta RT}_{epistemic} = -45.586 + 131.27\left[-\ln\left(1-\widehat{\Phi}\right)\right]^{\frac{1}{2.177}} \quad [°\text{F}]$$

$$\widehat{\Delta RT}_{epistemic-arrest} = \widehat{\Delta RT}_{epistemic} - 14.4 \quad [°\text{F}]$$

Retrieve the previously sampled unirradiated value of $\widehat{RT_{NDTo}}$ for this subregion and the sampled value of the irradiation shift for this flaw, $\widehat{\Delta RT_{NDT}}(r,\ldots)$, determined from the embrittlement model applied for this flaw at its current position in the RPV wall or from weld-chemistry resampling if Step P5 was executed. Calculate the shift in the arrest reference temperature, relative to the initiation reference temperature using Eqs. (152) in Step 11 of Sect. 4.5

$$\widehat{\Delta RT}_{ARREST} \leftarrow \Lambda(\widehat{\mu}_{\ln(\Delta RT_{ARREST})}, \widehat{\sigma}_{\ln(\Delta RT_{ARREST})}) \ \ [°\text{F}]$$

where (see Appendix F for the development of this protocol)

$$\widehat{\mu}_{\ln(\Delta RT_{ARREST})} = \ln\left[\widehat{\Delta RT}_{ARREST(mean)}\right] - \frac{\widehat{\sigma}^2_{\ln(\Delta RT_{ARREST})}}{2}$$

$$\widehat{\Delta RT}_{ARREST(mean)} = 44.122\exp\left[-0.005971\times\widehat{T}_0\right] \ \ [°\text{C}]$$

$$\widehat{T}_0 = \left(\widehat{RT}_{NDT_0} - \widehat{\Delta RT}_{epist-arrest} - 32\right)/1.8 \ \ [°\text{C}]$$

$$\widehat{\sigma}_{\ln(\Delta RT_{ARREST})} = \sqrt{\ln\left\{\exp\left[0.38998^2 + 2\ln(\widehat{\Delta RT}_{ARREST(mean)})\right] - \text{var}\left(\widehat{T}_0\right)\right\} - 2\ln\left[\widehat{\Delta RT}_{ARREST(mean)}\right]}$$

$$\text{var}(\widehat{T}_0) = \begin{cases} (12.778)^2 & \text{for } \widehat{T}_0 < -35.7\ °\text{C} \\ 99.905972 - 1.7748073\widehat{T}_0 & \text{for } -35.7\ °\text{C} \le \widehat{T}_0 \le 56\ °\text{C} \\ 0 & \text{for } \widehat{T}_0 > 56\ °\text{C} \end{cases}$$

Calculate the estimated arrest temperature[7] by Eq. (153) in Step 12 of Sect. 4.5

$$\widehat{RT}_{ARREST}(r,\ldots) = \widehat{RT}_{NDT_0} - \widehat{\Delta RT}_{epist-arrest} + \widehat{\Delta RT}_{ARREST} + \widehat{\Delta RT_{NDT}}(r,\ldots)$$

Calculate the normalized (relative to $\widehat{RT}_{ARREST}$) temperature of the vessel at the current location, *r*, in the RPV wall by Eq. (154) in Step 13 of Sect. 4.5

$$\widehat{\Delta T}_{RELATIVE}(r,\ldots) = T(r,t) - \widehat{RT}_{ARREST}(r,\ldots)$$

If this is the first pass through the submodel for this flaw, calculate (by Eqs. (155) and (156) in Steps 14 and 15 in Sect. 4.5) the fractile, $\Phi_{K_{I-initiation}}$, associated with this value of $K_{I\text{-}initiation}$ from the arrest model, given the current value of the applied $K_{I\text{-}initiation}$ from the infinite-length flaw in the *IGA* submodel

$$\Phi_{K_{I-initiation}} = \frac{1}{2}\left[\text{erf}\left(\frac{\ln(K_{I-initiation}) - \mu_{\ln(K_{Ia})}(\widehat{\Delta T}_{RELATIVE})}{\sigma_{\ln(K_{Ia})}\sqrt{2}}\right) + 1\right]$$

where

[7] The subregion value of $\widehat{RT_{NDTo}}$ is not re-sampled in this step.

$$\text{erf}(x) = \text{ error function} = \frac{2}{\sqrt{\pi}}\int_0^x \exp(-\xi^2)\,d\xi;\ \ \text{erf}(-x) = -\text{erf}(x)$$

if $K_{Ia}$_Model is equal to 1

$$K_{Ia(\text{mean})}(\widehat{\Delta T}_{RELATIVE}) = 27.302 + 69.962\exp\left[0.006057(\widehat{\Delta T}_{RELATIVE})\right] \ \ [\text{ksi}\sqrt{\text{in.}}]$$

$$\sigma_{\ln(K_{Ia})} = 0.18$$

else if $K_{Ia}$_Model is equal to 2

$$K_{Ia(\text{mean})}(\widehat{\Delta T}_{RELATIVE}) = 27.302 + 70.6998\exp\left[0.008991(\widehat{\Delta T}_{RELATIVE})\right] \ \ [\text{ksi}\sqrt{\text{in.}}]$$

$$\sigma_{\ln(K_{Ia})} = 0.34$$

$$\mu_{\ln(K_{Ia})}(\widehat{\Delta T}_{RELATIVE}) = \ln\left[K_{Ia(\text{mean})}(\widehat{\Delta T}_{RELATIVE})\right] - \frac{\sigma^2_{\ln(K_{Ia})}}{2}$$

In the above relation for $\Phi_{K_{I-initiation}}$, $\mu_{\ln(K_{Ia})}$ is calculated at the location of the initiation of the flaw. For this flaw, the value of $\Phi_{K_{I-initiation}}$ remains fixed in the *IGA Propagation* submodel until $P_f$ is resampled in Step G2 of the *IGA* submodel. Using the current value of $P_f$, scale by $\Phi_{K_{I-initiation}}$ (if this is the weld layer in which the crack initiation originally occurred) such that (from Eq. (157) in Step 15 of Sect. 4.5)

$$\Phi_{K_{Ia}} = (P_f)(\Phi_{K_{I-initiation}})$$

For subsequent weld layers do not perform the above scaling. When the flaw advances into a new weld layer, any linkage between the flaw's initiation and its continued propagation is assumed to be broken.

With this $\Phi_{K_{Ia}}$ fractile, draw a value of $K_{Ia}$ from its lognormal distribution as given by Eq. (158) of Step 15 in Sect. 4.5

$$K_{Ia}(\Phi_{K_{Ia}}, \widehat{\Delta T}_{RELATIVE}) = \exp\left[\sigma_{\ln(K_{Ia})} Z_{\Phi K_{Ia}} + \mu_{\ln(K_{Ia})}(\widehat{\Delta T}_{RELATIVE})\right]$$

$Z_{\Phi_{K_{Ia}}}$ = standard normal deviate corresponding to the $\Phi_{K_{Ia}}$ fractile

In the above relation for $K_{Ia}$, $\mu_{\ln(K_{Ia})}$ is calculated at the current location of the flaw. The scaling procedure in Step P6 ensures that the initial value of $K_{Ia}$, calculated immediately after initiation, does not exceed the initiating value of $K_{I\text{-}initiation}$, thus producing an initial extension. Once the value of $Z_{\Phi_{K_{Ia}}}$ has been determined for this *IGA* trial, the arrest toughness during flaw advancement through the wall changes due to changes in $\widehat{\Delta T}_{RELATIVE}$ only. These changes are caused by variations in $T(r,t)$ and $RT_{Arrest}$ (due to the resampling of the weld chemistry when passing into new weld layers).

For Ductile-Tearing Model No. 2, update the current value of the irradiated upper-shelf energy by

$$\widehat{USE}_{(i)} = A + 0.0570 \cdot \widehat{USE}_{(u)}^{1.456} - \left[ 17.5 \cdot f\left(\widehat{Cu}\right) \cdot \left(1 + 1.17 \widehat{Ni}^{0.8894}\right) + 305 \widehat{P} \right] \left( \frac{\widehat{\phi t}}{10^{19}} \right)^{0.2223} \quad \text{[ft-lbf]}$$

Go to Step P7.

Step P7. Check the current applied $K_I$ for the advancing flaw against the current value of the arrest fracture toughness $K_{Ia}$.

if $K_I < K_{Ia}$ then
the flaw has arrested
proceed to Step P8
else
the flaw has not arrested
proceed to Step P2

Step P8. Hold the flaw at this position, and advance the time to check for re-initiation or new ductile tearing.

$$NSTEP = NSTEP + 1$$

For this new time station, bring up the wall temperature, $T(r,\tau)$, at this position along with the current irradiated and attenuated value of $RT_{NDT}$ to calculate

$$\widehat{\Delta T}_{RELATIVE}(r,\ldots) = T(r,\tau) - \widehat{RT}_{RTNDT}(r,\ldots)$$

Now calculate the parameters of the $K_{Ic}$ model

$$a_{K_{Ic}}(\widehat{\Delta T}_{RELATIVE}) = 19.35 + 8.335 \exp\left[ 0.02254 (\widehat{\Delta T}_{RELATIVE}) \right] \text{ [ksi}\sqrt{\text{in.}}\text{]}$$
$$b_{K_{Ic}}(\widehat{\Delta T}_{RELATIVE}) = 15.61 + 50.132 \exp\left[ 0.008 (\widehat{\Delta T}_{RELATIVE}) \right] \text{ [ksi}\sqrt{\text{in.}}\text{]}$$
$$c_{K_{Ic}} = 4$$

with $K_{Ic}$ in ksi$\sqrt{\text{in}}$ and $\Delta T = (T\text{-}RT_{NDT})$ in °F.

The static initiation toughness, $K_{Ic}$, is calculated from its Weibull distribution by

$$K_{Ic}(\widehat{\Delta T}_{RELATIVE}) = \widehat{a_{K_{Ic}}}(\widehat{\Delta T}_{RELATIVE}) + \widehat{b_{K_{Ic}}}(\widehat{\Delta T}_{RELATIVE}) \left[ -\ln(1 - P_f) \right]^{1/c_{K_{Ic}}}$$

for $a_{K_{Ic}}(\widehat{\Delta T}_{RELATIVE}) \le K_{Ic} \le K_{Ic(\max)}$

Proceed to Step P9.

Step P9. If the warm prestressing (WPS) analysis option has been turned on by the user (see Sect. 3.3.4 for details on WPS effects as implemented in FAVOR$^{EP}$), check to see if the flaw is in a state of WPS. If the ductile-tearing option is turned on, then call the ductile-tearing model to determine if there is stable or unstable ductile tearing. If the WPS option is on and WPS = TRUE, go to Step P10. If the WPS option is off or WPS = FALSE, check the current applied $K_I$ for re-initiation by the test

if $K_I < K_{Ic}$ and $STABLE\_DT$ and $FAIL\_UDT$ are both FALSE then
No re-initiation.
Proceed to Step P10.
else if $WPS\_OPTION$ is on and $WPS$ is TRUE then
No re-initiation
Proceed to Step P10
else if $FAIL\_UDT$ is TRUE then
the vessel has failed by unstable ductile tearing
set vessel failure to TRUE
return to Step G5 of *IGA* model
else if $STABLE\_DT$ is TRUE and $K_{J_{Ic}}$ is less than $K_{Ic}$ then
the flaw has re-initiated by a ductile-tearing event
REINITIATED_BY_DUCTILE_TEARING = TRUE
the current level of tearing $\Delta a_0$ is set by the ductile-tearing model
Proceed to Step P3
else
The flaw has re-initiated by a cleavage event.
REINITIATED_BY_DUCTILE_TEARING = FALSE
Reset the current level of tearing $\Delta a_0 = 0$
Proceed to Step P2 and advance the flaw

Step P10. If there are time steps remaining in the transient, proceed to Step P8 and advance the time. If the transient is complete, set vessel failure = FALSE, and return to Step 5 of the *IGA* submodel.

Note that in the *IGA Propagation* submodel, the flaw is assumed to advance instantaneously; i.e., the time station remains fixed during flaw growth. Time will advance only if the flaw is in a state of arrest. If the flaw remains in arrest until the end of the transient, then the flaw is said to have experienced a *Stable Arrest*.

### 3.3.15 Ductile-Tearing Submodel

Figure 3.18c presents a flowchart of the *Ductile-Tearing Submodel*.

Step D1. The program enters the submodel with the current position and orientation of the crack tip and the time within the selected transient. The submodel first checks the current wall

temperature at the crack tip with the ductile-tearing transition temperature, $T_{DT}$. Based on a previous study, the value of $T_{DT}$ is set to 200 °F. If this is not the first entry into the model, a current value of $J_R^*$ will be known, where $J_R^*$ is a measure of the current deformation state due to tearing.

if $T_{wall} < T_{DT}$ then
  $FAIL\_UDT = \text{FALSE}$
  $STABLE\_DT = \text{FALSE}$
  Return to Step P3 or P9 of *IGA* Submodel
else
  Proceed to Step D2

Step D2. Given the location and orientation of the flaw tip, the submodel converts the known value of $K_{I\text{-}applied}$ to $J_{applied}$ using a plane-strain conversion. The submodel then proceeds to calculate/sample estimates for the $J_R$-curve parameters, $J_{Ic}$, $C$, and $m$.

$$J_{applied} = \frac{(1-\nu^2)}{E} K_{I-applied}^2 \ [\text{in-kips/in}^2]$$

get $\widehat{J_{Ic}}$ from either Ductile-Tearing Model No. 1 or 2
get $\widehat{C}$, and $\widehat{m}$ from either Ductile-Tearing Model No. 1 or 2
Proceed to Step D3

Step D3. The submodel then compares the $J_{applied}$ to the estimated value of $J_{Ic}$ obtained in Step D2 and the known value of $J_R^*$. If this is the first entry into the model or if a cleavage reinitiation has occurred since the last entry into the model, then $J_R^* = 0$. $J_R^*$ is the value of $J_{applied}$ corresponding to a previous time step at which a stable ductile tear ocurred. For a ductile tear to occur at the current time, it is necessary for $J_{applied}$ to be equal to or greater than the current value of $J_R^*$.

if $(J_{applied} < J_{Ic})$ or $(J_{applied} \le J_R^*)$ then
  $FAIL\_UDT = \text{FALSE}$
  $STABLE\_DT = \text{FALSE}$
  Return to Step P3 or P9 of *IGA* Submodel
else
  Proceed to Step D4

Step D4. The submodel then advances the position of the flaw, $a_0$, by the amount of ductile crack extension, $\Delta a$, produced by the known value of $J_{applied}$, and the new flaw depth is $a^* = a_0 + \Delta a$. The flaw then is advanced to a depth $a^{**}$, which is the first nodal position deeper than $a^*$. It is at this nodal position, $a^{**} = x_n$, that the local material tearing modulus, $T_R$, and applied tearing modulus, $T_{applied}$, are calculated. The local tearing modulus, $T_R$, characterizes the tearing resistance of the material.

$$J_R^* = J_{applied}$$

$$\Delta a = \exp\left[\frac{\ln(J_R^*) - \ln(C)}{m}\right], \text{ [in]}$$

$$a^* = a_0 + \Delta a$$

The *IGA Propagation* submodel mesh is searched to find the closest node point, node *n*, that is deeper into the wall than the current flaw position at $a^*$. The flaw is then repositioned to this node point such that $a^{**} = x_n$ (see Fig. 3.20). Based on the new position of the flaw, the local material tearing modulus is calculated at $a^{**}$ and the applied tearing modulus is estimated from a second-order finite-difference ratio.

$$\Delta a^{**} = a^{**} - a_0$$

$$T_R = \left(\frac{E}{\sigma_{flow}^2}\right)\left.\frac{dJ_R^*}{da}\right|_{\Delta a^{**}} = \left(\frac{E}{\sigma_{flow}^2}\right) \times m \times C \times \left(\Delta a^{**}\right)^{m-1}$$

and

$$\frac{dJ_{applied}}{da} \approx \frac{J_{n+1} + (\alpha - 1)J_n - \alpha^2 J_{n-1}}{\alpha(\alpha + 1)\Delta x} \quad , \quad \mathrm{O}\left(\Delta x^2\right)$$

where

$$\Delta x = x_n - x_{n-1}$$

$$\alpha = \frac{x_{n+1} - x_n}{x_n - x_{n-1}}$$

$$T_{applied} = \left(\frac{E}{\sigma_{flow}^2}\right)\left.\frac{dJ_{applied}}{da}\right|_{a=a^{**}}$$

Step D5. A check is now made for unstable ductile tearing. If the applied tearing modulus is greater than $T_R$, then a state of unstable ductile tearing is declared.

if $T_{applied} > T_R$ then

$FAIL\_UDT$ = TRUE

$STABLE\_DT$ = FALSE

Return to Step P3 or Step P9 in the *IGA Propagation* Submodel

else

$FAIL\_UDT$ = FALSE

$STABLE\_DT$ = TRUE

$\Delta a_0 = \Delta a$

$a_0 = a^*$

Return to Step P3 or Step P9 in the *IGA Propagation* Submodel

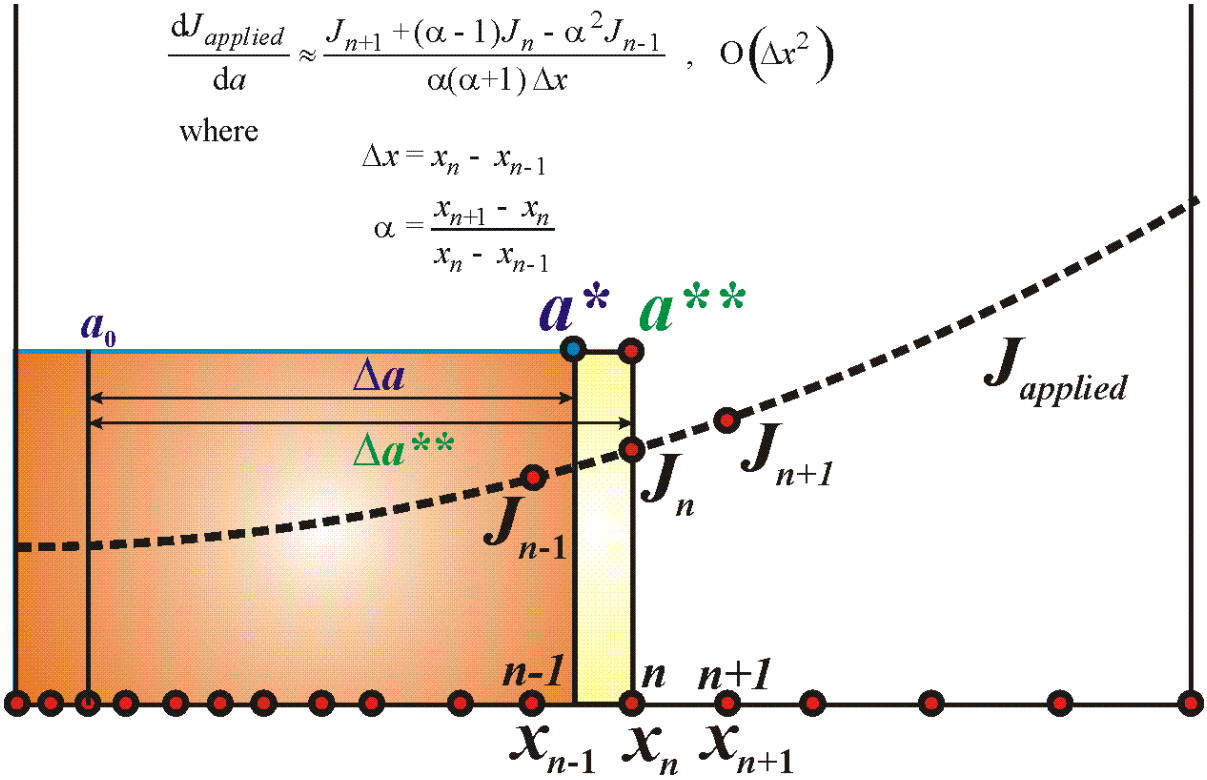


**Fig. 3.20. *IGA Propagation* submodel mesh used to estimate d$J_{applied}$ / d$a$ using a second-order central finite-difference ratio.**

### 3.3.16 Ductile Tearing as an Initiating Event

The ductile-tearing model, as implemented, should have no effect on the values of *CPI* produced by FAVOR$^{EP}$, and this was verified in a preliminary scoping study. However, a counter was implemented into FAVOR$^{EP}$ at the point where the conditional probability of initiation, *cpi*, by cleavage is calculated to determine if initiation of flaw growth by ductile tearing was a potential issue. In all of the studies carried out to date using the ductile-tearing models described in Sect. 3.3.13, no ductile-tearing initiating events were discovered.

## 3.4 FAVOR$^{EP}$ Post Module – FAVPost$^{EP}$

The distribution of the transient initiating frequencies obtained from PRA studies, the values of conditional probability of fracture (contained in the FAVPFM$^{EP}$-generated matrix *PFMI*), and the values of the conditional probability of vessel failure (contained in the FAVPFM$^{EP}$-generated matrix *PFMF*) are combined in the FAVPost$^{EP}$ module to generate discrete distributions of the frequency of vessel initiation, $\Phi(I)$, and frequency of vessel failure, $\Phi(F)$. This process is described by the following *pseudo code*:

For $j$ = 1, $N_{SIM}$ vessel simulations, increment by 1

For $i$ = 1, $N_{TRAN}$ transients, increment by 1

Sample the discrete cumulative distribution function of the transient-initiating frequency for this transient to generate a sample initiating frequency (in events per reactor year).

$\widehat{\phi(E)}_{(i)} \leftarrow CDF_{(i,j)}$ of transient-$i$ initiating frequency

End of Transient Loop

The above loop generates a vector of transient-initiating frequencies for this vessel simulation, $\left\{\widehat{\phi(E)}\right\}_{(1\times N_{TRAN})}$.

For the $j$th vessel, take the inner product of the transient initiating frequencies vector times the $j$th column-vectors in the *PFMI* and *PFMF* matrices.

$$\Phi(I)_{(j)} = \sum_{i=1}^{N_{TRAN}} \widehat{\phi(E)}_{(i)} PFMI(i,j)$$

$$\Phi(F)_{(j)} = \sum_{i=1}^{N_{TRAN}} \widehat{\phi(E)}_{(i)} PFMF(i,j)$$

End of Vessel Simulation Loop

The inner product of the row-vector of the sampled transient initiating frequencies and the $j$th column-vector of *PFMI* produces the frequency of crack initiation for the $j$th vessel simulation, $\Phi(I)_{(j)}$. Likewise, the inner product of the row-vector of sampled transient initiating frequencies and the $j$th column-vector of *PFMF* results in the frequency of vessel failure for the $j$th vessel simulation, $\Phi(F)_{(j)}$. The $(i,j)$ entry in matrix *PFMI* represents the conditional probability of crack initiation of

the *j*th vessel simulation subjected to the *i*th transient. The units are *crack initiations per event*. Therefore, the frequency of crack initiation, as determined from the inner product of the transient-initiating frequency and the conditional probability of crack initiation, is the number of *crack initiations per reactor year*. Likewise, the frequency of vessel failure, as determined from the inner product of the transient-initiating frequency and the conditional probability of vessel failure is the number of vessel *failures per reactor year*.

At the end of this process, there are discrete distributions of sample size $N_{SIM}$ for the frequency of crack initiation, $\{\Phi(I)\}_{N_{SIM}\times 1}$, and the frequency of vessel failure, $\{\Phi(F)\}_{N_{SIM}\times 1}$. The above process is described in Fig. 3.21.

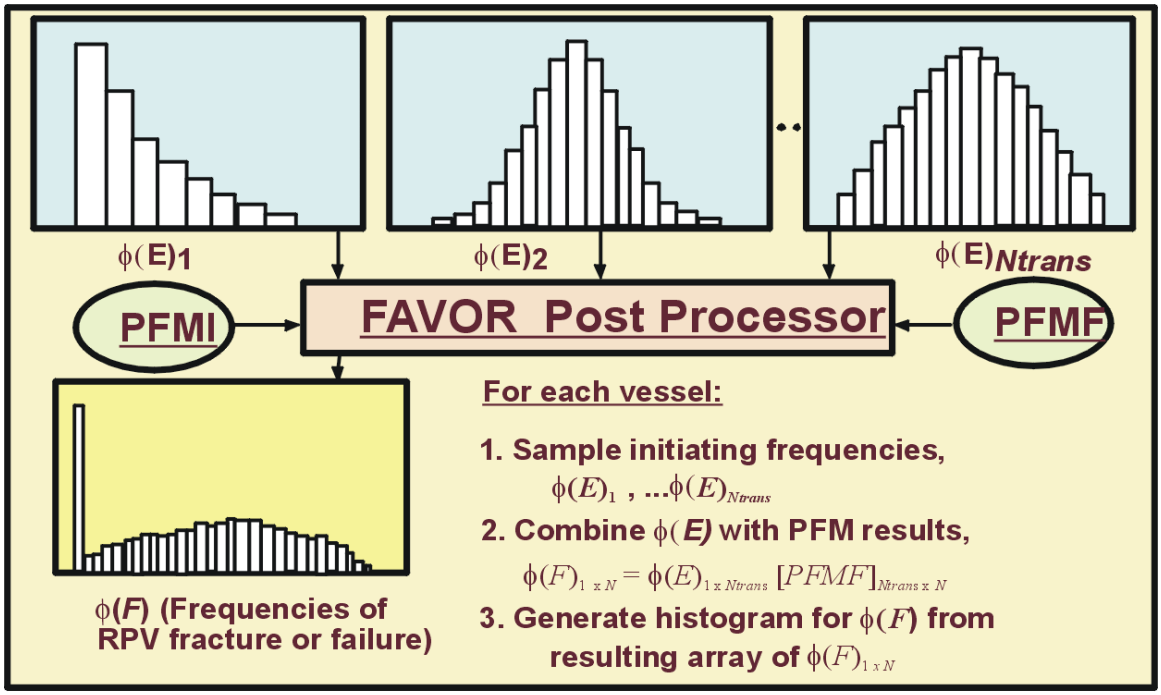


**Fig. 3.21. The FAVOR$^{EP}$ post-processor FAVPost$^{EP}$ combines the distributions of conditional probabilities of initiation and failure calculated by FAVPFM$^{EP}$ with initiating frequency distributions for all of the transients under study to create distributions of frequencies of RPV fracture and failure.**

# 4. Probabilistic Fracture Mechanics

A central feature of modern PRA/PFM analyses is an explicit treatment of model uncertainties with two types being distinguished, *aleatory* and *epistemic* [99]. *Aleatory uncertainties* arise due to the randomness inherent in any physical or human process, whereas *epistemic uncertainties* are caused by a limitation in the current state of knowledge (or understanding) of that process. Epistemic uncertainties can therefore, in principle, be reduced by an increased state of knowledge, whereas aleatory uncertainties are fundamentally irreducible. Playing a central role in the PTS Re-evaluation Project, the identification and classification of epistemic and aleatory uncertainties is a crucial aspect of PRA/PFM analyses, because the mathematical procedures used to account for them are different. A major effort in the development of improved fracture mechanics models for FAVOR$^{EP}$ has been the attempt to identify and classify the uncertainties in these models. Sections 4.2 through 4.5 will present the results of this effort. The deterministic analyses carried out to create a *loading definition* for each PTS transient are first discussed in Section 4.1.

It should be noted that during the investigation of new models for the FAVOR$^{EP}$ code, the basic requirements of the PTS Re-evaluation Project played a key role in the development process. To enable all commercial operators of pressurized water reactors to assess the state of their RPV relative to the new PTS screening criteria without the need to make new material property measurements, the initiation fracture toughness of the RPV needs to be estimated using only currently available $RT_{NDT}$ values. Moreover, to be consistent with the LEFM principals on which the FAVOR$^{EP}$ code is based, this $RT_{NDT}$ -based model needs to estimate $K_{Ic}$ values. These restrictions suggested that only very limited information, specifically a value of $RT_{NDT}$, would be available to define the initiation fracture-toughness model appropriate to a given steel in a plant-specific RPV.

## 4.1 Deterministic Analyses

The FAVLoad$^{EP}$ module carries out both thermal and stress analyses of a one-dimensional axisymmetric model of the RPV wall. The time-dependent temperature and stress distributions through the wall constitute the thermal and mechanical loading that will be applied to postulated flaws. In addition, Mode I stress-intensity factors are generated for a range of axially and circumferentially oriented infinite-length and finite-length (semi-elliptic) flaw geometries (flaw depths and lengths). The following subsections describe how these deterministic calculations are carried out in the FAVLoad$^{EP}$ module. The embedded-flaw model to be discussed has been implemented in the FAVPFM$^{EP}$ module.

### 4.1.1 Thermal Analysis

The temperature time-history, $T(r,\tau)$, for the vessel is determined by modeling the RPV wall as an axisymmetric one-dimensional structure with the temperature profile being dependent on the radial position, $r$, and elapsed time, $\tau$, in the transient. In the absence of internal heat generation, the transient heat conduction equation is a second-order parabolic partial differential equation:

$$\rho\, c_p(T)\, \frac{\partial T}{\partial \tau} = \frac{1}{r}\frac{\partial}{\partial r}\left[ k(T)\, r \frac{\partial T}{\partial r} \right] \tag{57}$$

where $\rho$ is the mass density, $c_p(T)$ is the temperature-dependent mass-specific heat capacity, and $k(T)$ is the temperature-dependent thermal conductivity. Note that any temperature dependencies in the mass density should be included in the characterization of the mass-specific heat capacity, leaving the mass density as a constant in the problem formulation. Equation (57) can be expressed in the following canonical form

$$\frac{\partial T}{\partial \tau} - \frac{1}{r}\frac{\partial}{\partial r}\left[ \lambda(T)\, r \frac{\partial T}{\partial r} \right] = 0 \text{ for } r \in \mathbb{R}^1; \tau \in (0,\infty) \tag{58}$$

where the property grouping $\lambda(T) = k(T) \big/ \rho\, c_p(T)$ is the temperature-dependent thermal diffusivity of the material. For Eq. (58) to be well posed, initial and boundary conditions must be applied.

$$\begin{aligned} &\underline{\text{Initial Condition}} \\ &T(r,0) = T_{initial} \text{ for } R_i \le r \le R_o \end{aligned} \tag{59}$$

$$\begin{aligned} &\underline{\text{Boundary Conditions}} \\ &q(R_i,t) = h(t)\left(T_\infty(t) - T(R_i,t)\right) \text{ at } r = R_i \\ &q(R_o,t) = 0 \text{ at } r = R_o \end{aligned} \tag{60}$$

where in Eqs. (59)-(60), $q$ is a prescribed boundary heat flux, $h(\tau)$ is the time-dependent convective film coefficient, $T_\infty(\tau)$ is the time-dependent bulk coolant temperature, and $R_i$ and $R_o$ are the inner and outer radii of the vessel wall, respectively. Input data to the thermal model include the mesh definition, property data, and prescribed time-histories for $h(\tau)$ and $T_\infty(\tau)$.

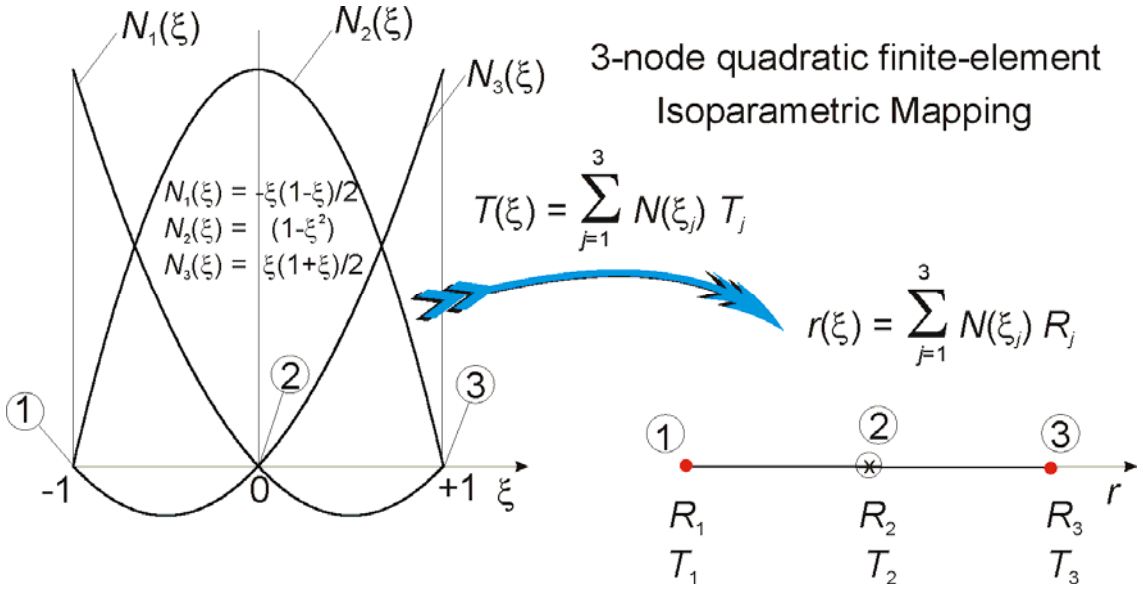


**Fig. 4.1. Isoparametric mapping from parameter space to axisymmetric $\mathbb{R}^1$ Euclidean space using three-node quadratic basis functions.**

Eqs. (58)-(60) can be solved using the finite-element method, where the variational formulation for the transient heat conduction equation is given in ref. [100]. The fundamental decisions required to implement the finite-element method are (1) choice of basis functions, (2) choice of mapping, and (3) choice of method for element integration. As shown in Fig. 4.1, FAVOR$^{EP}$ uses an isoparametric mapping with 3-node quadratic cardinal basis functions, specifically

$$\{N(\xi)\} = \begin{Bmatrix} N_1(\xi) \\ N_2(\xi) \\ N_3(\xi) \end{Bmatrix} = \frac{1}{2}\begin{Bmatrix} -\xi(1-\xi) \\ 2(1-\xi^2) \\ \xi(1+\xi) \end{Bmatrix}; \quad \left\{\frac{dN}{d\xi}\right\} = \begin{Bmatrix} \frac{dN_1}{d\xi} \\ \frac{dN_2}{d\xi} \\ \frac{dN_3}{d\xi} \end{Bmatrix} = \frac{1}{2}\begin{Bmatrix} (-1+2\xi) \\ -4\xi \\ (1+2\xi) \end{Bmatrix} \tag{61}$$

The elements of the thermal stiffness matrix [100] are calculated using a full-integration fourth-order Gauss-Legendre quadrature rule with the following weights, $\omega_i$, and Gauss sampling points, $\xi_i$,

$$\int_{-1}^{+1} g(\xi)d\xi \approx \sum_{i=1}^{4} \omega_i g(\xi_i) \quad \text{where} \quad \{\xi_i\} = \begin{Bmatrix} -\sqrt{\frac{3+2\sqrt{6/5}}{7}} \\ -\sqrt{\frac{3-2\sqrt{6/5}}{7}} \\ \sqrt{\frac{3-2\sqrt{6/5}}{7}} \\ \sqrt{\frac{3+2\sqrt{6/5}}{7}} \end{Bmatrix}; \{\omega_i\} = \begin{Bmatrix} \frac{1}{2} - \frac{1}{6\sqrt{6/5}} \\ \frac{1}{2} + \frac{1}{6\sqrt{6/5}} \\ \frac{1}{2} + \frac{1}{6\sqrt{6/5}} \\ \frac{1}{2} - \frac{1}{6\sqrt{6/5}} \end{Bmatrix} \tag{62}$$

In FAVOR$^{EP}$, a graded mesh (see Fig. 4.2) is generated through the wall thickness using ten three-noded quadratic isoparametric axisymmetric elements (21 nodes). Note that the FEM model does not use the same discretization applied in the *IGA* submodel. The first two elements represent the cladding, and the remaining eight elements model the base material. Explicit forward time integration is employed with a fixed time step of 1.0 second. Temperature and hoop-stress profiles are plotted in Fig. 4.2 for a fixed time in an example transient.

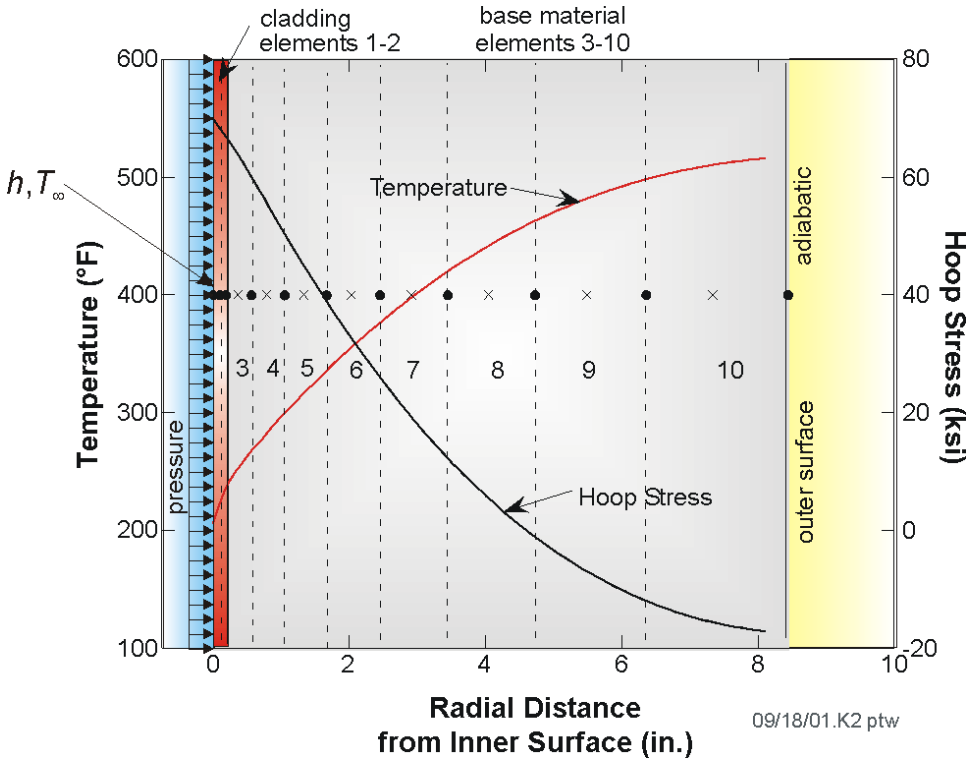


**Fig. 4.2. One-dimensional axisymmetric finite-element model used in FAVOR$^{EP}$ to calculate both temperature and stress histories through the wall of an RPV.**

### 4.1.2 Stress Analysis

FAVLoad$^{EP}$ carries out a displacement-based finite-element analysis of the vessel using a one-dimensional axisymmetric model of the vessel wall. The calculated displacements are converted into strains using strain-displacement relationships, and the associated stresses are then calculated using linear-elastic stress-strain relationships. At each time station during the transient, the structure is in a state of static equilibrium; thus the load history is considered *quasi-static.*

Let $(u,v,w)$ be the radial, circumferential, and axial displacements, respectively, of a material point in a cylindrical $(r,\theta,z)$ coordinate system. The general two-dimensional axisymmetric case requires that

$$v=0;\tau_{r\theta}=\tau_{\theta z}=0;\gamma_{r\theta}=\gamma_{\theta z}=0 \tag{63}$$

where $\tau_{r\theta},\tau_{\theta z}$ are shear stresses and $\gamma_{r\theta},\gamma_{\theta z}$ are engineering shear strains. The strain-displacement relationships for the two-dimensional case are

$$\begin{Bmatrix}\varepsilon_{rr}\\ \varepsilon_{\theta\theta}\\ \varepsilon_{zz}\\ \gamma_{zr}\end{Bmatrix}=\begin{bmatrix}\frac{\partial}{\partial r} & 0\\ \frac{1}{r} & 0\\ 0 & \frac{\partial}{\partial z}\\ \frac{\partial}{\partial z} & \frac{\partial}{\partial r}\end{bmatrix}\begin{Bmatrix}u\\ w\end{Bmatrix} \tag{64}$$

For the one-dimensional axisymmetric case, $(r,\theta,z)$ are principal directions, and $w=0;\partial/\partial z=0;$ such that

$$\varepsilon_{rr}=\frac{\partial u}{\partial r};\ \ \varepsilon_{\theta\theta}=\frac{u}{r};\ \ \varepsilon_{zz}=\frac{\partial w}{\partial z}=0;\ \ \gamma_{zr}=\frac{\partial u}{\partial z}+\frac{\partial w}{\partial r}=0 \tag{65}$$

For the case of a long cylinder with free ends and no axial or circumferential variations in temperature or material properties and with no radial variation in material properties, the radial and circumferential stresses for the one-dimensional axisymmetric case are calculated from the strains by

$$\sigma_{rr}=\frac{E}{(1+\nu)(1-2\nu)}\left[(1-\nu)\varepsilon_{rr}+\nu\varepsilon_{\theta\theta}\right]-\frac{\alpha E}{1-2\nu}(T-T_{s-free}) \tag{66}$$

$$\sigma_{\theta\theta}=\frac{E}{(1+\nu)(1-2\nu)}\left[(1-\nu)\varepsilon_{\theta\theta}+\nu\varepsilon_{rr}\right]-\frac{\alpha E}{1-2\nu}(T-T_{s-free}) \tag{67}$$

where

$\sigma_{rr}$ = radial normal stress
$\sigma_{\theta\theta}$ = circumferential (hoop) normal stress
$\varepsilon_{rr}$ = radial normal strain
$\varepsilon_{\theta\theta}$ = circumferential (hoop) normal strain
$T$ = wall temperature as a function of $r$
$T_{s-free}$ = thermal stress-free temperature for the RPV
$r$ = radial position in wall
$E$ = Young's modulus of elasticity
$\nu$ = Poisson's ratio
$\alpha$ = total coefficient of thermal expansion (scaled to $T_{s-free}$)

For generalized plane-strain conditions, the stress in the axial direction, $\sigma_{zz}^{PS}$, is given by

$$\sigma_{zz}^{PS} = \nu(\sigma_{rr} + \sigma_{\theta\theta}) - \alpha E(T - T_{s-free}) \tag{68}$$

To obtain the axial stresses with the ends free (assuming no cap load), it is necessary to remove the net end force associated with the plane-strain condition. This net load is

$$f^{PS} = 2\pi \int_{R_i}^{R_o} \sigma_{zz}^{PS} r dr \tag{69}$$

where $R_i$ and $R_o$ are the inner and outer radii of the cylinder.

In FAVOR$^{EP}$, the radial and hoop stresses are calculated using the finite-element method in which Eqs. (66) and (67) apply to each finite element, and thus radial variations in the material properties $E$, $\alpha$, and $\nu$ can be included by letting the properties vary from one element material group to another. To account for radial variations in properties when calculating the axial stresses, Eq. (68) is applied to each element $j$ such that

$$\sigma_{zz-j}^{PS} = \nu_j(\sigma_{rr-j} + \sigma_{\theta\theta-j}) - \alpha_j E_j(T_j - T_{s-free}) \tag{70}$$

is the axial stress in each element under plane-strain conditions. To achieve a free-end condition, the force $f_j^{PS}$ [Eq. (69)] must be released in such a manner that the change in axial strain (displacement) is the same for each element, because it is assumed that initial planes remain in plane under load. If $\Delta f_j$ is the reduction in the plane-strain force, $f_j^{PS}$, on element $j$, then

$$\frac{\Delta f_1}{A_1 E_1} = \frac{\Delta f_2}{A_2 E_2} = \cdots \frac{\Delta f_{nele}}{A_{nele} E_{nele}} \tag{71}$$

and

$$\sum_{j=1}^{nele} (f_j^{PS} + \Delta f_j) = 0 \tag{72}$$

where

$$f_j^{PS} = A_j\left[\nu_j\left(\sigma_{rr-j} + \sigma_{\theta\theta-j}\right) - \alpha_j E_j (T_j - T_{s-free})\right]$$
$$A_j = \pi(r_{o-j}^2 - r_{i-j}^2) \tag{73}$$

where $r_o$ and $r_i$ are the outer and inner radii of element $j$, respectively. Let $f_{p-j}$ be the axial forces that are the result of adding internal pressure, $p$. Specifying that the axial displacements for each element be the same gives

$$\frac{f_{p-1}}{A_1 E_1} = \frac{f_{p-2}}{A_2 E_2} = \cdots \frac{f_{p-nele}}{A_{nele} E_{nele}} \tag{74}$$

and

$$\sum_{j=1}^{nele} f_{p-j} = \pi R_o^2 p \tag{75}$$

where

$$f_j = \Delta f_j + f_{p-j}$$

Recalling that the uniform change in axial strain has no effect on $\sigma_{rr}$ and $\sigma_{\theta\theta}$, Eqs. (73), (74), and (75) can be solved for $f_j$ after calculating values of $\sigma_{rr-j}$ and $\sigma_{\theta\theta-j}$; then the axial stress is calculated from

$$\sigma_{zz-j} = \frac{\left(f_j^{PS} + f_j\right)}{A_j} \tag{76}$$

FAVOR[EP] uses a reduced-integration two-point Gauss-Legendre quadrature rule for the calculation of $\sigma_{rr}$ and $\sigma_{\theta\theta}$ in each element. The Gauss sample points and weights for two-point quadrature are:

$$\int_{-1}^{+1} g(\xi)d\xi \approx \sum_{i=1}^{2} \omega_i g(\xi_i) \quad \text{where} \quad \{\xi_i\} = \begin{Bmatrix} -\sqrt{\frac{1}{3}} \\ +\sqrt{\frac{1}{3}} \end{Bmatrix}; \{\omega_i\} = \begin{Bmatrix} 1 \\ 1 \end{Bmatrix} \tag{77}$$

For the calculation of the axial stresses, each of the elements is divided into two sub-elements, each containing one of the two Gauss points, and the axial stresses are calculated at each of the Gauss points. Stresses at the nodes of the finite-element mesh are obtained by interpolation and extrapolation using a cubic spline fit of the stresses at the Gauss points. The stress analysis uses the same mesh and quadratic elements that are applied in the thermal analysis described in the previous section. Details regarding the formation and assembly of the stiffness matrix and load vector for a static stress analysis are given in any text on finite-element methods. See, for example, ref. [101].

When temperature-dependency is included in the thermal stress analysis, FAVOR$^{EP}$ requires expansion coefficient data to be input that define the total thermal expansion from a specified reference temperature, $T_{ref}$. With $\alpha_0(T)$ data from handbook sources, this reference temperature is typically at room temperature. The thermal strains are calculated by

$$\varepsilon^{th} = \alpha_0(T)\left(T - T_{ref}\right) - \alpha_0(T_{s-free})\left(T_{s-free} - T_{ref}\right) \tag{78}$$

where the second term in Eq. (78) represents the total thermal strain due to the difference between the reference temperature, $T_{ref}$, and RPV stress-free temperature, $T_{s\text{-}free}$. This term is necessary to enforce the assumption that there is no initial thermal strain at the RPV stress-free temperature. Internally, FAVOR$^{EP}$ scales the input thermal expansion coefficient data by the relation

$$\alpha(T) = \frac{\alpha_0(T)\left(T - T_{ref}\right) - \alpha_0(T_{s-free})\left(T_{s-free} - T_{ref}\right)}{(T - T_{s-free})} \tag{79}$$

to ensure that the correct total thermal strain is being calculated with respect to $T_{s\text{-}free}$ in Eqs. (66)-(73)

.

### 4.1.3 Linear-Elastic Fracture Mechanics (LEFM)

The FAVOR$^{EP}$ code's linear-elastic stress model treats axial flaws exposed to a one-dimensional axisymmetric stress field and circumferential flaws exposed to a generalized-plane-strain stress field. These flaws are, therefore, assumed to experience only a Mode I loading, where the principal load is applied normal to the crack plane, thus tending to open the crack. It is also assumed that the plastic zone around the crack tip is fully contained, and the overall deformation-load response of the structure is linear. For these high-constraint conditions, the principles of linear-elastic fracture mechanics (LEFM) apply when calculating driving forces for the crack.

#### 4.1.3.1 Mode I Stress-Intensity Factors

For the cracked structure under LEFM conditions, the singular stress field in the vicinity of the crack tip can be characterized by a single parameter. This one-parameter model has the form

$$\begin{aligned} \sigma_{\theta\theta} &= \frac{K_I}{\sqrt{2\pi r}} \quad \text{for axial flaws} \\ \sigma_{zz} &= \frac{K_I}{\sqrt{2\pi r}} \quad \text{for circumferential flaws} \end{aligned} \tag{80}$$

where $r$ is the radial distance from the crack tip, and the crack plane is assumed to be a principal plane. The critical fracture parameter in Eq. (80) is the Mode I stress-intensity factor, $K_I$. When the

conditions for LEFM are met, the problem of calculating the stress-intensity factor can be formulated solely in terms of the flaw geometry and the stress distribution of the uncracked structure.

FAVOR$^{EP}$, v05.1, has an extensive stress-intensity-factor-influence coefficient (SIFIC) database for finite- and infinite-length surface flaws that has been implemented in the FAVLoad$^{EP}$ module for $R_i/t = 10$ only. The HSST program at ORNL has also developed a similar database for $R_i/t = 20$, which was implemented in earlier versions of FAVOR$^{EP}$ and could be re-installed for future releases if the need arises.

#### 4.1.3.2 Inner Surface-Breaking Flaw Models –Semi-Elliptic and Infinite Length

For inner surface-breaking flaws, the stress-intensity-factor, $K_I$, is calculated in FAVOR$^{EP}$ using a weighting-function approach originally introduced by Bückner [102] and applied by other researchers [103-106], including the developers of OCA-I [107] and OCA-P [108]. The HSST Program at ORNL generated a database of SIFICs for axial infinite-length [109] and axial semi-elliptic [110] surface flaws along with circumferential 360-degree [109] and circumferential semi-elliptic [111] surface flaws. These databases have been implemented in the FAVLoad$^{EP}$ module.

**Semi-Elliptic Finite Surface Flaws**

As mentioned above, the stress-intensity factor, $K_I$, is calculated by a linear superposition technique proposed by Bückner [102], where, instead of analyzing the cracked structure using actual loads, the analysis is performed with a distributed pressure loading applied to the crack surfaces only. This pressure is opposite in sign, but equal in magnitude and distribution, to the stresses along the crack line that are calculated for the uncracked structure with the actual loads applied. For an arbitrary stress distribution and for the case of a three-dimensional semi-elliptic surface flaw, the truncated stress distribution can be approximated by a third-order polynomial of the form

$$\sigma(x) = C_0 + C_1(x/a) + C_2(x/a)^2 + C_3(x/a)^3 \tag{81}$$

where $\sigma(x)$ is the stress normal to the crack plane at radial position, $x$. The variables $x$ and $a$ are defined in Fig. 4.3, and the coefficients ($C_0, C_1, C_2, C_3$) are calculated by a generalized least squares regression analysis in the FAVLoad$^{EP}$ module for the stress distribution calculated for the uncracked structure across the crack depth. The $K_I$ values are determined for each of the individual terms (stress distributions) in Eq. (81) and then added to obtain the total $K_I$ value as follows:

$$K_I(a) = \sum_{j=0}^{3} K_{Ij}(a) = \sum_{j=0}^{3} C_j \sqrt{\pi a} K_j^*(a) \tag{82}$$

where

$$K_j^*(a) = \frac{K_{Ij}^{'}(a)}{C_j^{'}\sqrt{\pi a}} \tag{83}$$

Values of $K_{Ij}^{'}(a)/C_j^{'}\sqrt{\pi a}$ were calculated for each of the normalized stress distributions corresponding to each term in Eq. (81) (see Fig. 4.4), using three-dimensional finite-element analysis results and an arbitrary value of $C_j^{'}=1$. The dimensionless quantity $K_j^*(a)$ is referred to as the *influence coefficient*. For semi-elliptic flaws, $K_j^*(a)$ values can be calculated for several points along the crack front, in which case Eq. (82) becomes

$$K_I(\phi) = \sum_{j=0}^{3} C_j\sqrt{\pi a}K_j^*(\phi) \tag{84}$$

where $\phi$ is the elliptic angle denoting the point on the crack front, and the crack-depth notation ($a$) has been dropped. Although SIFICs are available in the database for a range of elliptic angles, this baseline release of FAVOR$^{EP}$ only calculates the value of $K_I$ at the deepest point along the flaw front (i.e., $\phi = 90°$).

The presence of a thin layer of stainless steel cladding on the inner surface of reactor pressure vessels has a significant effect on the $K_I$ values for inner-surface flaws because of very high thermal stresses generated in the cladding during a thermal transient. When using influence coefficients for three-dimensional flaws, it is necessary to represent the stress distribution in the uncracked cylinder with a third-order polynomial, and thus the discontinuity in the thermal stress at the clad-base material interface presents a problem. To accommodate the stress discontinuity associated with the cladding, influence coefficients were calculated for the cladding stresses alone; the corresponding $K_I$ value can then be superimposed on the $K_I$ value due to the stresses in the base material. This is accomplished by first calculating a $K_I$ value for a continuous-function stress distribution obtained by a linear extrapolation of the stress distribution in the base material to the clad-base interface. Then a $K_I$ value is calculated for the stress distribution in the cladding by subtracting the extrapolated distribution from the actual assumed-linear distribution in the cladding. The total $K_I$ value is simply the sum of the two. Because the stress distribution in the cladding is essentially linear, only a first-order polynomial is used for the cladding stress-intensity-factor-influence coefficients.

The influence coefficients implemented in FAVOR$^{EP}$ were calculated using the ABAQUS [112] finite-element code. Three-dimensional finite-element models were generated for a range of relative crack depths ($a$ / $t$) and aspect ratios ($L$ / $a$) (see Fig. 4.3). The analysis matrix included relative crack depths of $0.01 \le (a/t) \le 0.5$ and aspect ratios of $L/a = 2, 6, 10$. In the process of calculating the SIFICs, careful attention was paid to using adequately converged finite-element meshes and an appropriate cylinder length. The number of elements in the circumferential and axial directions and around the crack front was increased, one at a time, until the addition of one element changed the

value of $K_I$ by less than one percent. With regard to cylinder length, a minimum incremental length of the cylinder that could be added to the length of the flaw to negate end effects was estimated from Eq. (85) [113]

$$\ell = 2\pi\left[\frac{R_i^2 t^2}{3(1-\nu^2)}\right]^{1/4} \tag{85}$$

where $\nu$ is Poisson's ratio, $R_i$ is the inner radius of the vessel, and $t$ is the wall thickness.

The analysis results in ref. [111] demonstrated that there were essentially no differences in SIFICs between the axial and circumferential orientations for relative flaw depths of $0.01 \le a/t < 0.5$ and flaw aspect ratios of $L/a = 2$, 6, and 10. This important finding implies that SIFICs for axial flaws can be used for circumferential flaws up to a relative flaw depth of 0.5 with very little error. The greatest difference ( ~ 5% ) between the two orientations occurs for flaw geometries with an $a/t$ = 0.5 and $L/a$ = 10. In Appendix B, SIFICs for both axial and circumferential orientations for relative flaw depths of $a/t$ = 0.01, 0.0184, 0.05, 0.075, 0.1, 0.2, and 0.3 are presented in Tables B1-B7, respectively. Table B8 presents the SIFICs for an axial flaw with $a/t$ = 0.5, and Table B9 presents the SIFICs for a circumferential flaw with $a/t$ = 0.5.

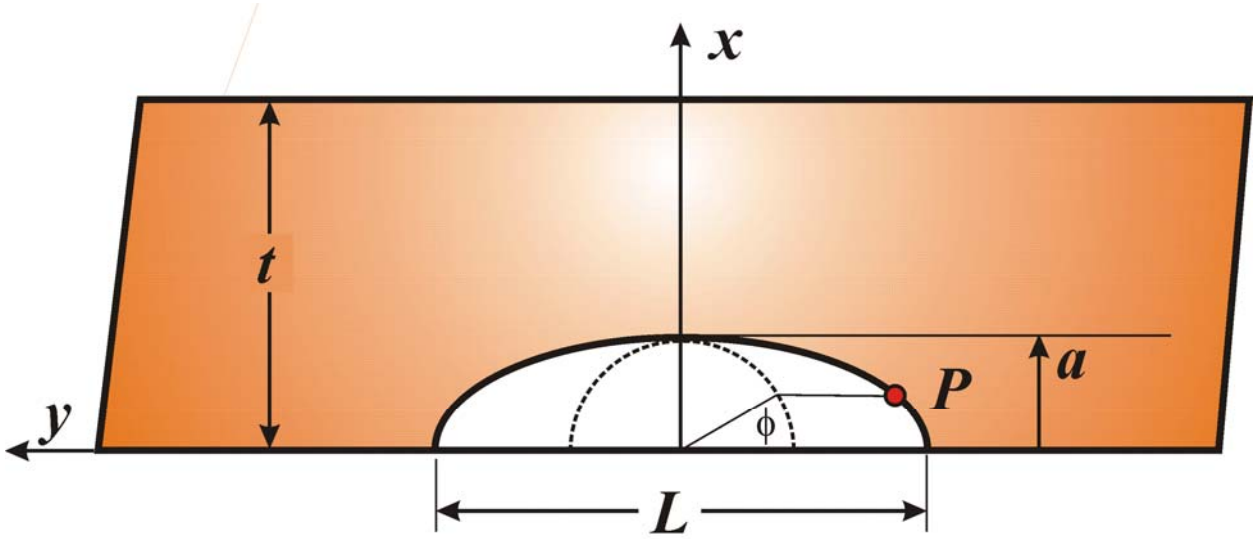


**Fig. 4.3. Influence coefficients, *K**, have been calculated for finite semi-elliptic flaws with aspect ratios *L* / *a* = 2, 6, and 10 for $R_i$ / *t* = 10.**

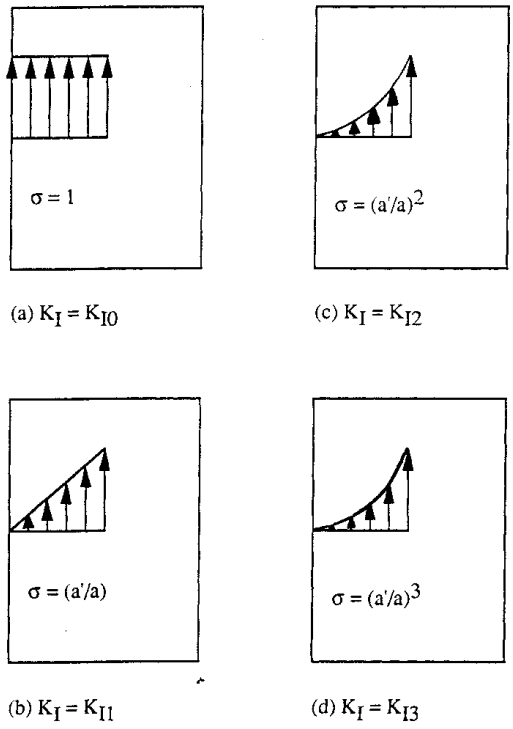


**Fig. 4.4. Crack-surface loading cases for determining finite 3D flaw influence coefficients: (a) uniform unit load, (b) linear load, (c) quadratic load, and (d) cubic load.**

**Infinite-Length Surface Flaws**

Figure 4.5 shows the geometries for the axial and circumferential infinite-length flaws. Figure 4.6 illustrates the decomposition of a cracked structure under actual loads into an equivalent problem with two components. One component is an uncracked structure under actual loads for which $K_I = 0$ , since there is no crack. The second component is a cracked structure having a crack face loading equal in magnitude and opposite in direction to the stress distribution in the uncracked structure at the location of the crack. Therefore, the problem of interest reduces to the calculation of the $K_I$ for the second component. This calculation can be accomplished by computing $K^*$ values for each of several unit loads applied at specified points along the crack face (see Fig. 4.7) and then weighting them by the truncated crack-free stress distribution associated with the equivalent problem [107]. The procedure can be summarized as follows:

axial flaws

$$K_I(a) = \sum_{i=1}^{n} \sigma_i \Delta a_i K_i^*(a_i', a) \tag{86}$$

circumferential flaws

$$K_I(a) = \sum_{i=1}^{n} 2\pi(R + a_i')\sigma_i \Delta a_i K_i^*(a_i', a) \tag{87}$$

where

$\Delta a_i =$ an increment of $a$ about $a_i'$ such that $\sum_{i=1}^{n} \Delta a_i = a$

$a_i' =$ radial distance from open end of crack to point of application of unit load,

$\sigma_i =$ average crack-free stress over $\Delta a_i$ for equivalent problem

$K_I =$ opening Mode I stress-intensity factor

$K_I^* =$ stress-intensity factor per unit load applied at $a_i'$, where load has dimensions of force/length for axial flaws and force for circumferential flaws

$n =$ number of points along length of crack for which $K_i^*$ are available,

$R =$ inside radius of vessel.

The ABAQUS (version 4.9.1) finite-element code was used to calculate the influence coefficients presented in Appendix B. The general procedure consisted of developing a finite-element model for each crack depth and then individually applying unit loads at corner nodes located along the crack face. The axial stress-intensity-factor influence coefficients given in Table B10 have been nondimensionalized by multiplying by the factor ($0.1\ t^{1/2}$), where $t$ is the wall thickness, and the circumferential stress-intensity-factor influence coefficients given in Table B11 have been nondimensionalized by multiplying by the factor ($10\ t^{3/2}$). These normalizing factors account for the fact that the applied load in the generalized plane-strain analyses for axial flaws is 1.0 kip/in. of model thickness, and the applied load in the axisymmetric analyses of the circumferential flaws is a 1.0 kip total "ring" load. For both orientations, the range of relative flaw depths are $a / t$ = {0.01, 0.02, 0.03, 0.05, 0.075, 0.1, 0.2, 0.3, 0.4, 0.5, 0.6, 0.7, 0.8, 0.9, and 0.95}. It should be noted that values in Tables B10 and B11 for $a'/a \geq 0.95$ represent "fitted" or extrapolated values rather than directly computed ones. ABAQUS version 4.9.1 did not correctly compute the *J*-integral for *J*-paths in which the load on the crack face was contained within the contour itself.

Finally, it should be pointed out that, as with the finite-surface flaws, great care was exercised in developing finite-element meshes that would produce converged solutions. Higher-order meshes were employed throughout the modeling. Starter finite-element meshes for each crack depth were examined for convergence by approximately doubling the mesh refinement, i.e., the number of nodes and elements, and performing a representative $K^*$ calculation with the more refined model. This procedure was repeated until the difference in $K^*$ values between successive models was less than one percent, at which time the more refined model was selected for the final computation.

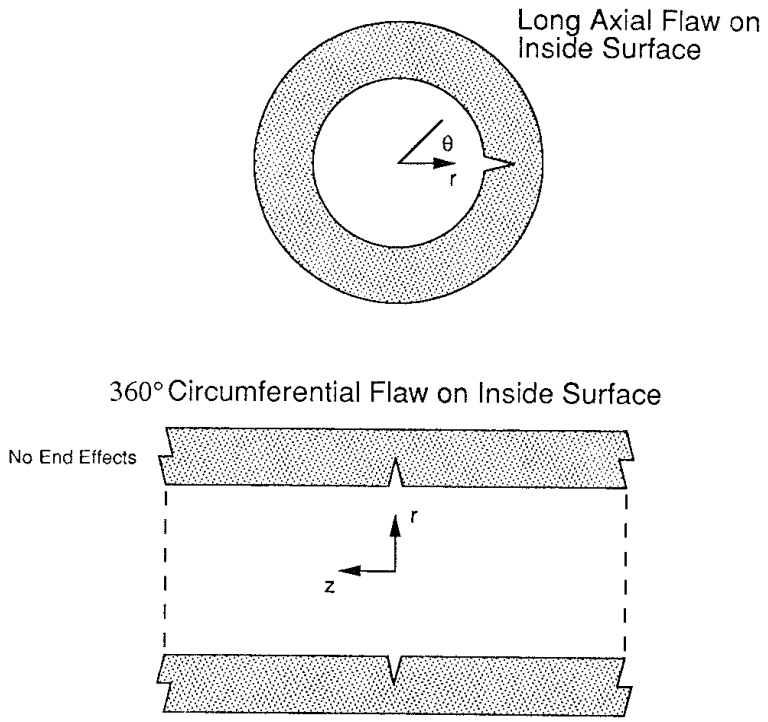


**Fig. 4.5. Influence coefficients have been computed for both infinite axial and 360-degree circumferential flaws.**

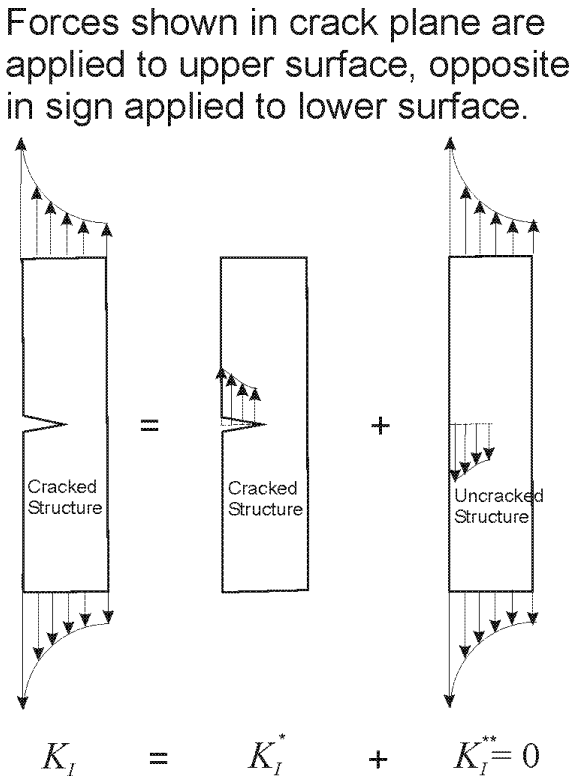


**Fig. 4.6. Superposition allows the use of an equivalent problem to compute the stress intensity factor.**

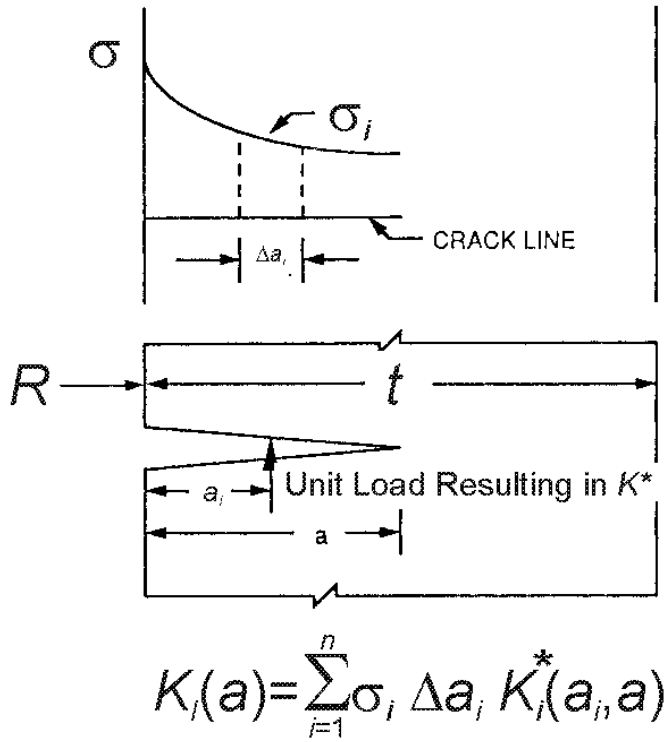


**Fig. 4.7. Influence coefficients, *K**, represent stress intensity factor per unit load applied to the crack face.**

#### 4.1.3.3 Embedded-Flaw Driving-Force Model for $K_I$

The computational methodology implemented in FAVOR$^{EP}$ for calculating Mode I stress-intensity factors, $K_I$ , for embedded flaws [114] is the EPRI NP-1181 analytical interpretation [115] of the ASME Section XI-Appendix A [116] model for embedded (or "subsurface" in the nomenclature of ref. [116]) flaws. Figure 4.8 is a schematic of the ASME embedded flaw model with the relevant descriptive variables.

The procedure for calculating Mode I stress-intensity factors, $K_I$ , is based on the resolution of nonlinear applied stresses through the RPV wall thickness into the linear superposition of approximate membrane and bending stress components. The $K_I$ factor is thus computed from the following relation:

$$K_I = (M_m \sigma_m + M_b \sigma_b)\sqrt{\pi a / Q} \tag{88}$$

where:

$2a$ = the minor axis of the elliptical subsurface flaw
$Q$ = flaw shape parameter
$M_m$ = free-surface correction factor for membrane stresses
$M_b$ = free-surface correction factor for bending stresses
$\sigma_m$ = membrane stress
$\sigma_b$ = bending stress

The stress-linearization procedure, depicted in Fig. 4.9 for a concave upward nonlinear stress profile, involves the interpolation of the applied stresses at two points on the flaw crack front – point 1 at a distance $x_1$ from the inner surface and point 2 at a distance $x_2$ from the inner surface. A straight line is fitted through these two points which represents a linear approximation, $\hat{\sigma}(x)$, of the original nonlinear stress profile, $\sigma(x)$, where $x$ is the distance from the inner surface. The effective membrane stress, $\sigma_m$ , is located at $x = t/2$ along this line, and the bending stress, $\sigma_b$, is the stress at the inner surface ($x = 0$) minus the membrane stress. The nonlinear stress profile, $\sigma(x)$, is resolved into the linear superposition of the membrane stress ($\sigma_m$) and bending stress ($\sigma_b$) (see Fig. 4.9) as follows:

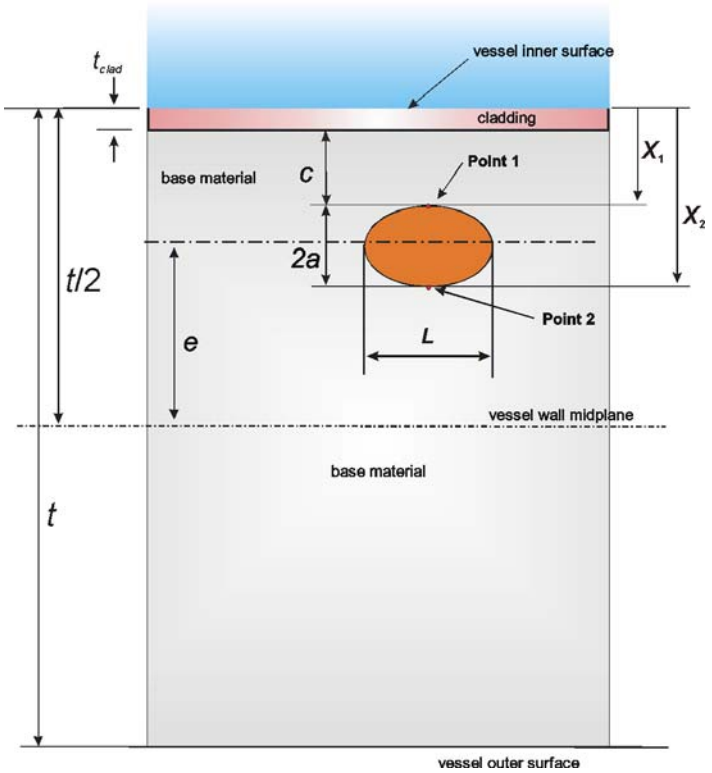


**Fig. 4.8. Geometry and nomenclature used in embedded-flaw model.**

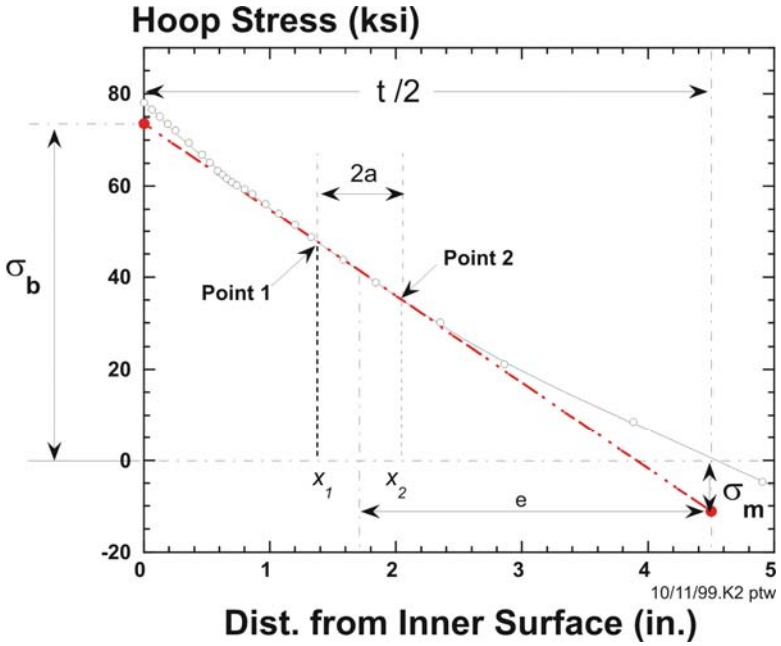


**Fig. 4.9. Resolution of computed nonlinear stress profile into the linear superposition of effective membrane and bending stresses.**

$$\sigma_m = \hat{\sigma}(t/2) = \frac{\left(\sigma(x_2) - \sigma(x_1)\right)}{2a} \times \left(t/2 - x_1\right) + \sigma(x_1) \tag{89}$$

$$\sigma_b = \hat{\sigma}(0) - \sigma_m = \frac{\left(\sigma(x_1) - \sigma(x_2)\right)}{2a} \times \left(t/2\right) \tag{90}$$

The formal definition of the flaw shape parameter $Q$ is based on the complete elliptic integral of the second kind, $E(x)$,

$$\begin{aligned} Q(x) &= E^2(x) \\ E(x) &= \int_0^{\pi/2} \sqrt{\left(1 - x\sin^2(\theta)\right)} d\theta \text{ for } 0 \le x \le 1 \\ x &= 1 - 4\left(\frac{a}{L}\right)^2 \end{aligned} \tag{91}$$

In ref. [115], the elliptic integral is replaced by an infinite-series approximation for $Q$ of the form

$$Q \approx \frac{\pi^2}{4(1+m)^2}\left[1 + \frac{m^2}{4} + \frac{m^4}{64} + \frac{m^6}{256} + \left(\frac{5}{128}\right)^2 m^8 + \left(\frac{7}{256}\right)^2 m^{10}\right]^2 \tag{92}$$

where

$$m = \frac{1 - 2(a/L)}{1 + 2(a/L)}$$

Equation (92) has been implemented in FAVOR$^{EP}$. The equation for the free-surface correction factor for the membrane stress ($M_m$ ) is as follows:

$$\begin{aligned} M_m = {} & D_1 + D_2(2a/t)^2 + D_3(2a/t)^4 + D_4(2a/t)^6 + D_5(2a/t)^8 + \\ & \frac{D_6(2a/t)^{20}}{\left[1 - \left(2e/t\right) - \left(2a/t\right)\right]^{1/2}} \end{aligned} \tag{93}$$

where:

$$D_1 = 1$$

$$D_2 = 0.5948$$

$$D_3 = 1.9502\left(e/a\right)^2 + 0.7816\left(e/a\right) + 0.4812$$

$$\begin{aligned} D_4 = {} & 3.1913\left(e/a\right)^4 + 1.6206\left(e/a\right)^3 + 1.8806\left(e/a\right)^2 + \\ & 0.4207\left(e/a\right) + 0.3963 \end{aligned}$$

$$D_5 = 6.8410(e/a)^6 + 3.6902(e/a)^5 + 2.7301(e/a)^4 + 1.4472(e/a)^3 + 1.8104(e/a)^2 + 0.3199(e/a) + 0.3354$$

$$D_6 = 0.303$$

The equation for the free-surface correction factor for bending stresses ($M_b$ ) is:

$$M_b = E_1 + \frac{\left[\begin{array}{l} E_2(2e/t) + E_3(2e/t)^2 + E_4(2e/t)(2a/t) + \\ E_5(2a/t)(2e/t)^2 + E_6(2a/t) + \\ E_7(2a/t)^2 + E_8(2e/t)(2a/t)^2 + E_9 \end{array}\right]}{\left[1-(2e/t)-(2a/t)\right]^{1/2}} \quad (94)$$

where:

$$E_1 = 0.8408685,\ E_2 = 1.509002,\ E_3 = -0.603778,$$
$$E_4 = -0.7731469,\ E_5 = 0.1294097,\ E_6 = 0.8841685,$$
$$E_7 = -0.07410377,\ E_8 = 0.04428577\ E_9 = -0.8338377$$

#### 4.1.3.4 Elastic $T_{stress}$ Models

The constraint-loss effects scaling model discussed in Sect. 3.3.4 requires, in addition to the driving force, $K_I$, the calculation of the $T_{stress}$ as a function of time for all of the flaw types simulated in FAVOR$^{EP}$.

The second term in Williams [117] series expansion for linear-elastic crack tip fields is referred to as the elastic T-stress, $T_{stress}$, and represents the stress acting parallel to the crack plane. It has been demonstrated [118, 119] that the sign and magnitude of the $T_{stress}$ substantially change the size and shape of the plane strain crack-tip plastic zone at finite load levels. Bilby et al. [120] also showed that the $T_{stress}$ can strongly affect the magnitude of hydrostatic triaxiality (and thus the state of crack-tip constraint) in the near-crack-tip elastic-plastic stress fields. Positive $T_{stress}$ strengthens the level of crack tip stress triaxiality and leads to high crack-tip constraint; while negative $T_{stress}$ reduces the level of crack-tip stress triaxiality and leads to the loss of crack-tip constraint [121].

As discussed in Sect. 4.1.3.2, the *Weight-Function Method* is the approach currently applied in FAVOR$^{EP}$ for calculating Stress Intensity Factors (SIFs) for surface-breaking flaws exposed to general non-uniform stress distributions. In refs. [122-125], the weight-function method has been extended to the calculation of *T*-stresses under non-uniform loading for 2D infinite-length surface

flaws. Wang and Bell [121] have extended the method further to finite 3D semi-elliptic surface flaws in plates under non-uniform loading.

**Semi-Elliptic Finite Surface Flaws**

Given a Mode I far-field loading on the semi-elliptic surface flaw shown in Fig. 4.3, the *T-stress* at a position *P* on the crack tip can be expressed as [121]:

$$T_{stress}(P) = \left[ \left( \sigma_{rr} - \sigma_{zz} \right)\Big|_{(\text{at } P)} \right] + \left[ \sum_{i=0}^{3} A_i V_i \left( a/t, \phi \,|\, L/a \right) \right] + \left[ \left( \frac{E\alpha}{(1-\nu)} \right) \left( T - T_{ref} \right)\Big|_{(\text{at } P)} \right] \tag{95}$$

where $\sigma_{xx}$ is the radial stress at the crack-tip position for the uncracked body, and $\sigma_{zz}$ is the open-mode stress (again for the uncracked body), with its radial through-wall profile being expressed in terms of a cubic polynomial curve fit of the form

$$\sigma_{zz}(x) = \sum_{i=0}^{3} A_i \left( 1 - \frac{x}{a} \right)^i = \begin{cases} \text{axial stress for circumferential flaw orientation} \\ \text{hoop stress for axial flaw orientation} \end{cases} ; \begin{array}{l} \text{uncracked body;} \\ \text{crack tip at } x = a \end{array} \tag{96}$$

The parameters $V_i$ are the *T-stress influence coefficients* for semi-elliptic surface flaws. These influence coefficients are a function of flaw geometry only and can be calculated from crack-face pressure loadings (see Eqs. (103) and (104) ) The final term in Eq. (95) arises from the thermal strain at position *P* and is independent of flaw orientation.

The curve-fit coefficients, $A_i$, in Eq. (96), use a different local coordinate system than the coefficients, $C_i$, in Eq. (84), but they can be can be calculated by the following linear mapping:

$$\begin{Bmatrix} A_0 \\ A_1 \\ A_2 \\ A_3 \end{Bmatrix} = \begin{bmatrix} 1 & 1 & 1 & 1 \\ 0 & -1 & -2 & -3 \\ 0 & 0 & 1 & 3 \\ 0 & 0 & 0 & -1 \end{bmatrix} \begin{Bmatrix} C_0 \\ C_1 \\ C_2 \\ C_3 \end{Bmatrix}$$

or (97)

$$\begin{aligned} A_0 &= C_0 + C_1 + C_2 + C_3 \\ A_1 &= -\left( C_1 + 2C_2 + 3C_3 \right) \\ A_2 &= C_2 + 3C_3 \\ A_3 &= -C_3 \end{aligned}$$

Wang and Bell [121] report $V_i$ values for semi-elliptic surface flaws in plates with aspect ratios of $L/a$ = 2, $3\frac{1}{3}$, 5, and 10 and relative flaw depths of $a/t$ = 0.2, 0.4, 0.6, and 0.8. For each of the four aspect

ratios, *L/a*, given by Wang and Bell [121], the HSST Program has fitted the coefficients, $V_i(a/t,\phi)$, ($i$ = 0,1,2,3) using a 10th order bivariate Chebyshev series polynomial:

$$
\begin{aligned}
&V_i\left(a/t,\phi\middle|L/a\right) = \\
&z_i(x,y) = c_{1(i)} + c_{2(i)}T_2(x) + c_{3(i)}T_1(y) + c_{4(i)}T_2(x) + c_{5(i)}T_1(x)T_1(y) + \\
&c_{6(i)}T_2(y) + c_{7(i)}T_3(x) + c_{8(i)}T_2(x)T_1(y) + c_{9(i)}T_1(x)T_2(y) + c_{10(i)}T_3(y) + \\
&c_{11(i)}T_4(x) + c_{12(i)}T_3(x)T_1(y) + c_{13(i)}T_2(x)T_2(y) + c_{14(i)}T_1(x)T_3(y) + c_{15(i)}T_4(y) + \\
&c_{16(i)}T_5(x) + c_{17(i)}T_4(x)T_1(y) + c_{18(i)}T_3(x)T_2(y) + c_{19(i)}T_2(x)T_3(y) + c_{20(i)}T_1(x)T_4(y) + \\
&c_{21(i)}T_5(y) + c_{22(i)}T_6(x) + c_{23(i)}T_5(x)T_1(y) + c_{24(i)}T_4(x)T_2(y) + c_{25(i)}T_3(x)T_3(y) + \\
&c_{26(i)}T_2(x)T_4(y) + c_{27(i)}T_1(x)T_5(y) + c_{28(i)}T_6(y) + c_{29(i)}T_7(x) + c_{30(i)}T_6(x)T_1(y) + \\
&c_{31(i)}T_5(x)T_2(y) + c_{32(i)}T_4(x)T_3(y) + c_{33(i)}T_3(x)T_4(y) + c_{34(i)}T_2(x)T_5(y) + c_{35(i)}T_1(x)T_6(y) + \\
&c_{36(i)}T_7(y) + c_{37(i)}T_8(x) + c_{38(i)}T_7(x)T_1(y) + c_{39(i)}T_6(x)T_2(y) + c_{40(i)}T_5(x)T_3(y) + \\
&c_{41(i)}T_4(x)T_{4(i)}(y) + c_{42(i)}T_3(x)T_5(y) + c_{43(i)}T_2(x)T_6(y) + c_{44(i)}T_1(x)T_7(y) + c_{45(i)}T_8(y) + \\
&c_{46(i)}T_9(x) + c_{47(i)}T_8(x)T_1(y) + c_{48(i)}T_7(x)T_2(y) + c_{49(i)}T_6(x)T_3(y) + c_{50(i)}T_5(x)T_4(y) + \\
&c_{51(i)}T_4(x)T_5(y) + c_{52(i)}T_3(x)T_6(y) + c_{53(i)}T_2(x)T_7(y) + c_{54(i)}T_1(x)T_8(y) + c_{55(i)}T_9(y) + \\
&c_{56(i)}T_{10}(x) + c_{57(i)}T_9(x)T_1(y) + c_{58(i)}T_8(x)T_2(y) + c_{59(i)}T_7(x)T_3(y) + c_{60(i)}T_6(x)T_4(y) + \\
&c_{61(i)}T_5(x)T_5(y) + c_{62(i)}T_4(x)T_6(y) + c_{63(i)}T_3(x)T_7(y) + c_{64(i)}T_2(x)T_8(y) + c_{65(i)}T_1(x)T_9(y) + c_{66(i)}T_{10}(y) \\
&\text{for } i = 0,1,2,3;\ 0.2 \le a/t \le 0.8;\ 0° \le \phi \le 90°
\end{aligned}
\tag{98}
$$

where the 264 parameters, $c_{j(i)}$, ($j$ = 1 to 66; $i$ = 0 to 3) required to complete the four surface fits for each aspect ratio were calculated using TableCurve 3D. Monotone piecewise cubic-Hermite interpolants [126,127] are constructed in FAVOR$^{EP}$ to estimate the coefficients for arbitrary aspect ratios bounded by $2 \le L/a \le 10$.

The independent $X = a/t$ and $Y = \phi$ geometric variables must first be scaled such that the $X$ and $Y$ values are mapped to the required $-1 < (X,Y) < +1$ range. In addition, the specific bivariate Chebyshev series polynomial selected for surface fitting performs a log transformation of either the $X$ or $Y$ values to improve the fidelity of the fitting. For example, at $L/a$ = 2 the scaling of the surface function $V_0\left(a/t,\phi\,|\,L/a=2\right)$ is:

$$
\begin{aligned}
x &= \min\left\{\max\left[\left(\frac{a/t-0.5}{0.3}\right),-1\right],+1\right\}\ ;\ 0.2 \le a/t \le 0.8 \\
y &= \min\left\{\max\left[\left(\frac{\ln(\phi)-3.054623791382183}{1.445185878948082}\right),-1\right],+1\right\}\ ;\ 0° < \phi \le 90°
\end{aligned}
\tag{99}
$$

In Eq. (98), an order $n$ Chebyshev polynomial *of the first kind* can be defined using Rodrigues' formula

$$T_n(x) = \frac{\sqrt{1-x^2}}{(-1)^n(2n-1)(2n-3)\ldots 1}\ \frac{d^n}{dx^n}\left(1-x^2\right)^{n-\frac{1}{2}}$$

or (100)

$$T_n(x) = \cos\left(n\cos^{-1}(x)\right)$$

Figure 4.10 shows the results of a benchmarking validation study in which ABAQUS finite-element $K_I$ and $T$-stress solutions are compared to FAVOR$^{EP}$ for a circumferentially-oriented semi-elliptic flaw with flaw depth, $a$, of 0.75 in. ($a/t$ = 0.0833) and $L/a$ = 6. Good agreement can be observed for both parameters.

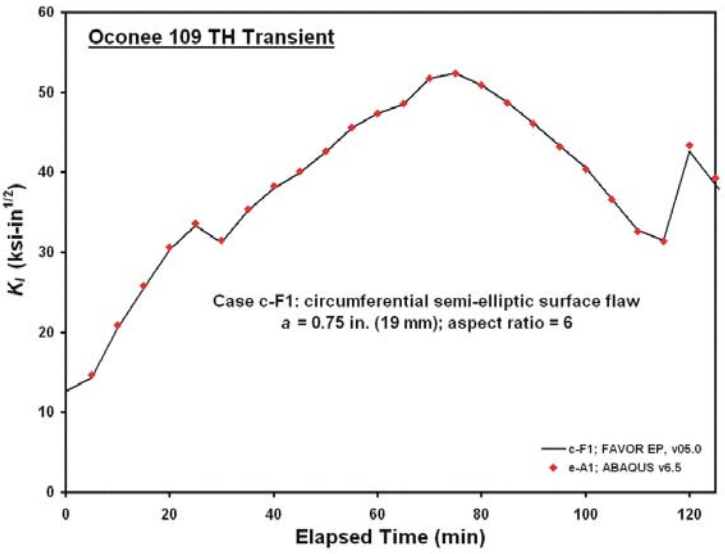


(a)

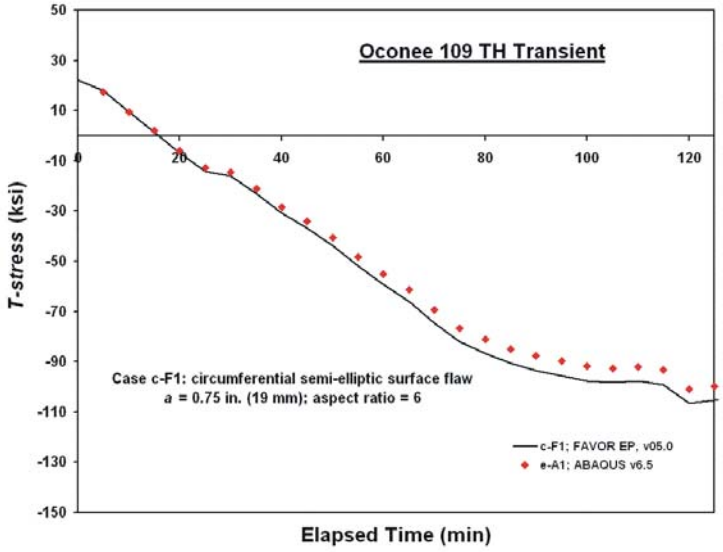


(b)

**Fig. 4.10 Comparison of benchmark ABAQUS solutions against FAVOR$^{EP}$ for a PTS transient: (a) $K_I$ driving force and (b) $T$-stress.**

**Infinite-Length Surface Flaws**

The *Weight-Function Method* applied in calculating stress-intensity factors and *T*-stresses for semi-elliptic surface flaws subjected to arbitrary stress distributions (as discussed in Sect. 4.1.3.2) has also been extended to *T*-stresses for infinite-length surface flaws. Sham [122] provided methods for the determination of weight functions for *T*-stress numerically, and Fett [123] and Hooton et al. [124] demonstrated procedures for the derivation of weight functions from reference *T*-stress solutions. The procedure (with an extension by HSST to estimate the *T*-stress due to thermal strain in an RPV cylindrical wall) described by Wang [125] for the determination of *T*-stress weight functions from reference solutions has been followed in FAVOR$^{EP}$.

The *T*-stress for an infinite-length axial or a 360-degree surface flaw can be approximated by the following model form:

$$T_{stress} = \sigma_{rr}(a) - \sigma_{zz}(a) + \frac{E\alpha}{(1-\nu)}\left(T(a) - T_{ref}\right) + \int_0^a \sigma_{zz}(x)\, t_n(x,a)\, dx \qquad (101)$$

where

$a =$ flaw depth

$\frac{E\alpha}{(1-\nu)}\left(T(a) - T_{ref}\right) = T$-stress due to thermal strain at $x = a$

$\sigma_{rr} =$ radial stress

$\sigma_{zz} =$ opening mode stress $= \begin{cases} \text{hoop stress for axial flaw orientation} \\ \text{axial stress for circumferential orientation} \end{cases}$

$T =$ wall temperature at time $\tau$ and radial wall position $x = a$

$T_{ref} =$ stress-free temperature

$E =$ elastic modulus

$\nu =$ Poisson's ratio

$\alpha =$ thermal expansion coefficient

The weight function, $t_n(x,a)$, is an $n^{th}$ order Green's function [128] for the *T*-stress:

$$t_n(x,a) = \frac{2}{\pi a}\left[ D_1\left(1-\frac{x}{a}\right)^{\frac{1}{2}} + D_2\left(1-\frac{x}{a}\right)^{\frac{3}{2}} + D_3\left(1-\frac{x}{a}\right)^{\frac{5}{2}} + D_4\left(1-\frac{x}{a}\right)^{\frac{7}{2}} + \ldots + D_n\left(1-\frac{x}{a}\right)^{\frac{2n-1}{2}} \right] \qquad (102)$$

The *T*-stress influence coefficients, $D_n$, are a function of geometry only and can be calculated from detailed finite-element models with applied reference crack-face pressure loadings. For example, an $n^{th}$ order crack-face pressure expressed by

$$\sigma_{crack-face(n)} = \sigma_0 \left(1 - \frac{x}{a}\right)^n \tag{103}$$

for a given geometry ( $a/t$ and $R_{inner}/t$ ) and orientation produces a normalized reference $T$-stress solution:

$$V_n = \frac{T_{stress(n)}}{\sigma_0} \text{ for a given } a/t \tag{104}$$

In Eqs. (101)-(103), $x$ is the radial distance from the inner surface into the cylindrical wall of the RPV. The integral in Eq. (101) is evaluated numerically in FAVOR$^{EP}$ by a first-order forward-Euler quadrature rule.

The HSST program calculated reference $T$-stress solutions $(V_0, V_1, V_2, V_3)$ with finite-element models of axial infinite-length flaws at $a/t$ = 0.2, 0.222, 0.3, 0.333, 0.4, 0.5, 0.6, 0.7, 0.8, 0.85, 0.9, 0.925, and 0.95 and 360-degree circumferential flaws at $a/t$ = 0.2, 0.3, 0.4, 0.5, 0.6, 0.6667, 0.7, 0.75, 0.8, 0.8333, 0.8611, 0.9, and 0.95. All of the above cases were for $R_{inner}/t$ = 10. At each value of $a/t$, the $T$-stress influence coefficients, $D_1$, $D_2$, $D_3$, $D_4$, were then calculated from the following linear mapping of the reference $T$-stress solutions, $V_0$, $V_1$, $V_2$, $V_3$:

$$\begin{Bmatrix} D_1 \\ D_2 \\ D_3 \\ D_4 \end{Bmatrix} = \frac{\pi}{4}[\Phi] \begin{Bmatrix} V_0 \\ V_1 \\ V_2 \\ V_3 \end{Bmatrix} \text{ at a given } a/t$$

where

$$[\Phi] = \begin{bmatrix} \frac{1}{3} & \frac{1}{5} & \frac{1}{7} & \frac{1}{9} \\ \frac{1}{5} & \frac{1}{7} & \frac{1}{9} & \frac{1}{11} \\ \frac{1}{7} & \frac{1}{9} & \frac{1}{11} & \frac{1}{13} \\ \frac{1}{9} & \frac{1}{11} & \frac{1}{13} & \frac{1}{15} \end{bmatrix}^{-1} \tag{105}$$

and then fitted to 10/10 order rational polynomials using the 38-digit high-precision math engine available in TableCurve 2D, version 5.01 [129]. These rational functions are expressed as

$$D_n(a/t) = g_n(x) =$$

$$\frac{g_{0(n)} + g_{2(n)}x + g_{4(n)}x^2 + g_{6(n)}x^3 + g_{8(n)}x^4 + g_{10(n)}x^5 + g_{12(n)}x^6 + g_{14(n)}x^7 + g_{16(n)}x^8 + g_{18(n)}x^9 + g_{20(n)}x^{10}}{1 + g_{1(n)}x + g_{3(n)}x^2 + g_{5(n)}x^3 + g_{7(n)}x^4 + g_{9(n)}x^5 + g_{11(n)}x^6 + g_{13(n)}x^7 + g_{15(n)}x^8 + g_{17(n)}x^9 + g_{19(n)}x^{10}} \quad (106)$$

$$\text{for } 0.2 \le (x = a/t) \le 0.95;\ n = 1,2,3,4$$

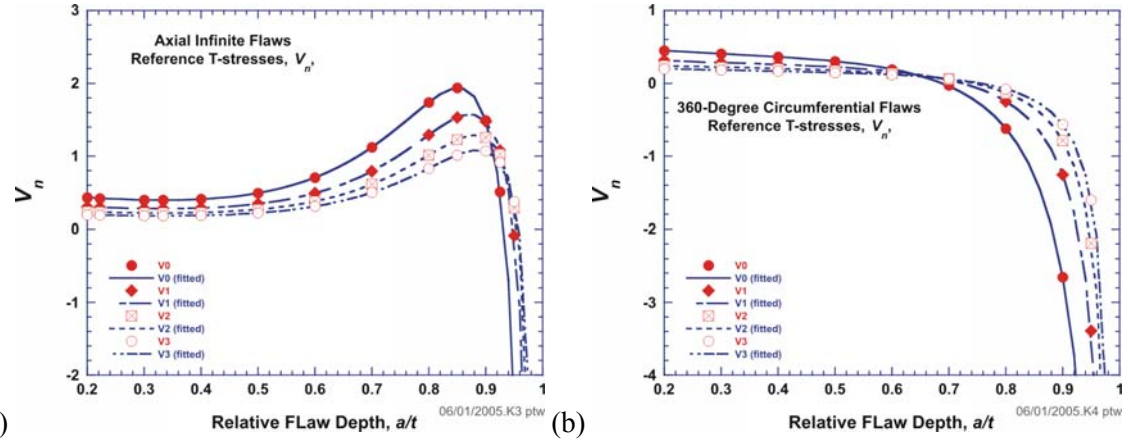


**Fig. 4.11 Normalized reference *T*-stresses, $V_n$, for (a) axial infinite and (b) 360-degree circumferential inner surface-breaking flaws as a function of relative flaw depth, *a/t*. $R_{inner}$ / *t* = 10 for a cylindrical RPV.**

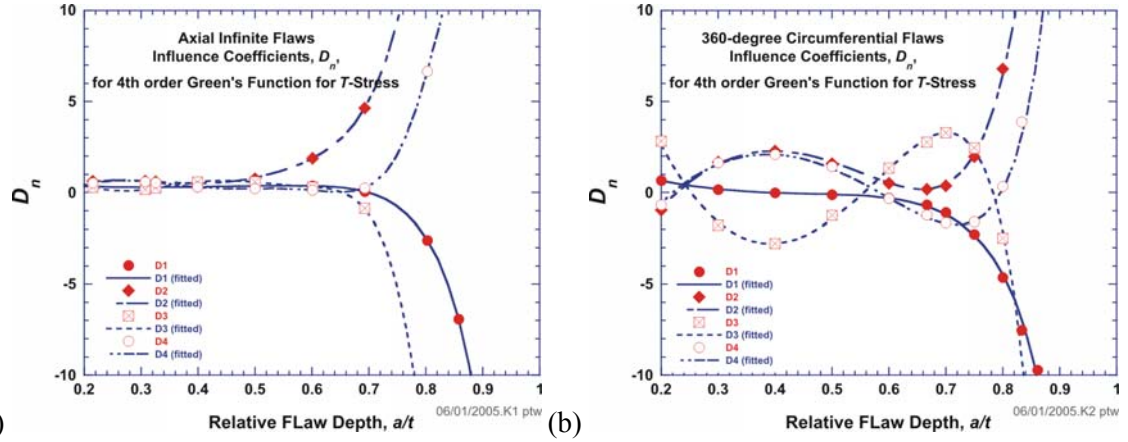


**Fig.4.12 *T*-stress influence coefficients, $D_n$, for (a) axial infinite and (b) 360-degree circumferential inner surface-breaking flaws as a function of relative flaw depth, *a/t*. $R_{inner}$ / *t* = 10 for a cylindrical RPV.**

See Figs. 4.11-4.12 for plots (as a function of relative flaw depth, *a*/*t*) of the calculated normalized reference *T*-stress solutions, $V_n$, and the resulting *T*-stress influence coefficients, $D_n$, (after performing the linear mapping of Eq. (105)) for axial-infinite and 360-degree surface breaking flaws.

Figures 4.13(a) and 4.13(b) present comparisons of benchmark ABAQUS ($K_I$,$T$-stress) solutions with FAVOR$^{EP}$ ($K_I$,$T$-stress) solutions for a given PTS transient over a range of relative flaw depths for axial infinite flaws.

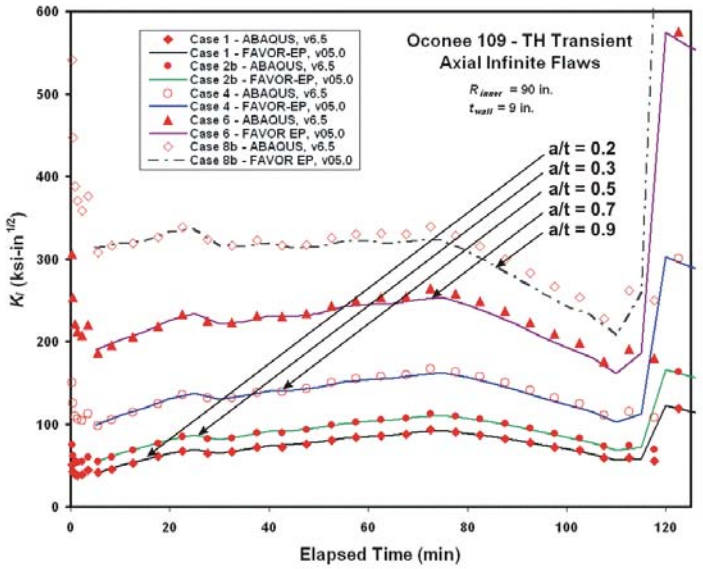


(a)

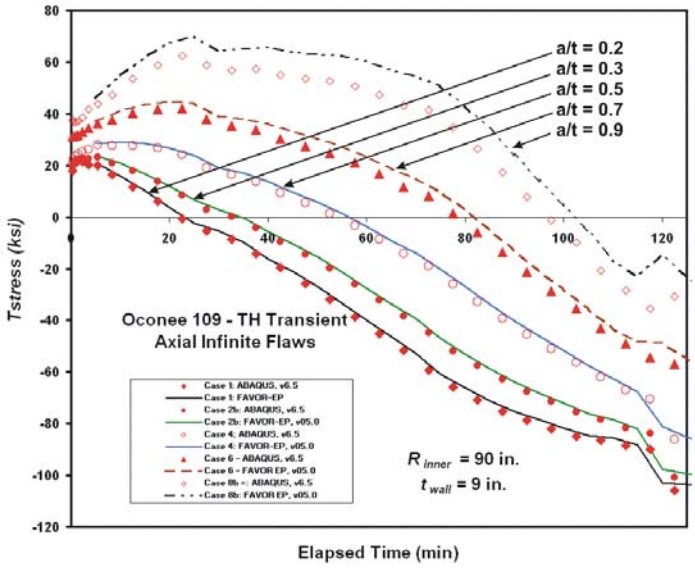


(b)

**Fig. 4.13 Comparison of benchmark ABAQUS solutions against FAVOR$^{EP}$ for a PTS transient: (a) $K_I$ driving force and (b) $T$-stress.**

**Embedded-Flaw $T_{stress}$ Model**

A simplified $T_{stress}$ procedure for embedded flaws, based on the embedded-flaw driving-force $K_I$ model, was developed by HSST for FAVOR$^{EP}$. The procedure for calculating Mode I stress-intensity factors, $K_I$ , requires the resolution of the nonlinear stresses through the RPV wall thickness into the linear superposition of approximate membrane and bending stress components. For Point 1 on the embedded flaw, the $K_I$ stress intensity factor is computed from the following model described in Sect. 4.1.3.3 by Eq. (88):

$$K_I = (M_m \sigma_m + M_b \sigma_b)\sqrt{\pi a / Q} \tag{88}$$

where:

$2a =$ the minor axis of the elliptical embedded (or subsurface) flaw
$Q =$ flaw shape parameter
$M_m =$ free-surface correction factor for membrane stresses
$M_b =$ free-surface correction factor for bending stresses
$\sigma_m =$ linearized membrane stress
$\sigma_b =$ linearized bending stress

See Fig. 4.8 for a description of the geometry and nomenclature used in both $K_I$ and $T_{stress}$ models.

The new $T_{stress}$ procedure (also for Point 1 on the embedded flaw) adopts a similar model form:

$$T_{stress} = \left(M_m T_{str-m} + M_b T_{str-b}\right)\sqrt{\pi^2/(5Q)} + T_{str-thermal} \tag{107}$$

where the $T_{stress}$ linearization is based on the solution for a penny-shaped flaw in an infinite medium developed by Wang (130):

$2a =$ the minor axis of the elliptical embedded (or subsurface) flaw
$Q =$ flaw shape parameter (from the $K_I$ model)
$M_m =$ free-surface correction factor for membrane stresses (from the $K_I$ model)
$M_b =$ free-surface correction factor for bending stresses (from the $K_I$ model)
$T_{str-m} =$ membrane T-stress (penny-shaped flaw model) $= -\left(\dfrac{1+2\nu}{2}\right)\sigma_{zz(\text{at } x=(X_1+X_2)/2)}$
$T_{str-b} =$ bending T-stress (penny-shaped flaw model) $= -\left(\dfrac{3}{4}+\dfrac{\nu}{2}\right)\left(\sigma_{zz(\text{at } x=X_1)} - \sigma_{zz(\text{at } x=(X_1+X_2)/2)}\right)$

$$T_{str-thermal} = \text{T-stress due to thermal strain} = \frac{E\alpha}{(1-\nu)}\left(T(X_1) - T_{ref}\right)$$

$$\sigma_{zz} = \text{opening mode stress} = \begin{cases} \text{hoop stress for axial flaw orientation} \\ \text{axial stress for circumferential orientation} \end{cases}$$

$T$ = wall temperature at time $\tau$ and wall position $X_1$

$T_{ref}$ = stress-free temperature

$E$ = elastic modulus

$\nu$ = Poisson's ratio

$\alpha$ = thermal expansion coefficient

Figures 4.14 show the results of a benchmarking study comparing ABAQUS, v6.5, finite-element embedded-flaw ($K_I$,$T_{stress}$) solutions (at Point 1 ($x = X_1$)) with those of the embedded-flaw ($K_I$,$T_{stress}$) models incorporated into FAVOR$^{EP}$. The embedded-flaw geometries used in this analysis were developed for the FAVOR, V&V, deterministic study and are described in detail in ref. (131). In Figs. 4.14(a) and 4.14(b), a purely mechanical (increasing internal pressure) loading is applied to the vessel with embedded flaw model e-A3. Figures 4.14(c) – 4.14 (f) compare the ABAQUS, v6.5, and FAVOR$^{EP}$ embedded-flaw ($K_I$,$T_{stress}$) solutions at Point 1 ($x = X_1$) for seven embedded-flaw geometries/positions using a thermal-hydraulic PTS transient that combines thermal and mechanical loading (Oconee TH 109). In Figs. 4.14(g) and 4.14(h), four embedded flaws are exposed to a PTS transient (Beaver Valley 007) which is predominantly thermal in character.

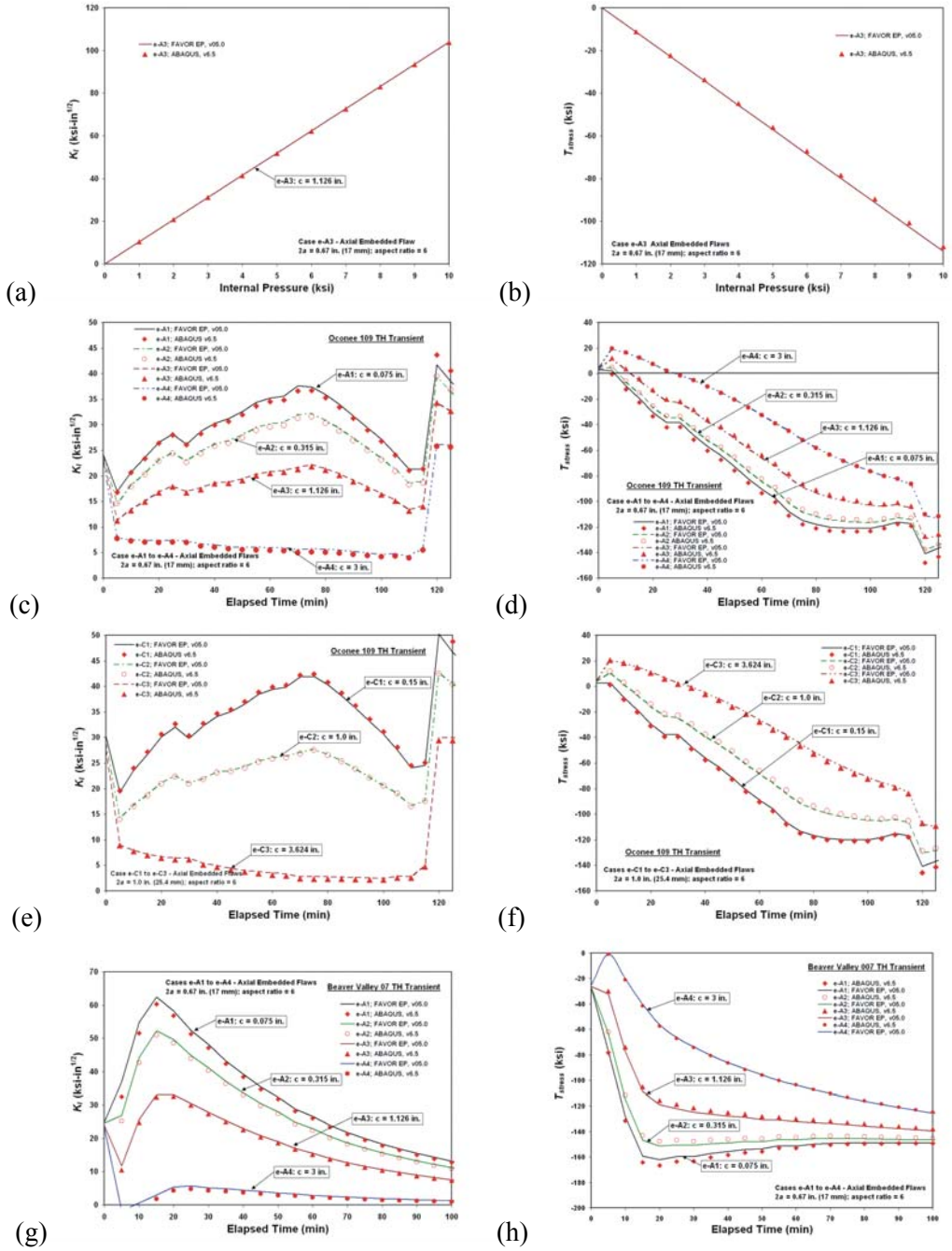


**Fig. 4.14 Comparison between ABAQUS, v6.5, (symbols) and FAVOR$^{EP}$, v05.1, (curves) ($K_I$,$T_{stress}$) embedded flaw solutions: (a) and (b) pure mechanical (increasing internal pressure) loading on flaw model e-A3, (c) and (d) combined mechanical and thermal loading on flaw models e-A1 to e-A4 (Oconee thermal hydraulic transient 109), (e) and (f) combined mechanical and thermal loading on flaw models e-C1 to e-C3 (Oconee thermal hydraulic transient 109), (g) and (h) predominantly thermal loading on flaw models e-A1 to e-A4 (Beaver Valley thermal hydraulic transient 007) – RPV inner radius = 90 in., $t_{wall}$ = 9 in., and $t_{clad}$ = 0.25 in., aspect ratio = $L/2a$.**

#### 4.1.3.5 Inclusion of Residual Stresses in Welds

The through-wall weld residual stress distribution was derived in the HSST program from a combination of experimental measurements taken from an RPV shell segment made available from a cancelled pressurized-water reactor plant and finite-element thermal and stress analyses [132,133].

The residual stresses in an RPV structural weld stem from (a) the clad-shell differential thermal expansion (DTE) and (b) the residual stresses, generated by the structural welding process, that are not completely relaxed by the post-weld heat-treatment [134]. Data required for calculation of these residual stresses were obtained by cutting a radial slot in the longitudinal weld in a shell segment from an RPV and then measuring the deformation of the slot width after cutting. The measured slot openings were assumed to be the sums of the openings due to the clad-base material differential thermal expansion (DTE) and the weld residual stresses. To evaluate the residual stresses in an RPV structural weld, a combined experimental and analytical process was used. Slot opening measurements were made during the machining of full-thickness clad beam specimens with two-dimensional flaws. The blanks measured 54-inches long (circumferential direction), 9-inches wide (longitudinal direction), and 9-inches thick (radial direction). The blanks were cut so as to have a segment of a longitudinal seam weld from the original RPV at the mid-length of the blank. Using the wire-EDM process, a slot was cut along the weld centerline in a radial direction from the inside (clad) surface of the blank. Measurements were made on three specimens having final slot depths of 0.045 inches, 0.90 inches, or 4.50 inches, respectively. After machining, the widths of the slots were measured along each radial face of the blanks. Finite-element analyses were used to develop a through-thickness stress distribution that gave a deformation profile matching the measured values. This distribution is shown in Fig. 4.15, where the contributions from clad and base DTE have been removed. The residual stress profile is modified to apply to an analysis of a vessel that has a wall thickness other than the one from which the stress distribution is derived. The through-wall weld residual stress distribution retains the shape and magnitude as derived from experiment/analysis; however, it is compressed or expanded to fit the current wall thickness by modifying the residual profile data by the ratio of the current RPV wall thickness to 8.936, i.e., the wall thickness from which the stress distribution was derived. The user has the option in the input deck for FAVLoad$^{EP}$ [45] to specify whether or not the weld residual stress profile will be superimposed on either the axial or circumferential through-wall stress distributions, or both.

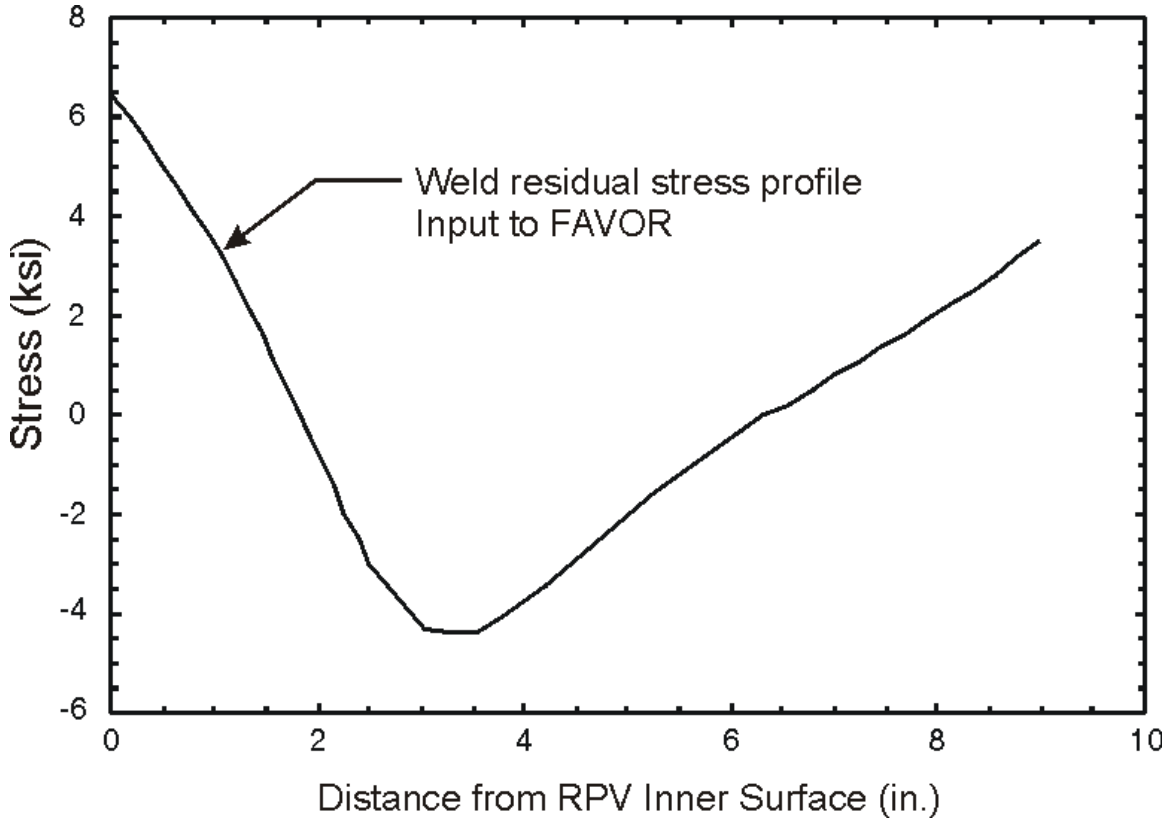


**Fig. 4.15. Weld residual stress through-thickness distribution developed for use in RPV integrity analyses.**

#### 4.1.3.6 Inclusion of Crack-Face Pressure Loading for Surface-Breaking Flaws

Crack-face pressure loading on the exposed faces of internal surface-breaking flaws is included as an option in the mechanical loading of the family of surface-breaking flaws in a FAVLoad$^{EP}$ deterministic analysis. The Mode I Stress Intensity Factor database provides a simple but accurate mechanism for including the effects of crack-face pressure loading.

**Semi-Elliptic Finite Surface Flaws**

For semi-elliptic finite surface flaws, the uniform unit-load 3D-flaw influence coefficients can be applied to calculate the contribution, $K_{I-cfp}$, of the crack-face pressure loading to the total stress intensity factor at the deepest point of the flaw $(\phi = 90°)$ by

$$K_{I-cfp} = \sqrt{\pi a}\ K_0^*\ p(\tau)$$

where $p(\tau)$ is the coolant pressure in ksi at time $\tau$ in the transient. By linear superposition, the crack-face pressure component, $K_{I-cfp}$, is then added to the total stress intensity factor.

**Infinite-Length Surface Flaws**

A similar procedure can be followed for infinite-length surface flaws.

for axial flaws

$$K_{I-cfp}(a) = \sum_{i=1}^{n} p(\tau)\ \Delta a_i K_i^*(a_i', a)$$

for circumferential flaws

$$K_{I-cfp}(a) = \sum_{i=1}^{n} 2\pi(R + a_i')\ p(\tau)\ \Delta a_i K_i^*(a_i', a)$$

where

$\Delta a_i =$ an increment of $a$ about $a_i'$ such that $\sum_{i=1}^{n} \Delta a_i = a$

$a_i' =$ radial distance from open end of crack to point of application of unit load,

$p(\tau) =$ coolant pressure at time $\tau$ uniformly applied over the crack face

$K_{I-cfp} =$ opening Mode I stress-intensity factor contribution due to crack-face pressure

$K_I^* =$ stress-intensity factor per unit load applied at $a_i'$, where load has dimensions of force/length for axial flaws and force for circumferential flaws

$n =$ number of points along length of crack for which $K_i^*$ are available,

$R =$ inside radius of vessel.

## 4.2 Sampled LEFM Material and Correlative Properties

A detailed description of the technical bases for the models in this section is presented in ref. [135]. A summary of the material in [135] is presented here with emphasis on the implementation of these models into FAVOR$^{EP}$.

### 4.2.1 Reference Nil-Ductility Transition Temperature, $RT_{NDT}$

For each major region, FAVOR$^{EP}$ calculates and reports a value of $RT_{NDT.}$ This value of $RT_{NDT}$ is the maximum of all the subregion $RT_{NDT}$ values within the given major region. The major-region $RT_{NDT}$ is not sampled from a distribution, is reported for comparison purposes only, and is not used in any subsequent analyses. Defined by

$$RT_{NDT(i)} \equiv \max\left(RT_{NDT(u)-(j)} + \Delta RT_{NDT(j)}\right);\ j \text{ subregion} \in \text{major region } i, \tag{108}$$

the major-region $RT_{NDT}$ is the mean irradiated value corresponding to the irradiation shift, $\Delta RT_{NDT}$, due to the neutron fluence at the inner surface of the vessel at the time in the operating life (typically designated in effective full-power years or EFPY) of the RPV for which the PFM anlaysis is being performed. Note that the major-region value for $RT_{NDT}$ does not include any margin term.

The fast-neutron fluence is attenuated through the wall by the relation

$$f(\delta) = f(0)\exp(-0.24 \times \delta) \tag{109}$$

where $\delta$ is in inches and $f(0)$ is the neutron fluence at the inner surface in neutrons/cm$^2$.

In FAVOR$^{EP}$, $\Delta RT_{NDT}$ may be calculated using either Regulatory Guide 1.99, Rev 2 (RG 1.99, Rev 2) [12], as defined above, or by $\Delta T_{30}$ (see Eq. (110)) as calculated by the Eason and Wright irradiation-shift model [98] to be discussed in the following section.

### 4.2.2 Radiation Embrittlement

Irradiation damage of RPV steels in U.S. PWRs occurs as a consequence of two hardening mechanisms: *matrix hardening* and *age hardening*. Details of these mechanisms are taken from [135]:

> **Matrix Hardening** – Matrix damage develops continuously during irradiation, producing hardening that has a square root dependence on fluence. Matrix damage can be divided into two components: unstable matrix defects (UMD), and stable matrix defects (SMD). Unstable matrix defects are formed at relatively low fluence and are small vacancy or interstitial clusters, complexed with solutes such as phosphorous. UMDs are produced in

displacement cascades. Increasing flux causes increasing hardening due to these defects, but they occur relatively independently of alloy composition. In low copper alloys, at low fluence and high flux, UMD is the dominant source of hardening; however, in high copper steels, these defects delay the copper-rich precipitate contribution to hardening by reducing the efficiency of radiation-enhanced diffusion. Stable matrix features form at high fluence and include nanovoids and more highly complexed clusters. These defects cause hardening that increases with the square root of exposure and is especially important at high fluence levels.

**Age Hardening** – Radiation accelerates the precipitation of copper held in solid solution, forming copper-rich precipitates (CRPs) that inhibit dislocation motion and, thereby, harden the material. This hardening rises to a peak value and is then unaffected by subsequent irradiation because no copper remains in solid solution to precipitate out and cause damage. The magnitude of this peak depends on the amount of copper initially in solution. This copper is available for subsequent precipitation. Post-weld heat treatment (PWHT) performed before the RPV is placed into service can also precipitate copper, removing its ability to cause further damage during irradiation. Thus, different materials are expected to have different peak hardening values due to differing pre-service thermal treatments. Additionally, the presence of nickel in the alloy further enhances its age-hardening capacity. Nickel precipitates together with copper, forming larger second-phase particles that present greater impediments to dislocation motion and, thereby, produce a greater hardening effect.

These physical insights helped to establish the functional form of a relationship between basic material composition, irradiation-condition variables, and measurable quantities such as yield-strength increase, Charpy-transition-temperature shift, and toughness-transition-temperature shift. A quantitative relationship was developed from the database of Charpy shift values, $\Delta T_{30}$, generated in US commercial reactor surveillance programs. Eason and Wright [98] recently developed the following physically motivated fit from these data.[8]

[8] A curved overbar, $\widehat{X}$, indicates a sampled random variate.

$$\Delta T_{30}(\widehat{Ni},\widehat{Cu},\widehat{P},\widehat{f_0}(r),\tau_{\text{exposure}},T_c,\text{product form}) =$$

$$A\exp\left(\frac{19310}{T_c+460}\right)\left(1+110\widehat{P}\right)\left(\widehat{f_0}(r)\right)^{0.4601}+B\left(1+2.40\widehat{Ni}^{1.250}\right)f(\widehat{Cu})g\left(\widehat{f_0}(r)\right)+Bias$$

$$A=\left\{\begin{array}{l}8.86\times10^{-17}\ \text{for welds}\\ 9.30\times10^{-17}\ \text{for forgings}\\ 12.7\times10^{-17}\ \text{for plates}\end{array}\right\}$$

$$B=\left\{\begin{array}{l}230\ \text{for welds}\\ 132\ \text{for forgings}\\ 206\ \text{for plates in CE vessels}\\ 156\ \text{for other plates}\end{array}\right\}$$

$$g(\widehat{f_0}(r))=\frac{1}{2}+\frac{1}{2}\tanh\left[\frac{\log_{10}\left(\widehat{f_0}(r)+4.579\times10^{12}\tau_{\text{exposure}}\right)-18.265}{0.713}\right]$$

$$f\left(\widehat{Cu}\right)=\left\{\begin{array}{ll}0 & \text{for } \widehat{Cu}\le 0.072\ \text{wt \%}\\ \left(\widehat{Cu}\text{-}0.072\right)^{0.659} & \text{for } \widehat{Cu}>0.072\ \text{wt \%}\end{array}\right\} \qquad (110)$$

subject to

$$Cu_{\max}=\left\{\begin{array}{l}0.25\ \text{for welds with Linde 80 or Linde 0091 flux}\\ 0.305\ \text{for everything else}\end{array}\right\}$$

and

$$Bias=\left\{\begin{array}{l}0\ \text{for}\ \tau_{\text{exposure}}<97000\ \text{h}\\ 9.4\ \text{for}\ \tau_{\text{exposure}}\ge 97000\ \text{h}\end{array}\right\}$$

where $\widehat{Cu}$ is the sampled copper content in wt%, $\widehat{Ni}$ is the sampled nickel content in wt%, $\widehat{P}$ is the sampled phosphorous content in wt%, $\widehat{f_0}(r)$ is the sampled and then attenuated neutron fluence in n/cm$^2$, $r$ is the position from the inner surface of RPV wall, $\tau_{exposure}$ is exposure time in hours (input to FAVOR$^{EP}$ in EFPY), and $T_c$ is coolant temperature in °F. The fast-neutron fluence at the inner surface of the vessel, $f_0(0)$, is sampled using the protocol given in Sect. 4.2.3. The sampled neutron fluence for the flaw is then attenuated (but not resampled) as the crack grows through the wall. The sampling distributions and protocols for plate and weld chemistry are presented in Sect. 4.2.9.

Reference [135] recommends that the uncertainty in the CVN transition shift values, $\Delta T_{30}$, be treated as *epistemic*. Having used information concerning composition and irradiation conditions to estimate the CVN transition temperature shift using Eq. (110), it is necessary to transform these $\Delta T_{30}$ values

into shifts in the fracture-toughness transition temperature. Figure 4.16 provides an empirical basis for the following least-squares fits for $\widehat{\Delta RT}_{NDT}$ using data extracted from the literature as discussed in [135].

$$\widehat{\Delta RT}_{NDT}(r,\ldots) = \begin{cases} 0.99\widehat{\Delta T_{30}}(r,\ldots) & \text{welds} \\ 1.10\widehat{\Delta T_{30}}(r,\ldots) & \text{plates and forgings} \end{cases} \tag{111}$$

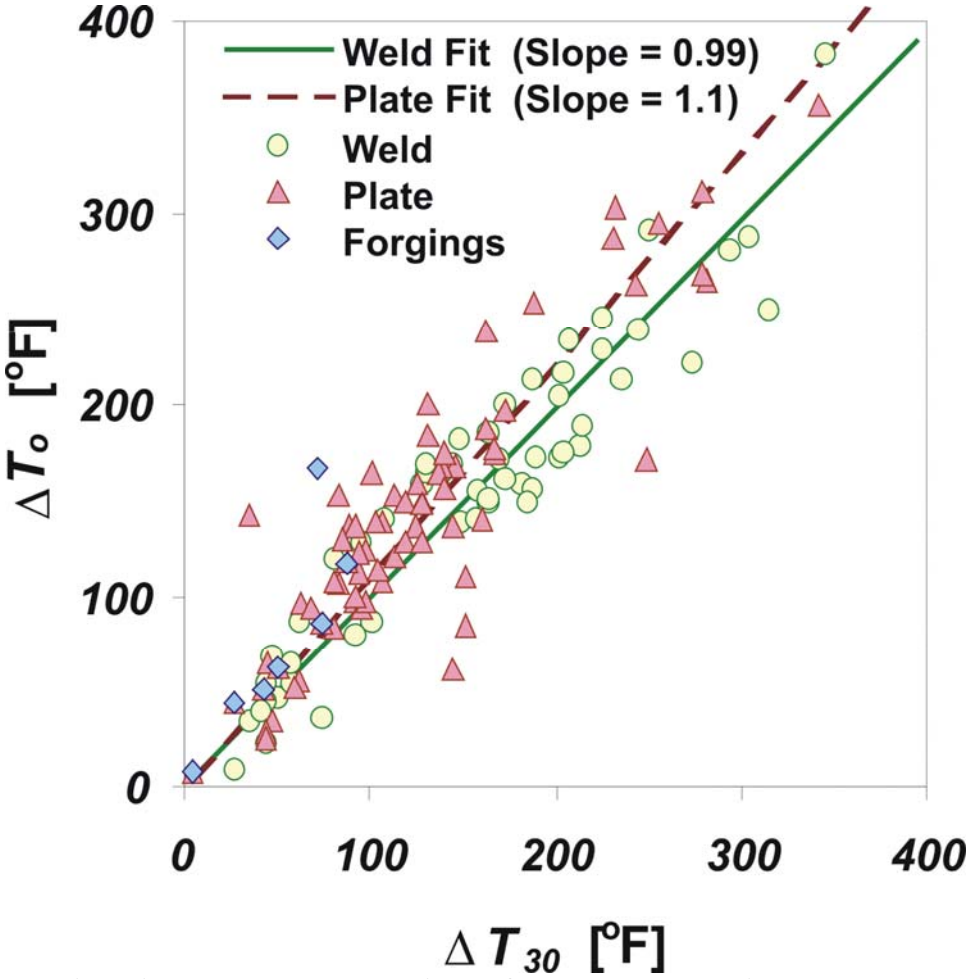


**Fig. 4.16. Relationship between the change in the fracture-toughness index temperature ($\Delta T_0 \approx \Delta RT_{NDT}$) change in the 30 ft-lbf CVN transition temperature ($\Delta T_{30}$) for welds and plates/forgings produced by irradiation. The difference in the best-fit slopes is statistically significant (from [135]).**

### 4.2.3 Fast-Neutron Fluence Attenuation and Sampling Distribution

The sampled fast-neutron fluence at the crack tip is attenuated from its sampled reference value, $\widehat{f_0}(0)$, at the inner surface of the RPV wall. This attenuation takes the following form

$$\widehat{f_0(a)} = \widehat{f}_0(0) \times \exp(-0.24a) \tag{112}$$

where $a$ is the position of the flaw tip (in inches) relative to the inner surface.

The inner surface fluence is sampled from two normal distributions such that

$$\begin{aligned} \sigma_{global} &= SIGFGL \times fluence_{subregion} \\ \widehat{f}_{mean} &\leftarrow N(fluence_{subregion}, \sigma_{global}) \\ \widehat{\sigma_{local}} &= SIGFLC \times \widehat{f}_{mean} \\ \widehat{f_0}(0) &\leftarrow N(\widehat{f}_{mean}, \widehat{\sigma_{local}}) \end{aligned} \tag{113}$$

where the best-estimate fluence, $fluence_{subregion}$, is input by the user at the subregion level. The global *SIGFGL* and local *SIGFLC* multipliers are supplied as input by the user. Recommended values are *SIGFGL* = 0.056 and *SIGFLC* = 0.118. Negative values of sampled fast-neutron fluence are handled as nonphysical exceptions in FAVOR$^{EP}$ using the truncation protocol described in Sect. 3.3.8, with 0.0 as a one-sided truncation boundary.

### 4.2.4 ORNL 99/27 $K_{Ic}$ and $K_{Ia}$ Databases

The EPRI $K_{Ic}$ database [85] as amended by Nanstad et al. [136] consists of 171 data points and includes data from 11 unirradiated pressure-vessel steels. These data were taken using compact tension C(T) and wedge-open-loading (WOL) test specimens ranging in size from 1T to 11T. A survey was recently conducted by ORNL to identify additional $K_{Ic}$ and $K_{Ia}$ data to augment the EPRI database. The result of this survey has been designated as the ORNL 99/27 extended $K_{Ic}$/$K_{Ia}$ database [86].

The candidate $K_{Ic}$ data were evaluated using the following criteria: (a) satisfaction of validity requirements given in ASTM Standard E 399 [137] to maintain consistency with the LEFM driving forces applied in the fracture model, (b) availability in tabular form, and (c) availability of unirradiated $RT_{NDT0}$, determined according to the *ASME Boiler and Pressure Vessel Code,* Section III, NB-2331 [138]. The ORNL survey produced an additional 84 $K_{Ic}$ fracture-toughness values obtained from Refs. [139-143]. The extended $K_{Ic}$ database, compiled from the amended EPRI data and from the ORNL survey, provided a total of 255 fracture-toughness data points from 18 materials for input

to the statistical model development procedures described in ref. [86] and applied herein. A plot of the extended $K_{Ic}$ database versus $(T - RT_{NDT0})$ is given in Fig. 4.17; the complete tabulation of the database is included in Appendix C of this report with a summary presented in Table 4.1.

A similar survey was carried out to compile an extended $K_{Ia}$ database that would include those data in the EPRI report (see Fig. 4.18a). Because the ASTM Standard E 1221 [144] is relatively new, many of the existing data were generated before the adoption of the standard. Thus, it was agreed that candidate $K_{Ia}$ data would be evaluated in a more general context, including engineering judgment of acknowledged experts and general acceptance by the nuclear technology community. The ORNL survey produced an additional 62 fracture-toughness, $K_{Ia}$, data points [145-147] to augment the existing 50 data points [148,149] in EPRI NP-719-SR. A complete tabulation of the 112 fracture-toughness values is given in Appendix C of this report with a summary presented in Table 4.2. A description of the chemistry and heat treatment of the principal steels in the ORNL 99/27 database is shown in Table 4.3.

In conjunction with the development of a ductile-tearing model, arrest data from large-specimen experiments carried out in the 1980s were also added to the $K_{Ia}$ database (see Fig. 4.18b). These additional large-specimen arrest data came from the HSST Wide Plate test program (WP-1 [38] and WP2 [39]), the HSST Pressurized Thermal Shock Experiments (PTSE-1[26] and PTSE-2 [27]), and the HSST Thermal Shock Experiments (TSE) [150].

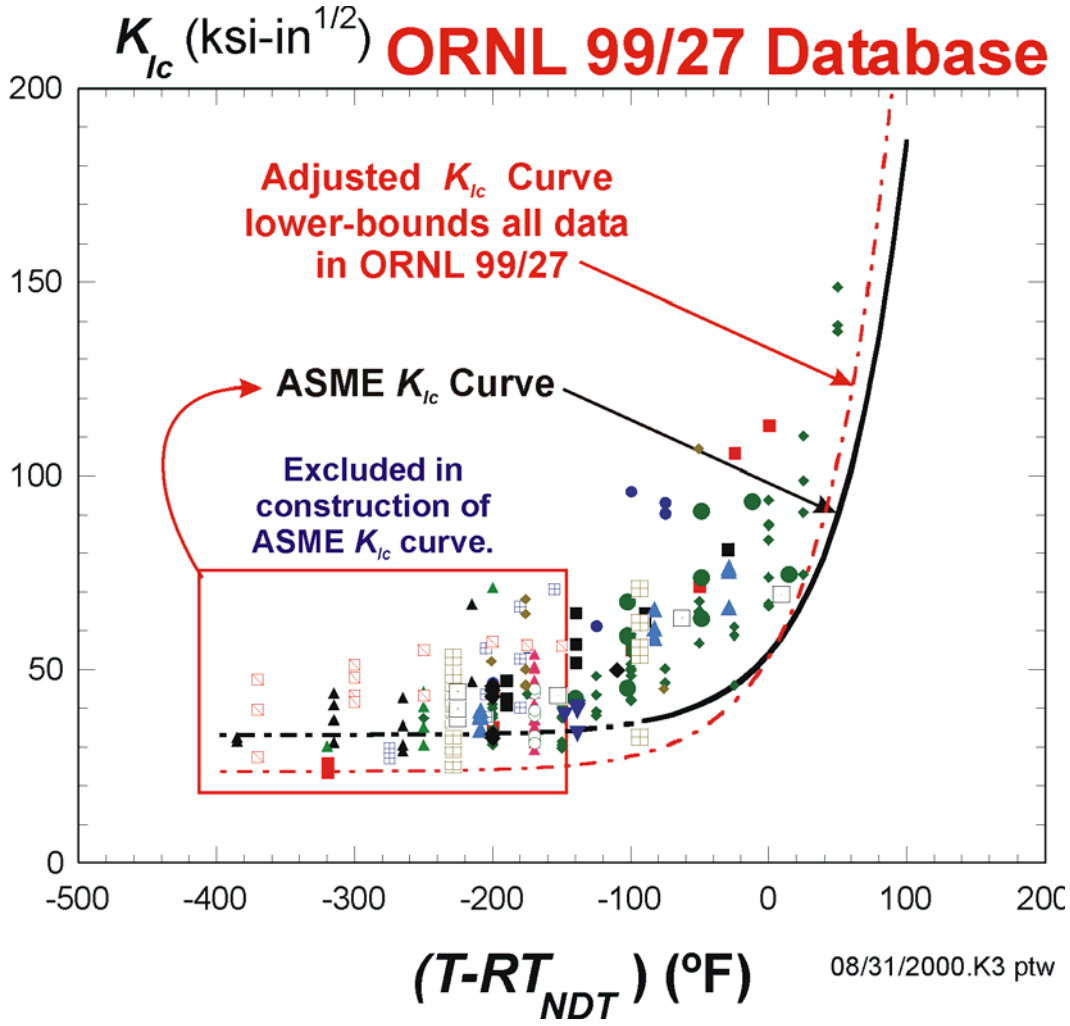


**Fig. 4.17. ORNL 99/27 $K_{Ic}$ database including modified ASME $K_{Ic}$ curve that served as a lower-bounding reference curve in the development of a new transition index temperature.**

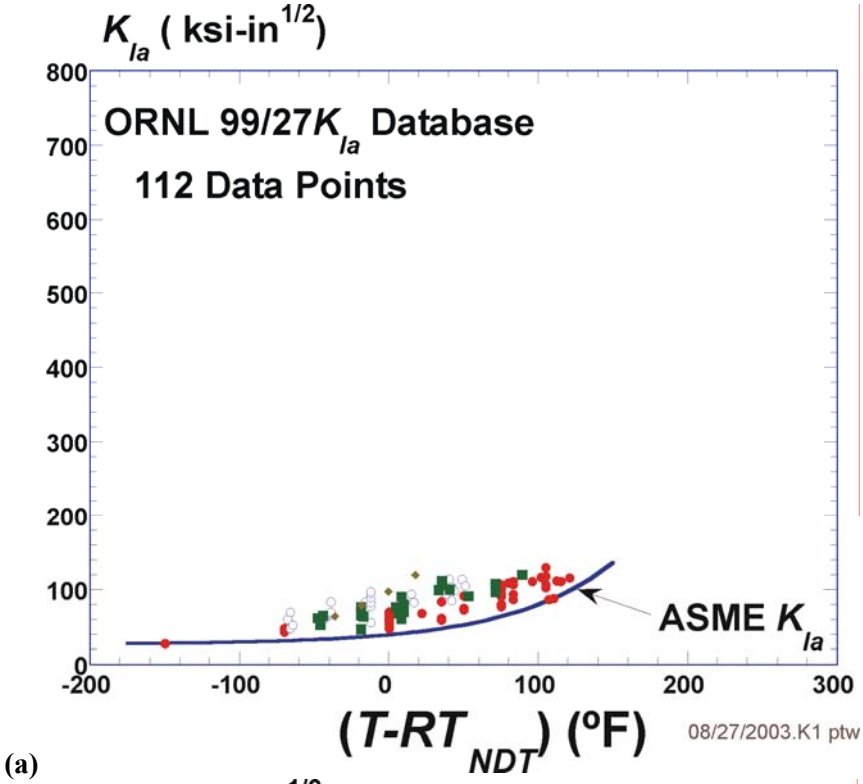


(a)

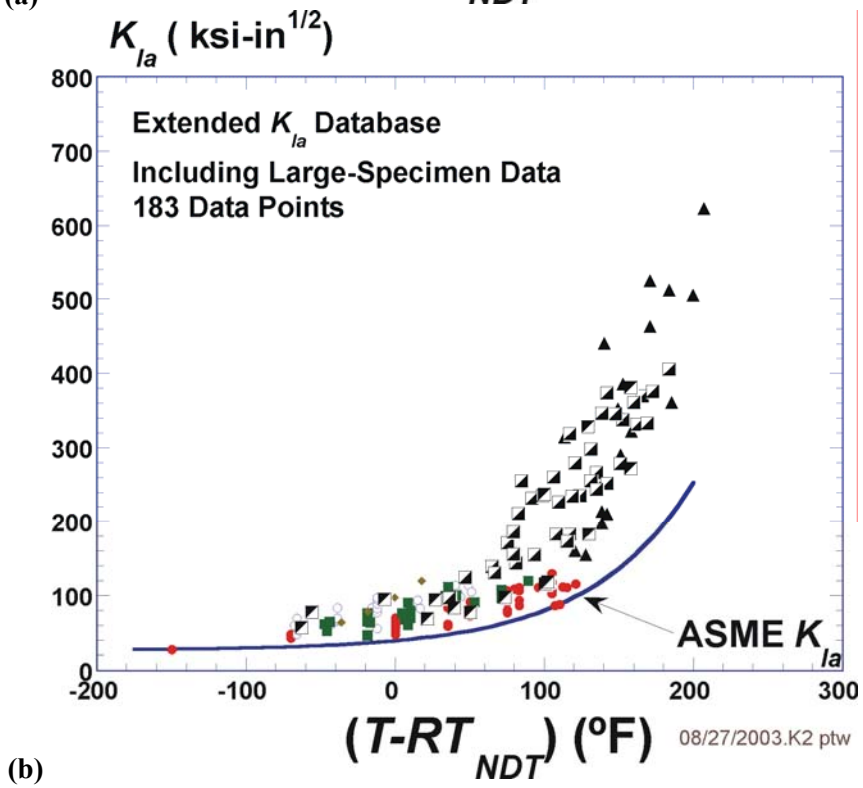


(b)

**Fig. 4.18. $K_{Ia}$ databases (a) ORNL 99/27 $K_{Ia}$ database and (b) Extended $K_{Ia}$ database.**

**Table 4.1. Summary of ORNL 99/27 $K_{Ic}$ Extended Database**

| | Material | Source | Specimen Type | Size Range | Temp. Range (°F) | ($T$-$RT_{NDT0}$) Range (°F) | No. of Data Points |
|---|---|---|---|---|---|---|---|
| **EPRI** | **Database** | EPRI NP-719-SR | | | | | |
| 1 | HSST 01 subarc weldment | Shabbits (1969) | C(T) | 1T - 6T | -200 to -50 | -200 to -50 | 8 |
| 2 | A533B Cl. 1 subarc weld | Shabbits (1969) | C(T) | 1T - 8T | -200 to 0 | -200 to 0 | 8 |
| 3 | HSST 01 | Mager (1970) | C(T) | 1T | -150 | -170 | 17 |
| 4 | HSST 03 | Mager (1970) | C(T) | 1T | -150 | -170 | 9 |
| 5 | A533B Cl. 1 | Mager (1969) | WOL | 1T - 2T | -320 to -150 | -385 to -215 | 13 |
| 6 | HSST 02 | Mager (1969) | WOL & C(T) | 1T - 2T | -200 to 0 | -200 to 0 | 41 |
| 6 | HSST 02 | Shabbits (1969) | C(T) | 1T - 11T | -250 to 50 | -250 to 50 | 28 |
| 7 | A533B Cl. 1 weldment | Mager (1969) | WOL | 1T - 2T | -320 to -200 | -275 to -155 | 10 |
| 8 | A533 B Cl. 1 weldment/HAZ | Mager (1969) | WOL | 1T - 2T | -320 to -200 | -320 to -200 | 6 |
| 9 | A508 Cl.2 European Forging | Mager (1969) | WOL | 1T - 2T | -320 to -100 | -370 to -150 | 12 |
| 10 | A508 Class 2 | unpublished | C(T) | 2T - 6T | -150 to 0 | -201 to -51 | 9 |
| 11 | A508 Class 2 | unpublished | C(T) | 2T - 8T | -125 to -75 | -190 to -30 | 10 |
| | | | | | | Total | 171 |
| **Additional** | **Data** | | | | | | |
| 12 | HSSI Weld 72W | NUREG/CR-5913. | C(T) | 1T-6T | -238 to 50 | -229 to 59 | 13 |
| 13 | HSSI Weld 73W | NUREG/CR-5913 | C(T) | 1T-4T | -238 to -58 | -209 to -29 | 10 |
| 14 | HSST Plate 13A | NUREG/CR-5788 | C(T) | ½T-4T | -238 to -103 | -229 to -94 | 43 |
| 15 | A508 Cl. 3 | ASTM STP 803 | Bx2B C(T) | 1T-4T | -238 to -4 | -225 to 9 | 6 |
| 16 | Midland Nozzle Course Weld | NUREG/CR-6249 | C(T) | 1T | -148 to -58 | -200 to -110 | 6 |
| 17 | Midland Beltline | NUREG/CR-6249 | C(T) | 1T | -148 | -171 | 2 |
| 18 | Plate 02 4th Irr. Series (68-71W) | NUREG/CR-4880 | C(T) | 1T | -148 to -139 | -148 to -139 | 4 |
| | | | | | | Total | 84 |
| | | | | | | Grand Total | 255 |

**Table 4.2. Summary of $K_{Ia}$ Extended Database**

| | Material | Source | Specimen Type | Size Range | Test Temp. Range (°F) | ($T$-$RTNDT$) Range (°F) | No. of Data Points |
|---|---|---|---|---|---|---|---|
| **EPRI** | **Database** | **EPRI NP-719-SR** | | | | | |
| **1** | **HSST 02** | **Ripling (1971)** | **CCA crack arrest** | **1T-3T** | **-150 to 121** | **-150 to 121** | **50** |
| **Additional Data** | **Additional Data** | | | | | | |
| **2** | **HSSI Weld 72W** | **NUREG/CR-5584** | **CCA crack arrest** | | **-78 to 41** | **-68 to 51** | **32** |
| **3** | **HSSI Weld 73W** | **NUREG/CR-5584** | **CCA crack arrest** | | **-78 to 59** | **-48 to 89** | **26** |
| **4** | **MW15J** | **NUREG/CR-6621** | **CCA crack arrest** | | **-4 to 50** | **-36 to 18** | **4** |
| **Large Specimen Data** | | | | | | | |
| **5** | **HSST WP1** | **NUREG/CR-5330** | **Wide Plate Tests** | **(-)** | **84 to 198** | **94 to 207** | **18** |
| **6** | **HSST WP2** | **NUREG/CR-5451** | **Wide Plate Tests** | **(-)** | **142 tp 324** | **2 to 184** | **38** |
| **7** | **HSST PTSE-1** | **NUREG/CR-4106** | **Pressurized Vessel** | **(-)** | **326 to 354** | **100 to 158** | **2** |
| **8** | **HSST PTSE-2** | **NUREG/CR-4888** | **Pressurized Vessel** | **(-)** | **267 tp 325** | **130 to 158** | **3** |
| **9** | **HSST TSE** | **NUREG/CR-4249** | **Thermally-Shocked Cylinder** | **(-)** | **72 to 268** | **-63 to 103** | **10** |
| | | | | | | **Total =** | **183** |

**Table 4.3. Chemistry and Heat Treatment of Principal Materials: ORNL 99/27 Database**

| Material ID | Specification | Source | Chemistry – wt (%) | | | | | | | | | | Heat Treatment |
|---|---|---|---|---|---|---|---|---|---|---|---|---|---|
| | | | C | P | Mn | Ni | Mo | Si | Cr | Cu | S | Al | |
| HSST 01 | A533B Cl. 1 | Mager (1970) | .22 | .012 | 1.48 | .68 | .52 | .25 | - | - | .018 | - | Note 1 |
| HSST 02 | A533B Cl. 1 | Mager (1969) | .22 | .012 | 1.48 | .68 | .52 | .25 | - | - | .018 | - | Note 2 |
| HSST 03 | A533B Cl. 1 | Mager (1970) | .20 | .011 | 1.26 | .56 | .45 | .25 | .10 | .13 | .018 | .034 | Note 3 |
| HSST 02 | A533B Cl. 1 | Shabbits (1969) | .22 | .012 | 1.48 | .68 | .52 | .25 | - | - | .018 | - | Note 4 |
| HSST 01 subarc weld | A533B Cl. 1 | Shabbits (1969) | .12 | .014 | 1.35 | .65 | .52 | .23 | - | - | .012 | - | Note 5 |
| B&W subarc weldment | A533B Cl. 1 | Shabbits (1969) | .10 | .009 | 1.77 | .64 | .42 | .36 | - | - | .015 | - | Note 6 |
| PW/PH weldment | A533B Cl. 1 | Mager (1969) | .09 | .019 | 1.25 | 1.08 | .52 | .23 | .05 | .22 | .13 | .037 | Note 7 |
| MD07 European | A508 Cl. 2 Ring forging | Mager (1969) | .18 | .009 | 1.16 | .72 | .51 | .24 | .28 | - | .10 | - | Note 8 |
| - | A533B Cl. 1 | Mager (1969) | .19 | .012 | 1.37 | .52 | .45 | .25 | .13 | .15 | .016 | .048 | Note 9 |
| 72W | A533B weld | 5788 | .09 | .006 | 1.66 | .60 | .58 | .04 | .27 | .23 | .006 | - | |
| 73W | A533B weld | 5788 | .10 | .005 | 1.56 | .60 | .58 | .04 | .25 | .21 | .005 | - | |

Notes:

| | | | |
|---|---|---|---|
| 1. | Normalizing: | 1675 °F | 4 hr, air cooled |
| | Austentizing: | 1600 °F | 4 hr |
| | Quenching: | Water quench | |
| | Tempering: | 1225 °F | 4 hr, furnace cooled |
| | Stress Relief: | 1150 °F | 40 hr, furnace cooled |
| 2. | Normalizing: | 1675 °F | 4 hr, air cooled |
| | Austentizing: | 1600 °F | 4 hr |
| | Quenching: | Water quench | |
| | Tempering: | 1225 °F | 4 hr, furnace cooled |
| | Stress Relief: | 1150 °F | 40 hr, furnace cooled |
| 3. | Normalizing: | 1675 °F | 12 hr, air cooled |
| | Austentizing: | 1575 °F | 12 hr |
| | Quenching: | Water quench | |
| | Tempering: | 1175 °F | 12 hr, furnace cooled |
| | Stress Relief: | 1125 °F | 40 hr, furnace cooled |
| 4. | Normalizing: | 1675 ± 25 °F | 4 hr |
| | Austentizing: | 1520 °F – 1620 °F | 4 hr |
| | Quenching: | Water quench. | |
| | Tempering: | 1200 °F – 1245 °F | 4 hr, air cooled |
| | Stress Relief: | 1150 ± 25 °F | 40 hr, furnace cooled to 600 °F |
| 5. | Post Weld: | 1150 ± 25 °F | 12 hr |
| | Intermediate | 1100 ± 25 °F | 15 min |
| 6. | Post Weld | 1100 °F – 1150 °F | 12 hr |
| | Intermediate | 1100 °F – 1150 °F | 15 min |
| 7. | | 620 °C | 27 hr, air cooled |
| 8. | | 925 °C | 5 hr |
| | Quenching: | Water quench | |
| | | 650 °C | 3 hr, furnace cooled |
| | | 620 °C | 24 hr, air cooled |
| 9. | | 910 °C | 8 hr |
| | Quenching: | Water quench | |
| | | 680 °C | 10 hr, furnace cooled |
| | | 850 °C | 8 hr |
| | Quenching: | Water quench | |
| | | 690 °C | 8 hr, air cooled |
| | | 620 °C | 24 hr, air cooled |

### 4.2.5 Index Temperature $RT_{NDT}$ – Uncertainty Classification and Quantification

Values of $RT_{NDT}$ are uncertain both due to epistemic and aleatory causes. The *epistemic* uncertainty is due to the conservative bias implicit in the ASME NB-2331 [138] definition of $RT_{NDT}$, the variety of inconsistent transition temperature metrics used to define $RT_{NDT}$, the lack of prescription in the test methods used to define $RT_{NDT}$, and the fact that the *CVN* and *NDT* values used to define $RT_{NDT}$ do not themselves measure fracture toughness. *Aleatory* uncertainties are due to material variability. It is expected that epistemic uncertainty sources outnumber aleatory ones [135]; however, this expectation alone is inadequate to classify the uncertainty in $RT_{NDT}$ as being primarily aleatory or primarily epistemic. To make this distinction, a comparison of the $RT_{NDT}$ index temperature to an exemplar index temperature (such as the *Master Curve* index $T_0$ [151]) associated with a physically motivated model of crack initiation toughness is needed.

The Master Curve index temperature $T_0$ is estimated directly from fracture-toughness data, and, by definition, it is therefore associated with the same location on the transition temperature curve of every steel, suggesting that the sources of epistemic uncertainty that are associated with $RT_{NDT}$ do not influence $T_0$. Thus, the uncertainty in $T_0$ is expected to be primarily aleatory, and a comparison between $T_0$ and $RT_{NDT}$ values can be used to quantify the epistemic uncertainty in $RT_{NDT}$. The numerical difference between $RT_{NDT}$ and $T_0$ has been used to quantify how far away from measured fracture-toughness data $RT_{NDT}$ positions a model of fracture toughness for a given heat of steel [135]. Figure 4.19 shows a cumulative distribution function (CDF) constructed from the difference between values of $RT_{NDT}$ and $T_0$ reported in the literature [152] for the RPV steels in the ORNL 99/27 database. See Appendix E for a description of the statistical procedures applied in the construction of this CDF. These data (see Table 4.4) demonstrate that the epistemic uncertainty in $RT_{NDT}$ almost always produces a high estimate of the actual fracture-toughness transition temperature.

Even though it quantifies the epistemic uncertainty in $RT_{NDT}$, the CDF illustrated in Fig. 4.19 cannot be used directly in FAVOR$^{EP}$ because of inconsistencies between $T_0$ and the requirements of the PTS re-evaluation project. Consequently, an alternative CDF (see Fig. 4.20) was developed that avoids the explicit treatment of size effects and the use of elastic-plastic fracture mechanics (EPFM) toughness data, but retains the important concept from the Master Curve that the index temperature should be quantitatively linked to the measured toughness data. This alternative CDF was determined based on the temperature shift values ($\Delta RT_{epistemic}$ in Table 4.5) needed to make a NB-2331 $RT_{NDT}$-positioned $K_{Ic}$ curve lower-bound the ASTM E-399 valid $K_{Ic}$ data for each of the 18 heats of RPV steel in the ORNL 99/27 database. See Fig. 4.21 for an example of this lower-bounding shift procedure for HSST Plate 02.

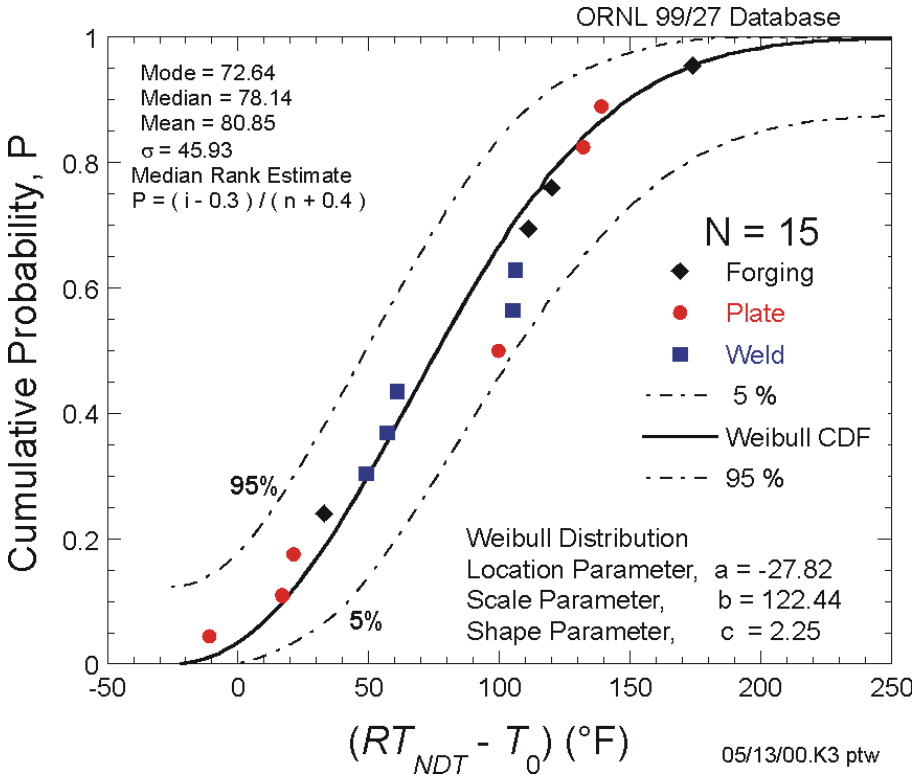


**Fig. 4.19. Cumulative distribution function of the observed difference in $RT_{NDT}$ and $T_o$ (with a size of 1T) using data in the ORNL 99/27 database.**

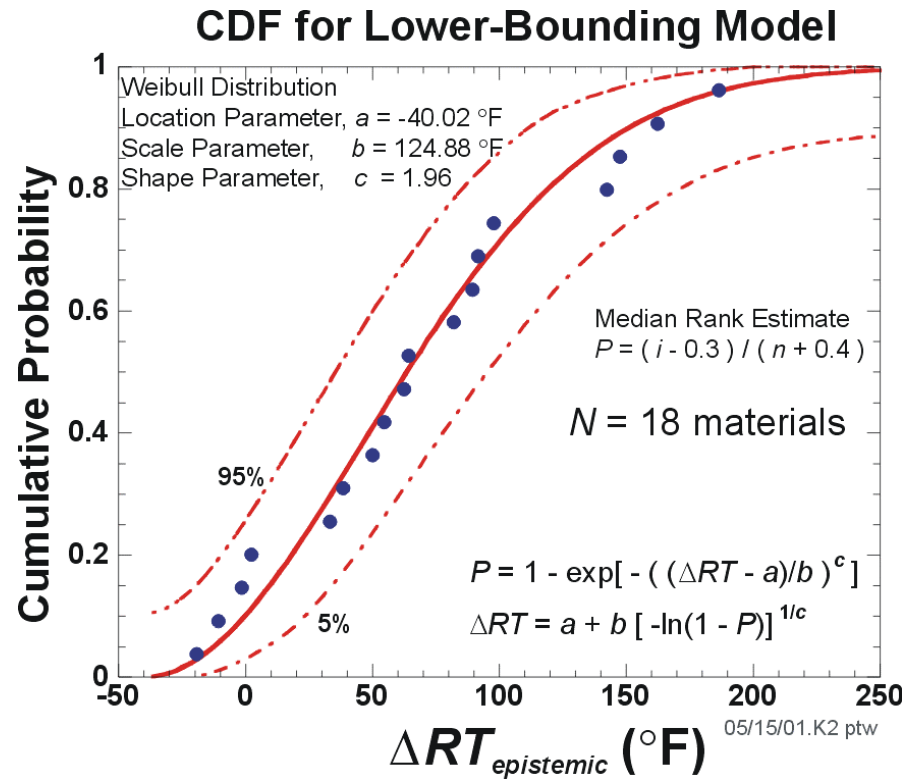


**Fig. 4.20 Cumulative distribution function of the difference (designated as $\Delta RT_{epistemic}$) between $RT_{NDT0}$ and a new lower-bounding reference index designated $RT_{LB}$.**

**Table 4.4. Materials Used from the ORNL 99/27 $K_{Ic}$ Extended Database**

| ID | Form | $RT_{NDT}$ (°F) | $T_0$ (°F)* | $RT_{NDT}$ - $T_0$ | $P$ | $T_q$ (°F)** |
|---|---|---|---|---|---|---|
| HSST-03 | Plate | 20 | 31 | -11 | 0.0455 | 26.1 |
| HSST-02 | Plate | 0 | -17 | 17 | 0.1104 | -17.4 |
| HSST-01 | Plate | 20 | -1 | 21 | 0.1753 | -2.9 |
| A508 Cl. 3 | Forging | -13 | -46 | 33 | 0.2403 | |
| 73W | Weld | -29.2 | -78 | 48.8 | 0.3052 | |
| A533B Cl. 1 | Weld | 0 | -57 | 57 | 0.3701 | -56.7 |
| 72W | Weld | -9.4 | -70 | 60.6 | 0.4351 | |
| A533B Cl. 1 | Plate | -9.4 | -109 | 99.6 | 0.5000 | |
| HSST-01 | Weld | 0 | -105 | 105 | 0.5649 | -104.4 |
| A533B Cl. 1 | Weld | -45 | -151 | 106 | 0.6299 | -151.5 |
| A508 Cl. 2 | Forging | 51 | -60 | 111 | 0.6948 | -59.9 |
| A508 Cl. 2 | Forging | 65 | -55 | 120 | 0.7597 | -5.8 |
| A533B Cl. 1 | HAZ | 0 | -132 | 132 | 0.8247 | -132.3 |
| A533B Cl. 1 | Plate | 65 | -74 | 139 | 0.8896 | -73.8 |
| A508 Cl. 2 | Forging | 50 | -124 | 174 | 0.9545 | -119.3 |

*$T_0$ values reported in [152]. Calculated using ASTM E-1921 valid data.
**Provisional $T_q$ values calculated using ASTM E-399 valid $K_{Ic}$ data in [86].

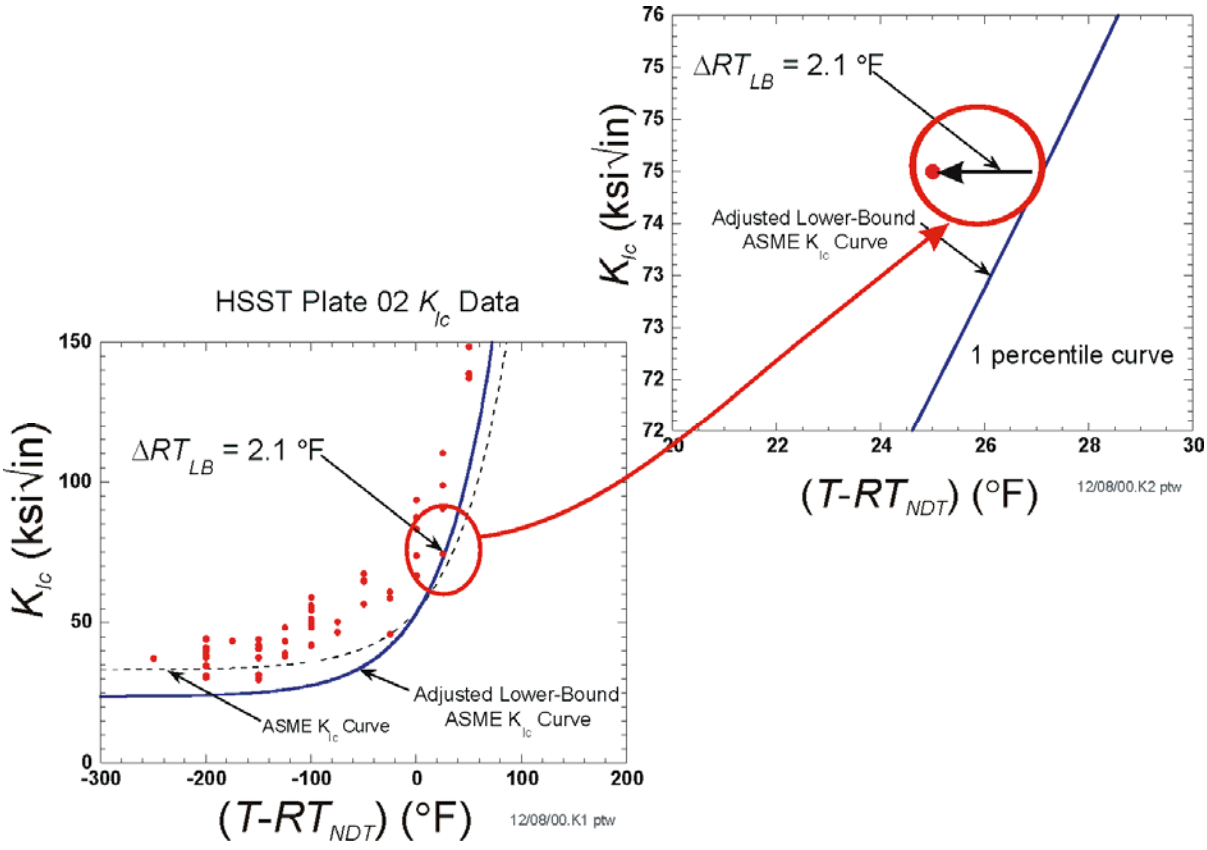


**Fig. 4.21The $\Delta RT_{LB}$ for HSST Plate 02. The lower-bounding transition reference temperature, $RT_{LB}$, was developed from 18 materials in the ORNL 99/27 database, where for each material $RT_{LB} = RT_{NDT0} - \Delta RT_{LB}$.**

**Table 4.5. Values of Lower-Bounding Reference Temperature with and without Sample-Size Adjustment: ORNL 99/27 Database**

| Material ID No. $k$ | Sample Size, $N$ | $RT_{NDT0}$ (°F) | $RT_{LB}^{(k)*}$ (°F) | $\Delta RT_{LB}^{(k)*}$ (°F) | Size Correct. (°F) | $RT_{LB}^{(k)**}$ (°F) | $\Delta RT_{epistemic}^{(k)**}$ (°F) |
|---|---|---|---|---|---|---|---|
| 1 | 8 | 0.0 | -75.2 | 75.2 | 10.9 | -64.3 | 64.3 |
| 2 | 8 | 0.0 | 0.0 | 0 | 10.9 | 10.9 | -10.9 |
| 3 | 17 | 20.0 | -82.4 | 102.4 | 4.6 | -77.8 | 97.8 |
| 4 | 9 | 20.0 | -81.1 | 101.1 | 9.6 | -71.5 | 91.5 |
| 5 | 13 | 65.0 | -127.6 | 192.6 | 6.4 | -121.2 | 186.2 |
| 6 | 69 | 0.0 | -2.1 | 2.1 | 0 | -2.1 | 2.1 |
| 7 | 10 | -45.0 | -195.7 | 150.7 | 8.5 | -187.2 | 142.2 |
| 8 | 6 | 0.0 | -176.9 | 176.9 | 14.5 | -162.4 | 162.4 |
| 9 | 12 | 50.0 | -104.5 | 154.5 | 6.9 | -97.6 | 147.6 |
| 10 | 9 | 51.0 | -8.7 | 59.7 | 9.6 | 0.9 | 50.1 |
| 11 | 10 | 65.0 | 1.9 | 63.1 | 8.5 | 10.4 | 54.6 |
| 12 | 13 | -9.4 | 3.6 | -13.0 | 6.4 | 10.0 | -19.4 |
| 13 | 10 | -29.2 | -76.1 | 46.9 | 8.5 | -67.6 | 38.4 |
| 14 | 43 | -9.4 | -43.5 | 34.1 | 0.9 | -42.6 | 33.2 |
| 15 | 6 | -13.0 | -25.8 | 12.8 | 14.5 | -11.3 | -1.7 |
| 16 | 6 | 52.0 | -51.9 | 103.9 | 14.5 | -37.4 | 89.4 |
| 17 | 2 | 23.0 | -99.7 | 122.7 | 40.8 | -58.9 | 81.9 |
| 18 | 4 | 0.0 | -83.8 | 83.8 | 21.5 | -62.3 | 62.3 |

$RT_{LB}^{(k)*}$ = lower-bounding reference temperature for the $k$th material without sample size-adjustment

$\Delta RT_{LB}^{(k)*} = RT_{NDT(0)}^{(k)} - RT_{LB}^{(k)*}$

$RT_{LB}^{(k)**}$ = lower-bounding reference temperature for the $k$th material with sample size-adjustment

$\Delta RT_{epistemic}^{(k)**} = RT_{NDT0}^{(k)} - RT_{LB}^{(k)**}$

The adjusted ASME lower-bounding curve shown in Fig. 4.21 has the following form:

$$K_{Ic} = 23.65 + 29.56\exp\left[0.02(T - RT_{NDT})\right] \text{ ksi}\sqrt{\text{in.}} \tag{114}$$

with $(T - RT_{NDT})$ in °F. The adjustment for sample size indicated in Table 4.5 assumes that Eq. (114) represents a 0.01 fractile. The $RT_{NDT0} - T_0$ CDF (Figs. 4.19 and 4.22) is a Weibull distribution with a flaw-size dependence

$$(RT_{NDT0} - T_0) \leftarrow W(a_{xT}, 122.4, 2.25)$$

$$a_{xT} = a_{1T} - \frac{1.8}{0.019}\ln\left[\frac{80\left(B_{xT}/B_{1T}\right)^{1/4} - 10}{70}\right] \text{ [°F]}$$

$$a_{1T} = -27.82 \text{ °F} \tag{115}$$

$B_{xT}$ = flaw length [in.]

$B_{1T}$ = 1.0 in.

The lower-bounding CDF, Eq. (116), quantifies the epistemic uncertainty in $RT_{NDT}$ in a manner fully consistent with the constraints placed on the toughness models used in the PTS re-evaluation effort. In Fig. 4.22, we also compare this quantification of epistemic uncertainty with that based on the Master Curve. This comparison illustrates that the implicit treatment of size effects adopted when developing the alternative CDF using ASTM E 399 valid data produces a result quite similar in form to that based on the Master Curve. The similarity of the alternative CDF to the Master Curve-based CDF provides a link between the $RT_{LB}$ concept developed to conform to the requirements of the PTS re-evaluation and the physical and empirical underpinnings of the Master Curve, thereby demonstrating that aleatory and epistemic uncertainties can be reasonably distinguished using $RT_{LB}$ and $\Delta RT_{LB}$. The epistemic uncertainty in the unirradiated value of $RT_{NDT0}$ is estimated by sampling from the following Weibull distribution (see Appendix F for details on the development of Eq. (116) ):

$$\widehat{\Delta RT}_{epistemic} \leftarrow W(-45.586, 131.27, 2.177)$$
$$\widehat{\Delta RT}_{epistemic} = -45.586 + 131.27\left[-\ln(1-\Phi)\right]^{1/2.177} \quad [°\mathrm{F}] \qquad (116)$$
$$\text{where } \Phi \leftarrow \mathrm{U}(0,1)$$

Combined with the sampled irradiation-shift term described in Sect. 4.2.2, the irradiated value of $\widehat{RT_{NDT}}$ is calculated by

$$\widehat{RT}_{NDT}(r,\ldots) = \widehat{RT}_{NDT0} - \widehat{\Delta RT}_{epistemic} + \widehat{\Delta RT}_{NDT}(r,\ldots) \qquad (117)$$

where $\widehat{RT}_{NDT0} \leftarrow N(\overline{RT}_{NDT0}, \sigma_{RT_{NDT0}})$ and $\widehat{RT_{NDT}}$ is a function of the position of the crack tip due to the attenuation of the fast-neutron fluence at position $r$ in the vessel wall.

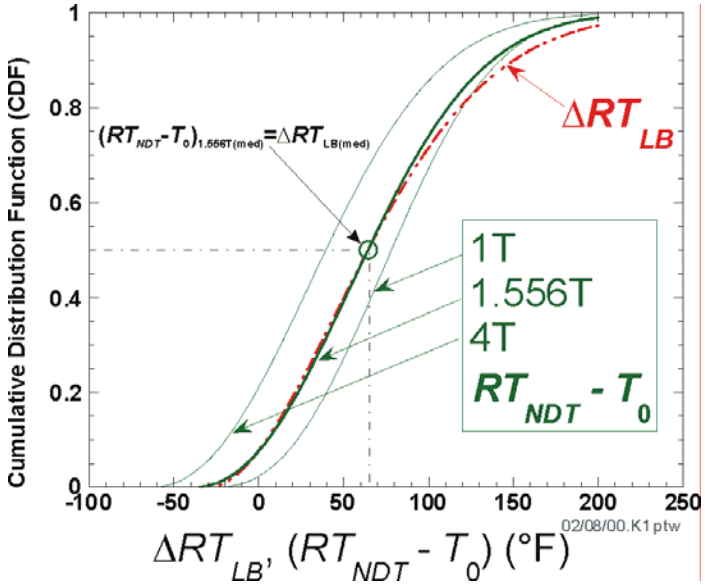


**Fig. 4.22Comparison of cumulative distribution functions developed for $RT_{NDT0}$-$T_0$ and $RT_{NDT0}$-$RT_{LB}$ .**

### 4.2.6 Index Temperature $RT_{Arrest}$ – Uncertainty Classification and Quantification

To enable all commercial operators of pressurized water reactors to assess the state of their RPV relative to new PTS screening criteria without the need to make new material property measurements, the arrest fracture toughness of the RPV needs to be estimated using only currently available unirradiated $RT_{NDT0}$ values. These restrictions suggest that very limited information, specifically a value of $RT_{NDT0}$, is available to define the arrest fracture-toughness model appropriate to a particular steel in a particular RPV. Consequently, the temperature dependency and uncertainty of the arrest fracture-toughness model will either have to be demonstrated or assumed to be invariant over a wide range of conditions because sufficient information is not available to establish these features on a heat-specific basis [135].

The information presented in [135] suggests that a relevant arrest reference temperature can be defined based on (a) an index temperature that defines the position of the plane-strain crack arrest toughness, $K_{Ia}$ , transition curve on the temperature axis and (b) a relationship between the index temperatures for the initiation and arrest fracture-toughness curves (assuming such a relationship exists). For this study, the temperature dependency of $K_{Ia}$ data was assumed to be universal to all reactor pressure vessel steels, or, more specifically, within this class of materials the temperature dependency was assumed to be insensitive to all individual and combined effects of alloying, heat treatment (and other thermal processing), mechanical processing, and irradiation. These material variables only influence the temperature range over which a particular steel experiences a transition from brittle behavior (at low temperatures) to ductile behavior (at higher temperatures), this being quantified by a heat-specific index temperature value. Furthermore, the information presented in [135] suggests that the relationship between the index temperatures for crack initiation and crack arrest toughness is also not expected to be influenced strongly by heat-specific factors.

From [135]:

> **Crack arrest occurs when dislocations can move faster than the crack propagates, resulting in crack tip blunting and arrest. Dislocation mobility therefore controls the ability of a ferritic steel to arrest a running cleavage crack, and thus its crack arrest toughness. The atomic lattice structure is the only feature of the material that controls the temperature dependence of the material properties that are controlled by dislocation motion. Consequently, as was the case for crack initiation toughness, the temperature dependency of crack arrest toughness depends only on the short-range barriers to dislocation motion established by the BCC lattice structure. Other features that vary with steel composition, heat treatment, and irradiation include grain size/boundaries, point defects, inclusions, precipitates, and dislocation substructures. These features all influence dislocation motion, and thereby both strength and toughness, but their large inter-barrier spacing relative to the atomic scale associated with the lattice structure makes these effects completely athermal.**

**This understanding suggests that the myriad of metallurgical factors that can influence absolute strength and toughness values, and thereby the transition temperature, exert no control over the temperature dependency of arrest toughness in fracture mode transition. Additionally, since $K_{Ic}$ and $K_{Ia}$ both depend on the ability of the material to absorb energy via dislocation motion, $K_{Ic}$ and $K_{Ia}$ are both expected to exhibit a similar temperature dependence.**

As described in [135], a strong physical basis supports a temperature dependency in arrest fracture-toughness data that is universal to all ferritic steels; this temperature dependence has a similar functional form to that of crack-initiation toughness. Mathematically, Wallin and co-workers proposed [153,154]:

$$K_{Ia(mean)} = 30 + 70\exp\left[0.019\left(T - T_{KIa}\right)\right] \quad [\mathrm{MPa}\sqrt{\mathrm{m}}] \tag{118}$$

where $(T - T_{KIa})$ is in °C. Equation (118) describes the temperature ($T$) dependency of the mean arrest toughness ($K_{Ia(mean)}$). In this equation, temperature is normalized to the index temperature $T_{KIa}$, where $T_{KIa}$ is defined as the temperature at which the mean arrest toughness is $100\ \mathrm{MPa}\sqrt{\mathrm{m}}$ ($91\ \mathrm{ksi}\sqrt{\mathrm{in.}}$). Wallin found that a lognormal distribution having a lognormal standard deviation of 0.18 fits the extensive database used in his study.

The physical understanding of the relationship between crack initiation and crack arrest presented in [135] suggests that the temperature separation between the $K_{Ic}$ and $K_{Ia}$ transition curves should progressively diminish as the material is hardened (e.g. by cold work, irradiation, etc.). Available empirical evidence supports this expectation, as illustrated in Fig. 4.23. An exponentially decaying functional form for the mean was selected to represent these data, because this relationship had the mathematical form anticipated from physical considerations (i.e. the separation between the $K_{Ic}$ and $K_{Ia}$ curves diminishes as $T_o$ increases). This nonlinear regression fit was:

$$\Delta RT_{ARREST(mean)} \equiv T_{K_{Ia}} - T_o = 44.123 \cdot \exp\left\{-0.006T_0\right\} \quad [°\mathrm{C}] \tag{119}$$

where $\Delta RT_{ARREST}$ is distributed lognormally about the mean given by Eq. (119), with an estimated log-normal standard deviation of 0.39 (see Fig. 4.24). Table 4.6 presents several reference-transition temperature indices for the steels in the ORNL 99/27 $K_{Ia}$ database including $\overline{RT}_{Arrest}$ calculated from Eq. (119).

**Table 4.6. ORNL 99/27 $K_{Ia}$ Database – Reference-Transition Temperatures**

| Material ID | Product Form | Sample Size | $RT_{NDT0}$ (°F) | $RT_{LB}$ (°F) | $T_0$ (°F) | $RT_{Arrest}$ (°F) | $T_{KIa}$ (°F) |
|---|---|---|---|---|---|---|---|
| HSST-02 | Plate | 50 | 0 | -2.1 | -17 | 76.8 | 75.2 |
| 72W | Weld | 32 | -9.4 | -42.6 | -70 | 49.8 | 8.6 |
| 73W | Weld | 26 | -29.2 | -67.6 | -78 | 34.1 | 6.8 |
| Midland | Weld | 4 | 32.2 | -58.9 | NA | NA | NA |

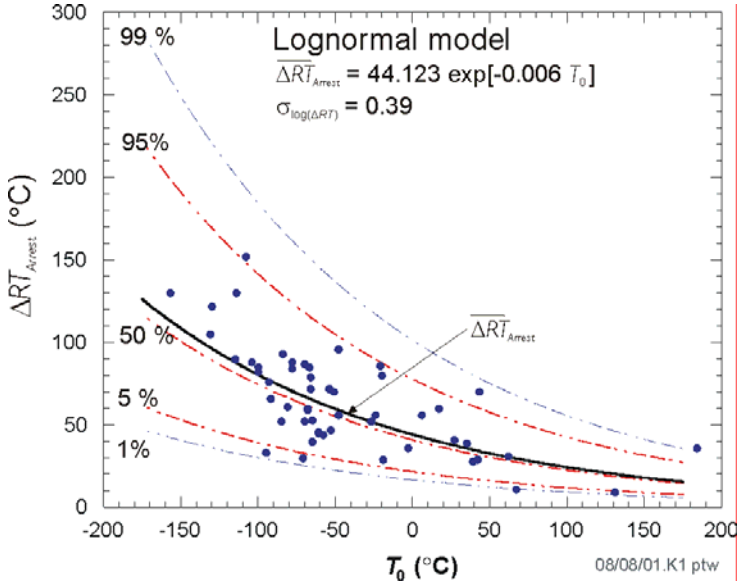


**Fig. 4.23 Lognormal distribution of $\Delta RT_{ARREST} = T_{K_{Ia}} - T_0$ as a function of $T_0$**

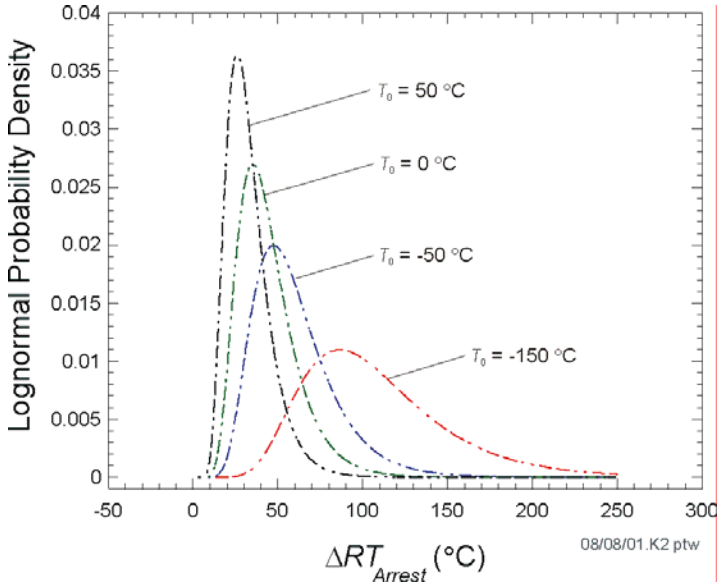


**Fig. 4.24 Lognormal probability densities for $\Delta RT_{Arrest}$ as function of $T_0$.**

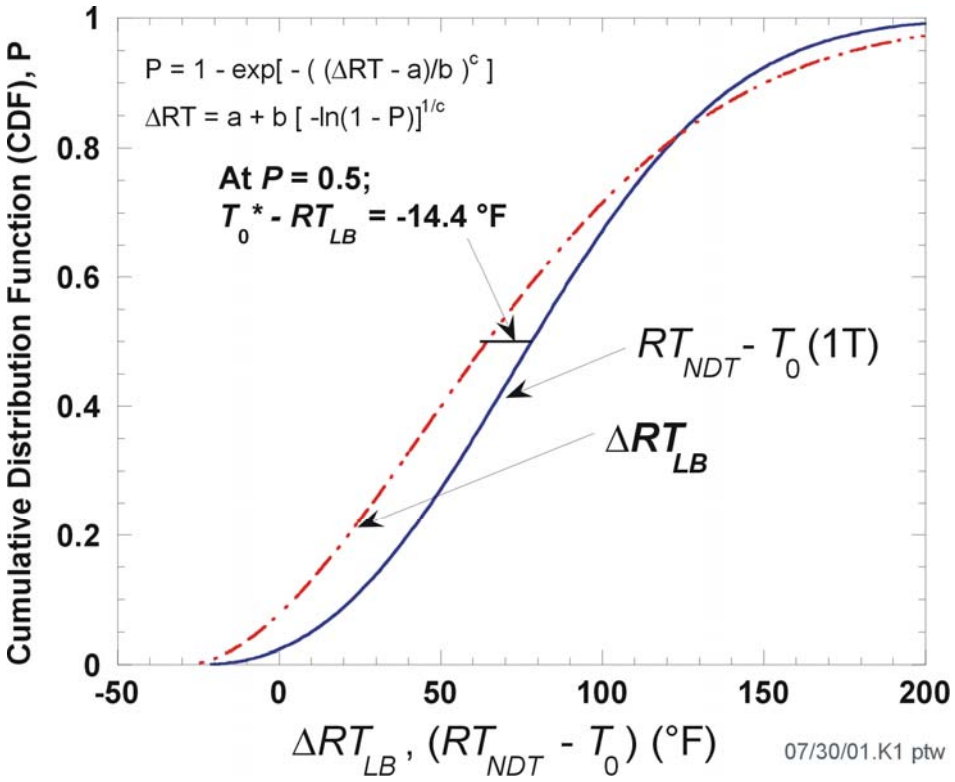


**Fig. 4.25 Proposed adjustment to $RT_{LB}$ arises from observed offset between $\Delta RT_{LB}$ CDF and $RT_{NDT} - T_0$ CDF at median ($P = 0.5$).**

An approximate connection between $T_0$ and the initiation reference temperature $RT_{LB}$ can be established from the observed offset of 14.4 °F between the medians of the $RT_{NDT0}$-$T_0$ CDF and the $\Delta RT_{LB}$ CDF in Fig. 4.25. This observation allows us to apply Eq. (119) to develop a distribution for the epistemic uncertainty in the arrest reference temperature linked to the epistemic uncertainty in the initiation reference temperature.

$$\widehat{\Delta RT}_{epist-arrest} = \widehat{\Delta RT}_{epistemic} - 14.4 \ \ [°F] \tag{120}$$

where $\widehat{\Delta RT}_{epistemic}$ has been sampled from the distribution given by Eq. (116). The sampled arrest reference temperature can now be calculated by

$$\widehat{RT}_{ARREST}(r,\ldots) = \widehat{RT_{NDT0}} - \widehat{\Delta RT}_{epist-arrest} + \widehat{\Delta RT}_{ARREST} + \widehat{\Delta RT_{NDT}}(r,\ldots) \tag{121}$$

where $\widehat{RT_{NDT0}}$, $\widehat{\Delta RT}_{epist-arrest}$, and $\widehat{\Delta RT_{NDT}}(r,\cdots)$ have not been re-sampled from their initiation values and $\widehat{\Delta RT}_{ARREST} \leftarrow \Lambda(\hat{\mu}_{\ln(\Delta RT_{ARREST})}, \hat{\sigma}_{\ln(\Delta RT_{ARREST})})$ is sampled from the following lognormal distribution:

$$\widehat{\mu}_{\ln(\Delta RT_{ARREST})} = \ln\left[\widehat{\Delta RT}_{ARREST(mean)}\right] - \frac{\widehat{\sigma}^2_{\ln(\Delta RT_{ARREST})}}{2}$$

where

$$\widehat{T_0} = \left(\widehat{RT}_{NDT_0} - \widehat{\Delta RT}_{epist-arrest} - 32\right)/1.8 \ \ [°\text{C}]$$

$$\widehat{\Delta RT}_{ARREST(mean)} = 44.122\exp\left[-0.005971 \times \widehat{T_0}\right] \ \ [°\text{C}] \tag{122}$$

$$\widehat{\sigma}_{\ln(\Delta RT_{ARREST})} = \sqrt{\ln\left\{\exp\left[0.38998^2 + 2\ln(\widehat{\Delta RT}_{ARREST(mean)})\right] - \text{var}\left(\widehat{T_0}\right)\right\} - 2\ln\left[\widehat{\Delta RT}_{ARREST(mean)}\right]}$$

where

$$\text{var}(\widehat{T_0}) = \begin{cases} (12.778)^2 & \text{for } \widehat{T_0} < -35.7 \ °\text{C} \\ 99.905972 - 1.7748073\widehat{T_0} & \text{for } -35.7 \ °\text{C} \le \widehat{T_0} \le 56 \ °\text{C} \\ 0 & \text{for } \widehat{T_0} > 56 \ °\text{C} \end{cases}$$

and $\widehat{\Delta RT}_{ARREST}$ is sampled from (see Step 11 in Sect. 4.5)

$$\widehat{\Delta RT}_{ARREST} = 1.8\exp\left[\widehat{\sigma}_{\ln(\Delta RT_{Arrest})}\widehat{Z_{P_f}} + \widehat{\mu}_{\ln(\Delta RT_{Arrest})}\right] \ \ [°\text{F}]$$

$\widehat{Z_{P_f}} \leftarrow N(0,1)$; $\widehat{Z_{P_f}}$ is the standard normal deviate corresponding to the $\widehat{P_f}$ fractile $(0 < \widehat{P_f} < 1)$ for this trial in the crack *Initiation - Growth - Arrest* model.

See Appendix F for the details of the development of Eq. (122).

### 4.2.7 Plane-Strain Static Cleavage Initiation Toughness – $K_{Ic}$

Using the $K_{Ic}$ data in the ORNL 99/27 fracture-toughness database (see Fig. 4.26) and the new lower-bounding reference temperature, $RT_{LB}$, a statistical model based on a Weibull distribution was developed by applying the statistical procedures given in [86]. The cumulative distribution function (CDF) for the Weibull model has the following form:

$$\Pr(K_{Ic} < K_I) = \Phi_{K_{Ic}}(K_I \mid \widehat{a_{K_{Ic}}}, \widehat{b_{K_{Ic}}}) = \begin{cases} 0; & K_I \le a_{K_{Ic}} \\ 1 - \exp\left[-\left(\dfrac{K_I - a_{K_{Ic}}(\widehat{\Delta T}_{RELATIVE})}{b_{K_{Ic}}(\widehat{\Delta T}_{RELATIVE})}\right)^{c_{K_{Ic}}}\right]; & a_{K_{Ic}} < K_I < \infty \end{cases} \tag{123}$$

where the inverse CDF or percentile function is given by

$$K_{Ic}(\widehat{\Delta T}) = \widehat{a_{K_{Ic}}}(\widehat{\Delta T}) + \widehat{b_{K_{Ic}}}(\widehat{\Delta T})\left[-\ln(1-\Phi_{K_{Ic}})\right]^{1/c_{K_{Ic}}} \quad \text{for } 0 < \Phi_{K_{Ic}} < 1$$
$$\text{for } a \le K_{Ic} \le K_{Ic(\max)} \tag{124}$$

where the bounding value of $K_{Ic(\max)}$ is input by the user to FAVOR$^{EP}$ (typically $K_{Ic(\max)} = 200 \ \text{ksi}\sqrt{\text{in.}}$). The parameters of the distribution are

$$a_{K_{Ic}}(\widehat{\Delta T}_{RELATIVE}) = 19.35 + 8.335\exp\left[0.02254(\widehat{\Delta T}_{RELATIVE})\right] \text{ [ksi}\sqrt{\text{in.}}\text{]}$$
$$b_{K_{Ic}}(\widehat{\Delta T}_{RELATIVE}) = 15.61 + 50.132\exp\left[0.008(\widehat{\Delta T}_{RELATIVE})\right] \text{ [ksi}\sqrt{\text{in.}}\text{]} \quad (125)$$
$$c_{K_{Ic}} = 4$$

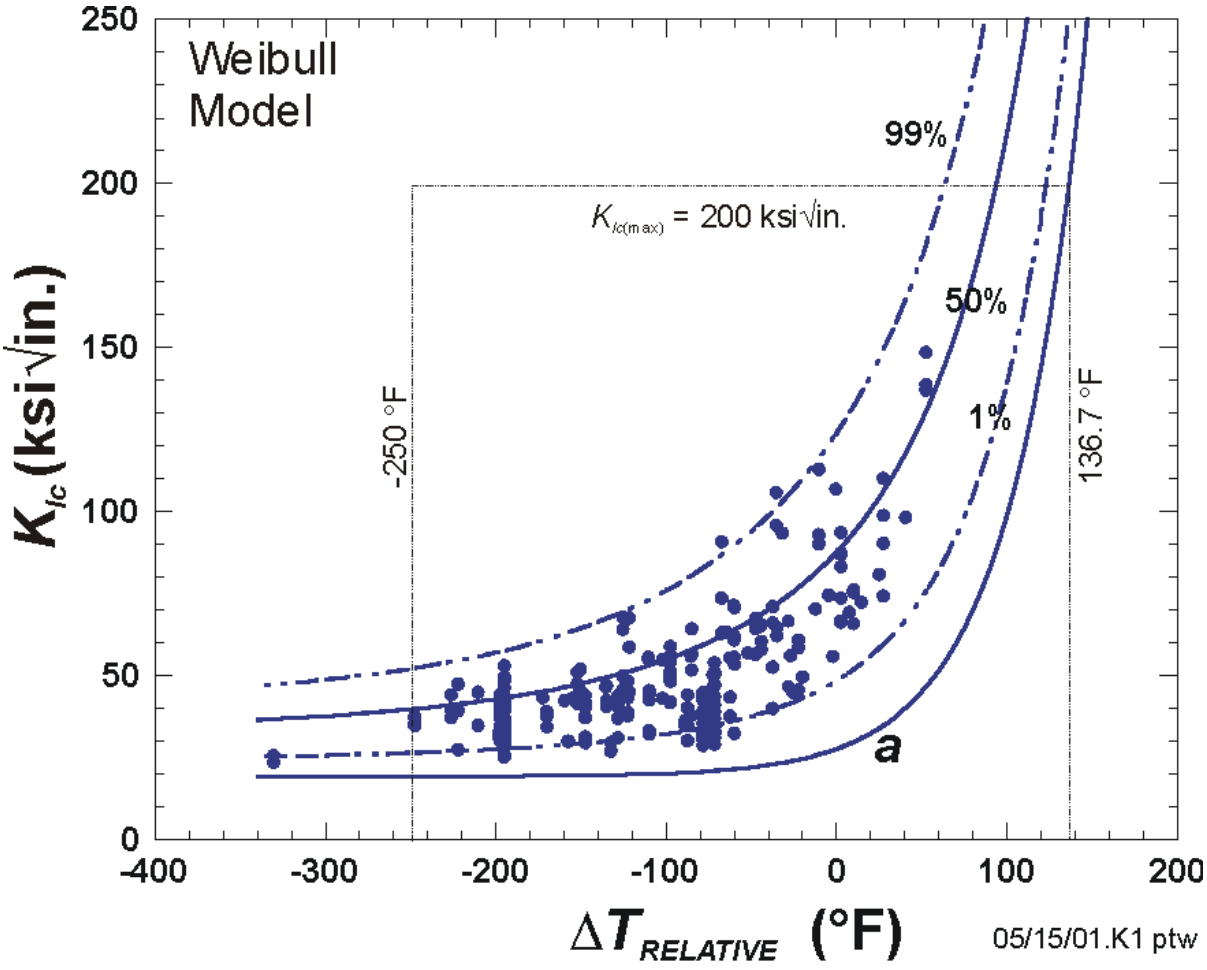


**Fig. 4.26 Weibull statistical distribution for plane-strain cleavage initiation fracture toughness, $K_{Ic}$, with prescribed validity bounds. The ORNL 99/27 $K_{Ic}$ database was used in the construction of the model.**

with $K_{Ic}$ in ksi√in and $\widehat{\Delta T_{RELATIVE}} = T(\tau) - \widehat{RT_{NDT}}(r,\cdots)$ in °F. Note that this Weibull statistical model describes the *aleatory* uncertainty in the plane-strain static initiation fracture toughness, since it is assumed that the *epistemic* uncertainty has been reduced by the sampled $\widehat{\Delta RT}_{epistemic}$ in Eq. (116)

.

### 4.2.8 Plane-Strain Crack Arrest Toughness – $K_{Ia}$

Two lognormal distributions (see Fig. 4.27) are available in FAVOR$^{EP}$ to describe the aleatory uncertainty in the plane-strain crack arrest toughness, $K_{Ia}$. For a lognormal distribution with random variate, $x$, the cumulative distribution function is expressed by

$$\Pr\{X \le x\} = \frac{1}{\sigma x\sqrt{2\pi}} \int_{-\infty}^{\ln(x)} \exp\left[-\left(\frac{(\xi-\mu)^2}{2\sigma^2}\right)\right] \mathrm{d}\xi = \Phi\left(\frac{\ln(x)-\mu}{\sigma}\right) = \frac{1}{\sqrt{2\pi}} \int_{-\infty}^{(\ln(x)-\mu)/\sigma} \exp\left[-\frac{\varsigma^2}{2}\right] \mathrm{d}\varsigma \tag{126}$$

The function $\Phi$ can be evaluated numerically through its relation to the *error function*, erf(x), such that for a given applied stress intensity factor, $K_I$, and normalized temperature, $\Delta T = T\text{-}RT_{Arrest}$,

$$\Pr\{K_{Ia} \le K_I\} = \Phi_{K_{Ia}}\left(\frac{\ln(K_I) - \mu_{\ln(K_{Ia})}(\Delta T)}{\sigma_{\ln(K_{Ia})}}\right) = \frac{1}{2}\left[\mathrm{erf}\left(\frac{\ln(K_I) - \mu_{\ln(K_{Ia})}(\Delta T)}{\sigma_{\ln(K_{Ia})}\sqrt{2}}\right) + 1\right] \tag{127}$$

where $\Phi_{K_{Ia}}$ is now the cumulative probability of crack extension and the error function (a special case of the incomplete gamma function, $P(a,x^2)$) is defined by

$$P\left(0.5, x^2\right) = \mathrm{erf}(x) = \frac{2}{\sqrt{\pi}} \int_0^x \exp(-\xi^2)\, \mathrm{d}\xi \qquad \mathrm{erf}(-x) = -\mathrm{erf}(x) \tag{128}$$

The inverse CDF for the lognormal distribution allows sampling of $K_{Ia}$ by

$$K_{Ia}(\widehat{\Phi}_{K_{Ia}}, \widehat{\Delta T}_{RELATIVE}) = \exp\left[\sigma_{\ln(K_{Ia})} \widehat{Z}_{\Phi K_{Ia}} + \mu_{\ln(K_{Ia})}(\widehat{\Delta T}_{RELATIVE})\right]$$
$$\widehat{Z}_{\Phi_{K_{Ia}}} = \text{standard normal deviate corresponding to the } \widehat{\Phi}_{K_{Ia}} \text{ fractile}$$
$$\widehat{\Phi}_{K_{Ia}} \leftarrow U(0,1) \tag{129}$$

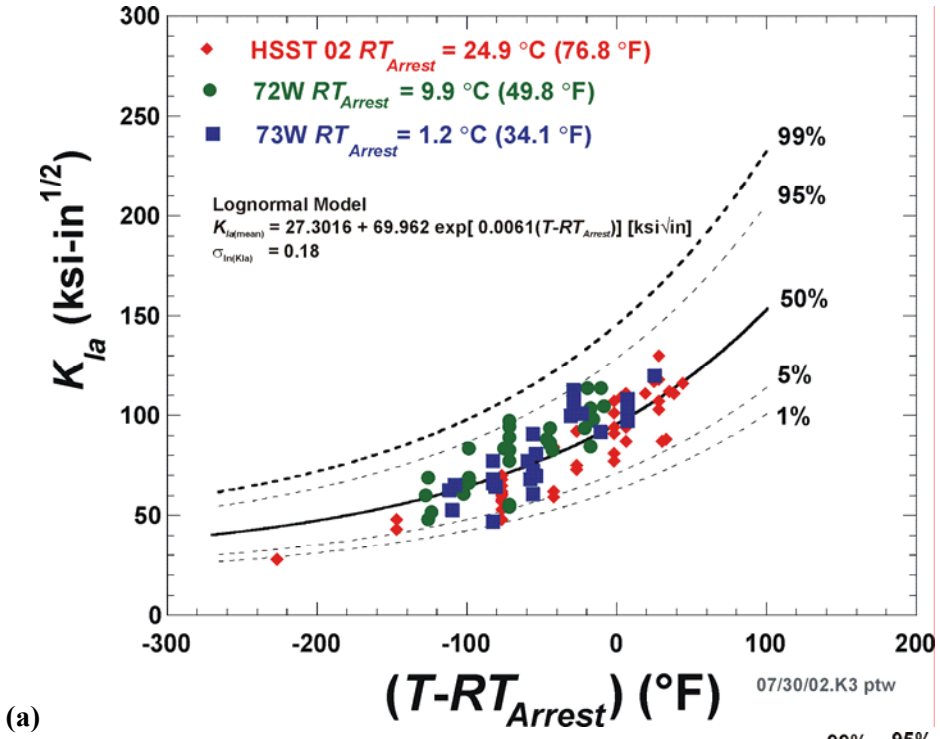


(a)

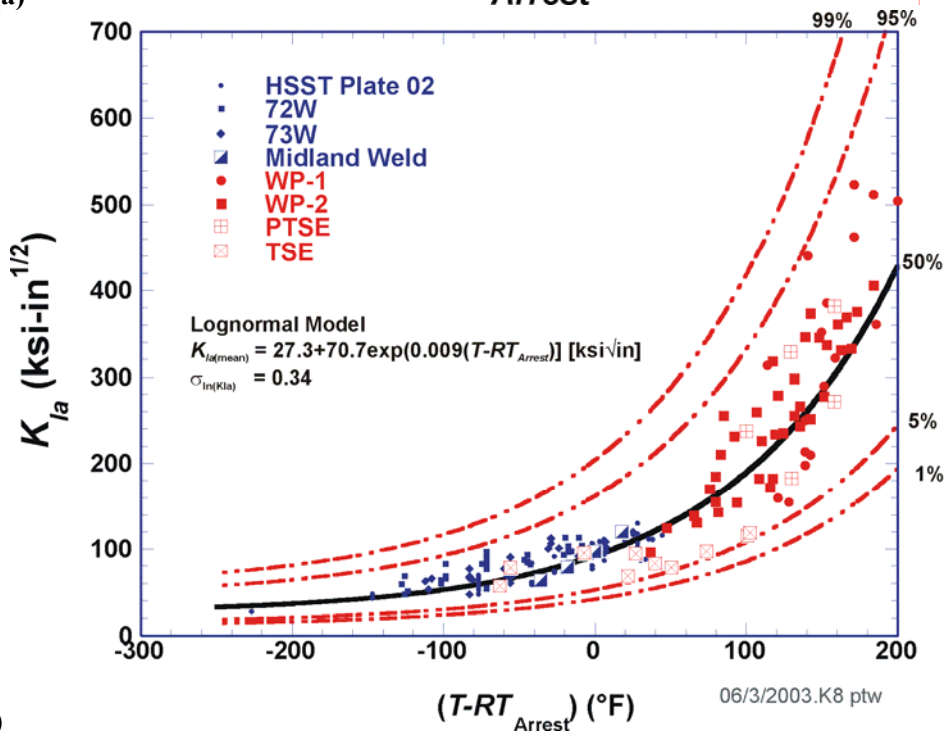


(b)

**Fig. 4.27 Lognormal statistical distribution for plane-strain crack arrest fracture toughness, $K_{Ia}$, constructed using the (a) Model 1: ORNL 99/27 $K_{Ia}$ database normalized by the arrest reference temperature, $RT_{Arrest}$ and (b) Model 2: Extended $K_{Ia}$ database normalized by the arrest reference temperature, $RT_{Arrest}$.**

Model 1 is based on the ORNL 99/27 $K_{Ia}$ database of 112 data points which were taken using CCA specimens. The parameters of the Model 1 $K_{Ia}$ lognormal distribution, shown in Fig. 4.27a, are

$$\mu_{\ln(K_{Ia})}(\widehat{\Delta T}_{RELATIVE}) = \ln\left[\bar{K}_{Ia}(\widehat{\Delta T}_{RELATIVE})\right] - \frac{\sigma^2_{\ln(K_{Ia})}}{2}$$

where

$$\sigma_{\ln(K_{Ia})} = 0.18 \tag{130}$$

$$K_{Ia(\text{mean})}(\widehat{\Delta T}_{RELATIVE}) = 27.302 + 69.962\exp\left[0.006057(\widehat{\Delta T}_{RELATIVE})\right] \ [\text{ksi}\sqrt{\text{in.}}]$$

$$\widehat{\Delta T}_{RELATIVE} = T(r,\tau) - \widehat{RT_{Arrest}}(r,\cdots) \ [°\text{F}]$$

The equation for the mean was developed by nonlinear regression of the data shown in Fig. 4.27a. Model 1 is recommended to be used when the ductile-tearing model is not activated, and an upper bound for $K_{Ia}$ of 200 $\text{ksi}\sqrt{\text{in.}}$ should be set in the FAVPFM$^{\mathbf{EP}}$ input file.

Model 2 is based on the Extended $K_{Ia}$ database of 183 data points which were taken using both CCA specimens and Large-Specimen experiments. The parameters of the Model 2 $K_{Ia}$ lognormal distribution, shown in Fig. 4.27b, are

$$\mu_{\ln(K_{Ia})}(\widehat{\Delta T}_{RELATIVE}) = \ln\left[\bar{K}_{Ia}(\widehat{\Delta T}_{RELATIVE})\right] - \frac{\sigma^2_{\ln(K_{Ia})}}{2}$$

where

$$\sigma_{\ln(K_{Ia})} = 0.34 \tag{131}$$

$$K_{Ia(\text{mean})}(\widehat{\Delta T}_{RELATIVE}) = 27.302 + 70.6998\exp\left[0.008991(\widehat{\Delta T}_{RELATIVE})\right] \ [\text{ksi}\sqrt{\text{in.}}]$$

$$\widehat{\Delta T}_{RELATIVE} = T(r,\tau) - \widehat{RT_{Arrest}}(r,\cdots) \ [°\text{F}]$$

Model 2 will be automatically selected when the ductile-tearing model is activated, and any specified upper bound on $K_{Ia}$ is ignored.

### 4.2.9 Material Chemistry –Sampling Protocols

The sampling protocol used by FAVOR$^{EP}$, v05.1, requires estimated chemistry (Cu, Ni, and P) content values for each weld and plate subregion used to model the beltline shells of the vessel. The user will, therefore, input best-heat estimates designated as $HE_{Cu}$, $HE_{Ni}$, and $HE_P$ in wt%.

FAVOR$^{EP}$ treats the vessel beltline as a collection of major regions of plates, forgings, and welds. These major regions are then discretized into subregions, where within a given subregion flaws are analyzed through Monte Carlo *realizations* of the RPV subjected to the PTS transients under study. The sampling protocols for plate and weld chemistry distinguish between the first flaw simulated in a subregion, designated as *Flaw*1, and all subsequent flaws in the subregion, designated as *Flawx*. The plate or weld chemistry for the set of *Flawx's* will be perturbations of the sampled *Flaw*1 chemistry for this subregion. This variation in chemistry is intended to simulate *local variability* in the subregion chemistry.

**Plate Subregion Chemistry**

**Flaw1**

The Cu, Ni, and P content (expressed in wt%) for the first flaw in a subregion are sampled from the following normal distributions:

$$\begin{aligned} \widehat{Cu}_{Flaw1} &\leftarrow N(HE_{Cu}, \sigma_{Cu}) \\ \widehat{Ni}_{Flaw1} &\leftarrow N(HE_{Ni}, \sigma_{Ni}) \\ \widehat{P}_{Flaw1} &\leftarrow N(HE_P, \sigma_P) \end{aligned} \tag{132}$$

where the recommended constant standard deviations are

$$\begin{aligned} \sigma_{Cu} &= 0.0073 \text{ wt\%} \\ \sigma_{Ni} &= 0.0244 \text{ wt\%} \\ \sigma_P &= 0.0013 \text{ wt\%} \end{aligned} \tag{133}$$

The triplet $(\sigma_{Cu}, \sigma_{Ni}, \sigma_P)$ is supplied by the user in the input file for the FAVPFM$^{\mathbf{EP}}$ module. Negative values of sampled $\widehat{Cu}_{Flaw1}$, $\widehat{Ni}_{Flaw1}$, and $\widehat{P}_{Flaw1}$ are handled as nonphysical exceptions in FAVOR$^{EP}$ using the truncation protocol described in Sect. 3.3.8, with 0.0 applied as a one-sided truncation boundary.

**Flawx – local variability**

All subsequent flaws in a given subregion should contain small local variability in Cu, Ni, and P content. This local variability is determined by sampling values from the following logistic distributions:

$$\begin{aligned}
\widehat{Cu}_{Flawx} &\leftarrow Cu_{Flaw1} + L(-3.89\times10^{-7}, 0.00191)\\
\widehat{Ni}_{Flawx} &\leftarrow Ni_{Flaw1} + L(-1.39\times10^{-7}, 0.00678)\\
\widehat{P}_{Flawx} &\leftarrow P_{Flaw1} + L(1.30\times10^{-5}, 0.000286)
\end{aligned} \tag{134}$$

$$\begin{aligned}
\widehat{\Delta_{Cu-Flawx}} &= -3.89\times10^{-7} - 0.00191\ln\left[\frac{1}{\Phi_{Cu}} - 1\right] \text{ for } \Phi_{Cu} \leftarrow U(0,1)\\
Cu_{Flawx} &= Cu_{Flaw1} + \widehat{\Delta_{Cu-Flawx}}\\
\widehat{\Delta_{Ni-Flawx}} &= -1.39\times10^{-7} - 0.00678\ln\left[\frac{1}{\Phi_{Ni}} - 1\right] \text{ for } \Phi_{Ni} \leftarrow U(0,1)\\
Ni_{Flawx} &= Ni_{Flaw1} + \widehat{\Delta_{Ni-Flawx}}\\
\widehat{\Delta_{P-Flawx}} &= 1.3\times10^{-5} - 0.000286\ln\left[\frac{1}{\Phi_{P}} - 1\right] \text{ for } \Phi_{P} \leftarrow U(0,1)\\
P_{Flawx} &= P_{Flaw1} + \widehat{\Delta_{P-Flawx}}
\end{aligned} \tag{135}$$

Negative values of sampled $\widehat{Cu}_{Flawx}$, $\widehat{Ni}_{Flawx}$, and $\widehat{P}_{Flawx}$ are handled as nonphysical exceptions in FAVOR$^{EP}$ using the truncation protocol described in Sect. 3.3.8, with 0.0 applied as a one-sided truncation boundary.

**Through-thickness sampling for Plates**

There is no resampling protocol for flaws growing through the thickness of plate subregions.

## Weld Subregion Chemistry

**Flaw1**

**Copper,** $Cu_{Flaw1}$:

The Cu content for the first flaw in a weld subregion is sampled from a normal distribution with mean equal to the heat estimate for Cu and a sampled standard deviation:

$$\begin{aligned}
\widehat{Cu}_{Flaw1} &\leftarrow N(HE_{Cu}, \widehat{\sigma_{Cu}})\\
\widehat{\sigma_{Cu}} &\leftarrow N\left(0.167\times HE_{Cu},\ \min\left(0.0718\times HE_{Cu}, 0.0185\right)\right)
\end{aligned} \tag{136}$$

**Nickel,** $Ni_{Flaw1}$:

Ni-addition welds (heats 34B009 and W5214)

The Ni content for the first flaw in a weld subregion is sampled from a normal distribution with mean equal to the heat estimate for Ni and standard deviation equal to 0.162.

$$\widehat{Ni}_{Flaw1} \leftarrow N(HE_{Ni}, 0.162) \tag{137}$$

All other heats

The Ni content for the first flaw in a weld subregion is sampled from a normal distribution with mean equal to the heat estimate for Ni and standard deviation sampled from a normal distribution with mean equal to 0.029 wt% and standard deviation equal to 0.0165 wt%.

$$\begin{aligned} \widehat{Ni}_{Flaw1} &\leftarrow N(HE_{Ni}, \widehat{\sigma}_{Ni_{Flaw1}}) \\ \widehat{\sigma}_{Ni_{Flaw1}} &\leftarrow N(0.029, 0.0165) \end{aligned} \tag{138}$$

**Phosphorous,** $P_{Flaw1}$:

The phosphorous content for the first flaw in a weld subregion is sampled from a normal distribution with mean equal to the heat estimate for phosphorous and standard deviation equal to 0.0013.

$$\widehat{P}_{Flaw1} \leftarrow N(HE_P, 0.0013) \tag{139}$$

Negative values of sampled $\widehat{Cu}_{Flaw1}$, $\widehat{Ni}_{Flaw1}$, and $\widehat{P}_{Flaw1}$ are handled as nonphysical exceptions in FAVOR$^{EP}$ using the truncation protocol described in Sect. 3.3.8, with 0.0 applied as a one-sided truncation boundary.

## Flawx – local variability

All subsequent flaws in a given weld subregion should contain small local variability in Cu, Ni, and P content.

**Copper,** $Cu_{Flawx}$:

The local variability for Cu is determined by sampling a $\Delta_{Cu}$ value drawn from a logistic distribution with parameters $\alpha = 6.85 \times 10^{-8}$ and $\beta = 0.0072$ such that

$$\begin{aligned} \widehat{\Delta_{Cu-Flawx}} &\leftarrow L(6.85 \times 10^{-8}, 0.0072) \\ \widehat{\Delta_{Cu-Flawx}} &= 6.85 \times 10^{-8} - 0.0072 \ln\left[\frac{1}{\Phi_{Cu}} - 1\right] \text{ for } \Phi_{Cu} \leftarrow U(0,1) \\ \widehat{Cu_{Flawx}} &= Cu_{Flaw1} + \widehat{\Delta_{Cu-Flawx}} \end{aligned} \tag{140}$$

**Nickel,** $Ni_{Flawx}$:

The local variability for Ni is determined by sampling a $\Delta_{Ni}$ value drawn from a logistic distribution with parameters $\alpha = -0.0014$ and $\beta = 0.00647$ such that

$$\begin{aligned}
&\hat{\Delta}_{Ni-Flawx} \leftarrow L(-0.0014, 0.00647) \\
&\hat{\Delta}_{Ni-Flawx} = -0.0014 - 0.00647 \ln\left[\frac{1}{\Phi_{Ni}} - 1\right] \text{ for } \Phi_{Ni} \leftarrow U(0,1) \\
&\widehat{Ni_{Flawx}} = Ni_{Flaw1} + \hat{\Delta}_{Ni-Flawx}
\end{aligned} \tag{141}$$

The same local variability samplings are applied to Ni-addition and non-Ni-addition welds.

**Phosphorous,** $P_{Flawx}$:

The local variability for phosphorous is determined by sampling a $\Delta_P$ value drawn from a logistic distribution with parameters $\alpha = 3.27 \times 10^{-6}$ and $\beta = 0.000449$.

$$\begin{aligned}
&\hat{\Delta}_{P-Flawx} \leftarrow L(3.27 \times 10^{-6}, 0.000449) \\
&\hat{\Delta}_{P-Flawx} = 3.27 \times 10^{-6} - 0.000449 \ln\left[\frac{1}{\Phi_P} - 1\right] \text{ for } \Phi_P \leftarrow U(0,1) \\
&\widehat{P_{Flawx}} = P_{Flaw1} + \hat{\Delta}_{Ni-Flawx}
\end{aligned} \tag{142}$$

Negative values of sampled $\widehat{Cu}_{Flawx}$, $\widehat{Ni}_{Flawx}$, and $\hat{P}_{Flawx}$ are handled as nonphysical exceptions in FAVOR$^{EP}$ using the truncation protocol described in Sect. 3.3.8, with 0.0 applied as a one-sided truncation boundary.

## Through-thickness re-sampling for Weld Layers

Due to their thickness, RPV welds were typically constructed using multiple coils of weld wire. The variability in chemistry from one coil or weld layer to another is resampled in FAVOR$^{EP}$ as a given crack grows through the wall and enters a new weld layer. The weld-layer thickness in which this variability is imposed is every 1/4T of the RPV. In general, when a flaw has initiated, the weld chemistry content is not resampled for each growth increment. However, if the inner crack tip of the flaw has moved from one 1/4T of the vessel wall thickness to an adjoining 1/4T region, then the chemistry of the weld is sampled as if the flaw had advanced into a new material.

## Additional Comments on Chemistry Sampling in Plate and Weld Subregions

When a sampled chemistry value for the first flaw in a subregion (*for the current RPV trial*) is truncated internally by FAVPFM$^{\mathbf{EP}}$, the non-truncated chemistry value for *Flaw1* continues to be used as the basis for subsequent *local variability* perturbation samplings. As an example, for a given RPV trial and first flaw in a given subregion, the sampled value of $Cu_{Flaw1}$ might be truncated back to 0.25 for Linde welds or to 0.305 for all other welds, plates, and forgings, when applying the Eason and Wright correlation [98] to calculate $\Delta RT_{NDT.}$ However, FAVPFM$^{\mathbf{EP}}$ will utilize the non-truncated value for $Cu_{Flaw1}$ in the determination of the local variability copper content, $\widehat{Cu}_{Flawx}$ , for all subsequent flaws located in this subregion for the current RPV trial. The rationale for this procedure is that the local variability random perturbation sampled for copper, $\hat{\Delta}_{Cu-Flawx}$, as determined from its logistic distribution, could possibly be sufficiently negative such that the perturbed value of $\widehat{Cu}_{Flawx}$ might take on a value below the truncation upper bound. However, if the value of $\widehat{Cu}_{Flawx}$ should exceed the upper truncation boundary, then FAVPFM$^{\mathbf{EP}}$ will automatically truncate back to the appropriate upper bound.

## 4.3 NRC RVID2 Database

The *Reactor Vessel Integrity Database*, RVID [155] , developed following the NRC staff review of licensee responses to Generic Letter (GL) 92-01, Revision 1, provides a key source of input data for FAVOR$^{EP}$. The most recent update of the database, RVID2 [156], was released in July of 2000. The RIVD2 summarizes the properties of the reactor vessel beltline materials for each operating commercial nuclear power plant. The RVID includes four tables for each plant: (1) background information table, (2) chemistry data table, (3) upper-shelf energy table, and (4) pressure-temperature limits or pressurized thermal shock table. References and notes follow each table to document the source(s) of data and to provide supplemental information. Appendix D presents a selection of RVID2 data relevant to FAVOR$^{EP}$ for the four power plants included in the PTS Re-evaluation Project. As of this writing, they are: (1) Beaver Valley 1, (2) Calvert Cliffs 1, (3) Oconee 1, and (4) Pallisades 1.

## 4.4 Discrete Flaw Density and Size Distributions

The method used to quantify the uncertainty in the flaw characterization is to include 1000 flaw-characterization records in each of the three data files: (1) inner surface-breaking flaws (2) embedded flaws in weld material, and (3) embedded flaws in plate material. The flaw-characterization file for inner surface- breaking flaws is applicable to weld and plate material. Each of these records contains separate discrete flaw-density and flaw-size distributions.

During the Monte Carlo PFM analysis, the RPV flaw-characterization data for the first stochastically generated RPV trial are taken from the first group of records, i.e., the first inner surface-breaking record, the first embedded-flaw weld material record, and the first embedded-flaw plate material record. The RPV flaw characterization for the second stochastically generated RPV trial is determined from the second group of records, etc. The RPV trials cycle through the flaw-characterization records sequentially up to 1000, and then restart at the first record.

Inner surface-breaking flaw density data are expressed in flaws per unit RPV-inner-surface area and weld subregion embedded flaws are flaws per unit area on the fusion line between the weld and adjacent plate subregions. These conventions are consistent with the physical model utilized by Pacific Northwest National Laboratory to derive the flaw characterization data input to FAVOR$^{EP}$. Embedded flaws in plate regions are expressed on a volumetric basis.

Figures 4.28a and 4.28b illustrate axial and circumferential weld subregion elements, respectively. The number of flaws in each of these weld elements is calculated (internally by FAVOR$^{EP}$) as the sum of the number of inner- surface breaking flaws and the number of embedded flaws as follows:

$$\begin{pmatrix}\text{Number of Flaws}\\ \text{in Weld Subregions}\end{pmatrix} = \rho_{SB}\left[\left(\frac{2\pi}{360}\right)R_i\ dz\ d\theta\right] + \rho_{EW}\left[2\left(\frac{3}{8}\right)dA\right]$$

$\rho_{SB}$ = inner surface-breaking flaw density (per unit surface area - flaws/in$^2$)
$\rho_{EW}$ = weld embedded-flaw density (per unit weld-fusion area - flaws/in$^2$)
$dA$ = user-input weld-fusion area (for one side of weld) (in$^2$ - input by user) (143)
$R_i$ = internal radius of RPV (in. - input by user)
$dz$ = height of subregion element (in. - input by user)
$d\theta$ = subtended angle of subregion element ( degrees - input by user)

where $\rho_{SB}$ and $\rho_{EW}$ are summed over all flaw depths.

For axial welds, the fusion lines are on the sides of the weld, whereas for circumferential welds, the fusion lines are on the top and bottom of the welds. In the term {2 (3/8) $dA$ }, the factor of 2 accounts for the fact that the user input data is the area on one side of the fusion line whereas flaws reside in fusion lines on both sides of the welds. The (3/8) accounts for the fact that embedded flaws that reside beyond the first 3/8 of the base metal are not included in a PTS analysis. All flaw densities are assumed to be uniform through the RPV wall thickness.

Figure 4.28c illustrates a plate subregion element. The number of flaws in each of these plate elements is calculated (internally by FAVOR$^{EP}$) as the sum of the number of inner surface-breaking flaws and the number of embedded flaws as follows:

$$\begin{pmatrix}\text{Number of Flaws}\\ \text{in Plate Subregions}\end{pmatrix} = \rho_{SB}\left[\left(\frac{2\pi}{360}\right)R_i\ dz\ d\theta\right] + \rho_{EP}\left[\left(\frac{3}{8}\right)\pi\left(R_o^2 - \left(R_i - CLTH\right)^2\right)dz\left(\frac{d\theta}{360}\right)\right]$$

$\rho_{SB}$ = inner surface-breaking flaw density (per unit surface area - flaws/in$^2$)
$\rho_{EP}$ = plate embedded-flaw density summed over all flaw depths (flaws per unit volume - flaws/in$^3$)
$R_o$ = external radius of RPV (in - input by user) (144)
$R_i$ = internal radius of RPV (in. - input by user)
$CLTH$ = cladding thickness (in. - input by user)
$dz$ = height of subregion element (in. - input by user)
$d\theta$ = subtended angle of subregion element ( degrees - input by user)

where $\rho_{SB}$ and $\rho_{EP}$ are summed over all flaw depths.

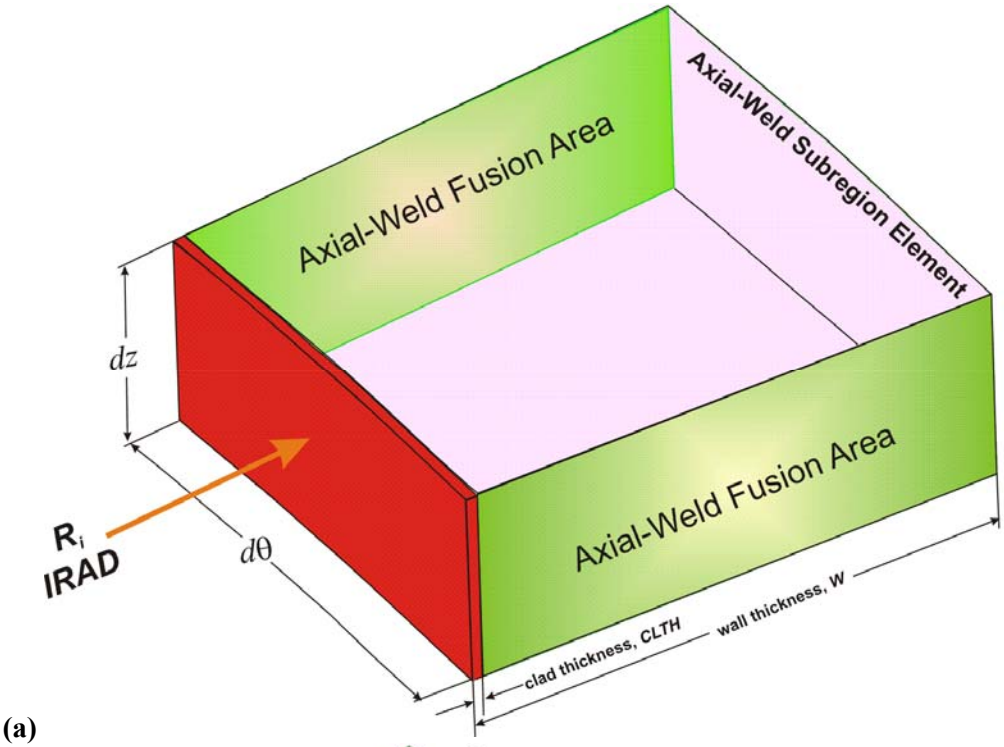


(a)

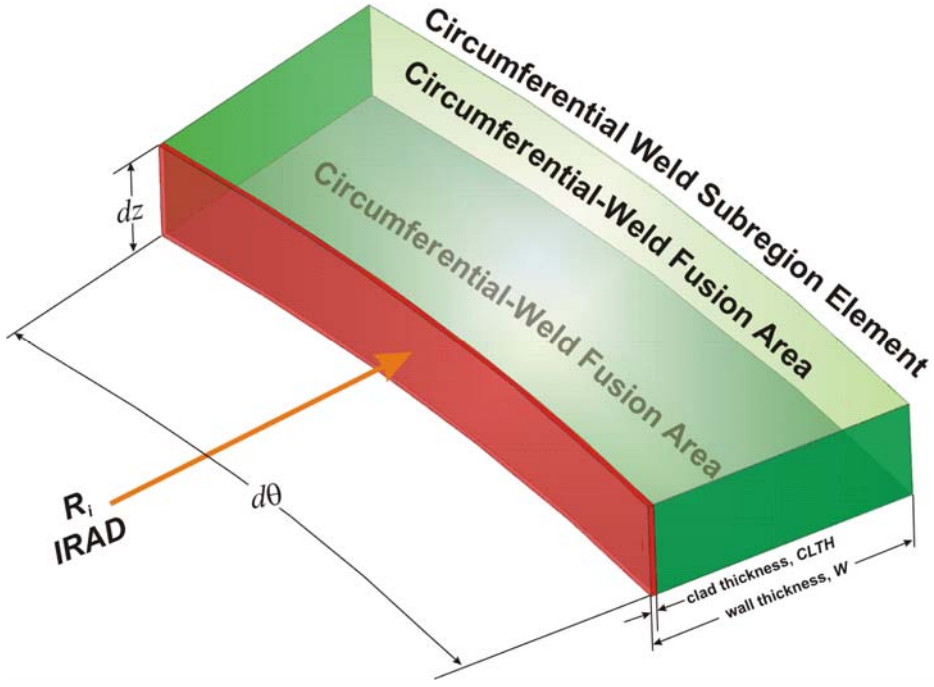


(b)

**Fig. 4.28 Weld fusion area definitions for (a) axial-weld subregion elements and (b) circumferential subregion elements.**

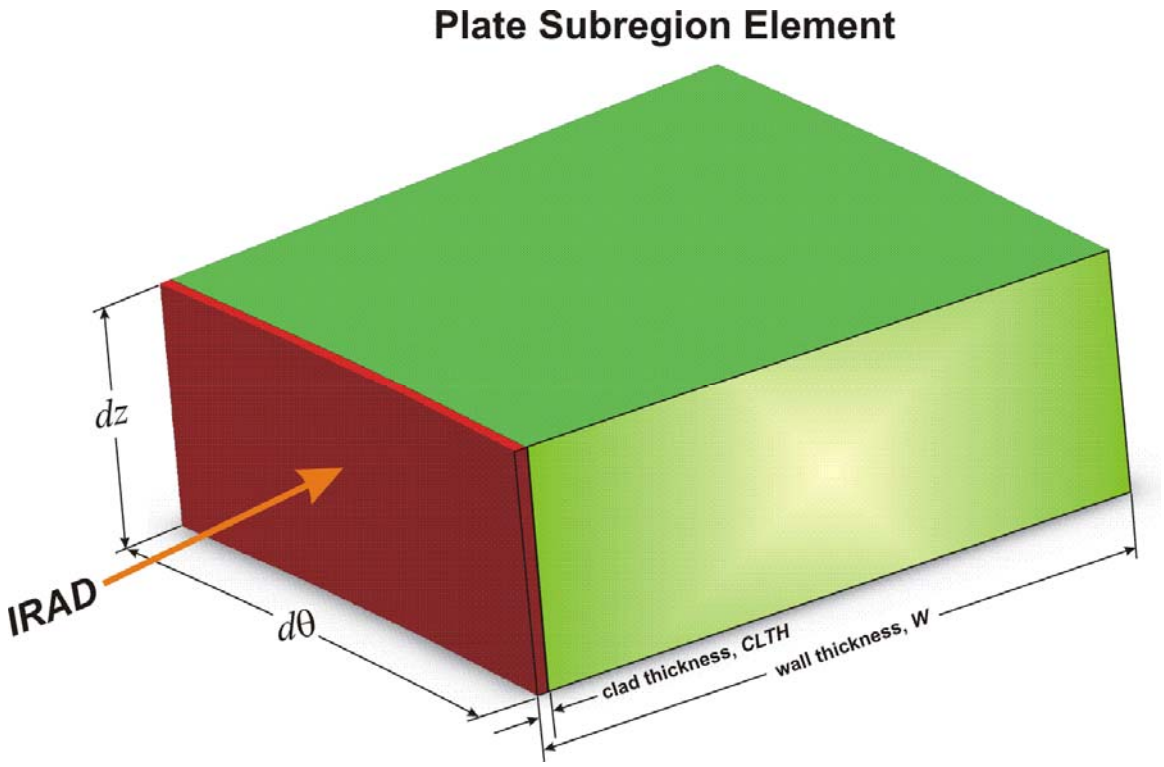


**Fig. 4.28 (continued) (c) Plate subregion element.**

## 4.5 Summary of Sampling Distributions and Protocols

**Plane-Strain Static Initiation**

The following sampling distribution and protocols have been implemented in the FAVOR$^{EP}$ code (FAVPFM$^{EP}$) to represent (for a given flaw at a given time in the specific PTS transient under study) the epistemic and aleatory uncertainties in the plane-strain static initiation fracture-toughness values used in determining the probability of cleavage initiation:

Step 1. For plate, forging, and weld product forms, provide the following input to FAVOR$^{EP}$:

Provide best estimates for the mean and standard deviation for normal distributions of copper, nickel, and phosphorous content, $N(\overline{Cu},\sigma_{Cu}), N(\overline{Ni},\sigma_{Ni}), N(\overline{P},\sigma_{P})$.[9]

Provide a best estimate for the mean and standard deviation for a normal distribution of fluence at the inside surface of the vessel, $N(\overline{f_0}(0),\sigma_{f_0(0)})$.

Provide a best estimate for the standard deviations, $\sigma_{RT_{NDT0}}$, of unirradiated $RT_{NDT0}$ and $\sigma_{\Delta RT_{NDT}}$ of the irradiation shift model $\Delta RT_{NDT}$. The value of $\sigma_{\Delta RT_{NDT}}$ is used only to calculate the regulatory value of $RT_{PTS}$ for reporting purposes.

Provide the coolant temperature, $T_c$ in °F, and RPV exposure time in EFPY, where $T_c$ is the temperature of the coolant on the inner surface of the RPV beltline region (adjacent to the active core) at the time the transient originates (at time = 0).

Determine the current regulatory estimate of the mean value of the unirradiated $RT_{NDT}$ from the Reactor Vessel Integrity Database (RVID2) [156] for the material of interest (see Appendix D).

a) If this $RT_{NDT}$ value was determined using either the ASME NB-2331 or MTEB 5-2 methods, designate the value of $RT_{NDT(RVID)}$ from RVID as $RT_{RTND0}$ and proceed directly to Step 2.

b) If this $RT_{NDT}$ value was determined using the *Generic* method, assign $\overline{RT}_{NDT0}$ as –8 °F for welds and 0 °F for plates and forgings; sample $\widehat{RT_{NDT0}} \leftarrow N(\overline{RT}_{NDT0},\sigma_{RT_{NDT0}})$; then proceed to Step 2.

[9] Note that negative values of $\widehat{Cu}, \widehat{Ni}$, and $\widehat{P}$ sampled from normal distributions are handled as nonphysical exceptions in FAVOR using the truncation protocol described in Sect. 3.3.8 with 0.0 as the truncation boundary.

Step 2. Generate a random number, $\widehat{\Phi}$, between 0 and 1 from a uniform distribution. Use this random number to sample[10] a value of $\widehat{\Delta RT}_{epistemic}$ from the following Weibull percentile function (inverse CDF):

$$\begin{aligned} &\widehat{\Delta RT}_{epistemic} \leftarrow W(-45.586, 131.27, 2.177) \\ &\widehat{\Delta RT}_{epistemic} = -45.586 + 131.27\left[-\ln\left(1-\widehat{\Phi}\right)\right]^{1/2.177} \quad [°\text{F}] \end{aligned} \tag{145}$$

$\widehat{\Delta RT}_{epistemic}$ represents the epistemic uncertainty in $RT_{NDT_0}$.

Step 3. Sample the irradiation shift, $\widehat{\Delta RT}_{NDT}$, using the Eason and Wright [98] embrittlement correlation from sampled values (sampled for each flaw) of neutron fluence, $\widehat{f}_0(r)$; copper content, $\widehat{Cu} \leftarrow N(\overline{Cu}, \sigma_{Cu})$; nickel content, $\widehat{Ni} \leftarrow N(\overline{Ni}, \sigma_{Ni})$; phosphorous content, $\widehat{P} \leftarrow N(\overline{P}, \sigma_P)$; and product form.

$$\widehat{\Delta RT}_{NDT}(r,\ldots) = \begin{cases} 0.99\widehat{\Delta T_{30}}(r,\ldots) & \text{weld} \\ 1.10\widehat{\Delta T_{30}}(r,\ldots) & \text{plate and forgings} \end{cases} \tag{146}$$

where

$$\Delta T_{30}(\widehat{Ni}, \widehat{Cu}, \widehat{P}, \widehat{f}_0(r), \tau_{\text{exposure}}, T_c, \text{product form}) =$$

$$A\exp\left(\frac{19310}{T_c + 460}\right)\left(1 + 110\widehat{P}\right)\left(\widehat{f}_0(r)\right)^{0.4601} + B\left(1 + 2.40\widehat{Ni}^{1.250}\right) f(\widehat{Cu}) g\left(\widehat{f}_0(r)\right) + Bias$$

$$A = \begin{Bmatrix} 8.86\times10^{-17} & \text{for welds} \\ 9.30\times10^{-17} & \text{for forgings} \\ 12.7\times10^{-17} & \text{for plates} \end{Bmatrix}$$

$$B = \begin{Bmatrix} 230 & \text{for welds} \\ 132 & \text{for forgings} \\ 206 & \text{for plates in CE vessels} \\ 156 & \text{for other plates} \end{Bmatrix}$$

$$g(\widehat{f}_0(r)) = \frac{1}{2} + \frac{1}{2}\tanh\left[\frac{\log_{10}\left(\widehat{f}_0(r) + 4.579\times10^{12}\tau_{\text{exposure}}\right) - 18.265}{0.713}\right]$$

$$f\left(\widehat{Cu}\right) = \begin{Bmatrix} 0 & \text{for } \widehat{Cu} \le 0.072 \text{ wt \%} \\ \left(\widehat{Cu} - 0.072\right)^{0.659} & \text{for } \widehat{Cu} > 0.072 \text{ wt \%} \end{Bmatrix}$$

[10] A curved overbar, $\widehat{X}$, indicates a sampled random variate. A braced overbar, $\overbrace{X}$, indicates that sampling has occurred in a prior step but not in the current step.

subject to

$$Cu_{\max} = \left\{ \begin{array}{l} 0.25 \text{ for welds with Linde 80 or Linde 0091 flux} \\ 0.305 \text{ for everything else} \end{array} \right\}$$

and

$$Bias = \left\{ \begin{array}{l} 0 \text{ for } t_{\text{exposure}} < 97000 \text{ h} \\ 9.4 \text{ for } t_{\text{exposure}} \geq 97000 \text{ h} \end{array} \right\}$$

where $\widehat{Cu}$ is the sampled copper content in wt%, $\widehat{Ni}$ is the sampled nickel content in wt%, $\widehat{P}$ is the sampled phosphorous content in wt%, $\hat{f}_0(r)$ is the sampled and then attenuated neutron fluence in n/cm$^2$, $r$ is the position from the inner surface of RPV wall, $\tau_{exposure}$ is exposure time in hours (input to FAVOR$^{EP}$ in EFPY), and $T_c$ is coolant temperature in °F. The fast-neutron fluence at the inner surface of the vessel is sampled using the protocol described in Sect. 4.2.3. The sampled neutron fluence for the flaw is then attenuated (but not resampled) as the crack grows through the wall to produce $\widehat{f_0}(r)$.

Step 4. Calculate the sampled, irradiated value of $RT_{NDT}$ from

$$\widehat{RT}_{NDT}(r,\ldots) = \widehat{RT}_{NDT0} - \widehat{\Delta RT}_{epistemic} + \widehat{\Delta RT}_{NDT}(r,\ldots) \tag{147}$$

where $\widehat{RT}_{NDT0} = \left\{ \begin{array}{l} \widehat{RT}_{NDT0} \leftarrow N(\overline{RT}_{NDT0}, \sigma_{RT_{NDT0}}) \text{ if RVID2 method is } \textit{Generic} \\ \text{Heat Estimate of } \widehat{RT}_{NDT0} \text{ if RVID2 method is NB-2331 or MTEB 5-2} \end{array} \right.$

Step 5. Calculate the normalized temperature of the vessel at the current location, $r$, of the crack tip in the RPV wall as

$$\widehat{\Delta T}_{RELATIVE}(r,\ldots) = T(r,\tau) - \widehat{RT}_{NDT}(r,\ldots) \tag{148}$$

Step 6. Calculate the parameters of the Weibull distribution of the $K_{Ic}$ Weibull statistical distribution by

$$\begin{aligned} a_{K_{Ic}}(\widehat{\Delta T}_{RELATIVE}) &= 19.35 + 8.335\exp\left[0.02254(\widehat{\Delta T}_{RELATIVE})\right] \text{ [ksi}\sqrt{\text{in.}}\text{]} \\ b_{K_{Ic}}(\widehat{\Delta T}_{RELATIVE}) &= 15.61 + 50.132\exp\left[0.008(\widehat{\Delta T}_{RELATIVE})\right] \text{ [ksi}\sqrt{\text{in.}}\text{]} \\ c_{K_{Ic}} &= 4 \end{aligned} \tag{149}$$

with $K_{Ic}$ in ksi$\sqrt{}$in and $\Delta T = (T\text{-}RT_{NDT})$ in °F.

Note that this Weibull statistical model describes the *aleatory* uncertainty in plane-strain static initiation.

Step 7. For a given applied $K_I$, calculate the instantaneous conditional probability of crack initiation, $\Pr\{K_{Ic} \le K_I\}$ with *aleatory* uncertainty, from the following Weibull distribution

$$\Pr(K_{Ic} < K_I) = \widehat{cpi} = \begin{cases} 0; & K_I \le a_{K_{Ic}} \\ 1 - \exp\left[ -\left( \dfrac{K_I - a_{K_{Ic}}(\widehat{\Delta T}_{RELATIVE})}{b_{K_{Ic}}(\widehat{\Delta T}_{RELATIVE})} \right)^{c_{K_{Ic}}} \right]; & K_I > a_{K_{Ic}} \end{cases} \quad (150)$$

If the flaw is determined to be in a warm-prestressing state (and the WPS option has been turned on by the user), then the conditional probability of initiation is set to zero. See Sect. 3.3.4 for a complete discussion of warm prestressing.

**Plane-Strain Static Crack Arrest**

Assuming that the given flaw at a given time (for the specific PTS transient under study) has a finite conditional probability of initiation that is increasing with time, the following protocol has been implemented in FAVOR$^{EP}$ as a part of the *Initiation-Growth-Arrest* (IGA) submodel (see Sect. 3.3.14) to represent the epistemic and aleatory uncertainties in plane-strain crack arrest fracture-toughness values.

Step 8. For plate, forging, and weld product forms, the following input will have been provided to FAVOR$^{EP}$:

Best estimates for the mean and standard deviation for normal distributions of copper, nickel, and phosphorous content: $N(\overline{Cu}, \sigma_{Cu}), N(\overline{Ni}, \sigma_{Ni}), N(\overline{P}, \sigma_P)$.[11]

Best estimate for the mean and standard deviation for a normal distribution of fluence at the inside surface of the vessel, $N(\overline{f_0}(0), \sigma_{f_0(0)})$.[12]

Best estimate for the standard deviation, $\sigma_{RT_{NDT0}}$, of unirradiated $RT_{NDT}$.

The coolant temperature, $T_c$ in °F, and RPV exposure time in EFPY.

From the initiation procedure for this flaw, the current regulatory estimate of the unirradiated $RT_{NDT}$ will have already been determined from the Reactor Vessel Integrity Database (RVID2) [156] for the material of interest (see Appendix D) and designated as either $RT_{NDT0}$ if the RVID2 $RT_{NDT(u)}$ method is NB-2331 or MTEB 5-2 or sampled from a normal distribution $\widehat{RT_{NDT0}} \leftarrow N(\overline{RT}_{NDT(RVID)}, \sigma_{RT_{NDT0}})$ if the RVID2 $RT_{NDT(u)}$ method is *Generic*.

[11] Note that negative values of chemistry content ($\widehat{Cu}, \widehat{Ni}$, and $\widehat{P}$) sampled from normal distributions are handled as nonphysical exceptions in FAVOR using the truncation protocol described in Sect. 3.3.4 with 0 as the truncation boundary.

[12] Note that sampled negative values of fluence, $\widehat{f_0}(0)$, are handled as nonphysical exceptions in FAVOR using the truncation protocol described in Sect. 3.3.4 with 0 as the truncation boundary.

Step 9. Retrieve the value of $\widehat{\Delta RT}_{epistemic}$ determined from Step 2 in the initiation procedure applied for this flaw and adjust the epistemic uncertainty in $RT_{NDT_0}$ by applying a shift of $-14.4$ °F

$$\widehat{\Delta RT}_{epist-arrest} = \widehat{\Delta RT}_{epistemic} - 14.4 \ \ [°F] \tag{151}$$

Note that this step does not involve a resampling of $\widehat{\Delta RT}_{epistemic}$.

Step 10. Retrieve the sampled value of the irradiation shift for this flaw, $\widehat{\Delta RT}_{NDT}(r,\ldots)$, determined from Step 3 in the initiation procedure applied for this flaw at its current position in the RPV wall. Note that this step does not involve a resampling of $\widehat{\Delta RT}_{NDT}(r,\ldots)$.

Step 11. Sample $\widehat{\Delta RT}_{ARREST} \leftarrow \Lambda(\widehat{\mu}_{\ln(\Delta RT_{ARREST})}, \widehat{\sigma}_{\ln(\Delta RT_{ARREST})})$ from a lognormal distribution (see Appendix F) where

$$\widehat{\mu}_{\ln(\Delta RT_{ARREST})} = \ln\left[\widehat{\Delta RT}_{ARREST(mean)}\right] - \frac{\widehat{\sigma}^2_{\ln(\Delta RT_{ARREST})}}{2}$$

where

$$\widehat{T_0} = \left(\widehat{RT}_{NDT_0} - \widehat{\Delta RT}_{epist-arrest} - 32\right)/1.8 \ \ [°C]$$

$$\widehat{\Delta RT}_{ARREST(mean)} = 44.122 \exp\left[-0.005971 \times \widehat{T_0}\right] \ \ [°C] \tag{152}$$

$$\widehat{\sigma}_{\ln(\Delta RT_{ARREST})} = \sqrt{\ln\left\{\exp\left[0.38998^2 + 2\ln(\widehat{\Delta RT}_{ARREST(mean)})\right] - \mathrm{var}\left(\widehat{T_0}\right)\right\} - 2\ln\left[\widehat{\Delta RT}_{ARREST(mean)}\right]}$$

where

$$\mathrm{var}(\widehat{T_0}) = \begin{cases} (12.778)^2 & \text{for } \widehat{T_0} < -35.7 \text{ °C} \\ 99.905972 - 1.7748073\widehat{T_0} & \text{for } -35.7 \text{ °C} \le \widehat{T_0} \le 56 \text{ °C} \\ 0 & \text{for } \widehat{T_0} > 56 \text{ °C} \end{cases}$$

$\widehat{\Delta RT}_{ARREST}$ is sampled from the lognormal percentile function and then converted into °F

$$\widehat{\Delta RT}_{ARREST} = 1.8 \exp\left[\widehat{\sigma}_{\ln(\Delta RT_{Arrest})} \widehat{Z_{P_f}} + \widehat{\mu}_{\ln(\Delta RT_{Arrest})}\right] \ \ [°F]$$

$\widehat{Z_{P_f}} \leftarrow N(0,1)$; $\widehat{Z_{P_f}}$ is the standard normal deviate corresponding to the $\widehat{P_f}$ fractile $(0 < \widehat{P_f} < 1)$ for this trial in the crack *Initiation - Growth - Arrest* model.

Step 12. Calculate the estimated arrest reference temperature, $\widehat{RT}_{ARREST}$

$$\widehat{RT}_{ARREST}(r,\ldots) = \widehat{RT}_{NDT_0} - \widehat{\Delta RT}_{epist-arrest} + \widehat{\Delta RT}_{ARREST} + \widehat{\Delta RT_{NDT}}(r,\ldots) \tag{153}$$

Step 13. Calculate the normalized (relative to $\widehat{RT}_{ARREST}$) temperature of the vessel at the current location, *r*, in the RPV wall

$$\widehat{\Delta T}_{RELATIVE}(r,\ldots) = T(r,t) - \widehat{RT}_{ARREST}(r,\ldots) \tag{154}$$

Step 14. Calculate the lognormal mean, $\mu_{\ln(K_{Ia})}(\widehat{\Delta T}_{RELATIVE})$, of the $K_{Ia}$ statistical distribution by

$$\mu_{\ln(K_{Ia})}(\widehat{\Delta T}_{RELATIVE}) = \ln\left[ K_{Ia(mean)}(\widehat{\Delta T}_{RELATIVE}) \right] - \frac{\sigma^2_{\ln(K_{Ia})}}{2}$$

where

if $K_{Ia}$_Model is equal to 1

$$K_{Ia(\text{mean})}(\widehat{\Delta T}_{RELATIVE}) = 27.302 + 69.962 \exp\left[ 0.006057(\widehat{\Delta T}_{RELATIVE}) \right] \text{ [ksi}\sqrt{\text{in.}}\text{]} \quad (155)$$

$$\sigma_{\ln(K_{Ia})} = 0.18$$

else if $K_{Ia}$_Model is equal to 2

$$K_{Ia(\text{mean})}(\widehat{\Delta T}_{RELATIVE}) = 27.302 + 70.6998 \exp\left[ 0.008991(\widehat{\Delta T}_{RELATIVE}) \right] \text{ [ksi}\sqrt{\text{in.}}\text{]}$$

$$\sigma_{\ln(K_{Ia})} = 0.34$$

Step 15. Given the current value of $K_{I\text{-}initiation}$ from the initiation model, we first calculate the fractile, $\widehat{\Phi}_{K_{I-initiation}}$, associated with this value in the arrest model by

$$\widehat{\Phi}_{K_{I-initiation}} = \frac{1}{2}\left[ \text{erf}\left( \frac{\ln(K_{I-initiation}) - \mu_{\ln(K_{Ia})}(\widehat{\Delta T}_{RELATIVE})}{\sigma_{\ln(K_{Ia})}\sqrt{2}} \right) + 1 \right] \quad (156)$$

where $\text{erf}(x) \equiv \frac{2}{\sqrt{\pi}} \int_0^x \exp(-\xi^2)\, d\xi$. Using the same value of $\widehat{P_f}$ from Step 11, scale by $\widehat{\Phi}_{K_{I-initiation}}$ such that

$$\widehat{\Phi}_{K_{Ia}} = (\widehat{P_f})(\widehat{\Phi}_{K_{I-initiation}}) \quad (157)$$

With this $\widehat{\Phi}_{K_{Ia}}$ fractile, draw a value of $K_{Ia}$ from its lognormal distribution

$$\widehat{K_{Ia}}(\Phi_{K_{Ia}}, \widehat{\Delta T}_{RELATIVE}) = \exp\left[ \sigma_{\ln(K_{Ia})} \widehat{Z}_{\Phi_{K_{Ia}}} + \mu_{\ln(K_{Ia})}(\widehat{\Delta T}_{RELATIVE}) \right] \quad (158)$$

$\widehat{Z}_{\Phi_{K_{Ia}}}$ = standard normal deviate corresponding to the $\widehat{\Phi}_{K_{Ia}}$ fractile

**Notes:**

**Note on Step 3:** The current sampled value of $\widehat{\Delta T_{30}}$ is also used to estimate the effects of irradiation on the unirradiated flow stress, $\sigma_{flow(u)}$, in the crack *Initiation-Growth-Arrest* model. After each resampling of $\widehat{\Delta T_{30}}$, the flow stress is adjusted by the following relation:

$$\sigma_{flow} = \sigma_{flow(u)} + \gamma \widehat{\Delta T_{30}} \text{ where } \gamma = \begin{cases} 0.112 \text{ ksi/°F for welds} \\ 0.131 \text{ ksi/°F for plates} \end{cases}$$

This value of $\sigma_{flow}$ is then used in the vessel-failure test against the pressure-induced membrane stress in the remaining ligament, checking for net-section plastic collapse.

**Note on Step 11**: The only random variate sampled in Step 11 is $\widehat{Z_{P_f}}$ . All other variates have been sampled in previous steps.

**Note on Step 15**: The scaling procedure in Step 15 ensures that the initial value of $K_{Ia}$ , calculated immediately after initiation, does not exceed the initiating value of $K_I$, thus ensuring an initial extension. For welds, the scaling procedure of Eq. (157) is used only in the weld layer in which the flaw originally initiated. If the flaw advances into other weld layers, then this scaling is not applied, since it is assumed that any linkage between the original initiation event and crack arrest is thereby broken.

For either an initiated ($cpi > 0$) surface-breaking or embedded flaw, the flaw is first assumed to extend to become an infinite-length flaw before it is allowed to advance through the RPV wall. It is the applied $K_I$ of the infinite-length flaw (designated as $K_{I\text{-}initiation}$ in Step 15, Eq. (156)) that is taken as the operative initiating $K_{Ic}$ to establish the required scaling factor and not the applied $K_I$ of the surface-breaking or embedded flaw at initiation. It was determined that scaling by the lower embedded-flaw $K_I$ at initiation was an overly restrictive constraint.

# 5. Summary and Conclusions

This report has provided a detailed description of the theory, algorithms, methods, and correlations that have been implemented in this baseline release of the FAVOR$^{EP}$, v05.1, computer code for performing probabilistic fracture mechanics analyses of nuclear reactor pressure vessels subjected to pressurized thermal shock and other pressure-thermal events. In support of the PTS Re-evaluation Project, the following advanced technologies and new capabilities have been incorporated into FAVOR$^{EP}$, v05.1:

- **the ability to incorporate new detailed flaw-characterization distributions from NRC research (with Pacific Northwest National Laboratory, PNNL),**
- **the ability to incorporate detailed neutron fluence regions – detailed fluence maps from Brookhaven National Laboratory, BNL,**
- **the ability to incorporate warm-prestressing effects into the analysis,**
- **the ability to include temperature-dependencies in the thermo-elastic properties of base and cladding,**
- **the ability to include crack-face pressure loading for surface-breaking flaws,**
- **a new ductile-fracture model simulating stable and unstable ductile tearing,**
- **a new embrittlement correlation,**
- **the ability to include multiple transients in one execution of FAVOR$^{EP}$,**
- **input from the Reactor Vessel Integrity Database, Revision 2, (RVID2) of relevant RPV material properties,**
- **fracture-toughness models based on extended databases and improved statistical distributions,**
- **a variable failure criterion, i.e., how far must a flaw propagate into the RPV wall for the vessel simulation to be considered as "failed" ?**
- **semi-elliptic surface-breaking and embedded-flaw models,**
- **through-wall weld residual stresses, and an**
- **improved PFM methodology that incorporates modern PRA procedures for the classification and propagation of input uncertainties and the characterization of output uncertainties as statistical distributions.**

The companion report *Fracture Analysis of Vessels – Oak Ridge, FAVOR$^{EP}$, v05.1 Computer Code: User's Guide* [45] gives complete details on input requirements and execution of FAVOR$^{EP}$, v05.1.

## References


1. T. L. Dickson, S. N. M. Malik, J. W. Bryson, and F. A. Simonen, "Revisiting the Integrated Pressurized Thermal Shock Studies of an Aging Pressurized Water Reactor," ASME PVP-Volume 388, *Fracture, Design Analysis of Pressure Vessels, Heat Exchangers, Piping Components, and Fitness for Service*, *ASME Pressure Vessels and Piping Conference*, August, 1999.
2. A. R. Foster and R. L. Wright, Jr., *Basic Nuclear Engineering*, 2nd ed., Allyn and Bacon, Inc., Boston, 1973.
3. K. Balkey, F. J. Witt, and B. A. Bishop, *Documentation of Probabilistic Fracture Mechanics Codes Used for Reactor Pressure Vessels Subjected to Pressurized Thermal Shock Loading, Parts 1 and 2*, EPRI TR-105001, Westinghouse Electric Corporation, Pittsburgh, PA, June 1995.
4. D. L. Selby, et al., *Pressurized Thermal Shock Evaluation of the H.B. Robinson Nuclear Power Plant,* NUREG/CR-4183 (ORNL/TM-9567), September 1985.
5. *Classification of TMI Action Plan Requirements*, U.S. Nuclear Regulatory Commission, NUREG-0737, November 1980.
6. D. L. Selby, et al., *Pressurized Thermal Shock Evaluation of the Calvert Cliffs Unit 1 Nuclear Power Plant*, NUREG/CR-4022 (ORNL/TM-9408), Oak Ridge National Laboratory, Oak Ridge, TN, September 1985.
7. T. J. Burns, et al., *Preliminary Development of an Integrated Approach to the Evaluation of Pressurized Thermal Shock as Applied to the Oconee Unit 1 Nuclear Power Plant*, NUREG/CR-3770 (ORNL/TM-9176), May 1986.
8. Policy Issue from J. W. Dircks to NRC Commissioners, *Enclosure A: NRC Staff Evaluation of Pressurized Thermal Shock, November 1982*, SECY-82-465, November 23, 1982, Division of Nuclear Reactor Regulation, U.S. Nuclear Regulatory Commission, Washington, D.C.
9. T. L. Dickson, *Review of Pressurized Thermal Shock Screening Criteria for Embrittled Pressurized Water Reactor Pressure Vessels,* ORNL/NRC/LTR-95/39, December, 1995.
10. *U.S. Code of Federal Regulations,* Title 10, Part 50, Section 50.61 and Appendix G.
11. U.S. Nuclear Regulatory Commission, Regulatory Guide 1.154 (1987), *Format and Content of Plant-Specific Pressurized Thermal Shock Safety Analysis Reports for Pressurized Water Reactors*.
12. U. S. Nuclear Regulatory Commission, Regulatory Guide 1.99, Revision 2 (1988), *Radiation Embrittlement of Reactor Vessel Materials*.
13. C. E. Pugh and B. R. Bass, *A Review of Large-Scale Fracture Experiments Relevant to Pressure Vessel Integrity Under Pressurized Thermal Shock Conditions,* NUREG/CR-6699 (ORNL/TM-2000/360), Oak Ridge National Laboratory, January 2001.
14. B. R. Bass, C. E. Pugh, J. Keeney-Walker, H. Schulz, and J. Sievers, *CSNI Project for Future Analyses of Large-Scale International Reference Experiments (Project FALSIRE),* NUREG/CR-5997 (ORNL/TM-12307), Oak Ridge National Laboratory, December 1992.
15. B. R. Bass, C. E. Pugh, J. Keeney-Walker, H. Schulz, and J. Sievers, *CSNI Project for Future Analyses of Large-Scale International Reference Experiments (FALSIRE II),* NUREG/CR-6460 (ORNL/TM-13207), Oak Ridge National Laboratory, April 1996.
16. J. Sievers and B. R. Bass, "Comparative Assessment of Project FALSIRE-Results," *Journal Nucl. Engr. Des.* **152**, (1994) 19-38.

17. B. R. Bass, et al., "CSNI Project for Fracture Analysis of Large-Scale International Reference Experiments (FALSIRE II)," *Proceedings of the International Conference on Nuclear Engineering-4 (ICONE-4),* Vol. 1, Part A, American society of Mechanical Engineers, (1996) 149-162.

18. B. R. Bass, C. E. Pugh, S. Crutzen, and R. Murgatroyd, *Relationship of NESC-1 to Other Large-Scale International Projects,* ORNL/NRC/LTR-99/20, Oak Ridge National Laboratory, Oak Ridge, TN, 1999.

19. J. G. Merkle, G. D. Whitman, and R. H. Bryan, *An Evaluation of the HSST Program Intermediate Pressure Vessel Tests in Terms of Light-Water-Reactor Pressure Vessel Safety*, ORNL/TM-5090, Oak Ridge National Laboratory, Oak Ridge, TN, November 1975.

20. G. D. Whitman, *Historical Summary of the Heavy-Section Steel Technology Program and Some Related Activities in Light-Water-Reactor Pressure Vessel Safety Research*, NUREG/CR-4489 (ORNL-6259), Oak Ridge National Laboratory, Oak Ridge, TN, March 1986.

21. R. W. Derby, et al., *Test of 6-Inch-Thick Pressure Vessels, Series 1: Intermediate Test Vessels V-1 and V-2*, ORNL-4895, Oak Ridge National Laboratory, Oak Ridge, TN, February 1974.

22. R. H. Bryan, et al., *Test of 6-Inch-Thick Pressure Vessels, Series 2: Intermediate Test Vessels V-3, V-4, and V-6*, ORNL-5059, Oak Ridge National Laboratory, Oak Ridge, TN, November 1975.

23. R. H. Bryan, et al., *Test of 6-Inch-Thick Pressure Vessels, Series 3: Intermediate Test Vessels V-7B*, NUREG/CR-0309 (ORNL/NUREG-38), Oak Ridge National Laboratory, Oak Ridge, TN, October 1978.

24. J. G. Merkle, et al., *Test of 6-Inch-Thick Pressure Vessels, Series 4: Intermediate Test Vessels V-5 and V-9 with Nozzle Corner Cracks,* ORNL/NUREG-7, Oak Ridge National Laboratory, Oak Ridge, TN, August 1977.

25. R. H. Bryan, et al., *Test of 6-Inch-Thick Pressure Vessels, Series 3: Intermediate Test Vessel V-8,* NUREG/CR-0675 (ORNL/NUREG-58), Oak Ridge National Laboratory, Oak Ridge, TN, December 1979.

26. R. H. Bryan, et al., *Pressurized-Thermal Shock Test of 6-Inch-Thick Pressure Vessel, PTSE-1: Investigations of Warm Prestressing and Upper-Shelf Arrest*, NUREG/CR-4106 (ORNL-6135), Oak Ridge National Laboratory, Oak Ridge, TN, April 1985.

27. R. H. Bryan, et al., *Pressurized Thermal Shock Test of 6-Inch-Thick Pressure Vessel PTSE-2: Investigation of Low Tearing Resistance and Warm Prestressing*, NUREG/CR-4888 (ORNL-6377), Oak Ridge National Laboratory, Oak Ridge, TN, December 1987.

28. H. Keinanen, et al., "Pressurized Thermal Shock Tests with Model Pressure Vessels Made of VVER-440 Reactor Steel," *IAEA/CSNI Specialists' Meeting on Fracture Mechanics Verification by Large-Scale Testing, Oak Ridge, Tennessee*, *October 26-29, 1992*, NUREG/CP-0131 (ORNL/TM-12413), October 1993, 275-288.

29. B. R. Bass, et al., *CSNI Project for Fracture Analyses of Large-Scale International Reference Experiments (FALSIRE II)*, NUREG/CR-6460 (ORNL/TM-13207), Oak Ridge National Laboratory, Oak Ridge, TN, April 1996.

30. L. Stumpfrock, "FALSIRE Results for NKS-3 and NKS-4," *IAEA/CSNI Specialists' Meeting on Fracture Mechanics Verification by Large-Scale Testing, Oak Ridge, Tennessee*, *October 26-29, 1992*, NUREG/CR-0131 (ORNL/TM-12413), October 1993, 151-188.

31. L. Stumpfrock, et al., "Fracture Mechanics Investigations on Cylindrical Large-Scale Specimens under Thermal-Shock Loading," *Journal of Nuclear Engineering Design* **144**, (1993) 31-44.

32. E. Morland, "Spinning Cylinder Experiments SC-I and SC-II: A Review of Results and Analyses Provided to the FALSIRE Project," *IAEA/CSNI Specialists' Meeting on Fracture Mechanics Verification by Large-Scale Testing, Oak Ridge, Tennessee*, *October 26-29, 1992*, NUREG/CR-0131 (ORNL/TM-12413), October 1993, 39-74.

33. D. J. Lacey, et al., *Spinning Cylinder Test 4: An Investigation of Transition Fracture Behavior for Surface Breaking Defects in Thick-Section Steel Specimens*, AEA Technology Report AEA TRS 4098, June 1991.

34. R. D. Cheverton, et al., "Review of Pressurized-Water-Reactor-Related Thermal Shock Studies," *Fracture Mechanics: Nineteenth Symposium (June 30-July 2, 1986)*, ASTM STP-969, American Society for Testing and Materials, (1988) 752-766.

35. R. D. Cheverton, "Thermal Shock Experiments with Flawed Clad Cylinders," *Journal of Nuclear Engineering and Design* **124**, (1990) 109-119.

36. B. R. Bass, J. Wintle, R. C. Hurst, and N. Taylor (eds), *NESC-1 Project Overview*, EUR 19051EN, European Commission, Directorate-General Joint Research Centre, Institute for Advanced Materials, Petten, The Netherlands, 2001.

37. H. Okumura, et al., "PTS Integrity Study in Japan," *Ninth International Conference on Structural Mechanics in Reactor Technology*, Vol. F, (1989) 7-12.

38. D. J. Naus, et al., *High-Temperature Crack Arrest Behavior in 152-mm-Thick SEN Wide Plates of Quenched and Tempered A533 Grade B Class 1 Steel*, NUREG/CR-5330 (ORNL-11083), Oak Ridge National Laboratory, Oak Ridge, TN, April 1989.

39. D. J. Naus, et al., *Crack-Arrest Behavior in SEN Wide Plates of Low-Upper-Shelf Base Metal Tested Under Nonisothermal Conditions: WP-2 Series*, NUREG/CR-5451 (ORNL-6584), Oak Ridge National Laboratory, Oak Ridge, TN, April 1989.

40. K. Kussmaul, R. Gillot, and T. Elenz, "Full Thickness Crack Arrest Investigations on Compact Specimens and a Heavy-Wide Plate," *IAEA/CSNI Specialists' Meeting on Fracture Mechanics Verification by Large-Scale Testing, Oak Ridge, Tennessee*, *October 26-29, 1992*, NUREG/CR-0131 (ORNL/TM-12413), October 1993, 551-572.

41. D. Moinerau, et al., "Cleavage Fracture of Specimens Containing an Underclad Crack, PVP Vol. 233, *Pressure Vessel Fracture, Fatigue and Life Management,* American Society of Mechanical Engineers, 1992.

42. J. A. Keeney, B. R. Bass, and W. J. McAfee, "Fracture Assessment of Weld Material from a Full-Thickness Clad RPV Shell Segment," *Fatigue and Fracture Mechanics, 20th Volume,* ASTM STP-1321, eds., J. H. Underwood, B. D. McDonald, and M. R. Mitchell, American Society of Materials and Testing, 1997.

43. J. A. Keeney and P. T. Williams, "Fracture Analysis of Ductile Crack Growth in Weld Material from a Full-Thickness Clad RPV Shell Segment," *Fatigue and Fracture Mechanics, 29th Volume*, ASTM STP-1332, eds. T. L. Panontin and S. D. Sheppard, American Society of Materials and Testing, 1998.

44. B. R. Bass, et al., "Evaluation of Constraint Methodologies Applied to Shallow-Flaw Cruciform Bend Specimens Tested under Biaxial Loading Conditions," PVP Vol. 365, *Proceedings of the 1998 ASME Pressure Vessel and Piping Conference,* San Diego, CA, July 1998, 11-26.

45. T. L. Dickson, P. T. Williams, and S. Yin, *Fracture Analysis of Vessels – FAVOR (v05.1): User's Guide*, NUREG - (ORNL/TM-2005/???), Oak Ridge National Laboratory, Oak Ridge, TN, 2005.

46. M. G. Morgan and M. Henrion, *Uncertainty – A Guide to Dealing with Uncertainty in Quantitative Risk and Policy Analysis*, Cambridge University Press, Cambridge, UK, 1990.

47. D. A. Jackson and L. Abramson, *Report on the Results of the Expert Judgment Process for the Generalized Flaw Size and Density Distribution for Domestic Reactor Pressure Vessels,* U.S. Nuclear Regulatory Commission Office of Research, FY 2000-2001 Operating Milestone 1A1ACE (1999).

48. G. J. Schuster, S. R. Doctor, S. L. Crawford, and A. F. Pardini, *Characterization of Flaws in U.S. Reactor Pressure Vessels: Density and Distribution of Flaw Indications in PVRUF*, USNRC Report NUREG/CR-6471, Vol. 1, U.S. Nuclear Regulatory Commission, Washington, D.C. (1998).

49. G. J. Schuster, S. R. Doctor, and P. G. Heasler, *Characterization of Flaws in U.S. Reactor Pressure Vessels: Validation of Flaw Density and Distribution in the Weld Metal of the PVRUF Vessel,* USNRC Report NUREG/CR-6471, Vol. 2, U.S. Nuclear Regulatory Commission, Washington, D.C. (2000).

50. G. J. Schuster, S. R. Doctor, S. L. Crawford, and A. F. Pardini, *Characterization of Flaws in U.S. Reactor Pressure Vessels: Density and Distribution of Flaw Indications in the Shoreham Vessel,* USNRC Report NUREG/CR-6471, Vol. 3, U.S. Nuclear Regulatory Commission, Washington, D.C. (1999).

51. A. M. Law and W. D. Kelton, *Simulation Modeling and Analysis*, 3rd ed., McGraw-Hill, New York, NY, (2000).

52. X. Gao and R. H. Dodds, Jr., "An Engineering Approach to Assess Constraint Effects on Cleavage Fracture Toughness," *Engineering Fracture Mechanics* **68**(3), (2001) 263-283.

53. A. H. Sherry, M. A. Wilkes, D. W. Beardsmore, and D. P. G. Lidbury, "Material Constraint Parameters for the Assessment of Shallow Defects in Structural Components – Part I: Parameter Solutions," submitted for publication in *Engineering Fracture Mechanics*, 8 March 2004.

54. *TableCurve 3D – Automated Surface Fitting and Equation Discovery, Version 3.0: User's Manual*, SPSS Inc., Chicago, IL, 1997.

55. R. Renka, "Algorithm 751: TRIPACK: A Constrained Two-Dimensional Delaunay Triangulation Package," *ACM Transactions on Mathematical Software* **22**(1), (1996) 1-8.

56. R. Renka, "Algorithm 752: SRFPACK: Software for Scattered Data Fitting with a Constrained Surface under Tension," *ACM Transactions on Mathematical Software* **22**(1), (1996) 9-17.

57 M. T. Kirk, M. A. E. Natishan, and M. Wagenhofer, "Microstructural Limits of Applicability of the Master Curve," *32nd National Fracture and Fatigue Symposium*, ASTM STP-1406, R. Chona, ed., American Society for Testing and Materials, West Conshohocken, PA, 2001.

58 F. J. Zerilli and R. W. Armstrong, "Dislocation-Mechanics-Based Constitutive Relations for Material Dynamics Calculations," *Journal of Applied Physics* **61**(5), (1987) 1816-1825.

59 M. Kirk, M. A. E. Natishan, "Shift in Toughness Transition Temperature Due to Irradiation, $\Delta T_0$ vs $\Delta T_{41J}$ : A Comparison and Rationalization of Differences, … .

60 M. Natishan, M. Kirk, H. Gunawardane, and M. Wagenhofer, "More Information from a Hardness Test than You Ever Thought Possible," *Small Specimen Test Techniques, Fourth Volume,* ASTM STP-1418, M. Sokolov, J. Landes, and G. Lucas, eds., American Society for Testing and Materials, West Conshohocken, PA, 2001.

61 Personal communication (e-mail) from M. T. EricksonKirk, "Material Models to Consider Using FAVOR-EP," May 3, 2005.

62 M. T. Kirk, C. S. Santos, E.D. Eason, J.E. Wright, and G. R. Odette, "Updated Embrittlement Trend Curve for Reactor Pressure Vessel Steels," Paper No. G01-5, *Transactions of the 17th International Conference on Structural Mechanics in Reactor Technology (SMiRT 17)*, Prague, Czech Republic, August 17-22, 2003.

63 T. J. Giesbach and J. F. Williams, "User's Guide to RPVDATA, Reactor Vessel Materials Database," Westinghouse Energy Systems Business Unit, WCAP-14616, 1966.

64. A. J. Brothers and S. Yukawa, "The Effect of Warm Prestressing on Notch Fracture Strength," *Journal of Basic Engineering*, *Transaction of the ASME*, Series D, **85**(1), (1963) 87-104.

65. R. W. Nichols, "The Use of Overstressing Techniques to Reduce the Risk of Subsequent Brittle Fracture: Parts 1 and 2," *British Welding Journal*, January and February 1968.

66. J. J. McGowan, "An Assessment of the Beneficial Effects of Warm Prestressing on the Fracture Properties of Nuclear Reactor Pressure Vessels Under Severe Thermal Shock," Westinghouse Electric Company, WCAP-9178, March 1978.

67. G. C. Chell, "A Theory of Warm Prestressing: Experimental Validation and the Implication for Elastic-Plastic Failure Criteria," CERL Lab Note RD/L/N78/79, September 1979.

68. G. C. Chell, "Some Fracture Mechanics Applications of Warm Prestressing to Pressure Vessels," *4th International Conference on Pressure Vessel Technology*, Paper C22/80, London, May 1980.

69. B. W. Pickles and A. Cowan, "A Review of Warm Prestressing Studies," *International Journal of Pressure Vessels and Piping* **14**, (1983) 95-131.

70. D. Lidbury and P. Birkett, "Effect of Warm Prestressing on the Transition Toughness Behaviour of an A533 Grade B Class 1 Pressure Vessel Steel," *ASTM STP 1074, Fracture Mechanics: 21st Symposium*, American Society for Testing and Materials, Philadelphia, PA, (1990) 264-285.

71. F. M. Burdekin and D. P. G. Lidbury, "Views of TAGSI on the Current Position with Regard to Benefits of Warm Prestressing," *International Journal of Pressure Vessels and Piping* **76**, (1999) 885-890.

72. H. Kordisch, R. Böschen, J. G. Blauel, W. Schmitt, and G. Nagel, "Experimental and Numerical Investigation of the Warm-Prestressing (WPS) Effect Considering Different Load Paths," *Nuclear Engineering Design* **198**, (2000) 89-96.

73. J. H. Chen, V. B. Wang, G. Z. Wang, and X. Chen, "Mechanism of Effects of Warm Prestressing on Apparent Toughness of Precracked Specimens of HSLA Steels," *Engineering Fracture Mechanics* **68**, (2001) 1669-1689.

74. W. Lefevre, G. Barbier, R. Masson, and G. Rousselier, "A Modified Beremin Model to Simulate the Warm Pre-Stress Effect," *Nuclear Engineering and Design* **216**, (2002) 27-42.

75. M. T. Kirk, "Inclusion of Warm Prestressing Effects in Probabilistic Fracture Mechanics Calculations Performed to Assess the Risk of RPV Failure Produced by Pressurized Thermal Shock Events: An Opinion," presented at the *NATO Advanced Research Workshop – Scientific Fundamentals for the Life Time Extension of Reactor Pressure Vessels*, Kiev, Ukraine, April 22-25, 2002.

76. B. W. Brown and J. Lovato, *RANLIB – A Library of Fortran Routines for Random Number Generation*, Department of Biomathematics, University of Texas, Houston, TX, 1994.

77. P. L'Ecuyer, "Efficient and Portable Combined Random Number Generators," *Communications of the ACM* **31**(6), (1988) 742-774.

78. P. L'Ecuyer and S. Cote, "Implementing a Random Number Package with Splitting Facilities." *ACM Transactions on Mathematical Software* **17**, (1991) 98-111.

79. A. Rukhin, et al., *A Statistical Test Suite for Random and Pseudorandom Number Generators for Cryptographic Applications*, NIST Special Publication 800-22, National Institute of Standards and Technology, Gaithersburg, MD, May 15, 2001.

80. G. E. P. Box and M. E. Müller, "A Note on the Generation of Random Normal Deviates," *Annals of Mathematical Statistics*, **29** (1958), 610-611.

81. M. E. Müller, "An Inverse Method for the Generation of Random Normal Deviates on Large Scale Computers," *Math. Tables Aids Comp.* **63**, (1958) 167-174.

82. M. Abramowitz and I. A. Stegun, *Handbook of Mathematical Functions*, Dover Publications, Inc., New York, (1972) 931.

83. J. H. Ahrens and U. Dieter, "Extensions of Forsythe's Method for Random Sampling from the Normal Distribution," *Math. Comput.* **27**(124), (1973) 927-937.

84. Kennedy and Gentle, *Statistical Computing*, Marcel Dekker, NY, (1980) 95.

85. EPRI Special Report, 1978, *Flaw Evaluation Procedures: ASME Section XI*, EPRI NP-719-SR, Electric Power Research Institute, Palo Alto, CA.

86. K. O. Bowman and P. T. Williams, *Technical Basis for Statistical Models of Extended $K_{Ic}$ and $K_{Ia}$ Fracture Toughness Databases for RPV Steels*, ORNL/NRC/LTR-99/27, Oak Ridge National Laboratory, Oak Ridge, TN, February, 2000.

87. R. D. Cheverton, et al., *Pressure Vessel Fracture Studies Pertaining to the PWR Thermal-Shock Issue: Experiment TSE-7,* NUREG/CR-4304 (ORNL/TM-6177), Oak Ridge National Laboratory, Oak Ridge, TN, August 1985.

88. F. Li, *Assessment of Pressure Vessel Failure Due to Pressurized Thermal Shock with Consideration of Probabilistic-Deterministic Screening and Uncertainty Analysis,* Ph.D. Dissertation, Center for Technology Risk Studies, University of Maryland, 2001.

89. T. Fang and M. Modarres, "Probabilistic and Deterministic Treatments for Multiple Flaws in Reactor Pressure Vessel Safety Analysis," *Transactions of the 17th International Conference on Structural Mechanics in Reactor Technology (SMiRT 17),* August 17-22, 2003, Prague, Czech Republic.

90. NUREG/CR-3506

91. D. E. McCabe, R. K. Nanstad, S. K. Iskander, D. W. Heatherly, and R. L. Swain, *Evaluation of WF-70 Weld Metal From the Midland Unit 1 Reactor Vessel*, USNRC Report NUREG/CR-5736 (ORNL/TM-13748), Oak Ridge National Laboratory, Oak Ridge, TN, November 2000.

92. NUREG/CR-5492

93. *Standard Test Method for Measurement of Fracture Toughness*, ASTM E 1820-1, Annual Book of ASTM Standards 2002, Section Three, Metals Test Methods and Analytical Procedures, Volume 03.01, American Society for Testing and Materials, West Conshohocken, PA (2002).

94. M. EricksonKirk and M. T. EricksonKirk, "The Relationship Between Upper Shelf and Transition Fracture Toughness of Ferritic Steels," NRC Internal Report, May 17, 2004.

95. M. T. Kirk, "Step-by-Step Instructions for Implementing a Revised Upper Shelf Model in FAVOR," NRC Internal Report, July 14, 2004.

96. M. T. Kirk, "Models for Upper-Shelf Fracture Toughness of RPV Steels for use in Analysis of Pressurized Thermal Shock, A Proposal," NRC Internal Report, May 29, 2003.

97. E. D. Eason, J. E. Wright, and G. R. Odette, "Improved Embrittlement Correlations for Reactor Pressure Vessel Steels," NUREG/CR-6551, U. S. Nuclear Regulatory Commission, Washington, DC, 1998.

98. M. T. Kirk, C. S. Santos, E.D. Eason, J.E. Wright, and G. R. Odette, "Updated Embrittlement Trend Curve for Reactor Pressure Vessel Steels," Paper No. G01-5, *Transactions of the 17th International Conference on Structural Mechanics in Reactor Technology (SMiRT 17)*, Prague, Czech Republic, August 17-22, 2003.

99. N. Siu, S. Malik, D. Bessette, R. Woods, A. Mosleh, and M. Modarres, "Treating Aleatory and Epistemic Uncertainties in Analyses of Pressurized Thermal Shock," *Proceedings of PSAM 5, International Conference on Probabilistic Safety Assessment and Management*, Osaka, Japan, (2000) 377-382.

100. R. W. Lewis, K. Morgan, H. R. Thomas, and K. N. Seetharamu, *The Finite-Element Method in Heat Transfer Analysis*, John Wiley & Sons, New York, 1996.

101. R. D. Cook, D. S. Malkus, and M. E. Plesha, *Concepts and Applications of Finite Element Analysis, 3rd ed.,* John Wiley & Sons, New York, 1989.

102. H. F. Bückner, "A Novel Principle for the Computation of Stress Intensity Factors," *Z. angew. Math. Mech.* **50**, (1970) 529-546.

103. C. B. Buchalet and W. H. Bamford, "Stress Intensity Factor Solutions for Continuous Surface Flaws in Reactor Pressure Vessels," ASTM STP 590, *Mechanics of Crack Growth*, American Society for Testing and Materials, (1976) 385-402.

104. J. Heliot, R. C. Labbens, and A. Pellissier-Tanon, "Semi-Elliptical Cracks in a Cylinder Subjected to Stress Gradients," ASTM STP 677, *Fracture Mechanics,* ed. C. W. Smith, American Society for Testing and Materials, (1979) 341-364.

105. J. J. McGowan and M. Raymund, "Stress Intensity Factor Solutions for Internal Longitudinal Semi-Elliptical Surface Flaws in a Cylinder Under Arbitrary Loadings," ASTM STP 677, *Fracture Mechanics*, ed. C. W. Smith, American Society for Testing and Materials, (1979) 365-380.

106. I. S. Raju and J. C. Newman, Jr., "Stress Intensity Factor Influence Coefficients for Internal and External Surface Cracks in Cylindrical Vessels," PVP Vol. 58, *Aspects of Fracture Mechanics in Pressure Vessels and Piping*, ASME Pressure Vessels and Piping Conference, (1982) 37-48.

107. S. K. Iskander, R. D. Cheverton, and D. G. Ball, OCA-I, A Code for Calculating the Behavior of Flaws on the Inner Surface of a Pressure Vessel Subjected to Temperature and Pressure Transients, NUREG/CR-2113 (ORNL/NUREG-84), Oak Ridge National Laboratory, Oak Ridge, TN, 1981.

108. R. D. Cheverton and D. G. Ball, *OCA-P, A Deterministic and Probabilistic Fracture Mechanics Code for Application to Pressure Vessels,* NUREG/CR-3618 (ORNL-5991), Oak Ridge National Laboratory, Oak Ridge, TN, May 1984.

109. J. W. Bryson and T. L. Dickson, "Stress-Intensity-Factor Influence Coefficients for Axial and Circumferential Flaws in Reactor Pressure Vessels," PVP Vol. 250, ASME Pressure Vessels and Piping Conference, (1993) 77-88.

110. T. L. Dickson, J. A. Keeney, and J. W. Bryson, "Validation of FAVOR Code Linear-Elastic Fracture Solutions for Finite-Length Flaw Geometries," PVP-Vol. 304, *Fatigue and Fracture Mechanics in Pressure Vessels and Piping*, ASME Pressure Vessels and Piping Conference, (1995) 51-58.

111. J. W. Bryson and T. L. Dickson, *Stress-Intensity-Factor Influence Coefficients for Circumferentially Oriented Semielliptic Inner Surface Flaws in Clad Pressure Vessels ($R_i$ / $t$ = 10)*, ORNL/NRC/LTR-94/8, Oak Ridge National Laboratory, Oak Ridge, TN, April, 1994.

112. *ABAQUS Theory Manual, Version 4.8,* Hibbit, Karlson, and Sorenesen, Inc., Providence, RI, 1989.

113. S. Timoshenko, *Theory of Plates and Shells*, McGraw-Hill, New York, 1940.

114. T. L. Dickson, B. R. Bass, and P. T. Williams, "Validation of a Linear-Elastic Fracture Methodology for Postulated Flaws Embedded in the Wall of a Nuclear Reactor Pressure Vessel," PVP-Vol. 403, *Severe Accidents and Other Topics in RPV Design*, American Society of Mechanical Engineering Pressure Vessels and Piping Conference, (2000) 145-151.

115. R.C. Cipolla, et al., Failure Analysis Associates, Computational Method to Perform the Flaw Evaluation Procedure as Specified in the ASME Code, Section XI, Appendix A, EPRI Report NP-1181, September, 1979.

116. *American Society of Mechanical Engineers Boiler and Pressure Vessel Code,* Section XI, Rules for Inservice Inspection of Nuclear Power Plant Components, Appendix A, Analysis of Flaws, Article A-3000, Method for $K_I$ Determination, American Society of Mechanical Engineers, New York, 1998.

117. M. L. Williams, "On the Stress Distribution at the Base of a Stationary Crack," *ASME J. Appl. Mech.* **24**, (1957) 109-114.

118. S. G. Larsson and A. J. Carlsson, "Influence of Non-singular Stress Terms and Specimen Geometry on Small-Scale Yielding at Crack-Tips in Elastic-Plastic Materials," *J. Mech. Phys Solids* **21**, (1973) 447-473.

119. J. R. Rice, "Limitations to the Small Scale Yielding Approximation for Crack-Tip Plasticity," *J. Mech. Solids* **22**, (1974) 17-26.

120. B. A. Bilby, G. E. Cardew, M. R. Goldthorpe, and I. C. Howard, "A Finite-Element Investigation of the Effect of Specimen Geometry on the Fields of Stress and Strain at the Tips of Stationary Cracks," *Size Effects in Fracture* London: Mechanical Engineering Publications Limited, (1986) 37-46.

121. X. Wang and R. Bell, "Elastic *T*-Stress Solutions for Semi-elliptic Surface Cracks in Finite Thickness Plates Subject to Non-Uniform Stress Distributions," *Engineering Fracture Mechanics* **71**, (2004) 1477-1496.

122. T. L. Sham, "The Determination of Elastic *T*-term Using Higher Order Weight Functions," *Int. J. Fract.* **48**, (1991) 81-102.

123. T. A. Fett, "Green's Function for *T*-Stress in an Edge Cracked Rectangular Plate," *Engineering Fracture Mechanics* **57**, (1997) 365-373.

124. D. G. Hooton, A. H. Sherry, D. J. Sanderson, and R. A. Ainsworth, "Application of R6 Constraint Methods Using Weight Functions for *T*-Stress," *ASME Pressure Vessel Piping Conf.*, **365**, (1998) 37-43.

125. X. Wang, "Elastic *T*-Stress for Cracks in Test Specimens Subjected to Non-Uniform Stress Distributions," *Engineering Fracture Mechanics* **69**, (2002) 1339-1352.

126. F. N. Fritsch and R. E. Carlson, "Monotone Piecewise Cubic Interpolation," *SIAM J. Numer. Anal.* **17**(2), (1980) 238-246.

127. F. N. Fritsch and J. Butland, "A Method for Constructing Local Monotone Piecewise Cubic Interpolants," *SIAM J. Sci. Stat. Comput.* **5**(2), (1984) 300-304.

128. T.-L. Sham, "The Theory of Higher Order Weight Functions for Linear Elastic Plane Problems," *Int. J. Solids Struct.* **25**, (1989) 357-380.

129. *TableCurve 2D, User's Manual*, *Version 5.01*, SYSTAT Software Inc., Richmond, CA (2002).

130. X. Wang, "Elastic *T*-stress Solutions for Penny-Shaped Cracks Under Tension and Bending," *Engineering Fracture Mechanics* **71**(16), (2004) 2283-2298.

131. T.L. Dickson, B.R. Bass, and P.T. Williams, "Validation of a Linear-Elastic Fracture Methodology for Postulated Flaws Embedded in the Wall of a Nuclear Reactor Pressure Vessel, Oak Ridge National Laboratory," PVP Vol. 403, *Severe Accidents and Other Topics in the RPV Design,* ed. S. Bhandari, *ASME 2000 Pressure Vessel and Piping Conference*, Seattle, WA, July, 2000, pp. 145-151.

132. T. L. Dickson, B. R. Bass, and W. J. McAfee, "The Inclusion of Weld Residual Stress In Fracture Margin Assessments of Embrittled Nuclear Reactor Pressure Vessels," PVP-Vol. 373, *Fatigue, Fracture, and Residual Stresses*, ASME Pressure Vessels and Piping Conference, (1998) 387-395.

133. T.L .Dickson, W.J. McAfee, W.E. Pennell, and P.T. Williams, *Evaluation of Margins in the ASME Rules for Defining the P-T Curve for an RPV*, NUREG/CP-0166, Oak Ridge National Laboratory, Oak Ridge, TN, *Proceedings of the Twenty-Sixth Water Reactor Safety Meeting* **1**, (1999) 47-72.

134. J. A. Keeney, et al., *Preliminary Assessment of the Fracture Behavior of Weld Material in Full-Thickness Clad Beams*, NUREG/CR-6228 (ORNL/TM-12735), Oak Ridge National Laboratory, Oak Ridge, TN, October 1994.

135. M. A. Kirk, et al., *Recommended Method to Account for Uncertainty in the Fracture Toughness Characterization Used to Re-evaluate the Pressurized Thermal Shock (PTS) Screening Criteria*, NUREG-????, U. S. Nuclear Regulatory Commission, (in publication).

136. R. K. Nanstad, J. A. Keeney , and D. E. McCabe, *Preliminary Review of the Bases for the $K_{Ic}$ Curve in the ASME Code*, ORNL/NRC/LTR-93/15, Oak Ridge National Laboratory, Oak Ridge, TN, 1993.

137. *Standard Test Method for Plane-Strain Fracture Toughness of Metallic Materials,* E 399-90, Annual Book of ASTM Standards - Section 3: Metals Test Methods and Analytical Procedures, vol. 03.01, *Metals – Mechanical Testing; Elevated and Low-Temperature Tests; Metallography*, American Society for Testing and Materials, West Conshohocken, PA, 1998.

138. *ASME Boiler and Pressure Vessel Code*, Section III, Article NB-2331, American Society of Mechanical Engineers, New York, NY, (1998).

139. R. K. Nanstad, F. M. Haggag, and D. E. McCabe, *Irradiation Effects on Fracture Toughness of Two High-Copper Submerged-Arc Welds, HSSI Series 5,* USNRC Report NUREG/CR-5913 (ORNL/TM-12156/V1 and V2) Vols. 1 and 2, Oak Ridge National Laboratory, Oak Ridge, TN, October 1992.

140. D. E. McCabe, *A Comparison of Weibull and $\beta_{Ic}$ Analysis of Transition Range Fracture Toughness Data,* USNRC Report NUREG/CR-5788 (ORNL/TM-11959), Oak Ridge National Laboratory, Oak Ridge, TN, January 1992.

141. T. Iawadate, Y. Tanaka, S. Ono, and J. Watanabe, "An Analysis of Elastic-Plastic Fracture Toughness Behavior for $J_{Ic}$ Measurements in the Transition Region," *Elastic-Plastic Fracture: Second Symposium, Vol. II-Fracture Resistance Curves and Engineering Applications*, (edited by C. F. Shih and J. P. Gudas) ASTM STP 803, (1983) II531-II561.

142. D. E. McCabe, R. K. Nanstad, S. K. Iskander, and R. L. Swain, *Unirradiated Material Properties of Midland Weld WF-70,* USNRC Report NUREG/CR-6249 (ORNL/TM-12777), Oak Ridge National Laboratory, Oak Ridge, TN, October 1994.

143. J. J. McGowan, R. K. Nanstad, and K. R. Thoms, *Characterization of Irradiated Current-Practice Welds and A533 Grade B Class 1 Plate for Nuclear Pressure Vessel Service*, USNRC Report NUREG/CR-4880 (ORNL-6484/V1 and V2), Oak Ridge National Laboratory, Oak Ridge, TN, July 1988.

144. American Society for Testing and Materials, *Standard Test Method for Determining Plane-Strain Crack Arrest Toughness, $K_{Ia}$, of Ferritic Steels,* E 1221-88, Annual Book of ASTM Standards, Section 3: Metals Test Methods and Analytical Procedures, vol. 03.01, *Metals – Mechanical Testing; Elevated and Low-Temperature Tests; Metallography*, American Society for Testing and Materials, West Conshohocken, PA, 1998.

145. S. K. Iskander, W. R. Corwin, R. K. Nanstad, *Results of Crack-Arrest Tests on Two Irradiated High-Copper Welds,* USNRC Report NUREG/CR-5584 (ORNL/TM-11575), Oak Ridge National Laboratory, Oak Ridge, TN, December 1990.

146. S. K. Iskander, C. A. Baldwin, D. W. Heatherly, D. E. McCabe, I. Remec, and R. L. Swain, *Detailed Results of Testing Unirradiated and Irradiated Crack-Arrest Toughness Specimens from the Low Upper-Shelf Energy, High Copper Weld, WF-70,* NUREG/CR-6621 (ORNL/TM-13764) under preparation.

147. S. K. Iskander, R. K. Nanstad, D. E. McCabe, and R. L. Swain, "Effects of Irradiation on Crack-Arrest Toughness of a Low Upper-Shelf Energy, High-Copper Weld," *Effects of Radiation on Materials: 19th International Symposium, ASTM STP 1366*, M. L. Hamilton, A. S. Kumar, S. T. Rosinski, and M. L. Grossbeck, eds., American Society for Testing and Materials, to be published.

148. E. J. Ripling and P. B. Crosley, "Strain Rate and Crack Arrest Studies," *HSST 5th Annual Information Meeting*, Paper No. 9, 1971.

149. E. J. Ripling and P. B. Crosley, "Crack Arrest Studies," *HSST 6th Annual Information Meeting*, Paper No. 10, 1972.

150. R. D. Cheverton, D. G. Ball, S. E. Bolt, S. K. Iskander, and R. K. Nanstad, *Pressure Vessel Fracture Studies Pertaining to the PWR Thermal-Shock Issue: Experiments TSE-5, TSE-5A, and TSE-6,* NUREG/CR-4249 (ORNL-6163), Oak Ridge National Laboratory, Oak Ridge, TN, June 1985.

151. "Standard Test Method for Determination of Reference Temperature, $T_0$, for Ferritic Steels in the Transition Range," E 1921-97, Annual Book of ASTM Standards Section 3: Metals Test Methods and Analytical Procedures, vol. 03.01, *Metals – Mechanical Testing; Elevated and Low-Temperature Tests; Metallography*, American Society for Testing and Materials, West Conshohocken, PA, 1998.

152. M. Kirk, R. Lott, W. L. Server, R. Hardies, and S. Rosinski, "Bias and Precision of $T_0$ Values Determined Using ASTM Standard E 1921-97 for Nuclear Reactor Pressure Vessel Steels," *Effects of Radiation on Materials: 19th International Symposium, ASTM STP 1366,* M. L. Hamilton, A. S. Kumar, S. T. Rosinski, and M. L. Grossbeck, Eds., American Society for Testing and Materials, West Conshococken, PA, (2000) 143-161.

153. K. Wallin, "Master Curve Based Correlation Between Static Initiation Toughness, $K_{Ic}$, and Crack Arrest Toughness, $K_{Ia}$," presented at *24th MPA Seminar*, Stuttgart, Germany, October 8 and 9, 1998.

154. K. Wallin, "Application of the Master Curve Method to Crack Initiation and Crack Arrest," *Fracture, Fatigue, and Weld Residual Stress*, PVP Vol. 393, ASME Pressure Vessels and Piping Conference, Boston, MA, August 1-5, 1999.

155. *Reactor Vessel Integrity Database (RVID), User's Manual,* Version 1.1, U. S. Nuclear Regulatory Commission, July 1995.

156. *Reactor Vessel Integrity Database (RVID)*, Version 2.1.1, U. S. Nuclear Regulatory Commission July 6, 2000.

## Appendix A – Background and Antecedents of FAVOR$^{EP}$, v05.1

An important element of the PTS plant-specific analysis is the calculation of the conditional probability of failure of the vessel by performing probabilistic fracture mechanics (PFM) analyses. The term *conditional* refers here to two assumed preconditions: (1) the specific PTS event under study has in fact occurred, and (2) the postulated flaws do exist on the surface or embedded within the RPV wall. Combined with an estimate of the frequency of occurrence for the event, a predicted frequency of vessel failure can then be calculated. OCA-P [1] and VISA-II [2] are PTS PFM computer programs, independently developed at Oak Ridge National Laboratory (ORNL) and Pacific Northwest National Laboratory (PNNL), respectively, in the 1980s with NRC funding, that are currently referenced in Regulatory Guide 1.154 as acceptable codes for performing plant-specific analyses.

There have also been other proprietary and public-domain PTS PFM codes independently developed in the US and internationally by reactor vendors and research laboratories. The development of the OCA-P code [1] (and its deterministic predecessors, OCA-I [3], and OCA-II [4]) and the VISA II code [2] was preceded by two earlier probabilistic computer programs developed by the NRC, specifically OCTAVIA [5] (**O**perationally **C**aused **T**ransients **a**nd **V**essel **I**ntegrity **A**nalysis) and a second unnamed code developed by Gamble and Strosnider [6].

OCTAVIA [5] was developed in the mid-1970s to calculate the probability of RPV failure from operationally caused pressure transients which can occur in a PWR vessel at low operating temperatures. OCTAVIA computed the pressure at which the vessel would fail for different-sized flaws existing in the beltline region, where only axially oriented flaws in the vessel beltline were considered. The probability of vessel failure was then calculated as the product of two factors: the probability that the maximum-sized flaw in the beltline is of a given size, and the probability that the transient would occur and would have a pressure exceeding the vessel failure pressure associated with the flaw size. The probabilities of vessel failure were summed over the various sizes to obtain the total vessel failure probability.

The code developed by Gamble and Strosnider [6] calculates the probability of flaw-induced failure in the vessel beltline region using mathematical relationships based on linear-elastic fracture mechanics to model variable interaction and to estimate a failure rate. The RPV failure criterion was based on a comparison of the driving-force stress-intensity factor, $K_I$, with the static initiation toughness, $K_{Ic}$, of the material. Monte Carlo methods were used to simulate independently each of the several variables and model their interaction to obtain values of $K_I$ and $K_{Ic}$ to predict the probabilities of vessel failure. Near the end of this study, an *importance-*

*sampling* scheme was developed and incorporated into the computer code to increase the code's efficiency for performing calculations in the transition-temperature region and to allow greater accuracy for analyzing conditions associated with low-failure probabilities (see Appendix B of ref. [6]).

An early version of the VISA code [7] was used in the NRC staff evaluation of PTS as described in SECY-82-465 [8]. VISA is a simulation model, which means that the failure probability is assessed by performing a large number of deterministic evaluations with random variables selected for various parameters. The user can specify the thermal transient with either a polynomial representation or an exponential decay model, and the pressure transient can be specified with a polynomial function. The deterministic analysis in VISA assumes linear-elastic material behavior, implying that the total maximum stresses are less than the yield strength of the material. This assumption of linear-elastic deformation response allows stress components to be added through linear superposition, and the principles of linear-elastic fracture mechanics (LEFM) can be applied. For rapid thermal transients, high stresses (potentially above the yield strength of the cladding) can occur locally at the inside surface of the vessel wall; however, acceptable stress distributions can still be obtained over the remaining section if the overstressed region is relatively thin. Stress intensity factors are calculated from influence coefficients developed by Heliot, Labbens, and Pellissier-Tanon [9, 10].

Examples of internationally developed PFM/PTS codes include PASCAL (**P**FM **A**nalysis of **S**tructural **C**omponents in **A**ging **L**WR) [11-13], OPERA [14], and PARISH (**P**robabilistic **A**ssessment of **R**eactor **I**ntegrity under pressurized thermal **SH**ock) [15]. In addition, other PFM codes such as PRAISE [16] and STAR6 [17] have been developed to calculate failure probabilities considering the aged condition of RCW piping systems allowing for factors such as fatigue crack growth, stress corrosion crack growth, and changes in mechanical properties.

The above codes perform PFM/PTS analyses using Monte Carlo techniques to estimate the increase in failure probability as the vessel accumulates radiation damage over its operating life. The results of such analyses, when compared with the limit of acceptable failure probability, provide an estimate of the residual life of a reactor pressure vessel. Also results of such analyses can be used to evaluate the potential benefits of plant-specific mitigating actions designed to reduce the probability of reactor vessel failure, thus potentially extending the operating life of the vessel [18].

Previous efforts at obtaining the same probabilistic solutions to a specified PTS problem using different PFM codes have met with varying degrees of success [19-21]. Experience with the

application of OCA-P, VISA-II, and other PFM codes as well as advancements in the science of probabilistic risk assessment (PRA) over the past 15 years have provided insights into areas where the PTS PFM methodology could be improved. The FAVOR$^{EP}$ computer code was initially developed at ORNL in the early 1990s [22] (see Fig. A1) in an effort to combine the best attributes of OCA-P and VISA-II. In the ensuing years, the NRC-funded FAVOREP code has continued its advancement with the goal of providing a computational platform for incorporating additional capabilities and new developments in relevant fracture-related disciplines, as illustrated in Fig. A1.

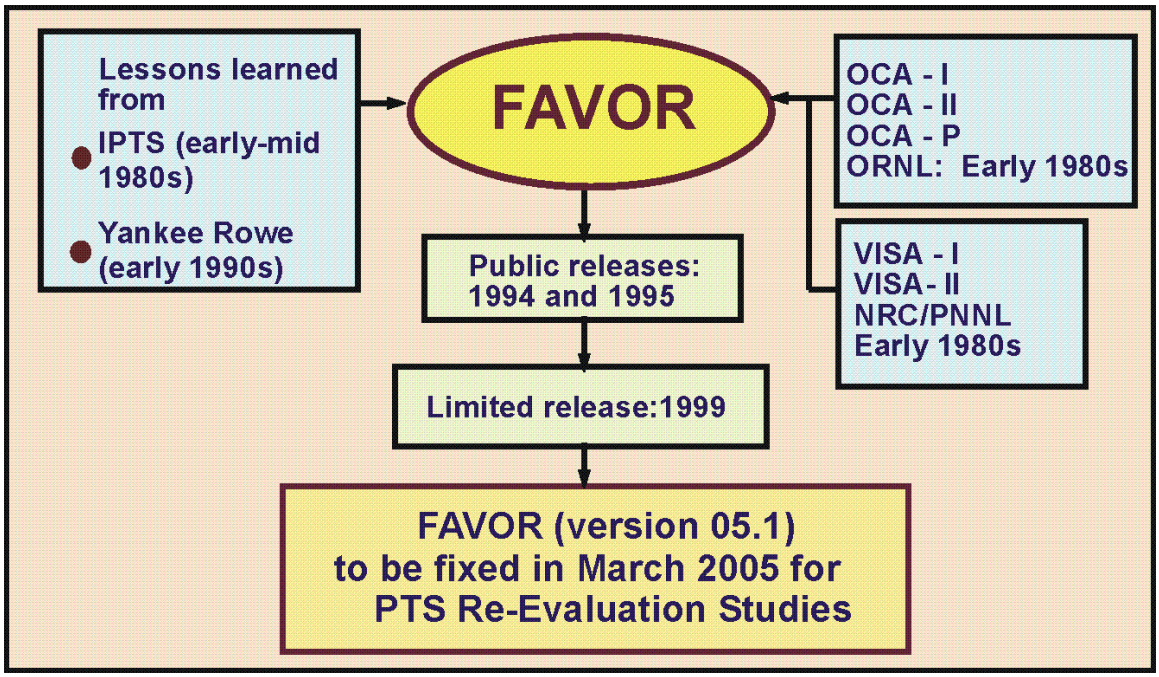


**Fig. A1. Depiction of the development history of the FAVOR$^{EP}$ code**

# References to Appendix A


1. R. D. Cheverton and D. G. Ball, *OCA-P, A Deterministic and Probabilistic Fracture Mechanics Code for Application to Pressure Vessels,* NUREG/CR-3618 (ORNL-5991), Oak Ridge National Laboratory, Oak Ridge, TN, May 1984.
2. F. A. Simonen, et al., *VISA-II – A Computer Code for Predicting the Probability of Reactor Pressure Vessel Failure*, NUREG/CR-4486 (PNL-5775), Pacific Northwest Laboratory, Richland, Washington, March 1986.
3. S. K. Iskander, R. D. Cheverton, and D. G. Ball, OCA-I, A Code for Calculating the Behavior of Flaws on the Inner Surface of a Pressure Vessel Subjected to Temperature and Pressure Transients, NUREG/CR-2113 (ORNL/NUREG-84), Oak Ridge National Laboratory, Oak Ridge, TN, 1981.
4. D. G. Ball, R. D. Cheverton, J. B. Drake, and S. K. Iskander, *OCA-II, A Code for Calculating the Behavior of 2-D and 3-D Surface Flaws in a Pressure Vessel Subjected to Temperature and Pressure Transients*, NUREG/CR-3491 (ORNL-5934), Oak Ridge National Laboratory, Oak Ridge, TN, 1983.
5. W. E. Vesely, E. K. Lynn, and F. F. Goldberg, *The Octavia Computer Code: PWR Reactor Pressure Vessel Failure Probabilities Due to Operationally Caused Pressure Transients*, NUREG-0258, U. S. Nuclear Regulatory Commission, Washington, D.C., 1978.
6. R. M. Gamble and J. Strosnider, Jr., *An Assessment of the Failure Rate for the Beltline Region of PWR Pressure Vessels During Normal Operation and Certain Transient Conditions*, NUREG-0778, U. S. Nuclear Regulatory Commission, Washington, D.C., 1981.
7. D. L. Stevens, F. A. Simonen, J. Strosnider, Jr., R. W. Klecker, D. W. Engel, and K. I. Johnson, *VISA – A Computer Code for Predicting the Probability of Reactor Pressure Vessel Failure*, NUREG/CR-3384, (PNL-4774), Pacific Northwest Laboratory, Richland, Washington, 1983.
8. Policy Issue from J. W. Dircks to NRC Commissioners, *Enclosure A: NRC Staff Evaluation of Pressurized Thermal Shock, November 1982*, SECY-82-465, November 23, 1982, Division of Nuclear Reactor Regulation, U.S. Nuclear Regulatory Commission, Washington, D.C.
9. R. Labbens, A. Pellissier-Tanon, and J. Heliot, "Practical Method for Calculating Stress-Intensity Factors Through Weight Functions," ASTM STP-590, *Mechanics of Crack Growth*, American Society for Testing and Materials, (1976) 368-384.
10. J. Heliot, R. C. Labbens, and A. Pellissier-Tanon, "Semi-Elliptical Cracks in the Mendional Plane of a Cylinder Subjected to Stress Gradients, Calculation of Stress Intensity Factors by the Boundary Integral Equations Method," *XIth National Symposium on Fracture Mechanics*, Blacksburg, VA, 1978.
11. G. Yagawa, Y. Kanto, S. Yoshimura, H. Machida, and K. Shibata, "Probabilistic Fracture Mechanics Analysis of Nuclear Structural Components: A Review of Recent Japanese Activities," *Nuclear Engineering and Design* **207**, (2001) 269-286.
12. K. Shibata, D. Kato, and Y. Li, "Development of a PFM Code for Evaluating Reliability of Pressure Components Subject to Transient Loading," *Nuclear Engineering and Design* **208**, (2001) 1-13.

13. Y. Li, D. Kato, K. Shibata, and K. Onizawa, "Improvements to a Probabilistic Fracture Mechanics Code for Evaluating the Integrity of an RPV Under Transient Loading," *International Journal of Pressure Vessels and Piping* **78**, (2001) 271-282.

14. M. Persoz, S. Hugonnard-Bruyere, et al., "Deterministic and Probabilistic Assessment of the Reactor Pressure Vessel Structural Integrity with a User-Friendly Software," PVP-Vol. 403, *presented at the ASME Pressure Vessels and Piping Conference*, (2000) 137-144.

15. B. K. Dutta, H. S. Kushwaha, and V. V. Raj, "Probabilistic Assessment of Reactor Pressure Vessel Integrity Under Pressurised Thermal Shock," *International Journal of Pressure Vessels and Piping* **76**, (1999) 445-453.

16. D. O. Harris, E. Y. Lim, et al., "Probability of Pipe Fracture in the Primary Coolant Loop of a PWR Plant," NUREG/CR-2189, 1981.

17. R. Wilson and R. A. Ainsworth, "A Probabilistic Fracture Mechanics Assessment Procedure," SMiRT 11, vol. G, (1991) 325-330.

18. T. L. Dickson and F. A. Simonen, "The Application of Probabilistic Fracture Analysis to Residual Life Evaluation of Embrittled Reactor Vessels," AD-Vol. 28, Reliability Technology, *American Society of Mechanical Engineers,* (1992) 43-55.

19. B. A. Bishop, T. L. Dickson, and F. A. Simonen, *Benchmarking of Probabilistic Fracture Mechanics Analyses of Reactor Vessels Subjected to Pressurized Thermal Shock (PTS) Loading,* Research Project 2975-5, Final Report, February 1993.

20. T. L. Dickson and R. D. Cheverton, *Review of Reactor Pressure Vessel Evaluation Report for Yankee Rowe Nuclear Power Station (YAEC No. 1735), Appendix D,* NUREG/CR-5799 (ORNL/TM-11982), Oak Ridge National Laboratory, Oak Ridge, TN, March 1992.

21. B. R. Bass, et al., *International Comparative Assessment Study of Pressurized Thermal Shock in Reactor Pressure Vessels,* NUREG/CR-6651 (ORNL/TM-1999/231), Oak Ridge National Laboratory, Oak Ridge, TN, December 1999.

22. T. L. Dickson, *FAVOR: A Fracture Analysis Code for Nuclear Reactor Pressure Vessels, Release 9401*, ORNL/NRC/LTR/94/1, Oak Ridge National Laboratory, Oak Ridge, TN, 1994.

## Appendix B – Stress-Intensity Factor Influence Coefficients

**Table B1. Influence Coefficients for Inside Axial and Circumferential Semi-elliptic Surface Flaws: $R/t$ =10 and $a/t$=0.01**
**Table B2. Influence Coefficients for Inside Axial and Circumferential Semi-elliptic Surface Flaws: $R/t$ =10 and $a/t$=0.0184**
**Table B3. Influence Coefficients for Inside Axial and Circumferential Semi-elliptic Surface Flaws: $R/t$ =10 and $a/t$=0.05**
**Table B4. Influence Coefficients for Inside Axial and Circumferential Semi-elliptic Surface Flaws: $R/t$ =10 and $a/t$=0.075**
**Table B5. Influence Coefficients for Inside Axial and Circumferential Semi-elliptic Surface Flaws: $R/t$ =10 and $a/t$=0.1**
**Table B6. Influence Coefficients for Inside Axial and Circumferential Semi-elliptic Surface Flaws: $R/t$ =10 and $a/t$=0.2**
**Table B7. Influence Coefficients for Inside Axial and Circumferential Semi-elliptic Surface Flaws: $R/t$ =10 and $a/t$=0.3**
**Table B8. Influence Coefficients for Inside Axial Semi-elliptic Surface Flaws: $R/t$ =10 and $a/t$=0.5**
**Table B9. Influence Coefficients for Inside Circumferential Semi-elliptic Surface Flaws: $R/t$ =10 and $a/t$=0.5**
**Table B10. Influence Coefficients for Inside Axial Infinite-Length Surface Flaws: $R/t$ =10**
**Table B11. Influence Coefficients for Inside Circumferential 360-Degree Surface Flaws: $R/t$ =10**

**Table B1. Influence Coefficients for Inside Axial and Circumferential Semi-elliptic Surface Flaws: $R / t = 10$ and $a / t = 0.01$**

| Aspect Ratio | Elliptic Angle (deg) | $K_0$ Uniform | $K_1$ Linear | $K_2$ Quadratic | $K_3$ Cubic | $K_0$ $t_{cl}$=0.25 in. | $K_1$ $t_{cl}$=0.25 in. | $K_0$ $t_{cl}$=0.156 in. | $K_1$ $t_{cl}$=0.156 in. |
|---|---|---|---|---|---|---|---|---|---|
| 2:1 | 0.00 | 0.764 | 0.153 | 0.061 | 0.034 | 0.764 | 0.153 | 0.764 | 0.153 |
| | 2.37 | 0.754 | 0.165 | 0.062 | 0.032 | 0.754 | 0.165 | 0.754 | 0.165 |
| | 16.60 | 0.690 | 0.192 | 0.079 | 0.040 | 0.690 | 0.192 | 0.690 | 0.192 |
| | 30.80 | 0.669 | 0.264 | 0.127 | 0.069 | 0.669 | 0.264 | 0.669 | 0.264 |
| | 45.00 | 0.660 | 0.335 | 0.196 | 0.124 | 0.660 | 0.335 | 0.660 | 0.335 |
| | 59.20 | 0.653 | 0.393 | 0.269 | 0.198 | 0.653 | 0.393 | 0.653 | 0.393 |
| | 73.40 | 0.651 | 0.434 | 0.329 | 0.268 | 0.651 | 0.434 | 0.651 | 0.434 |
| | 87.60 | 0.649 | 0.463 | 0.366 | 0.310 | 0.649 | 0.463 | 0.649 | 0.463 |
| | 90.00 | 0.649 | 0.468 | 0.372 | 0.317 | 0.649 | 0.468 | 0.649 | 0.468 |
| 6:1 | 0.00 | 0.670 | 0.134 | 0.048 | 0.024 | 0.670 | 0.134 | 0.670 | 0.134 |
| | 2.37 | 0.667 | 0.134 | 0.043 | 0.019 | 0.667 | 0.134 | 0.667 | 0.134 |
| | 16.60 | 0.654 | 0.170 | 0.055 | 0.009 | 0.654 | 0.170 | 0.654 | 0.170 |
| | 30.80 | 0.741 | 0.269 | 0.109 | 0.029 | 0.741 | 0.269 | 0.741 | 0.269 |
| | 45.00 | 0.827 | 0.381 | 0.199 | 0.100 | 0.827 | 0.381 | 0.827 | 0.381 |
| | 59.20 | 0.893 | 0.481 | 0.302 | 0.197 | 0.893 | 0.481 | 0.893 | 0.481 |
| | 73.40 | 0.938 | 0.559 | 0.389 | 0.290 | 0.938 | 0.559 | 0.938 | 0.559 |
| | 87.60 | 0.970 | 0.594 | 0.435 | 0.341 | 0.970 | 0.594 | 0.970 | 0.594 |
| | 90.00 | 0.975 | 0.601 | 0.443 | 0.350 | 0.975 | 0.601 | 0.975 | 0.601 |
| 10:1 | 0.00 | 0.515 | 0.090 | 0.020 | 0.006 | 0.515 | 0.090 | 0.515 | 0.090 |
| | 2.37 | 0.529 | 0.094 | 0.010 | 0.005 | 0.529 | 0.094 | 0.529 | 0.094 |
| | 16.60 | 0.610 | 0.146 | 0.033 | 0.005 | 0.610 | 0.146 | 0.610 | 0.146 |
| | 30.80 | 0.762 | 0.258 | 0.060 | 0.019 | 0.762 | 0.258 | 0.762 | 0.258 |
| | 45.00 | 0.889 | 0.389 | 0.171 | 0.066 | 0.889 | 0.389 | 0.889 | 0.389 |
| | 59.20 | 0.979 | 0.507 | 0.290 | 0.136 | 0.979 | 0.507 | 0.979 | 0.507 |
| | 73.40 | 1.033 | 0.593 | 0.389 | 0.249 | 1.033 | 0.593 | 1.033 | 0.593 |
| | 87.60 | 1.064 | 0.635 | 0.439 | 0.307 | 1.064 | 0.635 | 1.064 | 0.635 |
| | 90.00 | 1.069 | 0.642 | 0.447 | 0.316 | 1.069 | 0.642 | 1.069 | 0.642 |

**Table B2. Influence Coefficients for Inside Axial and Circumferential Semi-elliptic Surface Flaws: $R / t = 10$ and $a / t = 0.0184$**

| Aspect Ratio | Elliptic Angle (deg) | $K_0$ Uniform | $K_1$ Linear | $K_2$ Quadratic | $K_3$ Cubic | $K_0$ $t_{cl}$=0.25 in. | $K_1$ $t_{cl}$=0.25 in. | $K_0$ $t_{cl}$=0.156 in. | $K_1$ $t_{cl}$=0.156 in. |
|---|---|---|---|---|---|---|---|---|---|
| 2:1 | 0.00 | 0.777 | 0.155 | 0.061 | 0.034 | 0.777 | 0.155 | 0.777 | 0.155 |
| | 2.37 | 0.767 | 0.167 | 0.062 | 0.032 | 0.767 | 0.167 | 0.767 | 0.167 |
| | 16.60 | 0.700 | 0.194 | 0.079 | 0.040 | 0.700 | 0.194 | 0.700 | 0.194 |
| | 30.80 | 0.677 | 0.266 | 0.127 | 0.069 | 0.677 | 0.266 | 0.677 | 0.266 |
| | 45.00 | 0.667 | 0.338 | 0.196 | 0.125 | 0.667 | 0.338 | 0.667 | 0.338 |
| | 59.20 | 0.660 | 0.397 | 0.270 | 0.198 | 0.660 | 0.397 | 0.660 | 0.397 |
| | 73.40 | 0.657 | 0.438 | 0.330 | 0.267 | 0.657 | 0.438 | 0.657 | 0.438 |
| | 87.60 | 0.654 | 0.467 | 0.366 | 0.310 | 0.654 | 0.467 | 0.654 | 0.467 |
| | 90.00 | 0.653 | 0.472 | 0.373 | 0.317 | 0.653 | 0.472 | 0.653 | 0.472 |
| 6:1 | 0.00 | 0.653 | 0.127 | 0.043 | 0.021 | 0.653 | 0.127 | 0.653 | 0.127 |
| | 2.37 | 0.654 | 0.128 | 0.038 | 0.016 | 0.654 | 0.128 | 0.654 | 0.128 |
| | 16.60 | 0.654 | 0.168 | 0.045 | 0.021 | 0.654 | 0.168 | 0.654 | 0.168 |
| | 30.80 | 0.758 | 0.271 | 0.099 | 0.026 | 0.758 | 0.271 | 0.758 | 0.271 |
| | 45.00 | 0.852 | 0.387 | 0.192 | 0.085 | 0.852 | 0.387 | 0.852 | 0.387 |
| | 59.20 | 0.920 | 0.492 | 0.298 | 0.187 | 0.920 | 0.492 | 0.920 | 0.492 |
| | 73.40 | 0.963 | 0.569 | 0.387 | 0.283 | 0.963 | 0.569 | 0.963 | 0.569 |
| | 87.60 | 0.994 | 0.609 | 0.434 | 0.335 | 0.994 | 0.609 | 0.994 | 0.609 |
| | 90.00 | 0.999 | 0.616 | 0.442 | 0.344 | 0.999 | 0.616 | 0.999 | 0.616 |
| 10:1 | 0.00 | 0.525 | 0.092 | 0.019 | 0.007 | 0.525 | 0.092 | 0.525 | 0.092 |
| | 2.37 | 0.538 | 0.096 | 0.009 | 0.005 | 0.538 | 0.096 | 0.538 | 0.096 |
| | 16.60 | 0.621 | 0.149 | 0.039 | 0.005 | 0.621 | 0.149 | 0.621 | 0.149 |
| | 30.80 | 0.777 | 0.262 | 0.050 | 0.022 | 0.777 | 0.262 | 0.777 | 0.262 |
| | 45.00 | 0.899 | 0.392 | 0.164 | 0.075 | 0.899 | 0.392 | 0.899 | 0.392 |
| | 59.20 | 0.982 | 0.509 | 0.283 | 0.127 | 0.982 | 0.509 | 0.982 | 0.509 |
| | 73.40 | 1.033 | 0.595 | 0.383 | 0.242 | 1.033 | 0.595 | 1.033 | 0.595 |
| | 87.60 | 1.063 | 0.637 | 0.433 | 0.300 | 1.063 | 0.637 | 1.063 | 0.637 |
| | 90.00 | 1.068 | 0.644 | 0.441 | 0.310 | 1.068 | 0.644 | 1.068 | 0.644 |

**Table B3. Influence Coefficients for Inside Axial and Circumferential Semi-elliptic Surface Flaws: $R / t = 10$ and $a / t = 0.05$**

| Aspect Ratio | Elliptic Angle (deg) | $K_0$ Uniform | $K_1$ Linear | $K_2$ Quadratic | $K_3$ Cubic | $K_0$ $t_{cl}$=0.25 in. | $K_1$ $t_{cl}$=0.25 in. | $K_0$ $t_{cl}$=0.156 in. | $K_1$ $t_{cl}$=0.156 in. |
|---|---|---|---|---|---|---|---|---|---|
| 2:1 | 0.00 | 0.779 | 0.155 | 0.061 | 0.034 | 0.708 | 0.184 | 0.636 | 0.205 |
| | 2.37 | 0.769 | 0.166 | 0.062 | 0.031 | 0.701 | 0.194 | 0.624 | 0.213 |
| | 16.60 | 0.701 | 0.194 | 0.079 | 0.040 | 0.659 | 0.264 | 0.509 | 0.232 |
| | 30.80 | 0.678 | 0.267 | 0.128 | 0.070 | 0.581 | 0.340 | 0.246 | 0.124 |
| | 45.00 | 0.668 | 0.339 | 0.199 | 0.126 | 0.326 | 0.188 | 0.159 | 0.083 |
| | 59.20 | 0.661 | 0.398 | 0.273 | 0.201 | 0.233 | 0.127 | 0.128 | 0.067 |
| | 73.40 | 0.658 | 0.440 | 0.333 | 0.270 | 0.204 | 0.110 | 0.115 | 0.060 |
| | 87.60 | 0.656 | 0.469 | 0.370 | 0.313 | 0.185 | 0.099 | 0.106 | 0.055 |
| | 90.00 | 0.655 | 0.474 | 0.377 | 0.320 | 0.182 | 0.097 | 0.104 | 0.054 |
| 6:1 | 0.00 | 0.655 | 0.128 | 0.043 | 0.021 | 0.631 | 0.151 | 0.576 | 0.176 |
| | 2.37 | 0.655 | 0.128 | 0.039 | 0.016 | 0.628 | 0.156 | 0.570 | 0.177 |
| | 16.60 | 0.655 | 0.167 | 0.049 | 0.019 | 0.646 | 0.221 | 0.537 | 0.213 |
| | 30.80 | 0.758 | 0.270 | 0.104 | 0.013 | 0.688 | 0.357 | 0.340 | 0.167 |
| | 45.00 | 0.851 | 0.386 | 0.197 | 0.091 | 0.494 | 0.263 | 0.271 | 0.138 |
| | 59.20 | 0.918 | 0.492 | 0.305 | 0.193 | 0.422 | 0.217 | 0.253 | 0.128 |
| | 73.40 | 0.962 | 0.569 | 0.395 | 0.290 | 0.396 | 0.201 | 0.241 | 0.121 |
| | 87.60 | 0.992 | 0.609 | 0.443 | 0.342 | 0.374 | 0.189 | 0.231 | 0.115 |
| | 90.00 | 0.997 | 0.616 | 0.450 | 0.351 | 0.370 | 0.186 | 0.229 | 0.115 |
| 10:1 | 0.00 | 0.523 | 0.092 | 0.021 | 0.005 | 0.533 | 0.119 | 0.496 | 0.149 |
| | 2.37 | 0.537 | 0.095 | 0.011 | 0.015 | 0.543 | 0.121 | 0.504 | 0.146 |
| | 16.60 | 0.622 | 0.147 | 0.033 | 0.050 | 0.631 | 0.149 | 0.547 | 0.199 |
| | 30.80 | 0.778 | 0.261 | 0.061 | 0.080 | 0.718 | 0.348 | 0.376 | 0.182 |
| | 45.00 | 0.898 | 0.391 | 0.171 | 0.065 | 0.550 | 0.286 | 0.349 | 0.156 |
| | 59.20 | 0.981 | 0.509 | 0.292 | 0.138 | 0.474 | 0.241 | 0.287 | 0.144 |
| | 73.40 | 1.034 | 0.596 | 0.392 | 0.252 | 0.444 | 0.224 | 0.273 | 0.136 |
| | 87.60 | 1.063 | 0.638 | 0.442 | 0.310 | 0.418 | 0.221 | 0.260 | 0.130 |
| | 90.00 | 1.068 | 0.645 | 0.450 | 0.320 | 0.414 | 0.221 | 0.257 | 0.128 |

**Table B4. Influence Coefficients for Inside Axial and Circumferential Semi-elliptic Surface Flaws: $R / t = 10$ and $a / t = 0.075$**

| Aspect Ratio | Elliptic Angle (deg) | $K_0$ Uniform | $K_1$ Linear | $K_2$ Quadratic | $K_3$ Cubic | $K_0$ $t_{cl}$=0.25 in. | $K_1$ $t_{cl}$=0.25 in. | $K_0$ $t_{cl}$=0.156 in. | $K_1$ $t_{cl}$=0.156 in. |
|---|---|---|---|---|---|---|---|---|---|
| 2:1 | 0.00 | 0.740 | 0.128 | 0.045 | 0.023 | 0.650 | 0.197 | 0.572 | 0.210 |
| | 7.03 | 0.737 | 0.147 | 0.055 | 0.028 | 0.629 | 0.220 | 0.529 | 0.217 |
| | 14.20 | 0.721 | 0.179 | 0.067 | 0.033 | 0.593 | 0.271 | 0.400 | 0.177 |
| | 35.90 | 0.671 | 0.298 | 0.155 | 0.086 | 0.219 | 0.120 | 0.118 | 0.060 |
| | 48.70 | 0.661 | 0.355 | 0.220 | 0.143 | 0.161 | 0.085 | 0.094 | 0.048 |
| | 61.50 | 0.656 | 0.404 | 0.285 | 0.212 | 0.137 | 0.071 | 0.081 | 0.042 |
| | 74.30 | 0.654 | 0.439 | 0.336 | 0.273 | 0.125 | 0.065 | 0.075 | 0.038 |
| | 87.00 | 0.651 | 0.468 | 0.372 | 0.313 | 0.114 | 0.065 | 0.068 | 0.035 |
| | 90.00 | 0.651 | 0.475 | 0.381 | 0.322 | 0.111 | 0.065 | 0.067 | 0.034 |
| 6:1 | 0.00 | 0.650 | 0.098 | 0.029 | 0.013 | 0.591 | 0.170 | 0.527 | 0.188 |
| | 2.37 | 0.635 | 0.104 | 0.031 | 0.013 | 0.571 | 0.180 | 0.495 | 0.179 |
| | 16.60 | 0.672 | 0.140 | 0.040 | 0.014 | 0.590 | 0.243 | 0.441 | 0.187 |
| | 30.80 | 0.786 | 0.309 | 0.139 | 0.048 | 0.334 | 0.171 | 0.195 | 0.098 |
| | 45.00 | 0.862 | 0.410 | 0.229 | 0.125 | 0.294 | 0.149 | 0.180 | 0.090 |
| | 59.20 | 0.918 | 0.501 | 0.326 | 0.219 | 0.275 | 0.138 | 0.170 | 0.085 |
| | 73.40 | 0.952 | 0.566 | 0.404 | 0.303 | 0.265 | 0.133 | 0.164 | 0.082 |
| | 87.60 | 0.980 | 0.602 | 0.446 | 0.351 | 0.265 | 0.133 | 0.159 | 0.080 |
| | 90.00 | 0.987 | 0.611 | 0.456 | 0.362 | 0.265 | 0.132 | 0.157 | 0.079 |
| 10:1 | 0.00 | 0.547 | 0.073 | 0.016 | 0.006 | 0.514 | 0.148 | 0.469 | 0.171 |
| | 2.37 | 0.551 | 0.074 | 0.016 | 0.003 | 0.514 | 0.145 | 0.458 | 0.131 |
| | 16.60 | 0.636 | 0.113 | 0.023 | 0.009 | 0.583 | 0.220 | 0.465 | 0.173 |
| | 30.80 | 0.812 | 0.303 | 0.124 | 0.018 | 0.375 | 0.189 | 0.223 | 0.112 |
| | 45.00 | 0.914 | 0.419 | 0.225 | 0.111 | 0.335 | 0.168 | 0.206 | 0.103 |
| | 59.20 | 0.982 | 0.522 | 0.332 | 0.216 | 0.310 | 0.156 | 0.193 | 0.096 |
| | 73.40 | 1.022 | 0.593 | 0.416 | 0.307 | 0.298 | 0.149 | 0.185 | 0.093 |
| | 87.60 | 1.048 | 0.631 | 0.461 | 0.356 | 0.295 | 0.147 | 0.185 | 0.092 |
| | 90.00 | 1.055 | 0.639 | 0.471 | 0.368 | 0.295 | 0.147 | 0.184 | 0.092 |

**Table B5. Influence Coefficients for Inside Axial and Circumferential Semi-elliptic Surface Flaws: $R / t = 10$ and $a / t = 0.1$**

| Aspect Ratio | Elliptic Angle (deg) | $K_0$ Uniform | $K_1$ Linear | $K_2$ Quadratic | $K_3$ Cubic | $K_0$ $t_{cl}$=0.25 in. | $K_1$ $t_{cl}$=0.25 in. | $K_0$ $t_{cl}$=0.156 in. | $K_1$ $t_{cl}$=0.156 in. |
|---|---|---|---|---|---|---|---|---|---|
| 2:1 | 0.00 | 0.729 | 0.124 | 0.044 | 0.023 | 0.596 | 0.195 | 0.519 | 0.205 |
| | 5.27 | 0.741 | 0.139 | 0.053 | 0.027 | 0.582 | 0.208 | 0.483 | 0.198 |
| | 17.10 | 0.722 | 0.230 | 0.096 | 0.048 | 0.366 | 0.213 | 0.168 | 0.086 |
| | 31.10 | 0.676 | 0.273 | 0.133 | 0.072 | 0.176 | 0.097 | 0.095 | 0.048 |
| | 45.10 | 0.664 | 0.339 | 0.201 | 0.127 | 0.122 | 0.064 | 0.072 | 0.037 |
| | 59.10 | 0.658 | 0.396 | 0.274 | 0.200 | 0.101 | 0.052 | 0.061 | 0.031 |
| | 73.10 | 0.655 | 0.436 | 0.333 | 0.268 | 0.091 | 0.047 | 0.056 | 0.028 |
| | 87.00 | 0.653 | 0.470 | 0.373 | 0.313 | 0.082 | 0.047 | 0.050 | 0.025 |
| | 90.00 | 0.652 | 0.477 | 0.382 | 0.323 | 0.080 | 0.047 | 0.049 | 0.025 |
| 6:1 | 0.00 | 0.641 | 0.094 | 0.029 | 0.014 | 0.550 | 0.175 | 0.485 | 0.188 |
| | 2.37 | 0.630 | 0.098 | 0.031 | 0.015 | 0.532 | 0.176 | 0.454 | 0.168 |
| | 16.60 | 0.701 | 0.196 | 0.067 | 0.015 | 0.427 | 0.232 | 0.211 | 0.108 |
| | 30.80 | 0.756 | 0.273 | 0.115 | 0.039 | 0.258 | 0.131 | 0.152 | 0.077 |
| | 45.00 | 0.848 | 0.385 | 0.207 | 0.109 | 0.224 | 0.112 | 0.138 | 0.069 |
| | 59.20 | 0.915 | 0.489 | 0.312 | 0.207 | 0.208 | 0.104 | 0.129 | 0.065 |
| | 73.40 | 0.958 | 0.565 | 0.402 | 0.302 | 0.200 | 0.100 | 0.125 | 0.062 |
| | 87.60 | 0.989 | 0.607 | 0.450 | 0.356 | 0.200 | 0.100 | 0.120 | 0.060 |
| | 90.00 | 0.996 | 0.616 | 0.461 | 0.367 | 0.200 | 0.100 | 0.119 | 0.060 |
| 10:1 | 0.00 | 0.543 | 0.067 | 0.016 | 0.007 | 0.490 | 0.148 | 0.443 | 0.168 |
| | 2.37 | 0.536 | 0.069 | 0.016 | 0.006 | 0.479 | 0.144 | 0.421 | 0.138 |
| | 16.60 | 0.670 | 0.175 | 0.047 | 0.027 | 0.443 | 0.220 | 0.229 | 0.117 |
| | 30.80 | 0.778 | 0.269 | 0.102 | 0.030 | 0.291 | 0.143 | 0.176 | 0.088 |
| | 45.00 | 0.897 | 0.395 | 0.202 | 0.089 | 0.256 | 0.128 | 0.159 | 0.080 |
| | 59.20 | 0.979 | 0.512 | 0.318 | 0.199 | 0.236 | 0.118 | 0.147 | 0.074 |
| | 73.40 | 1.029 | 0.597 | 0.416 | 0.302 | 0.226 | 0.113 | 0.141 | 0.071 |
| | 87.60 | 1.060 | 0.640 | 0.466 | 0.358 | 0.224 | 0.111 | 0.140 | 0.070 |
| | 90.00 | 1.066 | 0.649 | 0.477 | 0.370 | 0.223 | 0.111 | 0.140 | 0.070 |

**Table B6. Influence Coefficients for Inside Axial and Circumferential Semi-elliptic Surface Flaws: $R / t = 10$ and $a / t = 0.2$**

| Aspect Ratio | Elliptic Angle (deg) | $K_0$ Uniform | $K_1$ Linear | $K_2$ Quadratic | $K_3$ Cubic | $K_0$ $t_{cl}$=0.25 in. | $K_1$ $t_{cl}$=0.25 in. | $K_0$ $t_{cl}$=0.156 in. | $K_1$ $t_{cl}$=0.156 in. |
|---|---|---|---|---|---|---|---|---|---|
| 2:1 | 0.00 | 0.692 | 0.127 | 0.046 | 0.024 | 0.457 | 0.173 | 0.393 | 0.178 |
| | 19.80 | 0.695 | 0.214 | 0.089 | 0.044 | 0.155 | 0.080 | 0.071 | 0.031 |
| | 31.10 | 0.679 | 0.273 | 0.133 | 0.073 | 0.090 | 0.050 | 0.048 | 0.023 |
| | 42.50 | 0.671 | 0.332 | 0.192 | 0.120 | 0.061 | 0.031 | 0.038 | 0.019 |
| | 53.80 | 0.665 | 0.383 | 0.255 | 0.182 | 0.052 | 0.026 | 0.032 | 0.016 |
| | 65.20 | 0.660 | 0.423 | 0.312 | 0.245 | 0.047 | 0.023 | 0.029 | 0.014 |
| | 76.50 | 0.658 | 0.450 | 0.354 | 0.296 | 0.044 | 0.022 | 0.027 | 0.014 |
| | 87.90 | 0.656 | 0.475 | 0.384 | 0.329 | 0.041 | 0.021 | 0.025 | 0.013 |
| | 90.00 | 0.656 | 0.479 | 0.389 | 0.335 | 0.040 | 0.020 | 0.025 | 0.013 |
| 6:1 | 0.00 | 0.617 | 0.101 | 0.034 | 0.017 | 0.434 | 0.163 | 0.377 | 0.171 |
| | 2.37 | 0.699 | 0.194 | 0.066 | 0.019 | 0.180 | 0.090 | 0.093 | 0.043 |
| | 16.60 | 0.781 | 0.280 | 0.118 | 0.045 | 0.127 | 0.063 | 0.079 | 0.039 |
| | 30.80 | 0.856 | 0.375 | 0.195 | 0.101 | 0.116 | 0.058 | 0.072 | 0.036 |
| | 45.00 | 0.915 | 0.464 | 0.283 | 0.180 | 0.110 | 0.055 | 0.069 | 0.034 |
| | 59.20 | 0.958 | 0.538 | 0.366 | 0.265 | 0.106 | 0.053 | 0.066 | 0.033 |
| | 73.40 | 0.986 | 0.590 | 0.430 | 0.336 | 0.104 | 0.052 | 0.065 | 0.032 |
| | 87.60 | 1.010 | 0.619 | 0.464 | 0.373 | 0.102 | 0.051 | 0.064 | 0.032 |
| | 90.00 | 1.020 | 0.624 | 0.470 | 0.380 | 0.101 | 0.051 | 0.063 | 0.032 |
| 10:1 | 0.00 | 0.525 | 0.077 | 0.022 | 0.009 | 0.402 | 0.149 | 0.355 | 0.160 |
| | 2.37 | 0.694 | 0.183 | 0.050 | 0.025 | 0.200 | 0.100 | 0.106 | 0.050 |
| | 16.60 | 0.815 | 0.280 | 0.107 | 0.011 | 0.149 | 0.073 | 0.093 | 0.046 |
| | 30.80 | 0.915 | 0.387 | 0.190 | 0.083 | 0.137 | 0.068 | 0.085 | 0.043 |
| | 45.00 | 0.991 | 0.488 | 0.287 | 0.170 | 0.130 | 0.065 | 0.081 | 0.040 |
| | 59.20 | 1.045 | 0.572 | 0.379 | 0.263 | 0.125 | 0.062 | 0.078 | 0.039 |
| | 73.40 | 1.080 | 0.631 | 0.449 | 0.340 | 0.122 | 0.061 | 0.077 | 0.038 |
| | 87.60 | 1.103 | 0.660 | 0.483 | 0.378 | 0.120 | 0.060 | 0.075 | 0.037 |
| | 90.00 | 1.107 | 0.666 | 0.490 | 0.385 | 0.119 | 0.060 | 0.075 | 0.037 |

**Table B7. Influence Coefficients for Inside Axial and Circumferential Semi-elliptic Surface Flaws: $R / t = 10$ and $a / t = 0.3$**

| Aspect Ratio | Elliptic Angle (deg) | $K_0$ Uniform | $K_1$ Linear | $K_2$ Quadratic | $K_3$ Cubic | $K_0$ $t_{cl}$=0.25 in. | $K_1$ $t_{cl}$=0.25 in. | $K_0$ $t_{cl}$=0.156 in. | $K_1$ $t_{cl}$=0.156 in. |
|---|---|---|---|---|---|---|---|---|---|
| 2:1 | 0.00 | 0.723 | 0.127 | 0.048 | 0.026 | 0.404 | 0.188 | 0.334 | 0.176 |
| | 17.40 | 0.708 | 0.203 | 0.083 | 0.042 | 0.102 | 0.049 | 0.056 | 0.025 |
| | 29.10 | 0.690 | 0.264 | 0.126 | 0.068 | 0.058 | 0.028 | 0.034 | 0.016 |
| | 40.90 | 0.680 | 0.326 | 0.185 | 0.114 | 0.043 | 0.021 | 0.026 | 0.013 |
| | 52.60 | 0.673 | 0.381 | 0.251 | 0.177 | 0.036 | 0.018 | 0.022 | 0.011 |
| | 64.40 | 0.668 | 0.423 | 0.310 | 0.242 | 0.032 | 0.016 | 0.020 | 0.010 |
| | 76.10 | 0.665 | 0.452 | 0.355 | 0.297 | 0.030 | 0.015 | 0.018 | 0.009 |
| | 87.90 | 0.662 | 0.478 | 0.385 | 0.331 | 0.028 | 0.014 | 0.017 | 0.009 |
| | 90.00 | 0.662 | 0.482 | 0.391 | 0.337 | 0.027 | 0.014 | 0.017 | 0.009 |
| 6:1 | 0.00 | 0.665 | 0.112 | 0.041 | 0.022 | 0.380 | 0.181 | 0.315 | 0.167 |
| | 2.37 | 0.715 | 0.190 | 0.068 | 0.027 | 0.117 | 0.054 | 0.069 | 0.032 |
| | 16.60 | 0.804 | 0.277 | 0.118 | 0.051 | 0.093 | 0.045 | 0.057 | 0.028 |
| | 30.80 | 0.886 | 0.376 | 0.194 | 0.104 | 0.085 | 0.042 | 0.053 | 0.026 |
| | 45.00 | 0.951 | 0.470 | 0.284 | 0.182 | 0.081 | 0.040 | 0.050 | 0.025 |
| | 59.20 | 0.998 | 0.549 | 0.372 | 0.270 | 0.078 | 0.039 | 0.049 | 0.024 |
| | 73.40 | 1.028 | 0.605 | 0.439 | 0.345 | 0.077 | 0.038 | 0.048 | 0.024 |
| | 87.60 | 1.053 | 0.635 | 0.475 | 0.384 | 0.075 | 0.038 | 0.047 | 0.024 |
| | 90.00 | 1.058 | 0.640 | 0.481 | 0.391 | 0.075 | 0.037 | 0.047 | 0.023 |
| 10:1 | 0.00 | 0.562 | 0.085 | 0.029 | 0.014 | 0.344 | 0.168 | 0.290 | 0.153 |
| | 2.37 | 0.707 | 0.176 | 0.052 | 0.016 | 0.128 | 0.059 | 0.078 | 0.037 |
| | 16.60 | 0.848 | 0.276 | 0.104 | 0.016 | 0.110 | 0.054 | 0.068 | 0.034 |
| | 30.80 | 0.962 | 0.389 | 0.188 | 0.082 | 0.102 | 0.051 | 0.064 | 0.032 |
| | 45.00 | 1.051 | 0.498 | 0.288 | 0.169 | 0.098 | 0.049 | 0.062 | 0.031 |
| | 59.20 | 1.115 | 0.590 | 0.385 | 0.265 | 0.096 | 0.048 | 0.060 | 0.030 |
| | 73.40 | 1.157 | 0.653 | 0.460 | 0.346 | 0.095 | 0.047 | 0.060 | 0.030 |
| | 87.60 | 1.183 | 0.685 | 0.496 | 0.387 | 0.094 | 0.047 | 0.059 | 0.029 |
| | 90.00 | 1.187 | 0.691 | 0.503 | 0.394 | 0.094 | 0.047 | 0.059 | 0.029 |

**Table B8. Influence Coefficients for Inside Axial Semi-elliptic Surface Flaws: $R / t = 10$ and $a / t = 0.5$**

| Aspect Ratio | Elliptic Angle (deg) | $K_0$ Uniform | $K_1$ Linear | $K_2$ Quadratic | $K_3$ Cubic | $K_0$ $t_{cl}$=0.25 in. | $K_1$ $t_{cl}$=0.25 in. | $K_0$ $t_{cl}$=0.156 in. | $K_1$ $t_{cl}$=0.156 in. |
|---|---|---|---|---|---|---|---|---|---|
| 2:1 | 0.00 | 0.736 | 0.132 | 0.053 | 0.029 | 0.327 | 0.162 | 0.272 | 0.150 |
| | 15.40 | 0.746 | 0.203 | 0.083 | 0.043 | 0.079 | 0.037 | 0.045 | 0.020 |
| | 27.50 | 0.719 | 0.263 | 0.124 | 0.067 | 0.042 | 0.020 | 0.025 | 0.012 |
| | 39.60 | 0.704 | 0.327 | 0.183 | 0.112 | 0.029 | 0.014 | 0.018 | 0.009 |
| | 51.70 | 0.693 | 0.383 | 0.249 | 0.175 | 0.023 | 0.012 | 0.015 | 0.007 |
| | 63.70 | 0.685 | 0.426 | 0.311 | 0.242 | 0.021 | 0.010 | 0.013 | 0.006 |
| | 75.80 | 0.681 | 0.456 | 0.357 | 0.299 | 0.019 | 0.009 | 0.012 | 0.006 |
| | 87.90 | 0.676 | 0.483 | 0.389 | 0.334 | 0.018 | 0.009 | 0.011 | 0.006 |
| | 90.00 | 0.676 | 0.488 | 0.395 | 0.340 | 0.017 | 0.009 | 0.011 | 0.005 |
| 6:1 | 0.00 | 0.758 | 0.142 | 0.059 | 0.033 | 0.322 | 0.163 | 0.268 | 0.149 |
| | 2.37 | 0.814 | 0.213 | 0.083 | 0.040 | 0.091 | 0.041 | 0.054 | 0.025 |
| | 16.60 | 0.908 | 0.302 | 0.132 | 0.065 | 0.070 | 0.034 | 0.043 | 0.021 |
| | 30.80 | 0.998 | 0.405 | 0.208 | 0.116 | 0.065 | 0.032 | 0.040 | 0.020 |
| | 45.00 | 1.069 | 0.504 | 0.300 | 0.195 | 0.062 | 0.031 | 0.039 | 0.019 |
| | 59.20 | 1.120 | 0.588 | 0.392 | 0.285 | 0.061 | 0.030 | 0.038 | 0.019 |
| | 73.40 | 1.153 | 0.647 | 0.463 | 0.363 | 0.060 | 0.030 | 0.038 | 0.019 |
| | 87.60 | 1.182 | 0.679 | 0.500 | 0.404 | 0.059 | 0.029 | 0.037 | 0.018 |
| | 90.00 | 1.187 | 0.685 | 0.506 | 0.411 | 0.059 | 0.029 | 0.037 | 0.018 |
| 10:1 | 0.00 | 0.666 | 0.119 | 0.049 | 0.028 | 0.302 | 0.156 | 0.254 | 0.140 |
| | 2.37 | 0.822 | 0.208 | 0.077 | 0.033 | 0.097 | 0.044 | 0.060 | 0.028 |
| | 16.60 | 0.995 | 0.316 | 0.131 | 0.056 | 0.086 | 0.042 | 0.054 | 0.027 |
| | 30.80 | 1.138 | 0.440 | 0.216 | 0.112 | 0.083 | 0.041 | 0.052 | 0.026 |
| | 45.00 | 1.251 | 0.560 | 0.321 | 0.198 | 0.083 | 0.041 | 0.052 | 0.026 |
| | 59.20 | 1.335 | 0.662 | 0.425 | 0.298 | 0.083 | 0.041 | 0.052 | 0.026 |
| | 73.40 | 1.390 | 0.734 | 0.506 | 0.383 | 0.083 | 0.041 | 0.052 | 0.026 |
| | 87.60 | 1.423 | 0.770 | 0.546 | 0.427 | 0.083 | 0.041 | 0.052 | 0.026 |
| | 90.00 | 1.429 | 0.776 | 0.553 | 0.434 | 0.083 | 0.041 | 0.052 | 0.026 |

**Table B9. Influence Coefficients for Inside Circumferential Semi-elliptic Surface Flaws: $R / t = 10$ and $a / t = 0.5$**

| Aspect Ratio | Elliptic Angle (deg) | $K_0$ Uniform | $K_1$ Linear | $K_2$ Quadratic | $K_3$ Cubic | $K_0$ $t_{cl}$=0.25 in. | $K_1$ $t_{cl}$=0.25 in. | $K_0$ $t_{cl}$=0.156 in. | $K_1$ $t_{cl}$=0.156 in. |
|---|---|---|---|---|---|---|---|---|---|
| 2:1 | 0.00 | 0.741 | 0.134 | 0.054 | 0.030 | 0.324 | 0.162 | 0.269 | 0.151 |
| | 15.40 | 0.750 | 0.205 | 0.084 | 0.044 | 0.079 | 0.038 | 0.045 | 0.020 |
| | 27.50 | 0.721 | 0.264 | 0.124 | 0.067 | 0.042 | 0.020 | 0.025 | 0.012 |
| | 39.60 | 0.706 | 0.328 | 0.183 | 0.112 | 0.029 | 0.014 | 0.018 | 0.009 |
| | 51.70 | 0.698 | 0.384 | 0.250 | 0.175 | 0.024 | 0.012 | 0.015 | 0.007 |
| | 63.70 | 0.692 | 0.430 | 0.312 | 0.243 | 0.021 | 0.010 | 0.013 | 0.007 |
| | 75.80 | 0.686 | 0.461 | 0.360 | 0.301 | 0.019 | 0.010 | 0.012 | 0.006 |
| | 87.90 | 0.682 | 0.488 | 0.392 | 0.336 | 0.020 | 0.010 | 0.012 | 0.006 |
| | 90.00 | 0.682 | 0.493 | 0.398 | 0.343 | 0.020 | 0.009 | 0.013 | 0.006 |
| 6:1 | 0.00 | 0.727 | 0.132 | 0.053 | 0.030 | 0.315 | 0.161 | 0.262 | 0.147 |
| | 15.40 | 0.786 | 0.205 | 0.079 | 0.037 | 0.087 | 0.039 | 0.052 | 0.024 |
| | 27.50 | 0.882 | 0.295 | 0.128 | 0.062 | 0.067 | 0.032 | 0.041 | 0.020 |
| | 39.60 | 0.974 | 0.398 | 0.205 | 0.114 | 0.062 | 0.031 | 0.038 | 0.019 |
| | 51.70 | 1.049 | 0.499 | 0.298 | 0.193 | 0.060 | 0.030 | 0.037 | 0.019 |
| | 63.70 | 1.103 | 0.584 | 0.390 | 0.284 | 0.058 | 0.029 | 0.036 | 0.018 |
| | 75.80 | 1.138 | 0.644 | 0.462 | 0.362 | 0.057 | 0.029 | 0.036 | 0.018 |
| | 87.90 | 1.166 | 0.676 | 0.499 | 0.403 | 0.058 | 0.029 | 0.036 | 0.018 |
| | 90.00 | 1.171 | 0.682 | 0.506 | 0.410 | 0.058 | 0.029 | 0.036 | 0.018 |
| 10:1 | 0.00 | 0.616 | 0.101 | 0.040 | 0.023 | 0.291 | 0.152 | 0.247 | 0.138 |
| | 15.40 | 0.770 | 0.195 | 0.071 | 0.028 | 0.090 | 0.039 | 0.055 | 0.026 |
| | 27.50 | 0.936 | 0.301 | 0.125 | 0.053 | 0.078 | 0.038 | 0.049 | 0.024 |
| | 39.60 | 1.076 | 0.424 | 0.211 | 0.109 | 0.075 | 0.037 | 0.047 | 0.024 |
| | 51.70 | 1.190 | 0.544 | 0.315 | 0.196 | 0.075 | 0.037 | 0.047 | 0.023 |
| | 63.70 | 1.275 | 0.647 | 0.420 | 0.295 | 0.075 | 0.037 | 0.047 | 0.023 |
| | 75.80 | 1.330 | 0.719 | 0.501 | 0.381 | 0.075 | 0.037 | 0.047 | 0.023 |
| | 87.90 | 1.363 | 0.755 | 0.542 | 0.425 | 0.075 | 0.037 | 0.047 | 0.024 |
| | 90.00 | 1.368 | 0.762 | 0.549 | 0.433 | 0.075 | 0.037 | 0.047 | 0.024 |

**Table B10. Influence Coefficients for Inside Axial Infinite-Length Surface Flaws, $R / t = 10$**

| | $0.1\ t^{1/2}\ K^*$ | | | | | |
|---|---|---|---|---|---|---|
| $a' / a$ | $a/t$=0.01 | $a/t$=0.02 | $a/t$=0.03 | $a/t$=0.05 | $a/t$=0.075 | $a/t$=0.10 |
| 0 | 1.434 | 1.029 | 0.846 | 0.667 | 0.565 | 0.511 |
| 0.0556 | 1.435 | 1.029 | 0.846 | 0.667 | 0.564 | 0.510 |
| 0.1111 | 1.436 | 1.029 | 0.846 | 0.666 | 0.563 | 0.508 |
| 0.1667 | 1.436 | 1.028 | 0.846 | 0.665 | 0.562 | 0.506 |
| 0.2222 | 1.438 | 1.029 | 0.846 | 0.665 | 0.561 | 0.505 |
| 0.2778 | 1.442 | 1.032 | 0.848 | 0.666 | 0.561 | 0.504 |
| 0.3333 | 1.450 | 1.037 | 0.852 | 0.669 | 0.563 | 0.505 |
| 0.3888 | 1.463 | 1.046 | 0.859 | 0.674 | 0.566 | 0.507 |
| 0.4444 | 1.482 | 1.058 | 0.869 | 0.682 | 0.571 | 0.511 |
| 0.500 | 1.509 | 1.077 | 0.884 | 0.693 | 0.580 | 0.517 |
| 0.5556 | 1.546 | 1.103 | 0.905 | 0.708 | 0.592 | 0.527 |
| 0.6111 | 1.598 | 1.138 | 0.934 | 0.731 | 0.609 | 0.541 |
| 0.6666 | 1.669 | 1.188 | 0.974 | 0.761 | 0.633 | 0.561 |
| 0.7222 | 1.768 | 1.258 | 1.031 | 0.804 | 0.668 | 0.590 |
| 0.7778 | 1.913 | 1.360 | 1.113 | 0.868 | 0.718 | 0.632 |
| 0.8333 | 2.138 | 1.518 | 1.242 | 0.967 | 0.798 | 0.699 |
| 0.8888 | 2.534 | 1.798 | 1.470 | 1.143 | 0.940 | 0.821 |
| 0.9166 | 2.878 | 2.041 | 1.668 | 1.294 | 1.064 | 0.927 |
| 0.9444 | 3.499 | 2.624 | 2.187 | 1.749 | 1.385 | 1.224 |
| 0.9639 | 5.831 | 4.227 | 3.499 | 2.770 | 2.187 | 1.895 |
| 0.9778 | 11.225 | 7.289 | 5.685 | 4.227 | 3.426 | 2.916 |
| 0.9889 | 17.493 | 11.662 | 8.746 | 6.414 | 5.102 | 4.373 |

| a'/a | a/t=0.2 | a/t=0.3 | a/t=0.4 |
|---|---|---|---|
| 0 | 0.461 | 0.510 | 0.617 |
| 0.0552 | 0.457 | 0.502 | 0.602 |
| 0.1103 | 0.452 | 0.492 | 0.586 |
| 0.1655 | 0.447 | 0.483 | 0.571 |
| 0.2206 | 0.443 | 0.475 | 0.556 |
| 0.2757 | 0.439 | 0.466 | 0.542 |
| 0.3309 | 0.436 | 0.459 | 0.527 |
| 0.3861 | 0.434 | 0.451 | 0.513 |
| 0.4412 | 0.432 | 0.445 | 0.500 |
| 0.4963 | 0.433 | 0.440 | 0.488 |
| 0.5515 | 0.435 | 0.436 | 0.477 |
| 0.6066 | 0.440 | 0.434 | 0.467 |
| 0.6618 | 0.450 | 0.435 | 0.460 |
| 0.7169 | 0.464 | 0.440 | 0.456 |
| 0.7721 | 0.487 | 0.453 | 0.457 |
| 0.8272 | 0.526 | 0.477 | 0.468 |
| 0.8824 | 0.598 | 0.527 | 0.501 |
| 0.9118 | 0.665 | 0.577 | 0.538 |
| 0.9412 | 0.875 | 0.729 | 0.671 |
| 0.9618 | 1.385 | 1.020 | 0.948 |
| 0.9765 | 2.187 | 1.749 | 1.604 |
| 0.9882 | 2.916 | 2.478 | 2.187 |

| a'/a | a/t=0.5 |
|---|---|
| 0 | 0.781 |
| 0.059 | 0.755 |
| 0.118 | 0.730 |
| 0.176 | 0.704 |
| 0.235 | 0.679 |
| 0.294 | 0.654 |
| 0.353 | 0.630 |
| 0.412 | 0.605 |
| 0.471 | 0.582 |
| 0.529 | 0.559 |
| 0.588 | 0.538 |
| 0.647 | 0.518 |
| 0.706 | 0.501 |
| 0.750 | 0.491 |
| 0.794 | 0.485 |
| 0.838 | 0.486 |
| 0.882 | 0.501 |
| 0.912 | 0.526 |
| 0.941 | 0.656 |
| 0.962 | 0.875 |
| 0.976 | 1.312 |
| 0.988 | 2.041 |

**Table B10. (continued) Influence Coefficients for Inside Axial Infinite-Length Surface Flaws, $R / t = 10$**

$0.1\, t^{1/2} K^*$

| a'/a | a/t=0.6 | a'/a | a/t=0.7 | a'/a | a/t=0.8 | a'/a | a/t=0.9 | a/t=0.95 |
|---|---|---|---|---|---|---|---|---|
| 0 | 1.021 | 0 | 1.35 | 0 | 1.739 | 0 | 1.952 | 1.902 |
| 0.0564 | 0.983 | 0.057 | 1.294 | 0.058 | 1.661 | 0.058 | 1.866 | 1.827 |
| 0.1127 | 0.946 | 0.115 | 1.238 | 0.116 | 1.583 | 0.117 | 1.779 | 1.752 |
| 0.1691 | 0.908 | 0.172 | 1.182 | 0.174 | 1.506 | 0.175 | 1.694 | 1.678 |
| 0.2255 | 0.871 | 0.229 | 1.127 | 0.232 | 1.428 | 0.233 | 1.608 | 1.604 |
| 0.2819 | 0.834 | 0.286 | 1.071 | 0.289 | 1.351 | 0.292 | 1.523 | 1.529 |
| 0.3382 | 0.798 | 0.343 | 1.016 | 0.347 | 1.275 | 0.35 | 1.438 | 1.456 |
| 0.3946 | 0.761 | 0.401 | 0.961 | 0.405 | 1.198 | 0.409 | 1.354 | 1.381 |
| 0.451 | 0.725 | 0.458 | 0.906 | 0.463 | 1.122 | 0.467 | 1.27 | 1.308 |
| 0.5074 | 0.69 | 0.515 | 0.852 | 0.521 | 1.047 | 0.526 | 1.186 | 1.234 |
| 0.5637 | 0.655 | 0.572 | 0.799 | 0.579 | 0.971 | 0.584 | 1.102 | 1.162 |
| 0.6201 | 0.622 | 0.63 | 0.747 | 0.637 | 0.897 | 0.643 | 1.019 | 1.088 |
| 0.6765 | 0.59 | 0.687 | 0.696 | 0.695 | 0.824 | 0.701 | 0.936 | 1.017 |
| 0.7328 | 0.561 | 0.744 | 0.648 | 0.753 | 0.752 | 0.759 | 0.854 | 0.947 |
| 0.7892 | 0.536 | 0.802 | 0.604 | 0.811 | 0.685 | 0.818 | 0.773 | 0.878 |
| 0.8456 | 0.521 | 0.859 | 0.569 | 0.869 | 0.627 | 0.876 | 0.699 | 0.815 |
| 0.902 | 0.528 | 0.916 | 0.562 | 0.927 | 0.598 | 0.935 | 0.651 | 0.768 |
| 0.9265 | 0.549 | 0.937 | 0.575 | 0.945 | 0.607 | 0.951 | 0.654 | 0.766 |
| 0.951 | 0.671 | 0.958 | 0.729 | 0.963 | 0.7 | 0.967 | 0.729 | 0.781 |
| 0.9681 | 0.933 | 0.973 | 1.02 | 0.976 | 1.02 | 0.979 | 0.875 | 0.826 |
| 0.9804 | 1.399 | 0.983 | 1.458 | 0.985 | 1.458 | 0.987 | 1.166 | 0.911 |
| 0.9902 | 2.041 | 0.992 | 2.041 | 0.993 | 2.041 | 0.993 | 1.749 | 1.093 |

**Table B11. Influence Coefficients for Inside Circumferential 360 Degree Surface Flaws, $R / t = 10$**

| | 10t $t^{1/2}$ $K^*$ | | | | | |
|---|---|---|---|---|---|---|
| $a' / a$ | $a / t$=0.01 | a/t=0.02 | a/t=0.03 | a/t=0.05 | a/t=0.075 | a/t=0.10 |
| 0 | 2.255 | 1.616 | 1.325 | 1.036 | 0.867 | 0.771 |
| 0.0556 | 2.256 | 1.616 | 1.324 | 1.036 | 0.865 | 0.769 |
| 0.1111 | 2.257 | 1.616 | 1.324 | 1.035 | 0.864 | 0.767 |
| 0.1667 | 2.258 | 1.616 | 1.323 | 1.034 | 0.863 | 0.765 |
| 0.2222 | 2.260 | 1.617 | 1.324 | 1.035 | 0.862 | 0.764 |
| 0.2778 | 2.267 | 1.621 | 1.327 | 1.037 | 0.863 | 0.764 |
| 0.3333 | 2.280 | 1.629 | 1.334 | 1.041 | 0.866 | 0.766 |
| 0.3888 | 2.300 | 1.642 | 1.344 | 1.049 | 0.872 | 0.770 |
| 0.4444 | 2.329 | 1.662 | 1.361 | 1.061 | 0.880 | 0.777 |
| 0.5000 | 2.372 | 1.691 | 1.384 | 1.079 | 0.894 | 0.788 |
| 0.5556 | 2.431 | 1.732 | 1.417 | 1.104 | 0.914 | 0.804 |
| 0.6111 | 2.511 | 1.788 | 1.462 | 1.138 | 0.941 | 0.826 |
| 0.6666 | 2.623 | 1.866 | 1.526 | 1.187 | 0.979 | 0.859 |
| 0.7222 | 2.779 | 1.975 | 1.615 | 1.255 | 1.034 | 0.905 |
| 0.7778 | 3.008 | 2.135 | 1.744 | 1.355 | 1.114 | 0.972 |
| 0.8333 | 3.361 | 2.383 | 1.946 | 1.510 | 1.239 | 1.079 |
| 0.8888 | 3.986 | 2.823 | 2.305 | 1.786 | 1.462 | 1.271 |
| 0.9166 | 4.520 | 3.199 | 2.611 | 2.022 | 1.654 | 1.425 |
| 0.9444 | 6.195 | 3.965 | 3.346 | 2.478 | 1.982 | 1.735 |
| 0.9639 | 8.674 | 5.948 | 4.956 | 3.717 | 2.974 | 2.602 |
| 0.9778 | 13.630 | 9.913 | 8.054 | 6.195 | 4.956 | 4.337 |
| 0.9889 | 18.586 | 14.249 | 11.771 | 9.045 | 7.682 | 6.567 |

| a'/a | a/t=0.2 | a/t=0.3 | a/t=0.4 | a'/a | a/t=0.5 |
|---|---|---|---|---|---|
| 0 | 0.645 | 0.644 | 0.691 | 0 | 0.764 |
| 0.0552 | 0.640 | 0.635 | 0.678 | 0.059 | 0.744 |
| 0.1103 | 0.635 | 0.626 | 0.664 | 0.118 | 0.724 |
| 0.1655 | 0.630 | 0.617 | 0.651 | 0.176 | 0.704 |
| 0.2206 | 0.625 | 0.609 | 0.638 | 0.235 | 0.684 |
| 0.2757 | 0.622 | 0.601 | 0.625 | 0.294 | 0.666 |
| 0.3309 | 0.619 | 0.594 | 0.613 | 0.353 | 0.647 |
| 0.3861 | 0.618 | 0.588 | 0.602 | 0.412 | 0.630 |
| 0.4412 | 0.618 | 0.584 | 0.592 | 0.471 | 0.614 |
| 0.4963 | 0.622 | 0.581 | 0.584 | 0.529 | 0.600 |
| 0.5515 | 0.628 | 0.581 | 0.578 | 0.588 | 0.589 |
| 0.6066 | 0.639 | 0.584 | 0.574 | 0.647 | 0.580 |
| 0.6618 | 0.656 | 0.592 | 0.575 | 0.706 | 0.577 |
| 0.7169 | 0.681 | 0.607 | 0.581 | 0.750 | 0.579 |
| 0.7721 | 0.721 | 0.633 | 0.596 | 0.794 | 0.588 |
| 0.8272 | 0.784 | 0.678 | 0.626 | 0.838 | 0.608 |
| 0.8824 | 0.900 | 0.764 | 0.691 | 0.882 | 0.650 |
| 0.9118 | 1.007 | 0.845 | 0.793 | 0.912 | 0.702 |
| 0.9412 | 1.363 | 1.078 | 0.954 | 0.941 | 0.843 |
| 0.9618 | 1.921 | 1.487 | 1.301 | 0.962 | 1.115 |
| 0.9765 | 2.912 | 2.354 | 1.982 | 0.976 | 1.859 |
| 0.9882 | 3.841 | 3.346 | 2.912 | 0.988 | 2.726 |

**Table B11. (continued) Influence Coefficients for Inside Circumferential 360 Degree Surface Flaws, $R / t = 10$**

| $10t\,t^{1/2}\,K^*$ | | | | | | | |
|---|---|---|---|---|---|---|---|
| **a'/a** | **a/t=0.6** | **a'/a** | **a/t=0.7** | **a'/a** | **a/t=0.8** | **a'/a** | **a/t=0.9** |
| 0 | 0.852 | 0 | 0.944 | 0 | 1.028 | 0 | 1.129 |
| 0.0564 | 0.827 | 0.057 | 0.913 | 0.058 | 0.995 | 0.058 | 1.099 |
| 0.1127 | 0.802 | 0.115 | 0.883 | 0.116 | 0.962 | 0.117 | 1.070 |
| 0.1691 | 0.778 | 0.172 | 0.853 | 0.174 | 0.929 | 0.175 | 1.041 |
| 0.2255 | 0.753 | 0.229 | 0.823 | 0.232 | 0.897 | 0.233 | 1.013 |
| 0.2819 | 0.729 | 0.286 | 0.794 | 0.289 | 0.866 | 0.292 | 0.986 |
| 0.3382 | 0.706 | 0.343 | 0.766 | 0.347 | 0.835 | 0.350 | 0.959 |
| 0.3946 | 0.684 | 0.401 | 0.739 | 0.405 | 0.805 | 0.409 | 0.932 |
| 0.4510 | 0.663 | 0.458 | 0.712 | 0.463 | 0.776 | 0.467 | 0.907 |
| 0.5074 | 0.642 | 0.515 | 0.687 | 0.521 | 0.748 | 0.526 | 0.882 |
| 0.5637 | 0.624 | 0.572 | 0.663 | 0.579 | 0.721 | 0.584 | 0.857 |
| 0.6201 | 0.608 | 0.630 | 0.641 | 0.637 | 0.695 | 0.643 | 0.832 |
| 0.6765 | 0.595 | 0.687 | 0.622 | 0.695 | 0.671 | 0.701 | 0.809 |
| 0.7328 | 0.586 | 0.744 | 0.607 | 0.753 | 0.651 | 0.759 | 0.786 |
| 0.7892 | 0.586 | 0.802 | 0.600 | 0.811 | 0.636 | 0.818 | 0.767 |
| 0.8456 | 0.601 | 0.859 | 0.608 | 0.869 | 0.637 | 0.876 | 0.757 |
| 0.9020 | 0.653 | 0.916 | 0.661 | 0.927 | 0.686 | 0.935 | 0.786 |
| 0.9265 | 0.703 | 0.937 | 0.709 | 0.945 | 0.729 | 0.951 | 0.820 |
| 0.9510 | 0.867 | 0.958 | 0.855 | 0.963 | 0.880 | 0.967 | 0.892 |
| 0.9681 | 1.140 | 0.973 | 1.155 | 0.976 | 1.128 | 0.979 | 1.115 |
| 0.9804 | 1.797 | 0.983 | 1.760 | 0.985 | 1.722 | 0.987 | 1.735 |
| 0.9902 | 2.602 | 0.992 | 2.602 | 0.993 | 2.466 | 0.993 | 2.478 |

# Appendix C – Listings of $K_{Ic}$ And $K_{Ia}$ Extended Databases

## Table C1 – Static Initiation Toughness $K_{Ic}$ Extended Database

## Table C2 - Crack Arrest Toughness $K_{Ia}$ ORNL 99/27 Database

## Table C3. Crack Arrest Toughness $K_{Ia}$ Extended $K_{Ia}$ Database – Large Specimen Data

**Table C1. Static Initiation Toughness $K_{Ic}$ Extended Database**

| Material | Reference Source | Specimen ID | Type No. | Orientation | $T$ (°F) | $RT_{NDT}$ (°F) | $T - RT_{NDT}$ (°F) | $K_{Ic}$ (ksi√in) |
|---|---|---|---|---|---|---|---|---|
| HSST 01 | Shabbits | 1T-C(T) | 1 | | -200 | 0 | -200 | 46.6 |
| subarc | (1969) | 1T-C(T) | 1 | | -175 | 0 | -175 | 55.8 |
| weldment | | 4T-C(T) | 4 | | -150 | 0 | -150 | 56.1 |
| | | 4T-C(T) | 4 | | -125 | 0 | -125 | 61.1 |
| | | 4T-C(T) | 4 | | -100 | 0 | -100 | 96.0 |
| | | 4T-C(T) | 4 | | -75 | 0 | -75 | 90.3 |
| | | 4T-C(T) | 4 | | -75 | 0 | -75 | 93.1 |
| | | 6T-C(T) | 6 | | -50 | 0 | -50 | 72.6 |
| A533B Class 1 | Shabbits | 1T-C(T) | 1 | | -200 | 0 | -200 | 35.1 |
| subarc | (1969) | 1T-C(T) | 1 | | -200 | 0 | -200 | 45.2 |
| weldment | | 1T-C(T) | 1 | | -320 | 0 | -320 | 25.9 |
| | | 1T-C(T) | 1 | | -320 | 0 | -320 | 23.7 |
| | | 4T-C(T) | 4 | | -100 | 0 | -100 | 55.2 |
| | | 4T-C(T) | 4 | | -50 | 0 | -50 | 71.6 |
| | | 4T-C(T) | 4 | | -25 | 0 | -25 | 105.9 |
| | | 8T-C(T) | 8 | | 0 | 0 | 0 | 113.1 |
| HSST 01 | Mager (1969) | 1T-C(T) | 1 | RW | -150 | 20 | -170 | 43.9 |
| | | 1T-C(T) | 1 | RW | -150 | 20 | -170 | 39.4 |
| | | 1T-C(T) | 1 | RW | -150 | 20 | -170 | 31.3 |
| | | 1T-C(T) | 1 | RW | -150 | 20 | -170 | 47.3 |
| | | 1T-C(T) | 1 | RW | -150 | 20 | -170 | 50.4 |
| | | 1T-C(T) | 1 | RW | -150 | 20 | -170 | 41.2 |
| | | 1T-C(T) | 1 | RW | -150 | 20 | -170 | 54.0 |
| | | 1T-C(T) | 1 | RW | -150 | 20 | -170 | 50.9 |
| | | 1T-C(T) | 1 | RW | -150 | 20 | -170 | 35.5 |
| | | 1T-C(T) | 1 | RW | -150 | 20 | -170 | 33.2 |
| | | 1T-C(T) | 1 | RW | -150 | 20 | -170 | 37.2 |
| | | 1T-C(T) | 1 | RW | -150 | 20 | -170 | 37.1 |
| | | 1T-C(T) | 1 | RW | -150 | 20 | -170 | 37.1 |
| | | 1T-C(T) | 1 | RW | -150 | 20 | -170 | 34.7 |
| | | 1T-C(T) | 1 | RW | -150 | 20 | -170 | 35.0 |
| | | 1T-C(T) | 1 | RW | -150 | 20 | -170 | 32.6 |
| | | 1T-C(T) | 1 | RW | -150 | 20 | -170 | 29.4 |
| HSST 03 | Mager (1969) | 1T-C(T) | 1 | RW | -150 | 20 | -170 | 44.0 |
| | | 1T-C(T) | 1 | RW | -150 | 20 | -170 | 31.4 |
| | | 1T-C(T) | 1 | RW | -150 | 20 | -170 | 39.3 |
| | | 1T-C(T) | 1 | RW | -150 | 20 | -170 | 31.3 |
| | | 1T-C(T) | 1 | RW | -150 | 20 | -170 | 33.0 |
| | | 1T-C(T) | 1 | RW | -150 | 20 | -170 | 38.1 |
| | | 1T-C(T) | 1 | RW | -150 | 20 | -170 | 31.1 |
| | | 1T-C(T) | 1 | RW | -150 | 20 | -170 | 44.9 |
| | | 1T-C(T) | 1 | RW | -150 | 20 | -170 | 39.4 |
| A533B Class 1 | Mager (1969) | 1X-WOL | 1 | RW | -320 | 65 | -385 | 31.6 |
| | | 1T-WOL | 1 | RW | -320 | 65 | -385 | 32.5 |
| | | 1X-WOL | 1 | RW | -250 | 65 | -315 | 40.9 |
| | | 1X-WOL | 1 | RW | -250 | 65 | -315 | 37.1 |
| | | 1X-WOL | 1 | RW | -250 | 65 | -315 | 44.0 |
| | | 1T-WOL | 1 | RW | -250 | 65 | -315 | 40.8 |
| | | 1T-WOL | 1 | RW | -250 | 65 | -315 | 31.2 |
| | | 1X-WOL | 1 | RW | -200 | 65 | -265 | 30.6 |

| Material | Reference Source | Specimen ID | Type No. | Orientation | $T$ (°F) | $RT_{NDT}$ (°F) | $T - RT_{NDT}$ (°F) | $K_{Ic}$ (ksi√in) |
|---|---|---|---|---|---|---|---|---|
| | | 1X-WOL | 1 | RW | -200 | 65 | -265 | 29.0 |
| | | 1T-WOL | 1 | RW | -200 | 65 | -265 | 35.6 |
| | | 1T-WOL | 1 | RW | -200 | 65 | -265 | 42.8 |
| | | 2T-WOL | 2 | RW | -150 | 65 | -215 | 46.9 |
| | | 2T-WOL | 2 | RW | -150 | 65 | -215 | 66.9 |
| HSST 02 | Mager (1969) | 1X-WOL | 1 | RW | -200 | 0 | -200 | 30.5 |
| | | 1X-WOL | 1 | RW | -200 | 0 | -200 | 37.5 |
| | | 1X-WOL | 1 | RW | -200 | 0 | -200 | 41.0 |
| | | 1T-WOL | 1 | RW | -200 | 0 | -200 | 31.2 |
| | | 1T-WOL | 1 | RW | -200 | 0 | -200 | 30.8 |
| | | 1T-WOL | 1 | RW | -175 | 0 | -175 | 43.5 |
| | | 1X-WOL | 1 | RW | -150 | 0 | -150 | 29.7 |
| | | 1X-WOL | 1 | RW | -150 | 0 | -150 | 31.5 |
| | | 1X-WOL | 1 | RW | -150 | 0 | -150 | 41.2 |
| | | 1X-WOL | 1 | RW | -150 | 0 | -150 | 30.5 |
| | | 1X-WOL | 1 | RW | -125 | 0 | -125 | 39.1 |
| | | 1T-WOL | 1 | RW | -125 | 0 | -125 | 48.3 |
| | | 1T-WOL | 1 | RW | -125 | 0 | -125 | 43.4 |
| | | 1T-WOL | 1 | RW | -125 | 0 | -125 | 38.1 |
| | | 2T-WOL | 2 | RW | -100 | 0 | -100 | 51.4 |
| | | 2T-WOL | 2 | RW | -100 | 0 | -100 | 59.0 |
| | | 2T-WOL | 2 | RW | -100 | 0 | -100 | 56.2 |
| | | 2T-WOL | 2 | RW | -100 | 0 | -100 | 50.2 |
| | | 2T-WOL | 2 | RW | -50 | 0 | -50 | 65.1 |
| | | 2T-WOL | 2 | RW | -50 | 0 | -50 | 65.0 |
| | | 2T-WOL | 2 | RW | -50 | 0 | -50 | 67.5 |
| | | 2T-WOL | 2 | RW | -50 | 0 | -50 | 65.0 |
| | | 1X-WOL | 1 | RW | -250 | 0 | -250 | 37.3 |
| | | 1X-WOL | 1 | RW | -200 | 0 | -200 | 44.0 |
| | | 1X-WOL | 1 | RW | -200 | 0 | -200 | 34.6 |
| | | 1X-WOL | 1 | RW | -200 | 0 | -200 | 39.9 |
| | | 1X-WOL | 1 | RW | -200 | 0 | -200 | 38.5 |
| | | 1T-C(T) | 1 | RW | -150 | 0 | -150 | 42.1 |
| | | 1T-C(T) | 1 | RW | -150 | 0 | -150 | 37.7 |
| | | 1T-C(T) | 1 | RW | -150 | 0 | -150 | 40.7 |
| | | 1T-C(T) | 1 | RW | -100 | 0 | -100 | 42.2 |
| | | 1T-C(T) | 1 | RW | -100 | 0 | -100 | 48.5 |
| | | 1T-C(T) | 1 | RW | -100 | 0 | -100 | 48.5 |
| | | 1T-C(T) | 1 | RW | -75 | 0 | -75 | 50.3 |
| | | 1T-C(T) | 1 | RW | -75 | 0 | -75 | 46.6 |
| | | 1T-C(T) | 1 | RW | -100 | 0 | -100 | 54.8 |
| | | 1T-C(T) | 1 | RW | -100 | 0 | -100 | 54.4 |
| | | 2T-WOL | 2 | RW | -50 | 0 | -50 | 56.7 |
| | | 2T-WOL | 2 | RW | 0 | 0 | 0 | 66.4 |
| | | 2T-WOL | 2 | RW | 0 | 0 | 0 | 93.7 |
| | | 2T-WOL | 2 | RW | 0 | 0 | 0 | 83.4 |
| A533B Class 1 weld | Mager (1969) | 1X-WOL | 1 | | -320 | -45 | -275 | 29.7 |
| | | 1X-WOL | 1 | | -320 | -45 | -275 | 27.2 |
| | | 1X-WOL | 1 | | -250 | -45 | -205 | 37.6 |
| | | 1X-WOL | 1 | | -250 | -45 | -205 | 37.8 |
| | | 1T-WOL | 1 | | -250 | -45 | -205 | 43.6 |
| | | 2T-WOL | 2 | | -250 | -45 | -205 | 55.6 |
| | | 1T-WOL | 1 | | -225 | -45 | -180 | 40.1 |
| | | 1T-WOL | 1 | | -225 | -45 | -180 | 52.8 |

| Material | Reference Source | Specimen ID | Type No. | Orientation | $T$ (°F) | $RT_{NDT}$ (°F) | $T - RT_{NDT}$ (°F) | $K_{Ic}$ (ksi√in) |
|---|---|---|---|---|---|---|---|---|
| | | 2T-WOL | 2 | | -225 | -45 | -180 | 66.2 |
| | | 2T-WOL | 2 | | -200 | -45 | -155 | 70.7 |
| A533B Class 1 | Mager (1969) | 1X-WOL | 1 | | -320 | 0 | -320 | 30.3 |
| weld-HAZ | | 1X-WOL | 1 | | -250 | 0 | -250 | 35.2 |
| | | 1X-WOL | 1 | | -250 | 0 | -250 | 40.4 |
| | | 1T-WOL | 1 | | -250 | 0 | -250 | 30.5 |
| | | 1T-WOL | 1 | | -250 | 0 | -250 | 44.2 |
| | | 2T-WOL | 2 | | -200 | 0 | -200 | 71.2 |
| A508 Class 2 | Mager (1969) | 1X-WOL | 1 | | -320 | 50 | -370 | 39.6 |
| European | | 1X-WOL | 1 | | -320 | 50 | -370 | 27.5 |
| Forging | | 1T-WOL | 1 | | -320 | 50 | -370 | 47.5 |
| "ring forging" | | 1X-WOL | 1 | | -250 | 50 | -300 | 43.2 |
| | | 1X-WOL | 1 | | -250 | 50 | -300 | 47.9 |
| | | 1X-WOL | 1 | | -250 | 50 | -300 | 41.6 |
| | | 1T-WOL | 1 | | -250 | 50 | -300 | 51.3 |
| | | 1T-WOL | 1 | | -200 | 50 | -250 | 55.0 |
| | | 2T-WOL | 2 | | -200 | 50 | -250 | 43.3 |
| | | 2T-WOL | 2 | | -150 | 50 | -200 | 57.2 |
| | | 2T-WOL | 2 | | -125 | 50 | -175 | 56.2 |
| | | 2T-WOL | 2 | | -100 | 50 | -150 | 56.0 |
| HSST 02 | Shabbits | 6T-C(T) | 6 | RW | 25 | 0 | 25 | 98.9 |
| | (1969) | 6T-C(T) | 6 | RW | 25 | 0 | 25 | 74.5 |
| | | 6T-C(T) | 6 | RW | 25 | 0 | 25 | 90.5 |
| | | 6T-C(T) | 6 | RW | 0 | 0 | 0 | 73.9 |
| | | 6T-C(T) | 6 | RW | 0 | 0 | 0 | 66.9 |
| | | 11T-C(T) | 11 | RW | 50 | 0 | 50 | 148.6 |
| | | 10T-C(T) | 10 | RW | 50 | 0 | 50 | 137.3 |
| | | 10T-C(T) | 10 | RW | 50 | 0 | 50 | 139.0 |
| | | 4T-C(T) | 4 | RW | 0 | 0 | 0 | 87.2 |
| | | 4T-C(T) | 4 | RW | -25 | 0 | -25 | 61.0 |
| | | 4T-C(T) | 4 | RW | -25 | 0 | -25 | 58.7 |
| | | 4T-C(T) | 4 | RW | -25 | 0 | -25 | 45.9 |
| | | 10T-C(T) | 10 | RW | 0 | 0 | 0 | 87.5 |
| | | 10T-C(T) | 10 | RW | 25 | 0 | 25 | 110.3 |
| | | 1T-C(T) | 1 | RW | -250 | 0 | -250 | 37.3 |
| | | 1T-C(T) | 1 | RW | -200 | 0 | -200 | 44.4 |
| | | 1T-C(T) | 1 | RW | -200 | 0 | -200 | 34.6 |
| | | 1T-C(T) | 1 | RW | -200 | 0 | -200 | 39.9 |
| | | 1T-C(T) | 1 | RW | -200 | 0 | -200 | 34.8 |
| | | 1T-C(T) | 1 | RW | -150 | 0 | -150 | 44.1 |
| | | 1T-C(T) | 1 | RW | -150 | 0 | -150 | 37.4 |
| | | 1T-C(T) | 1 | RW | -150 | 0 | -150 | 41.8 |
| | | 1T-C(T) | 1 | RW | -100 | 0 | -100 | 48.3 |
| | | 1T-C(T) | 1 | RW | -100 | 0 | -100 | 48.3 |
| | | 1T-C(T) | 1 | RW | -100 | 0 | -100 | 41.9 |
| | | 2T-C(T) | 2 | RW | -100 | 0 | -100 | 49.7 |
| | | 2T-C(T) | 2 | RW | -50 | 0 | -50 | 64.6 |
| | | 2T-C(T) | 2 | RW | -50 | 0 | -50 | 64.7 |
| A508 Class 2 | unpublished | 2T-C(T) | 2 | | -150 | 51 | -201 | 52.2 |
| | outside of | 2T-C(T) | 2 | | -150 | 51 | -201 | 45.5 |
| | EPRI NP-719-SR | 2T-C(T) | 2 | | -125 | 51 | -176 | 46.0 |
| | | 2T-C(T) | 2 | | -125 | 51 | -176 | 64.3 |
| | | 2T-C(T) | 2 | | -125 | 51 | -176 | 50.0 |
| | | 4T-C(T) | 4 | | -25 | 51 | -76 | 45.0 |

| Material | Reference Source | Specimen ID | Type No. | Orientation | $T$ (°F) | $RT_{NDT}$ (°F) | $T - RT_{NDT}$ (°F) | $K_{Ic}$ (ksi√in) |
|---|---|---|---|---|---|---|---|---|
| | | 6T-C(T) | 6 | | 0 | 51 | -51 | 107.0 |
| | | 2T-C(T) | 2 | | -125 | 51 | -176 | 45.6 |
| | | 2T-C(T) | 2 | | -125 | 51 | -176 | 68.0 |
| A508 Class 2 | unpublished | 2T-C(T) | 2 | | -75 | 65 | -140 | 52.0 |
| | outside of | 2T-C(T) | 2 | | -75 | 65 | -140 | 64.6 |
| | EPRI NP-719-SR | 2T-C(T) | 2 | | -75 | 65 | -140 | 56.6 |
| | | 2T-C(T) | 2 | | -25 | 65 | -90 | 64.7 |
| | | 2T-C(T) | 2 | | -25 | 65 | -90 | 62.4 |
| | | 8T-C(T) | 8 | | 35 | 65 | -30 | 81.0 |
| | | 2T-C(T) | 2 | | -125 | 65 | -190 | 47.2 |
| | | 2T-C(T) | 2 | | -125 | 65 | -190 | 40.9 |
| | | 2T-C(T) | 2 | | -125 | 65 | -190 | 42.5 |
| | | 2T-C(T) | 2 | | -125 | 65 | -190 | 42.5 |
| HSSI Weld | NUREG/CR- | 1T-C(T) | 1 | T-L | -238 | -9.4 | -228.6 | 35.09 |
| 72W | 5913 | 1T-C(T) | 1 | T-L | -238 | -9.4 | -228.6 | 35.45 |
| | | 1T-C(T) | 1 | T-L | -238 | -9.4 | -228.6 | 37.82 |
| | | 1T-C(T) | 1 | T-L | -149.8 | -9.4 | -140.4 | 42.55 |
| | | 1T-C(T) | 1 | T-L | -112 | -9.4 | -102.6 | 45.09 |
| | | 2T-C(T) | 2 | T-L | -112 | -9.4 | -102.6 | 58.73 |
| | | 2T-C(T) | 2 | T-L | -112 | -9.4 | -102.6 | 67.64 |
| | | 2T-C(T) | 2 | T-L | -58 | -9.4 | -48.6 | 63.27 |
| | | 4T-C(T) | 4 | T-L | -58 | -9.4 | -48.6 | 73.82 |
| | | 4T-C(T) | 4 | T-L | -58 | -9.4 | -48.6 | 90.91 |
| | | 4T-C(T) | 4 | T-L | -22 | -9.4 | -12.6 | 93.45 |
| | | 4T-C(T) | 4 | T-L | 5 | -9.4 | 14.4 | 74.64 |
| HSSI | NUREG/CR- | 1T-C(T) | 1 | T-L | -238 | -29.2 | -208.8 | 34.64 |
| 73W | 5913 | 1T-C(T) | 1 | T-L | -238 | -29.2 | -208.8 | 37.82 |
| | | 1T-C(T) | 1 | T-L | -238 | -29.2 | -208.8 | 38.18 |
| | | 1T-C(T) | 1 | T-L | -238 | -29.2 | -208.8 | 39.45 |
| | | 2T-C(T) | 2 | T-L | -112 | -29.2 | -82.8 | 58.18 |
| | | 2T-C(T) | 2 | T-L | -112 | -29.2 | -82.8 | 60.64 |
| | | 2T-C(T) | 2 | T-L | -112 | -29.2 | -82.8 | 65.55 |
| | | 2T-C(T) | 2 | T-L | -58 | -29.2 | -28.8 | 66.09 |
| | | 4T-C(T) | 4 | T-L | -58 | -29.2 | -28.8 | 75.55 |
| | | 4T-C(T) | 4 | T-L | -58 | -29.2 | -28.8 | 76.45 |
| HSST Plate 13 | NUREG/CR- | 1T-C(T) | 1 | L-T | -103 | -9.4 | -93.6 | 32.64 |
| | 5788 (A533B | 2T-C(T) | 2 | L-T | -103 | -9.4 | -93.6 | 55.82 |
| | Plate 13A) | 4T-C(T) | 4 | L-T | -103 | -9.4 | -93.6 | 53.73 |
| | | 4T-C(T) | 4 | L-T | -103 | -9.4 | -93.6 | 62.09 |
| | | 4T-C(T) | 4 | L-T | -103 | -9.4 | -93.6 | 70.82 |
| | | ½T-C(T) | 0.5 | L-T | -238 | -9.4 | -228.6 | 25.36 |
| | | ½T-C(T) | 0.5 | L-T | -238 | -9.4 | -228.6 | 26.18 |
| | | ½T-C(T) | 0.5 | L-T | -238 | -9.4 | -228.6 | 29.27 |
| | | ½T-C(T) | 0.5 | L-T | -238 | -9.4 | -228.6 | 29.45 |
| | | ½T-C(T) | 0.5 | L-T | -238 | -9.4 | -228.6 | 30.18 |
| | | ½T-C(T) | 0.5 | L-T | -238 | -9.4 | -228.6 | 31.00 |
| | | ½T-C(T) | 0.5 | L-T | -238 | -9.4 | -228.6 | 32.82 |
| | | ½T-C(T) | 0.5 | L-T | -238 | -9.4 | -228.6 | 33.82 |
| | | ½T-C(T) | 0.5 | L-T | -238 | -9.4 | -228.6 | 36.00 |
| | | ½T-C(T) | 0.5 | L-T | -238 | -9.4 | -228.6 | 36.36 |
| | | 1T-C(T) | 1 | L-T | -238 | -9.4 | -228.6 | 32.09 |
| | | 1T-C(T) | 1 | L-T | -238 | -9.4 | -228.6 | 33.73 |
| | | 1T-C(T) | 1 | L-T | -238 | -9.4 | -228.6 | 34.27 |
| | | 1T-C(T) | 1 | L-T | -238 | -9.4 | -228.6 | 34.91 |

| Material | Reference Source | Specimen ID | Type No. | Orientation | $T$ (°F) | $RT_{NDT}$ (°F) | $T - RT_{NDT}$ (°F) | $K_{Ic}$ (ksi√in) |
|---|---|---|---|---|---|---|---|---|
| | | 1T-C(T) | 1 | L-T | -238 | -9.4 | -228.6 | 35.09 |
| | | 1T-C(T) | 1 | L-T | -238 | -9.4 | -228.6 | 36.00 |
| | | 1T-C(T) | 1 | L-T | -238 | -9.4 | -228.6 | 37.45 |
| | | 1T-C(T) | 1 | L-T | -238 | -9.4 | -228.6 | 37.45 |
| | | 1T-C(T) | 1 | L-T | -238 | -9.4 | -228.6 | 39.55 |
| | | 1T-C(T) | 1 | L-T | -238 | -9.4 | -228.6 | 39.73 |
| | | 1T-C(T) | 1 | L-T | -238 | -9.4 | -228.6 | 40.36 |
| | | 1T-C(T) | 1 | L-T | -238 | -9.4 | -228.6 | 42.36 |
| | | 1T-C(T) | 1 | L-T | -238 | -9.4 | -228.6 | 43.73 |
| | | 1T-C(T) | 1 | L-T | -238 | -9.4 | -228.6 | 46.45 |
| | | 1T-C(T) | 1 | L-T | -238 | -9.4 | -228.6 | 49.55 |
| | | 1T-C(T) | 1 | L-T | -238 | -9.4 | -228.6 | 49.64 |
| | | 2T-C(T) | 2 | L-T | -238 | -9.4 | -228.6 | 30.09 |
| | | 2T-C(T) | 2 | L-T | -238 | -9.4 | -228.6 | 33.00 |
| | | 2T-C(T) | 2 | L-T | -238 | -9.4 | -228.6 | 36.55 |
| | | 2T-C(T) | 2 | L-T | -238 | -9.4 | -228.6 | 37.00 |
| | | 2T-C(T) | 2 | L-T | -238 | -9.4 | -228.6 | 39.36 |
| | | 2T-C(T) | 2 | L-T | -238 | -9.4 | -228.6 | 39.91 |
| | | 2T-C(T) | 2 | L-T | -238 | -9.4 | -228.6 | 40.91 |
| | | 2T-C(T) | 2 | L-T | -238 | -9.4 | -228.6 | 41.45 |
| | | 2T-C(T) | 2 | L-T | -238 | -9.4 | -228.6 | 42.18 |
| | | 2T-C(T) | 2 | L-T | -238 | -9.4 | -228.6 | 46.45 |
| | | 2T-C(T) | 2 | L-T | -238 | -9.4 | -228.6 | 48.64 |
| | | 2T-C(T) | 2 | L-T | -238 | -9.4 | -228.6 | 53.18 |
| A508 Class 3 | Iwadate, et al. | Bx2B | 1 | NA | -238 | -13 | -225 | 37.29 |
| | ASTM STP | Bx2B | 1 | NA | -238 | -13 | -225 | 39.89 |
| | 803 | Bx2B | 1 | NA | -238 | -13 | -225 | 44.22 |
| | | Bx2B | 4 | NA | -166 | -13 | -153 | 43.36 |
| | | Bx2B | 4 | NA | -76 | -13 | -63 | 63.30 |
| | | Bx2B | 3 | NA | -4 | -13 | 9 | 69.37 |
| Midland Nozzle | NUREG/CR- | 1T-C(T) | 1 | | -58 | 52 | -110 | 49.81 |
| Course Weld | 6249 | 1T-C(T) | 1 | | -148 | 52 | -200 | 45.63 |
| | | 1T-C(T) | 1 | | -148 | 52 | -200 | 44.63 |
| | | 1T-C(T) | 1 | | -148 | 52 | -200 | 42.81 |
| | | 1T-C(T) | 1 | | -148 | 52 | -200 | 33.45 |
| | | 1T-C(T) | 1 | | -148 | 52 | -200 | 32.36 |
| Midland Beltline | NUREG/CR- | 1T-C(T) | 1 | | -148 | 23 | -171 | 36.45 |
| | 6249 | 1T-C(T) | 1 | | -148 | 23 | -171 | 34.91 |
| Plate 02 4th Irr. | NUREG/CR- | 1T-C(T) | 1 | T-L | -148 | 0 | -148 | 38.09 |
| Series | 4880, 1988 | 1T-C(T) | 1 | T-L | -139 | 0 | -139 | 33.45 |
| | Plate 02 | 1T-C(T) | 1 | T-L | -139 | 0 | -139 | 39.27 |
| | (68-71W) | 1T-C(T) | 1 | T-L | -139 | 0 | -139 | 40.09 |

**References for Table C1**

EPRI Special Report, 1978, *Flaw Evaluation Procedures: ASME Section XI*, EPRI NP-719-SR, Electric Power Research Institute, Palo Alto, CA.

W. O. Shabbits, W. H. Pryle, and E. T. Wessel, *Heavy Section Fracture Toughness Properties of A533, Grade B, Class-1 Steel Plate and Submerged Arc Weldments*, HSST Technical Report 6, WCAP-7414, December 1969.

T. R. Mager, F. O. Thomas, and W. S. Hazelton, *Evaluation by Linear Elastic Fracture Mechanics of Radiation Damage to Pressure Vessel Steels,* HSST Technical Report 5, WCAP-7328, Revised, October 1969.

T. R. Mager, *Fracture Toughness Characterization Study of A533, Grade B, Class-1 Steel*, HSST Technical Report 10, WCAP-7578, October 1970.

R. K. Nanstad, F. M. Haggag, and D. E. McCabe, *Irradiation Effects on Fracture Toughness of Two High-Copper Submerged-Arc Welds, HSSI Series 5,* USNRC Report NUREG/CR-5913 (ORNL/TM-12156/V1 and V2) Vol. 1 and 2, Oak Ridge National Laboratory, Oak Ridge, TN, October 1992.

D. E. McCabe., *A Comparison of Weibull and $\beta_{Ic}$ Analysis of Transition Range Fracture Toughness Data,* USNRC Report NUREG/CR-5788 (ORNL/TM-11959), Oak Ridge National Laboratory, Oak Ridge, TN, January 1992.

T. Iawadate, Y. Tanaka, S. Ono, and J. Watanabe, "An Analysis of Elastic-Plastic Fracture Toughness Behavior for $J_{Ic}$ Measurements in the Transition Region," *Elastic-Plastic Fracture: Second Symposium, Vol. II-Fracture Resistance Curves and Engineering Applications*, ASTM STP 803, (1983) II531-II561.

D. E. McCabe, R. K. Nanstad, S. K. Iskander, R. L. Swain, *Unirradiated Material Properties of Midland Weld WF-70,* USNRC Report NUREG/CR-6249 (ORNL/TM-12777), Oak Ridge National Laboratory, Oak Ridge, TN, October 1994.

J. J. McGowan, R. K. Nanstad, and K. R. Thoms, *Characterization of Irradiated Current-Practice Welds and A533 Grade B Class 1 Plate for Nuclear Pressure Vessel Service*, USNRC Report NUREG/CR-4880 (ORNL-6484/V1 and V2), Oak Ridge National Laboratory, Oak Ridge, TN, July 1988.

**Table C2. Crack Arrest Toughness $K_{Ia}$ ORNL 99/27 Database**

| Material | Reference Source | Specimen ID | Size No. | Orientation | $T$ (°F) | $RT_{NDT}$ (°F) | $T$-$RT_{NDT}$ (°F) | $K_{Ia}$ (ksi√in) |
|---|---|---|---|---|---|---|---|---|
| HSST-02 | EPRI NP | CCA | 1.4 | L-T | -150 | 0 | -150 | 28.0 |
| HSST-02 | 719-SR | CCA | 1 | L-T | -70 | 0 | -70 | 43.0 |
| HSST-02 | Ripling (1971) | CCA | 2 | L-T | -70 | 0 | -70 | 48.0 |
| HSST-02 | | CCA | 2 | L-T | -70 | 0 | -70 | 43.0 |
| HSST-02 | | CCA | 1 | L-T | 0 | 0 | 0 | 68.0 |
| HSST-02 | | CCA | 1 | L-T | 0 | 0 | 0 | 58.0 |
| HSST-02 | | CCA | 1 | L-T | 0 | 0 | 0 | 48.0 |
| HSST-02 | | CCA | 1 | L-T | 0 | 0 | 0 | 57.0 |
| HSST-02 | | CCA | 1 | L-T | 0 | 0 | 0 | 62.0 |
| HSST-02 | | CCA | 1.3 | L-T | 0 | 0 | 0 | 58.0 |
| HSST-02 | | CCA | 1.3 | L-T | 0 | 0 | 0 | 60.0 |
| HSST-02 | | CCA | 1.3 | L-T | 0 | 0 | 0 | 65.0 |
| HSST-02 | | CCA | 1.6 | L-T | 0 | 0 | 0 | 60.0 |
| HSST-02 | | CCA | 1.6 | L-T | 0 | 0 | 0 | 58.0 |
| HSST-02 | | CCA | 2 | L-T | 0 | 0 | 0 | 53.0 |
| HSST-02 | | CCA | 2 | L-T | 0 | 0 | 0 | 58.0 |
| HSST-02 | | CCA | 2 | L-T | 0 | 0 | 0 | 70.0 |
| HSST-02 | | CCA | 2 | L-T | 0 | 0 | 0 | 57.0 |
| HSST-02 | | CCA | 3 | L-T | 0 | 0 | 0 | 57.0 |
| HSST-02 | | CCA | 3 | L-T | 0 | 0 | 0 | 61.0 |
| HSST-02 | | CCA | 2 | L-T | 22 | 0 | 22 | 68.0 |
| HSST-02 | | CCA | 1.4 | L-T | 35 | 0 | 35 | 59.0 |
| HSST-02 | | CCA | 1.6 | L-T | 35 | 0 | 35 | 84.0 |
| HSST-02 | | CCA | 2 | L-T | 35 | 0 | 35 | 62.0 |
| HSST-02 | | CCA | 1.4 | L-T | 50 | 0 | 50 | 92.0 |
| HSST-02 | | CCA | 2 | L-T | 50 | 0 | 50 | 73.0 |
| HSST-02 | | CCA | 3 | L-T | 50 | 0 | 50 | 75.0 |
| HSST-02 | | CCA | 1 | L-T | 75 | 0 | 75 | 94.0 |
| HSST-02 | | CCA | 1.6 | L-T | 75 | 0 | 75 | 107.0 |
| HSST-02 | | CCA | 2 | L-T | 75 | 0 | 75 | 77.0 |
| HSST-02 | | CCA | 2 | L-T | 75 | 0 | 75 | 81.0 |
| HSST-02 | | CCA | 2 | L-T | 75 | 0 | 75 | 91.0 |
| HSST-02 | | CCA | 2 | L-T | 75 | 0 | 75 | 102.3 |
| HSST-02 | | CCA | 2 | L-T | 80 | 0 | 80 | 109.0 |
| HSST-02 | | CCA | 2 | L-T | 83 | 0 | 83 | 87.0 |
| HSST-02 | | CCA | 3 | L-T | 83 | 0 | 83 | 94.0 |
| HSST-02 | | CCA | 3 | L-T | 83 | 0 | 83 | 107.0 |
| HSST-02 | | CCA | 3 | L-T | 83 | 0 | 83 | 111.0 |
| HSST-02 | | CCA | 2 | L-T | 96 | 0 | 96 | 111.0 |
| HSST-02 | | CCA | 2 | L-T | 102 | 0 | 102 | 117.0 |
| HSST-02 | | CCA | 1.8 | L-T | 105 | 0 | 105 | 118.0 |
| HSST-02 | | CCA | 2 | L-T | 105 | 0 | 105 | 103.0 |
| HSST-02 | | CCA | 2 | L-T | 105 | 0 | 105 | 107.0 |
| HSST-02 | | CCA | 3 | L-T | 105 | 0 | 105 | 130.0 |
| HSST-02 | | CCA | 2 | L-T | 107 | 0 | 107 | 87.0 |
| HSST-02 | | CCA | 2 | L-T | 110 | 0 | 110 | 88.0 |
| HSST-02 | | CCA | 2 | L-T | 110 | 0 | 110 | 88.0 |
| HSST-02 | | CCA | 1.1 | L-T | 112 | 0 | 112 | 112.0 |
| HSST-02 | | CCA | 2 | L-T | 115 | 0 | 115 | 111.0 |
| HSST-02 | | CCA | 1.1 | L-T | 121 | 0 | 121 | 116.0 |
| 72W | NUREG/CR-5584 | CCA | | Crack | -77.8 | -10 | -68 | 60.1 |

| Material | Reference Source | Specimen ID | Size No. | Orientation | $T$ (°F) | $RT_{NDT}$ (°F) | $T$-$RT_{NDT}$ (°F) | $K_{Ia}$ (ksi√in) |
|---|---|---|---|---|---|---|---|---|
| 72W | | CCA | | runs | -76 | -10 | -66 | 48.2 |
| 72W | | CCA | | in | -76 | -10 | -66 | 69.2 |
| 72W | | CCA | | welding | -74.2 | -10 | -64.2 | 51.9 |
| 72W | | CCA | | direction | -52.6 | -10 | -42.6 | 61.0 |
| 72W | | CCA | | | -52.6 | -10 | -42.6 | 64.6 |
| 72W | | CCA | | | -49 | -10 | -39 | 66.4 |
| 72W | | CCA | | | -49 | -10 | -39 | 67.3 |
| 72W | | CCA | | | -49 | -10 | -39 | 69.2 |
| 72W | | CCA | | | -49 | -10 | -39 | 83.7 |
| 72W | | CCA | | | -25.6 | -10 | -15.6 | 83.7 |
| 72W | | CCA | | | -22 | -10 | -12 | 54.6 |
| 72W | | CCA | | | -22 | -10 | -12 | 55.5 |
| 72W | | CCA | | | -22 | -10 | -12 | 77.4 |
| 72W | | CCA | | | -22 | -10 | -12 | 82.8 |
| 72W | | CCA | | | -22 | -10 | -12 | 89.2 |
| 72W | | CCA | | | -22 | -10 | -12 | 94.6 |
| 72W | | CCA | | | -22 | -10 | -12 | 97.4 |
| 72W | | CCA | | | 3.2 | -10 | 13.2 | 88.3 |
| 72W | | CCA | | | 5 | -10 | 15 | 85.5 |
| 72W | | CCA | | | 5 | -10 | 15 | 85.5 |
| 72W | | CCA | | | 5 | -10 | 15 | 86.5 |
| 72W | | CCA | | | 5 | -10 | 15 | 93.7 |
| 72W | | CCA | | | 6.8 | -10 | 16.8 | 82.8 |
| 72W | | CCA | | | 28.4 | -10 | 38.4 | 93.7 |
| 72W | | CCA | | | 30.2 | -10 | 40.2 | 113.8 |
| 72W | | CCA | | | 32 | -10 | 42 | 84.6 |
| 72W | | CCA | | | 32 | -10 | 42 | 97.4 |
| 72W | | CCA | | | 32 | -10 | 42 | 103.7 |
| 72W | | CCA | | | 33.8 | -10 | 43.8 | 98.3 |
| 72W | | CCA | | | 39.2 | -10 | 49.2 | 113.8 |
| 72W | | CCA | | | 41 | -10 | 51 | 104.7 |
| 73W | NUREG/CR-5584 | CCA | | Crack | -77.8 | -30 | -47.8 | 62.8 |
| 73W | | CCA | | runs | -76 | -30 | -46 | 52.8 |
| 73W | | CCA | | in | -74.2 | -30 | -44.2 | 65.5 |
| 73W | | CCA | | welding | -49 | -30 | -19 | 47.3 |
| 73W | | CCA | | direction | -49 | -30 | -19 | 66.4 |
| 73W | | CCA | | | -49 | -30 | -19 | 68.3 |
| 73W | | CCA | | | -49 | -30 | -19 | 77.4 |
| 73W | | CCA | | | -47.2 | -30 | -17.2 | 64.6 |
| 73W | | CCA | | | -25.6 | -30 | 4.4 | 77.4 |
| 73W | | CCA | | | -23.8 | -30 | 6.2 | 68.3 |
| 73W | | CCA | | | -22 | -30 | 8 | 61.0 |
| 73W | | CCA | | | -22 | -30 | 8 | 72.8 |
| 73W | | CCA | | | -22 | -30 | 8 | 91.0 |
| 73W | | CCA | | | -20.2 | -30 | 9.8 | 70.1 |
| 73W | | CCA | | | -20.2 | -30 | 9.8 | 81.0 |
| 73W | | CCA | | | 3.2 | -30 | 33.2 | 100.1 |
| 73W | | CCA | | | 5 | -30 | 35 | 106.5 |
| 73W | | CCA | | | 5 | -30 | 35 | 111.9 |
| 73W | | CCA | | | 5 | -30 | 35 | 112.8 |
| 73W | | CCA | | | 10.4 | -30 | 40.4 | 102.3 |
| 73W | | CCA | | | 23 | -30 | 53 | 91.9 |
| 73W | | CCA | | | 41 | -30 | 71 | 97.4 |
| 73W | | CCA | | | 41 | -30 | 71 | 101.9 |

| Material | Reference Source | Specimen ID | Size No. | Orientation | $T$ (°F) | $RT_{NDT}$ (°F) | $T$-$RT_{NDT}$ (°F) | $K_{Ia}$ (ksi√in) |
|---|---|---|---|---|---|---|---|---|
| 73W | | CCA | | | 41 | -30 | 71 | 102.8 |
| 73W | | CCA | | | 41 | -30 | 71 | 108.3 |
| 73W | | CCA | | | 59 | -30 | 89 | 120.1 |
| MW15JC | NUREG/CR-6621 | CCA | | Crack | -4 | 32.2 | -36.2 | 63.7 |
| MW15JB*r* | | CCA | | runs | 14 | 32.2 | -18.2 | 79.0 |
| MW15JE*r1* | | CCA | | in welding | 32 | 32.2 | -0.2 | 97.1 |
| MW15JF | | CCA | | direction | 50 | 32.2 | 17.8 | 119.7 |

**References for Table C2**

EPRI Special Report, 1978, *Flaw Evaluation Procedures: ASME Section XI*, EPRI NP-719-SR, Electric Power Research Institute, Palo Alto, CA.

E. J. Ripling and P. B. Crosley, "Strain Rate and Crack Arrest Studies," *HSST 5th Annual Information Meeting*, Paper No. 9, 1971.

S. K. Iskander, W. R. Corwin, R. K. Nanstad, *Results of Crack-Arrest Tests on Two Irradiated High-Copper Welds,* USNRC Report NUREG/CR-5584 (ORNL/TM-11575), Oak Ridge National Laboratory, Oak Ridge, TN, December 1990.

S. K. Iskander, C. A. Baldwin, D. W. Heatherly, D. E. McCabe, I. Remec, and R. L. Swain, *Detailed Results of Testing Unirradiated and Irradiated Crack-Arrest Toughness Specimens from the Low Upper-Shelf Energy, High Copper Weld, WF-70,* NUREG/CR-6621 (ORNL/TM-13764) under preparation.

S. K. Iskander, R. K. Nanstad, D. E. McCabe, and R. L. Swain, "Effects of Irradiation on Crack-Arrest Toughness of a Low Upper-Shelf Energy, High-Copper Weld," *Effects of Radiation on Materials: 19th International Symposium, ASTM STP 1366*, M. L. Hamilton, A. S. Kumar, S. T. Rosinski, and M. L. Grossbeck, eds., American Society for Testing and Materials, 2000.

## Table C3. Crack Arrest Toughness $K_{Ia}$ Extended $K_{Ia}$ Database – Large Specimen Data

| Material Test No. | Reference Source | $T$ (°F) | $RT_{NDT}$ (°F) | $T$-$RT_{NDT}$ (°F) | $K_{Ia}$ (ksi-in$^{1/2}$) |
|---|---|---|---|---|---|
| WP 1.2A | NUREG/CR-4930 | -9.4 | 143.6 | 153.0 | 385.81 |
| WP 1.2B | | -9.4 | 197.6 | 207.0 | 623.29 |
| WP 1.3 | | -9.4 | 129.2 | 138.6 | 213.83 |
| WP 1.4B | | -9.4 | 140.0 | 149.4 | 352.14 |
| WP 1.5A | | -9.4 | 132.8 | 142.2 | 210.19 |
| WP 1.5B | | -9.4 | 161.6 | 171.0 | 463.15 |
| WP 1.6A | | -9.4 | 129.2 | 138.6 | 250.23 |
| WP 1.6B | | -9.4 | 176.0 | 185.4 | 361.24 |
| WP 1.7A | NUREG/CR-5330 | -9.4 | 141.8 | 151.2 | 290.26 |
| WP 1.7B | | -9.4 | 190.4 | 199.8 | 505.00 |
| WP 1.8A | | -9.4 | 104.0 | 113.4 | 313.92 |
| WP 1.8B | | -9.4 | 131.0 | 140.4 | 440.40 |
| WP 1.8C | | -9.4 | 174.2 | 183.6 | 512.28 |
| WP CE-1 | | -31.0 | 96.8 | 127.8 | 154.69 |
| WP CE-2A | | -31.0 | 107.6 | 138.6 | 198.36 |
| WP CE-2B | | -31.0 | 127.4 | 158.4 | 322.11 |
| WP CE-2C | | -31.0 | 140.0 | 171.0 | 524.11 |
| SP 1.3 | Smirt 10 Vol F, p37 | -9.4 | 111.2 | 120.6 | 160.15 |
| WP 2.1A | NUREG/CR-5451 | 140.0 | 176.0 | 36.0 | 96.45 |
| WP 2.1B | | 140.0 | 204.8 | 64.8 | 139.22 |
| WP 2.1D | | 140.0 | 221.0 | 81.0 | 143.77 |
| WP 2.1E | | 140.0 | 233.6 | 93.6 | 154.69 |
| WP 2.1F | | 140.0 | 257.0 | 117.0 | 182.89 |
| WP 2.1H | | 140.0 | 275.0 | 135.0 | 266.61 |
| WP 2.1I | | 140.0 | 293.0 | 153.0 | 337.58 |
| WP 2.1J | | 140.0 | 305.6 | 165.6 | 369.43 |
| WP 2.2A | | 140.0 | 248.0 | 108.0 | 182.89 |
| WP 2.2B | | 140.0 | 264.2 | 124.2 | 235.67 |
| WP 2.2C | | 140.0 | 271.4 | 131.4 | 255.69 |
| WP 2.2D | | 140.0 | 282.2 | 142.2 | 252.05 |
| WP 2.2E | | 140.0 | 287.6 | 147.6 | 345.77 |
| WP 2.2F | | 140.0 | 302.0 | 162.0 | 331.21 |
| WP 2.2G | | 140.0 | 323.6 | 183.6 | 405.82 |
| WP 2.3A | | 140.0 | 206.6 | 66.6 | 131.03 |
| WP 2.3B | | 140.0 | 222.8 | 82.8 | 211.10 |
| WP 2.3D | | 140.0 | 231.8 | 91.8 | 232.03 |
| WP 2.3F | | 140.0 | 258.8 | 118.8 | 234.76 |
| WP 2.4B | | 140.0 | 186.8 | 46.8 | 124.66 |
| WP 2.4C | | 140.0 | 215.6 | 75.6 | 171.06 |
| WP 2.4D | | 140.0 | 224.6 | 84.6 | 255.69 |
| WP 2.4E | | 140.0 | 249.8 | 109.8 | 226.57 |
| WP 2.4F | | 140.0 | 260.6 | 120.6 | 279.34 |
| WP 2.4G | | 140.0 | 278.6 | 138.6 | 346.68 |
| WP 2.4H | | 140.0 | 300.2 | 160.2 | 361.24 |
| WP 2.5B | | 140.0 | 219.2 | 79.2 | 155.60 |
| WP 2.5C | | 140.0 | 255.2 | 115.2 | 172.88 |
| WP 2.5D | | 140.0 | 275.0 | 135.0 | 243.86 |
| WP 2.5E | | 140.0 | 291.2 | 151.2 | 278.43 |
| WP 2.5F | | 140.0 | 309.2 | 169.2 | 333.03 |
| WP 2.6A | | 140.0 | 219.2 | 79.2 | 185.62 |
| WP 2.6B | | 140.0 | 239.0 | 99.0 | 235.67 |
| WP 2.6C | | 140.0 | 246.2 | 106.2 | 260.24 |
| WP 2.6D | | 140.0 | 257.0 | 117.0 | 318.47 |
| WP 2.6F | | 140.0 | 271.4 | 131.4 | 298.45 |
| WP 2.6G | | 140.0 | 282.2 | 142.2 | 373.98 |
| WP 2.6H | | 140.0 | 312.8 | 172.8 | 375.80 |
| PTSE 1B | NUREG/CR-4106 | 196.3 | 326.3 | 130.0 | 182.80 |
| PTSE 1C | | 196.3 | 354.2 | 157.9 | 271.97 |
| PTSE 2A | NUREG/CR-4888 | 167.0 | 267.1 | 100.1 | 237.85 |
| PTSE 2B | | 167.0 | 296.2 | 129.2 | 329.03 |
| PTSE 2C | | 167.0 | 325.2 | 158.2 | 381.53 |
| TSE 4 | NUREG/CR-4249 | 167.0 | 267.8 | 100.8 | 115.56 |
| TSE 5-1 | | 152.6 | 96.8 | -55.8 | 78.25 |
| TSE 5-2 | | 152.6 | 179.6 | 27.0 | 94.63 |
| TSE 5-3 | | 152.6 | 192.2 | 39.6 | 83.71 |
| TSE 5A-1 | | 50.0 | 71.6 | 21.6 | 69.15 |
| TSE 5A-2 | | 50.0 | 100.4 | 50.4 | 78.25 |
| TSE 5A-3 | | 50.0 | 123.8 | 73.8 | 97.36 |
| TSE 5A-4 | | 50.0 | 152.6 | 102.6 | 118.29 |
| TSE 6-1 | | 152.6 | 89.6 | -63.0 | 57.32 |
| TSE 6-2 | | 152.6 | 145.4 | -7.2 | 95.54 |

**References for Table C3**

D. J. Naus, et al., *High-Temperature Crack Arrest Behavior in 152-mm-Thick SEN Wide Plates of Quenched and Tempered A533 Grade B Class 1 Steel*, NUREG/CR-5330 (ORNL-11083), Oak Ridge National Laboratory, Oak Ridge, TN, April 1989.

D. J. Naus, et al., *Crack-Arrest Behavior in SEN Wide Plates of Low-Upper-Shelf Base Metal Tested Under Nonisothermal Conditions: WP-2 Series*, NUREG/CR-5451 (ORNL-6584), Oak Ridge National Laboratory, Oak Ridge, TN, April 1989.

R. H. Bryan, et al., *Pressurized-Thermal Shock Test of 6-Inch-Thick Pressure Vessel, PTSE-1: Investigations of Warm Prestressing and Upper-Shelf Arrest*, NUREG/CR-4106 (ORNL-6135), Oak Ridge National Laboratory, Oak Ridge, TN, April 1985.

R. H. Bryan, et al., *Pressurized Thermal Shock Test of 6-Inch-Thick Pressure Vessel PTSE-2: Investigation of Low Tearing Resistance and Warm Prestressing*, NUREG/CR-4888 (ORNL-6377), Oak Ridge National Laboratory, Oak Ridge, TN, December 1987.

R. D. Cheverton, D. G. Ball, S. E. Bolt, S. K. Iskander, and R. K. Nanstad, *Pressure Vessel Fracture Studies Pertaining to the PWR Thermal-Shock Issue: Experiments TSE-5, TSE-5A, and TSE-6,* NUREG/CR-4249 (ORNL-6163), Oak Ridge National Laboratory, Oak Ridge, TN, June 1985.

# Appendix D – Summary of RVID2 Data for Use in FAVOR Calculations

| Product Form | Heat | Beltline | $\sigma_{flow(u)}$ [ksi] | $RT_{NDT(u)}$ [°F] | | | Composition[2] | | | |
|---|---|---|---|---|---|---|---|---|---|---|
| | | | | $RT_{NDT(u)}$ Method | $RT_{NDT(u)}$ Value | $\sigma_{(u)}$ Value | Cu | Ni | P | $USE_0$ (ft-lbf) |
| **Beaver Valley 1, (Designer: Westinghouse, Manufacturer: CE) Coolant Temperature = 547°F, Vessel Thickness = 7-7/8 in.** | | | | | | | | | | |
| PLATE | C4381-1 | INTERMEDIATE SHELL B6607-1 | 83.8 | MTEB 5-2 | 43 | 0 | 0.14 | 0.62 | 0.015 | 90 |
| | C4381-2 | INTERMEDIATE SHELL B6607-2 | 84.3 | MTEB 5-2 | 73 | 0 | 0.14 | 0.62 | 0.015 | 84 |
| | C6293-2 | LOWER SHELL B7203-2 | 78.8 | MTEB 5-2 | 20 | 0 | 0.14 | 0.57 | 0.015 | 84 |
| | C6317-1 | LOWER SHELL B6903-1 | 72.7 | MTEB 5-2 | 27 | 0 | 0.2 | 0.54 | 0.01 | 80 |
| LINDE 1092 WELD | 305414 | LOWER SHELL AXIAL WELD 20-714 | 75.3 | Generic | -56 | 17 | 0.337 | 0.609 | 0.012 | 98 |
| | 305424 | INTER SHELL AXIAL WELD 19-714 | 79.9 | Generic | -56 | 17 | 0.273 | 0.629 | 0.013 | 112 |
| LINDE 0091 WELD | 90136 | CIRC WELD 11-714 | 76.1 | Generic | -56 | 17 | 0.269 | 0.07 | 0.013 | 144 |
| **Calvert Cliffs 1, (Designer and Manufacturer: CE) Coolant Temperature = 545°F, Vessel Thickness = 8 5/8-in.** | | | | | | | | | | |
| PLATE | B-8489-1 | LOWER SHELL D-7207-3 | 78.8 | MTEB 5-2 | -20 | 0 | 0.11 | 0.53 | 0.008 | 81 |
| | B-8489-2 | LOWER SHELL D-7207-2 | 80.3 | MTEB 5-2 | -10 | 0 | 0.11 | 0.56 | 0.009 | 90 |
| | C-4351-2 | INTERMEDIATE SHELL D-7206-1 | 74.7 | MTEB 5-2 | 20 | 0 | 0.11 | 0.55 | 0.011 | 90 |
| | C-4420-1 | LOWER SHELL D-7207-1 | 78.0 | MTEB 5-2 | 10 | 0 | 0.13 | 0.54 | 0.01 | 77 |
| | C-4441-1 | INTERMEDIATE SHELL D-7206-3 | 78.5 | ASME NB-2331 | 10 | 0 | 0.12 | 0.64 | 0.011 | 112 |
| | C-4441-2 | INTERMEDIATE SHELL D-7206-2 | 82.6 | ASME NB-2331 | -30 | 0 | 0.12 | 0.64 | 0.011 | 81 |
| LINDE 1092 WELD | 20291/12008 | INTERMEDIATE SHELL AXIAL WELD 2-203 | 78.8 | ASME NB-2331 | -50 | 0 | 0.22 | 0.83 | 0.01 | 110 |
| | 21935 | LOWER SHELL AXIAL WELD 3-203A/C | 78.6 | Generic | -56 | 17 | 0.18 | 0.72 | 0.015 | 109 |
| LINDE 0091 WELD | 33A277 | INT. TO LOWER SHELL CIRC. WELD 9-203 | 78.6 | ASME NB-2331 | -80 | 0 | 0.24 | 0.16 | 0.014 | 160 |
| **Oconee 1, (Designer and Manufacturer: B&W) Coolant Temperature = 556°F, Vessel Thickness = 8.44-in.** | | | | | | | | | | |
| FORGING | AHR54 (ZV2861) | LOWER NOZZLE BELT | (4) | B&W Generic | 3 | 31 | 0.16 | 0.65 | 0.006 | 109 |
| PLATE | C2197-2 | INTERMEDIATE SHELL | (4) | B&W Generic | 1 | 26.9 | 0.15 | 0.5 | 0.008 | 81 |
| | C2800-1 | LOWER SHELL | (4) | B&W Generic | 1 | 26.9 | 0.11 | 0.63 | 0.012 | 81 |
| | C2800-2 | LOWER SHELL | 69.9 | B&W Generic | 1 | 26.9 | 0.11 | 0.63 | 0.012 | 119 |
| | C3265-1 | UPPER SHELL | 75.8 | B&W Generic | 1 | 26.9 | 0.1 | 0.5 | 0.015 | 108 |
| | C3278-1 | UPPER SHELL | (4) | B&W Generic | 1 | 26.9 | 0.12 | 0.6 | 0.01 | 81 |
| LINDE 80 WELD | 1P0962 | INTERMEDIATE SHELL AXIAL WELDS SA-1073 | 79.4 | B&W Generic | -5 | 19.7 | 0.21 | 0.64 | 0.025 | 70 |
| | 299L44 | INT./UPPER SHL CIRC WELD (OUTSIDE 39%) WF-25 | (4) | B&W Generic | -7 | 20.6 | 0.34 | 0.68 | (3) | 81 |
| | 61782 | NOZZLE BELT/INT. SHELL CIRC WELD SA-1135 | (4) | B&W Generic | -5 | 19.7 | 0.23 | 0.52 | 0.011 | 80 |
| | 71249 | INT./UPPER SHL CIRC WELD (INSIDE 61%) SA-1229 | 76.4 | ASME NB-2331 | 10 | 0 | 0.23 | 0.59 | 0.021 | 67 |
| | 72445 | UPPER/LOWER SHELL CIRC WELD SA-1585 | (4) | B&W Generic | -5 | 19.7 | 0.22 | 0.54 | 0.016 | 65 |
| | 8T1762 | LOWER SHELL AXIAL WELDS SA-1430 | 75.5 | B&W Generic | -5 | 19.7 | 0.19 | 0.57 | 0.017 | 70 |
| | 8T1762 | UPPER SHELL AXIAL WELDS SA-1493 | (4) | B&W Generic | -5 | 19.7 | 0.19 | 0.57 | 0.017 | 70 |
| | 8T1762 | LOWER SHELL AXIAL WELDS SA-1426 | 75.5 | B&W Generic | -5 | 19.7 | 0.19 | 0.57 | 0.017 | 70 |

| Product Form | Heat | Beltline | $\sigma_{flow(u)}$ [ksi] | $RT_{NDT(u)}$ [°F] | | | Composition[2] | | | $USE_0$ (ft-lbf) |
|---|---|---|---|---|---|---|---|---|---|---|
| | | | | $RT_{NDT(u)}$ Method | $RT_{NDT(u)}$ Value | $\sigma_{(u)}$ Value | Cu | Ni | P | |
| **Palisades, (Designer and Manufacturer: CE) Coolant Temperature = 532°F, Vessel Thickness = 8½ in.** | | | | | | | | | | |
| PLATE | A-0313 | D-3803-2 | (4) | MTEB 5-2 | -30 | 0 | 0.24 | 0.52 | 0.01 | 87 |
| | B-5294 | D-3804-3 | (4) | MTEB 5-2 | -25 | 0 | 0.12 | 0.55 | 0.01 | 73 |
| | C-1279 | D-3803-3 | (4) | ASME NB-2331 | -5 | 0 | 0.24 | 0.5 | 0.011 | 102 |
| | C-1279 | D-3803-1 | 74.7 | ASME NB-2331 | -5 | 0 | 0.24 | 0.51 | 0.009 | 102 |
| | C-1308A | D-3804-1 | (4) | ASME NB-2331 | 0 | 0 | 0.19 | 0.48 | 0.016 | 72 |
| | C-1308B | D-3804-2 | (4) | MTEB 5-2 | -30 | 0 | 0.19 | 0.5 | 0.015 | 76 |
| LINDE 0124 WELD | 27204 | CIRC. WELD 9-112 | 76.9 | Generic | -56 | 17 | 0.203 | 1.018 | 0.013 | 98 |
| LINDE 1092 WELD | 34B009 | LOWER SHELL AXIAL WELD 3-112A/C | 76.1 | Generic | -56 | 17 | 0.192 | 0.98 | (3) | 111 |
| | W5214 | LOWER SHELL AXIAL WELDS 3-112A/C | 72.9 | Generic | -56 | 17 | 0.213 | 1.01 | 0.019 | 118 |
| | W5214 | INTERMEDIATE SHELL AXIAL WELDS 2-112 A/C | 72.9 | Generic | -56 | 17 | 0.213 | 1.01 | 0.019 | 118 |

Notes:

(1) Information taken directly from the July 2000 release of the NRCs Reactor Vessel Integrity (RVID2) database.

(2) These composition values are as reported in RVID2. In FAVOR calculations these values should be treated as the central tendency of the Cu, Ni, and P distributions.

(3) No values of phosphorus are recorded in RVID2 for these heats. A generic value of 0.012 should be used, which is the mean of 826 phosphorus values taken from the surveillance database used by Eason and Wright [98] to calibrate the embrittlement trend curve.

(4) No values strength measurements are available in PREP4 for these heats [PREP]. A value of 77 ksi should be used, which is the mean of other flow strength values reported in this Appendix.

## Appendix E – Statistical Point-Estimation Techniques for Weibull Distributions

The three parameters for the Weibull distributions of $RT_{NDT} - T_0$ and $\Delta RT_{LB}$ were calculated using a combination of two point-estimation procedures, *Maximum Likelihood* and the *Method of Moments*. The parameters to estimate are the location parameter, *a*, of the random variate, the scale parameter, *b*, of the random variate, and the shape parameter, *c*.

Maximum likelihood estimators for the shape parameter $c'$ and the scale parameter $b'$ can be derived from the likelihood function, *L*, for the Weibull distribution. The Weibull density is given by

$$w(\Delta RT \,|\, a,b,c) = \frac{c}{b} y^{c-1} \exp\left(-y^c\right), \quad \text{for} \quad (y = (\Delta RT - a)/b, \Delta RT > a,\ b,c > 0) \tag{E1}$$

and the corresponding likelihood function is the joint density (see ref.[E1]) (given the location parameter, *a*)

$$L(b,c \,|\, \Delta RT, a) = \prod_{i=1}^{N} \frac{c}{b}\left(\frac{\Delta RT_{(i)} - a}{b}\right)^{c-1} \exp\left[-\left(\frac{\Delta RT_{(i)} - a}{b}\right)^{c}\right] \tag{E2}$$

The maximum likelihood (*ML*) estimators for the scale, $b'$, and shape parameters, $c'$, are defined as the unique values of $(b',c')$ that maximize the joint probability that the *N* members of the sample set all come from the same parent population. The *ML* estimators are, therefore, calculated by finding the stationary point of Eq. (E2). Upon taking the logarithm of Eq. (E2), the derivatives with respect to the individual parameters $(b',c')$ are set to zero. The resulting *ML* estimator for the shape parameter, $c'$, is found by solving iteratively for $c'$ in the following nonlinear equation

$$\frac{\partial(\ln(L(c')))}{\partial c'} = \frac{\sum_{i=1}^{N} (\Delta RT_{(i)} - a)^{c'} \ln(\Delta RT_{(i)} - a)}{\sum_{i=1}^{N} (\Delta RT_{(i)} - a)^{c'}} - \frac{1}{N}\sum_{i=1}^{N} \ln(\Delta RT_{(i)} - a) - \frac{1}{c'} = 0 \tag{E3}$$

Upon obtaining a solution for $c'$, the *ML* estimator for the scale parameter, $b'$, follows directly from

$$\frac{\partial(\ln(L))}{\partial b'} = b' - \left[ \sum_{i=1}^{N} \frac{\left(\Delta RT_{(i)} - a\right)^{c'}}{N} \right]^{\frac{1}{c'}} = 0 \tag{E4}$$

For the *ML* point estimators for $(b', c')$, the location parameter, *a*, was assumed given. The *Method of Moments* (*MM*) can now be applied to provide a point estimate for the location parameter, $a^*$. In the *Method of Moments*, the sample moments are used as estimators for the population moments. The *MM* point estimator for the scale parameter, $b^*$, is (given the shape parameter, *c*),

$$b^* = \sqrt{m_2 / [\Gamma(1+2/c) - \Gamma^2(1+1/c)]} \tag{E5}$$

where $m_2$ is the second moment of the sample about the sample mean and $\Gamma$ is Euler's gamma function. The *MM* estimator for the location parameter, $a^*$, follows from

$$a^* = m_1' - b^* \Gamma(1+1/c) \tag{E6}$$

where $m_1'$ is the 1st crude moment of the sample (the sample mean) and the sample moments are defined by

$$\begin{aligned} m_1' &= \sum_{i=1}^{N} \frac{\Delta RT_{NDT(i)}}{N} \\ m_2 &= \sum_{i=1}^{N} \frac{\left(\Delta RT_{NDT}(i) - m_1'\right)^2}{N} \end{aligned} \tag{E7}$$

From ref. [B.2], a moment estimator for the shape parameter, $c^*$, also exists

$$c^* = \frac{4.104683 - 1.148513\sqrt{b_1} + 0.44326(\sqrt{b_1})^2 - 0.053025(\sqrt{b_1})^3}{\sqrt{b_1} + 1.139547} \tag{E8}$$

where $\sqrt{b_1}$ is the sample skewness. However, for sample sizes as small as 20, there will be a high level of uncertainty in the $(a^*, b^*, c^*)$ estimates derived from $c^*$ (ref. [B.2]).

The three parameters for the Weibull distribution of $\Delta RT$ were estimated through the following iterative sequence:

1) For the discrete set $(\Delta RT_{(i)}, i = 1, N)$, calculate the sample moments, $(m_1', m_2)$ from Eqs. (E7).
2) Select a trial value for the location parameter, $a_{trial}$ where $a_{trial} < \min(\Delta RT_{(i)}, i = 1, 2, \ldots N)$.
3) Calculate ***ML*** estimates for $(c', b')$ from Eqs. (E3)-(E4) by letting $a = a_{trial}$.

4) Calculate MM estimates for $(a^*, b^*)$ from Eqs. (E5)-(E6) by letting $c = c'$ as determined in Step 3.

5) Calculate a relative deviation between the trial $a_{trial}$ and the MM estimate of $a^*$ from Step 4 by

$$\delta = \frac{a_{trial} - a^*}{a_{trial}} \tag{E9}$$

6) Given $\varepsilon_{tolerance}$, as a pre-selected convergence tolerance, if $\delta > \varepsilon_{tolerance}$, then select a new trial location parameter, $a_{trial}$, and repeat Steps 3-6 until convergence, defined as $\delta \le \varepsilon_{tolerance}$.

Upon convergence, there will be two triplets $(a_{trial}, b', c')$ and $(a^*, b^*, c')$ where in general $a_{trial} \approx a^*$ and $b' \neq b^*$ although $b'$ was typically close to $b^*$ in this study. The triplet $(a^*, b', c')$ was taken as the converged estimate for the parameters of the Weibull distribution for $\Delta RT$.

**References**

E1. A. Ghosh, "A FORTRAN Program for Fitting Weibull Distribution and Generating Samples," *Computers & Geosciences* **25**, (1999) 729-738.

E2. K. O. Bowman and P. T. Williams, *Technical Basis for Statistical Models of Extended $K_{Ic}$ and $K_{Ia}$ Fracture Toughness Databases for RPV Steels*, ORNL/NRC/LTR-99/27, Oak Ridge National Laboratory, Oak Ridge, TN, February 2000.

# Appendix F – Development of Stochastic Models for $\Delta RT_{epistemic}$ and $\Delta RT_{arrest}$

## F.1 Stochastic Model for $\Delta RT_{epistemic}$

### F.1.1 Initial Weibull Model for $\Delta RT_{epistemic}$

Initially, the epistemic uncertainty in the unirradiated value for $RT_{NDTo}$ was modeled by a continuous 3-parameter Weibull distribution of the form

$$f_W(\Delta RT \mid a,b,c) = \frac{c}{b}\left(\frac{\Delta RT - a}{b}\right)^{c-1} \exp\left[-\left(\frac{\Delta RT - a}{b}\right)^{c}\right], \qquad (\Delta RT > a, \;\; (b,c) > 0)$$
$$\Pr(X \le \Delta RT) = F_W(\Delta RT \mid a,b,c) = P = 1 - \exp\left[-\left(\frac{\Delta RT - a}{b}\right)^{c}\right], \;\; (\Delta RT > a, \;\; (b,c) > 0) \qquad \text{(F1)}$$

where $f_W$ is the probability density function (PDF), $F_W$ is the cumulative distribution function (CDF), and *a, b,* and *c* are the location, scale, and shape parameters, respectively, of the Weibull distribution. In FAVOR, the epistemic uncertainty term is sampled using the inverse CDF

$$\Delta RT = a + b\left[-\ln(1-P)\right]^{\frac{1}{c}}; \quad 0 < P < 1 \qquad \text{(F2)}$$

where *P* is randomly sampled from a uniform distribution on the open interval (0,1). The *epistemic* uncertainty in $RT_{NDT(u)}$ can then be reduced by

$$RT_{LB} = RT_{NDT(u)} - \Delta RT \qquad \text{(F3)}$$

Using a combination of the *Maximum Likelihood* and *Method of Moments* point-estimation procedures (as described in Appendix E, the following values were determined for the three Weibull parameters in Eqs. (F1) and (F2):

$$\begin{aligned} a &= -40.02 \text{ °F} \\ b &= 124.88 \text{ °F} \\ c &= 1.96 \end{aligned} \qquad \text{(F4)}$$

based on the sample ($N$ = 18) given in Table 8 and repeated in Table F1.

**Table F1.** $\Delta RT_{epistemic}$ **Ranked Data with Order-Statistic Estimates of** ***P***

| $i$ | $\Delta RT_i$, (°F) | $\boldsymbol{P}_i$ | ln( - ln(1 - $\boldsymbol{P}_i$)) |
|---|---|---|---|
| 1 | -19.4 | 0.03804 | -3.24970 |
| 2 | -10.9 | 0.09239 | -2.33364 |
| 3 | -1.7 | 0.14674 | -1.84080 |
| 4 | 2.1 | 0.20109 | -1.49387 |
| 5 | 33.2 | 0.25543 | -1.22093 |
| 6 | 38.4 | 0.30978 | -0.99223 |
| 7 | 50.1 | 0.36413 | -0.79239 |
| 8 | 54.6 | 0.41848 | -0.61229 |
| 9 | 62.3 | 0.47283 | -0.44594 |
| 10 | 64.3 | 0.52717 | -0.28898 |
| 11 | 81.9 | 0.58152 | -0.13796 |
| 12 | 89.4 | 0.63587 | 0.01019 |
| 13 | 91.5 | 0.69022 | 0.15861 |
| 14 | 97.8 | 0.74457 | 0.31100 |
| 15 | 142.2 | 0.79891 | 0.47251 |
| 16 | 147.6 | 0.85326 | 0.65186 |
| 17 | 162.4 | 0.90761 | 0.86782 |
| 18 | 186.2 | 0.96196 | 1.18449 |

| Sample | |
|---|---|
| mean = | 70.67 |
| variance = | 3669.77 |
| stdv = | 60.58 |

$P_i = (i - 0.3)/(n + 0.4)$

From the following asymptotic relations for the mean and variance of a Weibull distribution,

$$\mu = a + b\,\Gamma\left(1 + \frac{1}{c}\right)$$

$$\sigma^2 = b^2\left[\Gamma\left(1 + \frac{2}{c}\right) - \Gamma^2\left(1 + \frac{1}{c}\right)\right] \quad , \tag{F5}$$

$$\Gamma(x) = \int_0^\infty t^{x-1} e^{-t}\,dt$$

the mean and variance for the Weibull model for $\Delta RT_{epistemic}$ compared to the corresponding sample estimators are:

| Model | Sample |
|---|---|
| $\mu$ = 70.70 °F | $m_1'$ = 70.67 °F |
| $\sigma^2$ = 3473.65 | $s^2$ = 3669.77 |
| $\sigma$ = 58.94 °F | $s$ = 60.58 °F |

### F.1.2 New Model Developed Using Orthogonal Distance Regression (ODR)

The initial statistical model for $\Delta RT_{epistemic}$ was developed using point-estimation procedures that did not take into account any uncertainty in the data sample of Table F1. An analytical procedure, called *orthogonal distance regression* (ODR), can be employed to solve the *errors-in-variables* problem in which uncertainties are assumed to exist in the data. The computational procedure implemented into the software package, ODRPACK [F1], can be used to fit a model equation to data using orthogonal distance regression.

The explicit ODR problem is defined as follows. Let $(x_i, y_i), i = 1, 2, \ldots n$ be an observed set of data. Assume that the values $y_i$ are a (possibly nonlinear) function of $x_i$ and a set of unknown parameters $\beta \in \Re^p$, where both $y_i$ and $x_i$ contain the uncertainties, $\varepsilon_i^* \in \Re^1$ and $\delta_i^* \in \Re^1$, respectively. The superscript "*" denotes an actual but unknown value. The observed value, $y_i$, can be expressed in terms of a *model equation*

$$y_i + \varepsilon_i^* = f_i\left(x_i + \delta_i^* \left| \left\{\beta_k^*\right\}\right.\right); \quad \left(i = 1, 2, \ldots n\right) \tag{F6}$$

for some actual values of the parameter vector $\left(\left\{\beta_k^*\right\}; k = 1, 2, \ldots p\right)$. The variables $y_i$ are sometimes referred to as the *dependent* or *response* variables, and $x_i$ are the *independent* (*regressor* or *explanatory*) variables.

The explicit *orthogonal distance regression* problem approximates $\left\{\beta^*\right\}$ by finding the estimate $\{\beta\}$ for which the sum of the squares of the *n* orthogonal distances from the curve $f(x; \{\beta\})$ to the *n* data points is minimized [F1]. This can be accomplished by the following minimization problem

$$\min_{\beta, \delta, \varepsilon} \sum_{i=1}^{n} \left(\varepsilon_i^2 + \delta_i^2\right) \tag{F7}$$

subject to the constraints

$$y_i = f_i\left(x_i + \delta_i \left| \{\beta\}\right.\right) - \varepsilon_i \qquad i = 1, 2, \ldots n. \tag{F8}$$

Since the constraints are linear in $\varepsilon_i$, they and thus $\varepsilon_i$ can be eliminated from the minimization problem, obtaining

$$\min_{\{\beta\}, \{\delta\}} \sum_{i=1}^{n} \left( \left[ f_i\left(x_i + \delta_i \left| \{\beta\}\right.\right) - y_i \right]^2 + \delta_i^2 \right) \tag{F9}$$

The algorithm implemented in ODRPACK uses the Levenberg-Marquardt *trust region* method to iteratively solve the nonlinear minimization problem of Eq. (F9).

**Derivation of the Model Equation Form**

To proceed, the form of the problem-specific model equation must be derived. The CDF in Eq.(F1) can be rewritten as

$$\begin{aligned} P &= 1-\exp\left[-\left(\frac{\Delta RT-a}{b}\right)^c\right] \\ 1-P &= \exp\left[-\left(\frac{\Delta RT-a}{b}\right)^c\right] \\ -\ln(1-P) &= \left(\frac{\Delta RT-a}{b}\right)^c \\ \ln\left[-\ln(1-P)\right] &= c\ln(\Delta RT-a)-c\ln(b) \end{aligned} \tag{F10}$$

The location parameter, *a*, is related to the scale, *b*, and shape, *c*, parameters through its *moment estimator*

$$a \approx m_1' - b\,\Gamma\left(1+\frac{1}{c}\right) \tag{F11}$$

where $m_1'$ is the 1st crude moment of the sample (or sample mean). The use of the Eq. (F11) as a constraint in the model equation forces the mean of the resulting Weibull model to be identical to the sample mean, $m_1'$. Introducing Eq. (F11) into Eq. (F10), the final form of the nonlinear model equation is

$$y_i = \beta_1 \ln\left[x_i - m_1' + \beta_2\,\Gamma\left(1+\frac{1}{\beta_1}\right)\right] - \beta_1\ln(\beta_2);\ (i=1,2,\ldots n)$$

where (F12)

$$\left(\{\beta\}=\begin{Bmatrix}\beta_1\\ \beta_2\end{Bmatrix}=\begin{Bmatrix}c\\ b\end{Bmatrix};\quad \{x_i\}=\left\{\Delta RT_{(i)}\right\};\{y_i\}=\left\{\ln\left[-\ln(1-P_i)\right]\right\}\right)$$

Values for $P_i$ can be estimated by ranking the data in Table F1 and applying the median-rank order statistic

$$P_i \approx \frac{i-0.3}{n+0.4} \tag{F13}$$

ODRPACK iteratively solves for the solution vector $\begin{Bmatrix} \beta_1 \\ \beta_2 \\ \delta_1 \\ \delta_2 \\ \vdots \\ \delta_n \end{Bmatrix}_{n+2}$

The results of the ODRPACK analysis are presented in Table F2. In summary, the ODR analysis produced the following estimates for the Weibull model for $\Delta RT_{epistemic}$ :

| | | |
|---|---|---|
| Location Parameter, $a =$ | -45.586 | 95% Confidence Intervals |
| Scale Parameter, $b =$ | $130.899 \pm 10.259$ | 109.15 to 152.65 |
| Shape Parameter, $c =$ | $1.855 \pm 0.227$ | 1.374 to 2.337 |
| $\Delta RT_{ODR} =$ | $-45.586 + 130.899\left[-\ln\left(1-P\right)\right]^{\frac{1}{1.855}};$ | $0 < P < 1$ |
| Sample Mean, $m'_1 =$ | 70.67 | |
| Weibull Mean, $\mu =$ | 70.667 | |
| Sample Stdv, $s =$ | 60.58 | |
| Weibull Stdv, $\sigma =$ | 65.036 | |
| Sample Variance, $s^2 =$ | 3669.77 | |
| Weibull Variance, $\sigma^2 =$ | 4229.692 | |

The 95% confidence intervals for the two parameters $\beta_1 = c$ and $\beta_2 = b$ are calculated by ODRPACK using $\beta_k \pm t_{(0.975,\mu)}\sigma_{\beta_k}$ where $t_{(0.975,\mu)}$ is the appropriate value for constructing a two-sided confidence interval using Student's *t* distribution with $\mu$ degrees of freedom. The computational procedure used by ODRPACK to calculate the standard deviations for the parameters, $\sigma_{\beta_k}$, is given in [F2]. See Fig. F1 for a comparison of the initial Weibull model and the model produced by the ODR analysis. The application of ODR has resulted in an increase in the Weibull model's standard deviation from 58.94 °F to 65.04 °F compared to the sample's standard deviation of 60.58 °F.

**Table F2. ODRPACK Results of ODR Analysis of $\Delta RT_{epistemic}$ Model Equation**

```
*****************************************************
* ODRPACK VERSION 2.01 OF 06-19-92 (DOUBLE PRECISION) *
*****************************************************

    ODR Analysis of DRTLB Weibull Model Parameters

   BETA(1) = c >> Shape Parameter
   BETA(2) = b >> Scale Parameter

   a = M1 - b*Gamma[1 + 1/c]

*** INITIAL SUMMARY FOR FIT BY METHOD OF ODR ***

--- PROBLEM SIZE:
          N =    18          (NUMBER WITH NONZERO WEIGHT =    18)
         NQ =     1
          M =     1
         NP =     2          (NUMBER UNFIXED =     2)

--- CONTROL VALUES:
         JOB = 00010
             = ABCDE, WHERE
                      A=0 ==> FIT IS NOT A RESTART.
                      B=0 ==> DELTAS ARE INITIALIZED TO ZERO.
                      C=0 ==> COVARIANCE MATRIX WILL BE COMPUTED USING
                              DERIVATIVES RE-EVALUATED AT THE SOLUTION.
                      D=1 ==> DERIVATIVES ARE ESTIMATED BY CENTRAL
DIFFERENCES.
                      E=0 ==> METHOD IS EXPLICIT ODR.
      NDIGIT =    16          (ESTIMATED BY ODRPACK)
      TAUFAC =     1.00D+00

--- STOPPING CRITERIA:
       SSTOL =     1.49D-08   (SUM OF SQUARES STOPPING TOLERANCE)
      PARTOL =     3.67D-11   (PARAMETER STOPPING TOLERANCE)
       MAXIT =    50          (MAXIMUM NUMBER OF ITERATIONS)

--- INITIAL WEIGHTED SUM OF SQUARES        =   1.15671908D+00
        SUM OF SQUARED WEIGHTED DELTAS     =   0.00000000D+00
        SUM OF SQUARED WEIGHTED EPSILONS   =   1.15671908D+00

*** ITERATION REPORTS FOR FIT BY METHOD OF ODR ***


        CUM.                 ACT. REL.   PRED. REL.
 IT.  NO. FN     WEIGHTED   SUM-OF-SQS   SUM-OF-SQS              G-N
NUM.   EVALS   SUM-OF-SQS    REDUCTION    REDUCTION  TAU/PNORM  STEP
----  ------  -----------  -----------  -----------  ---------  ----

   1      12  5.36253D-01   5.3640D-01   5.3739D-01  1.333D-01   YES
   2      19  5.33419D-01   5.2849D-03   4.2184D-03  4.265D-02   YES
   3      26  5.33152D-01   4.9976D-04   3.9259D-04  1.461D-02   YES
   4      33  5.33130D-01   4.1577D-05   3.2561D-05  4.323D-03   YES
   5      40  5.33128D-01   3.2902D-06   2.5746D-06  1.224D-03   YES
   6      47  5.33128D-01   2.5647D-07   2.0064D-07  3.423D-04   YES
   7      54  5.33128D-01   1.9907D-08   1.5572D-08  9.542D-05   YES
   8      61  5.33128D-01   1.5432D-09   1.2072D-09  2.657D-05   YES
```

**Table F2. ODRPACK Results of ODR Analysis of $\Delta RT_{epistemic}$ Model Equation (continued)**

```
*** FINAL SUMMARY FOR FIT BY METHOD OF ODR ***

 --- STOPPING CONDITIONS:
        INFO =     1 ==> SUM OF SQUARES CONVERGENCE.
       NITER =     8          (NUMBER OF ITERATIONS)
        NFEV =    67          (NUMBER OF FUNCTION EVALUATIONS)
       IRANK =     0          (RANK DEFICIENCY)
       RCOND =     1.20D-01   (INVERSE CONDITION NUMBER)
       ISTOP =     0          (RETURNED BY USER FROM SUBROUTINE FCN)

 --- FINAL WEIGHTED SUMS OF SQUARES       =    5.33127879D-01
        SUM OF SQUARED WEIGHTED DELTAS   =    7.67684538D-04
        SUM OF SQUARED WEIGHTED EPSILONS =    5.32360195D-01

 --- RESIDUAL STANDARD DEVIATION          =    1.82539016D-01
        DEGREES OF FREEDOM               =    16

 --- ESTIMATED BETA(J), J = 1, ..., NP:

           BETA        S.D. BETA     ---- 95%  CONFIDENCE INTERVAL ----

 1   1.85530498D+00     2.2706D-01     1.37390691D+00 TO  2.33670305D+00
 2   1.30899017D+02     1.0259D+01     1.09149592D+02 TO  1.52648443D+02

 --- ESTIMATED EPSILON(I) AND DELTA(I,*), I = 1, ..., N:

        I    EPSILON(I,1)      DELTA(I,1)

        1  2.62841903D-01 -1.86361603D-02
        2 -1.29977011D-01  6.95094427D-03
        3 -1.86382404D-01  7.87802505D-03
        4 -3.79012096D-01  1.47415688D-02
        5  2.78865897D-01 -6.56742977D-03
        6  1.68817068D-01 -3.72942044D-03
        7  2.10949482D-01 -4.09035239D-03
        8  1.16154880D-01 -2.15105581D-03
        9  8.71915578D-02 -1.49943300D-03
       10 -3.56507199D-02  6.01915026D-04
       11  8.89342397D-02 -1.29426169D-03
       12  4.68465281D-02 -6.43875329D-04
       13 -7.29122682D-02  9.86768713D-04
       14 -1.41925842D-01  1.83636941D-03
       15  1.97009129D-01 -1.94642622D-03
       16  7.02764840D-02 -6.74910438D-04
       17 -8.73096746D-03  7.78822029D-05
       18 -1.24381318D-01  9.95579717D-04
```

### F.1.3. Final Stochastic Model for $\Delta RT_{epistemic}$ in FAVOR$^{EP}$

The epistemic uncertainty in $RT_{NDT(u)}$ is estimated in FAVOR$^{EP}$ by

$$\Delta RT_{epistemic} = RT_{NDT(u)} - RT_{LB} \tag{F14}$$

where $RT_{NDT(u)}$ is the unirradiated reference nil-ductility transition temperature and $RT_{LB}$ is a new temperature index developed for FAVOR$^{EP}$ analyses. If we assume that $RT_{NDT(u)}$ and $RT_{LB}$ are statistically independent and, therefore, uncorrelated, then the variance of $\Delta RT_{epistemic}$ is

$$\text{var}(\Delta RT_{epistemic}) = \text{var}(RT_{NDT}) + \text{var}(RT_{LB}) \tag{F15}$$

where the $\text{cov}\left(RT_{NDT(u)} RT_{LB}\right)$ has been assumed to be zero. The statistical model developed for $\Delta RT_{epistemic}$ using the ODR procedure contains the following four sources of uncertainty

1. Measurement uncertainty and material variability in $RT_{NDT(u)}$, $\sigma_{(1)}^2$
2. Measurement uncertainty and material variability in $RT_{LB}$, $\sigma_{(2)}^2$
3. Model uncertainty in $RT_{NDT(u)}$, $\sigma_{(3)}^2$
4. Model uncertainty in $RT_{LB}$, $\sigma_{(4)}^2$

such that the components of the variances for $RT_{NDT(u)}$ and $RT_{LB}$ are the following:

$$\begin{aligned} \text{var}(RT_{NDT(u)}) &= \sigma_{(1)}^2 + \sigma_{(3)}^2 \\ \text{var}(RT_{LB}) &= \sigma_{(2)}^2 + \sigma_{(4)}^2 \end{aligned} \tag{F16}$$

Therefore, the variance (uncertainty) in the ODR-developed Weibull distribution for $\Delta RT_{epistemic}$ can be expressed as

$$\sigma_{\Delta RT}^2 = \sigma_{(1)}^2 + \sigma_{(2)}^2 + \sigma_{(3)}^2 + \sigma_{(4)}^2 = 4229.69 \tag{F17}$$

As a result of the sampling protocols in FAVOR$^{EP}$, the uncertainties associated with sources (1) and (2) have already been accounted for at the point in FAVOR$^{EP}$ where $\Delta RT_{epistemic}$ is sampled. The Weibull model for $\Delta RT_{epistemic}$ can be revised such that it reflects the uncertainties associated with sources (3) and (4) only, specifically

$$\sigma_{\Delta RT(rev)}^2 = \sigma_{(3)}^2 + \sigma_{(4)}^2 = \sigma_{\Delta RT}^2 - \sigma_{(1)}^2 - \sigma_{(2)}^2 \tag{F18}$$

Two cases were examined:

**Case 1:**

$$\sigma_{(1)}^2 = (23°\text{F})^2$$
$$\sigma_{(2)}^2 = 0$$

**Case 2:**

$$\sigma_{(1)}^2 = (23°\text{F})^2$$
$$\sigma_{(2)}^2 = (23°\text{F})^2$$

The required adjustments to the Weibull model for $\Delta RT_{epistemic}$ can be calculated by solving the following nonlinear system of equations

$$\begin{aligned} \mu_{\Delta RT} - a - b\Gamma\left(1+\frac{1}{c}\right) &= 0 \\ \sigma_{\Delta RT(rev)}^2 - b^2\left[\Gamma\left(1+\frac{2}{c}\right) - \Gamma^2\left(1+\frac{1}{c}\right)\right] &= 0 \end{aligned} \tag{F19}$$

for the new parameters *b* and *c*, where $\mu_{\Delta RT} = 70.67$ °F and the location parameter for the ODR-developed model, $a$ = -45.586 °F, remain fixed. Equations (F19) are the asymptotic relations for the mean and variance of a Weibull distribution.

**Case 1:**

$$\sigma_{\Delta RT(rev)}^2 = \sigma_{\Delta RT}^2 - \sigma_{(1)}^2 - \sigma_{(2)}^2$$
$$\sigma_{\Delta RT(rev)}^2 = 4229.692 - 23^2 - 0 = 3700.692$$
$$\sigma_{\Delta RT(rev)} = 60.83 \text{ °F}$$

The solutions for ($b$,$c$) are

$$b = 131.18 \text{ °F}$$
$$c = 1.998$$

**Case 2:**

$$\sigma^2_{\Delta RT(rev)} = \sigma^2_{\Delta RT} - \sigma^2_{(1)} - \sigma^2_{(2)}$$
$$\sigma^2_{\Delta RT(rev)} = 4229.692 - 23^2 - 23^2 = 3171.692$$
$$\sigma_{\Delta RT(rev)} = 56.32 \text{ °F}$$

The solutions for ($b$,$c$) are

$$b = 131.27 \text{ °F}$$
$$c = 2.177$$

See Fig. F2 for a comparison of the ODR-derived model with the revised models of Cases 1 and 2. Figure F3 compares the CDF of the initial Weibull model to that of Case 2 with emphasis placed on the lower-left tail. Note that Case 2 produces a more negative $\Delta RT_{epistemic}$ adjustment than the initial model for cumulative probabilities less than approximately 3.5%. A comparison between the ODR-derived model and Case 2 is shown in Fig. F4. For cumulative probabilities less than approximately 60%, Case 2 produces more positive values of $\Delta RT_{epistemic}$ than the ODR model.

In summary the revised Weibull models for Cases (1) and (2) are:

**Summary:**

Case 1:

$$\Delta RT_{(rev)} = -45.586 + 131.18\left[-\ln\left(1-P\right)\right]^{\frac{1}{1.998}}; \quad 0 < P < 1$$

Case 2:

$$\Delta RT_{(rev)} = -45.586 + 131.27\left[-\ln\left(1-P\right)\right]^{\frac{1}{2.177}}; \quad 0 < P < 1$$

Case 2 was selected for implementation into FAVOR$^{EP}$.

## F.2. Stochastic Model for $\Delta RT_{arrest}$ in FAVOR$^{EP}$

### F.2.1 Initial Model for $\Delta RT_{arrest}$

The initial stochastic model developed for FAVOR$^{EP}$ to describe the statistical distribution of $\Delta RT_{arrest} = T_0 - T_{K_{Ia}}$ was based on a lognormal distribution (see Fig. F5) with the parameters

$$\begin{aligned} &\overline{\Delta RT}_{arrest} = \mu(T_0) = 44.123\exp(-0.006\,T_0); \quad T_0[^\circ c] \\ &\sigma^2_{\log} = 0.39^2 = 0.1521 \text{ (constant)} \end{aligned} \tag{F20}$$

The asymptotic relations for the log-mean and variance of the model are:

$$\begin{aligned} &\mu_{\log}(T_0) = \ln\left[\mu(T_0)\right] - \frac{\sigma^2_{\log}}{2} \\ &\text{var}(\Delta RT_{arrest}) = \sigma^2(T_0) = \omega(\omega-1)\exp\left[2\mu_{\log}(T_0)\right]; \quad \omega = \exp(\sigma^2_{\log}) \end{aligned} \tag{F21}$$

The initial model was derived from an ordinary least squares regression analysis using the log-transformed data shown in Table F3.

### F.2.2 Model Developed Using Orthogonal Distance Regression (ODR)

The ORDPACK program was used to reanalyze the following model equation

$$\ln(\overline{\Delta RT}_{arrest}) = \beta_1 T_0 + \beta_2 \tag{F22}$$

where, upon reversing the log-transformation, the mean value for $\Delta RT_{arrest}$ is

$$\overline{\Delta RT}_{arrest} = \exp(\beta_2)\exp\left(\beta_1 T_0\right) \tag{F23}$$

The results of the ODR analysis are presented in Table F4 with the following ODR estimates for the model parameters:

$$\begin{aligned} &\beta_1 = -0.00597110744 \pm 0.00082458 \\ &\beta_2 = 3.78696343 \pm 0.065299 \\ &\exp(\beta_2) = 44.12221645 \pm 2.908036613 \end{aligned} \tag{F24}$$

$$\begin{aligned} &\overline{\Delta RT}_{arrest} = 44.1222\exp(-0.00597 T_0); \quad [^\circ\text{C}] \\ &\sigma_{\log} = 0.389987535; \quad \sigma^2_{\log} = 0.1520903 \end{aligned}$$

**Table F3. Data Used in the Development of the $\Delta RT_{arrest}$ Model**

| N | $T_0$ (°C) | $T_{KIa}$ (°C) | $T_{KIa}$ - $T_0$ (°C) | $\ln(T_{KIa} - T_0)$ |
|---|---|---|---|---|
| 1 | -114 | 16 | 130 | 4.8675 |
| 2 | 131 | 140 | 9 | 2.1972 |
| 3 | -66 | 13 | 79 | 4.3694 |
| 4 | -78 | 6 | 84 | 4.4308 |
| 5 | -104 | -16 | 88 | 4.4773 |
| 6 | -108 | 44 | 152 | 5.0239 |
| 7 | 43 | 113 | 70 | 4.2485 |
| 8 | -20 | 60 | 80 | 4.3820 |
| 9 | -71 | -41 | 30 | 3.4012 |
| 10 | -66 | 6 | 72 | 4.2767 |
| 11 | -84 | 9 | 93 | 4.5326 |
| 12 | -21 | 65 | 86 | 4.4543 |
| 13 | -53 | -6 | 47 | 3.8501 |
| 14 | -54 | 18 | 72 | 4.2767 |
| 15 | 62 | 93 | 31 | 3.4340 |
| 16 | -65 | -12 | 53 | 3.9703 |
| 17 | -100 | -15 | 85 | 4.4427 |
| 18 | -130 | -8 | 122 | 4.8040 |
| 19 | -100 | -18 | 82 | 4.4067 |
| 20 | -27 | 25 | 52 | 3.9512 |
| 21 | -78 | 10 | 88 | 4.4773 |
| 22 | -115 | -25 | 90 | 4.4998 |
| 23 | -68 | -9 | 59 | 4.0775 |
| 24 | -70 | 17 | 87 | 4.4659 |
| 25 | -65 | -25 | 40 | 3.6889 |
| 26 | -51 | 19 | 70 | 4.2485 |
| 27 | 17 | 77 | 60 | 4.0943 |
| 28 | -48 | 48 | 96 | 4.5643 |
| 29 | -92 | -26 | 66 | 4.1897 |
| 30 | -70 | -18 | 52 | 3.9512 |
| 31 | -81 | -20 | 61 | 4.1109 |
| 32 | -157 | -27 | 130 | 4.8675 |
| 33 | 67 | 78 | 11 | 2.3979 |
| 34 | -84 | 9 | 93 | 4.5326 |
| 35 | -67 | 18 | 85 | 4.4427 |
| 36 | -58 | -14 | 44 | 3.7842 |
| 37 | 35 | 74 | 39 | 3.6636 |
| 38 | 39 | 67 | 28 | 3.3322 |
| 39 | -61 | -15 | 46 | 3.8286 |
| 40 | 6 | 62 | 56 | 4.0254 |
| 41 | -61 | -16 | 45 | 3.8067 |
| 42 | -48 | 8 | 56 | 4.0254 |
| 43 | -24 | 32 | 56 | 4.0254 |
| 44 | -19 | 10 | 29 | 3.3673 |
| 45 | -85 | -33 | 52 | 3.9512 |
| 46 | -131 | -26 | 105 | 4.6540 |
| 47 | -3 | 33 | 36 | 3.5835 |
| 48 | -95 | -62 | 33 | 3.4965 |
| 49 | -93 | -17 | 76 | 4.3307 |
| 50 | -68 | -8 | 60 | 4.0943 |
| 51 | 184 | 220 | 36 | 3.5835 |
| 52 | 42 | 71 | 29 | 3.3673 |
| 53 | 27 | 68 | 41 | 3.7136 |

**Table F4. ODRPACK Results of ODR Analysis of $\Delta RT_{arrest}$ Model Equation**

```
*******************************************************
* ODRPACK VERSION 2.01 OF 06-19-92 (DOUBLE PRECISION) *
*******************************************************

    ODR Analysis of DARTarrest Lognormal Model

   BETA(1) = slope
   BETA(2) = intercept of log-transformed data

   LN(DRTarrest) = BETA(1)*T0 + BETA(2)

   DRTArrest = EXP(BETA(2))*EXP(BETA(1)*T0)


*** DERIVATIVE CHECKING REPORT FOR FIT BY METHOD OF ODR ***


    FOR RESPONSE  1 OF OBSERVATION     1

                            USER
                        SUPPLIED     RELATIVE    DERIVATIVE
       DERIVATIVE WRT      VALUE   DIFFERENCE    ASSESSMENT

            BETA(  1)   -1.57D+02     4.25D-07    VERIFIED
            BETA(  2)    1.00D+00     7.87D-08    VERIFIED
          DELTA( 1, 1)   -5.84D-03     4.30D-07    VERIFIED

    NUMBER OF RELIABLE DIGITS IN FUNCTION RESULTS          16
       (ESTIMATED BY ODRPACK)

    NUMBER OF DIGITS OF AGREEMENT REQUIRED BETWEEN
    USER SUPPLIED AND FINITE DIFFERENCE DERIVATIVE FOR
    USER SUPPLIED DERIVATIVE TO BE CONSIDERED VERIFIED      4

    ROW NUMBER AT WHICH DERIVATIVES WERE CHECKED            1

      -VALUES OF THE EXPLANATORY VARIABLES AT THIS ROW

         X( 1, 1)  -1.57000000D+02
*******************************************************
* ODRPACK VERSION 2.01 OF 06-19-92 (DOUBLE PRECISION) *
*******************************************************


*** INITIAL SUMMARY FOR FIT BY METHOD OF ODR ***

--- PROBLEM SIZE:
           N =    53          (NUMBER WITH NONZERO WEIGHT =    53)
          NQ =     1
           M =     1
          NP =     2          (NUMBER UNFIXED =     2)

--- CONTROL VALUES:
         JOB = 00020
             = ABCDE, WHERE
                      A=0 ==> FIT IS NOT A RESTART.
                      B=0 ==> DELTAS ARE INITIALIZED TO ZERO.
                      C=0 ==> COVARIANCE MATRIX WILL BE COMPUTED USING
                              DERIVATIVES RE-EVALUATED AT THE SOLUTION.
                      D=2 ==> DERIVATIVES ARE SUPPLIED BY USER.
                              DERIVATIVES WERE CHECKED.
                              RESULTS APPEAR CORRECT.
                      E=0 ==> METHOD IS EXPLICIT ODR.
      NDIGIT =    16          (ESTIMATED BY ODRPACK)
      TAUFAC =     1.00D+00
```

**Table F4. ODRPACK Results of ODR Analysis of $\Delta RT_{arrest}$ Model Equation (continued)**

```
--- STOPPING CRITERIA:
       SSTOL =     1.49D-08   (SUM OF SQUARES STOPPING TOLERANCE)
      PARTOL =     3.67D-11   (PARAMETER STOPPING TOLERANCE)
       MAXIT =    50          (MAXIMUM NUMBER OF ITERATIONS)

--- INITIAL WEIGHTED SUM OF SQUARES        =   7.76381810D+00
        SUM OF SQUARED WEIGHTED DELTAS     =   0.00000000D+00
        SUM OF SQUARED WEIGHTED EPSILONS   =   7.76381810D+00

*** ITERATION REPORTS FOR FIT BY METHOD OF ODR ***


        CUM.                  ACT. REL.   PRED. REL.
 IT.  NO. FN     WEIGHTED   SUM-OF-SQS   SUM-OF-SQS              G-N
NUM.   EVALS   SUM-OF-SQS    REDUCTION    REDUCTION  TAU/PNORM  STEP
----  ------  -----------  -----------  -----------  ---------  ----

   1      15  7.75660D+00   9.2916D-04   9.2766D-04  3.063D-02   YES
   2      16  7.75660D+00   1.7592D-08   1.7540D-08  5.224D-05   YES
   3      17  7.75660D+00   6.0973D-13   6.0818D-13  1.064D-06   YES


*** FINAL SUMMARY FOR FIT BY METHOD OF ODR ***

--- STOPPING CONDITIONS:
        INFO =     1 ==> SUM OF SQUARES CONVERGENCE.
       NITER =     3          (NUMBER OF ITERATIONS)
        NFEV =    17          (NUMBER OF FUNCTION EVALUATIONS)
        NJEV =     4          (NUMBER OF JACOBIAN EVALUATIONS)
       IRANK =     0          (RANK DEFICIENCY)
       RCOND =     1.02D-01   (INVERSE CONDITION NUMBER)
       ISTOP =     0          (RETURNED BY USER FROM SUBROUTINE FCN)

--- FINAL WEIGHTED SUMS OF SQUARES       =    7.75660416D+00
        SUM OF SQUARED WEIGHTED DELTAS   =    2.76544656D-04
        SUM OF SQUARED WEIGHTED EPSILONS =    7.75632762D+00

--- RESIDUAL STANDARD DEVIATION          =    3.89987535D-01
        DEGREES OF FREEDOM               =   51

--- ESTIMATED BETA(J), J = 1, ..., NP:

            BETA          S.D. BETA     ---- 95%  CONFIDENCE INTERVAL ----

   1  -5.97110744D-03     8.2458D-04    -7.62651413D-03 TO -4.31570076D-03
   2   3.78696343D+00     6.5299D-02     3.65587019D+00 TO  3.91805666D+00
   2a  44.1222164         1.06747815    38.70118385     TO 50.30259469
```

**Table F4. ODRPACK Results of ODR Analysis of $\Delta RT_{arrest}$ Model Equation (continued)**

```
--- ESTIMATED EPSILON(I) AND DELTA(I,*), I = 1, ..., N:

        I    EPSILON(I,1)      DELTA(I,1)

        1 -1.43102053D-01 -8.54477100D-04
        2 -8.47788261D-02 -5.06223103D-04
        3 -2.40805066D-01 -1.43787185D-03
        4 -2.61679548D-02 -1.56251554D-04
        5 -3.99850519D-01 -2.38754864D-03
        6 -5.92016383D-01 -3.53499080D-03
        7 -6.93757401D-02 -4.14249691D-04
        8 -5.85749970D-02 -3.49757341D-04
        9 -2.26442691D-02 -1.35211263D-04
       10  8.57680493D-01  5.12129857D-03
       11  1.15426669D-02  6.89224532D-05
       12  1.46645341D-01  8.75634434D-04
       13  3.43251602D-01  2.04959067D-03
       14 -2.44054340D-01 -1.45727360D-03
       15 -2.44054340D-01 -1.45727360D-03
       16  1.59743570D-01  9.53845309D-04
       17 -1.78100642D-01 -1.06345728D-03
       18 -2.24618999D-01 -1.34122318D-03
       19  8.09685804D-01  4.83471734D-03
       20 -2.60957867D-01 -1.55820631D-03
       21  2.53688183D-01  1.51479827D-03
       22  1.15457172D-01  6.89406666D-04
       23  9.86506532D-02  5.89053212D-04
       24 -2.55614517D-01 -1.52630061D-03
       25 -1.88384618D-01 -1.12486396D-03
       26 -9.56061927D-02 -5.70874424D-04
       27  2.04786195D-01  1.22279946D-03
       28  4.86188622D-01  2.90308234D-03
       29  3.22548084D-01  1.92596784D-03
       30  3.44526207D-01  2.05720147D-03
       31  3.49085578D-01  2.08442594D-03
       32 -1.67256927D-01 -9.98708341D-04
       33  2.53275489D-01  1.51233403D-03
       34 -1.56999738D-01 -9.37461609D-04
       35 -4.90754110D-01 -2.93034334D-03
       36  4.82231733D-02  2.87945535D-04
       37 -3.06028247D-03 -1.82732618D-05
       38 -9.50782960D-02 -5.67722299D-04
       39 -5.41971290D-01 -3.23616640D-03
       40 -4.75624102D-01 -2.84000050D-03
       41  5.33099631D-01  3.18319281D-03
       42  2.21349919D-01  1.32170317D-03
       43 -2.74205133D-01 -1.63730709D-03
       44 -4.08875384D-01 -2.44143703D-03
       45 -8.78254100D-02 -5.24414570D-04
       46 -8.55839285D-02 -5.11030452D-04
       47  2.21877816D-01  1.32485529D-03
       48  1.68875063D-01  1.00837040D-03
       49 -7.18263826D-01 -4.28882729D-03
       50 -1.72318244D-02 -1.02892998D-04
       51  9.88968694D-01  5.90523394D-03
       52  8.07494984D-01  4.82163573D-03
       53 -8.95207363D-01 -5.34537537D-03
```

Comparison of Eqs. (F20) with Eqs. (F24) indicates that the ODR analysis produced essentially the same model as resulted from the ordinary least squares analysis (see Fig. F6).

### F.2.3 Final Model for $\Delta RT_{arrest}$

The variance of $\Delta RT_{arrest} = T_0 - T_{K_{Ia}}$ is

$$\text{var}(\Delta RT_{arrest}) = \text{var}(T_0) + \text{var}(T_{K_{Ia}}) - 2\,\text{cov}(T_0 T_{K_{Ia}}) \tag{F25}$$

In the absence of data to the contrary, we assume the statistical independence of $T_0$ and $T_{KIa}$ such that $\text{cov}(T_0 T_{K_{Ia}}) = 0$, and Eq. (F25) becomes

$$\text{var}(\Delta RT_{arrest}) = \text{var}(T_0) + \text{var}(T_{K_{Ia}}) \tag{F26}$$

The variance of both the initial and ODR lognormal model is a decreasing function of increasing $T_0$

$$\begin{aligned} \text{var}(\Delta RT_{arrest(ODR)}) &= \sigma^2_{ODR}(T_0) \\ &= \exp(0.38998^2) \times \left[\exp(0.38998^2) - 1\right] \times \exp\left[2\ln\left[\mu(T_0)\right] - 0.38998^2\right] \end{aligned} \tag{F27}$$

as shown in Fig. F7. By $T_0 \approx$ 56 °C, $\text{var}(\Delta RT_{arrest}) = (12.78\ ^\circ\text{C})^2$.

The variance for $T_0$ has been accounted for in a separate sampling protocol prior to the sampling of $\Delta RT_{arrest}$, and the statistical model for $\Delta RT_{arrest}$ should, therefore, reflect only the remaining variance in $T_{K_{Ia}}$. If we assume that the $\text{var}(T_0) = (23\,^\circ\text{F})^2 = (12.778\ ^\circ\text{C})^2$, then

$$\begin{aligned} &\text{var}(\Delta RT_{arrest(rev)}) = \text{var}(T_{K_{Ia}}) = \text{var}(\Delta RT_{arrest}) - \text{var}(T_0) \\ &\text{var}(\Delta RT_{arrest(rev)}) = \sigma^2_{rev}(T_0) = \\ &\left\{\exp(0.38998^2) \times \left[\exp(0.38998^2) - 1\right] \times \exp\left[2\mu_{\log}(T_0)\right]\right\} - \text{var}(T_0) = \\ &\qquad \exp\left[\sigma^2_{\log}(T_0)_{rev}\right] \times \left\{\exp\left[\sigma^2_{\log}(T_0)_{rev}\right] - 1\right\} \times \exp\left[2\mu_{\log}(T_0)_{rev}\right] \end{aligned} \tag{F28}$$

where

$$\mu_{\log}(T_0)_{rev} = \ln\left[\mu(T_0)\right] - \frac{\sigma^2_{\log}(T_0)_{rev}}{2}$$

and $\mu(T_0)$ remains a fixed function of $T_0$. Solving Eq. (F28) for $\sigma^2_{\log}(T_0)_{rev}$ results in

$$\sigma^2_{\log}(T_0)_{rev} = \ln\left\{\exp\left[0.38998^2 + 2\ln(\mu(T_0)\right] - \text{var}(T_0)\right\} - 2\ln\left[\mu(T_0)\right] \tag{F29}$$

and solving for $\text{var}(\Delta RT_{arrest(rev)}) = \sigma^2(T_0)_{rev}$ gives

$$\sigma^2(T_0)_{rev} = \exp\left[\sigma^2_{\log}(T_0)_{rev}\right] \times \left\{\exp\left[\sigma^2_{\log}(T_0)_{rev}\right] - 1\right\} \times \exp\left\{2\ln\left[\mu(T_0)\right] - \sigma^2_{\log}(T_0)_{rev}\right\} \quad \text{(F30)}$$

However, as noted earlier and indicated in Fig. F7, at $T_0 \approx 56$ °C, $\text{var}(\Delta RT_{arrest}) = \text{var}(T_0) = (12.78\ °\text{C})^2$ which would produce $\sigma^2(T_0)_{rev} = 0$. In order to prevent a nonphysical zero variance at this point, the assumed constant value of $\text{var}(T_0)$ can be replaced by the following function with a transition region:

$$\text{var}(T_0) = \begin{cases} (12.778)^2 & \text{for } T_0 < -35.7\ °\text{C} \\ 99.905972 - 1.7748073 T_0 & \text{for } -35.7\ °\text{C} \le T_0 \le 56\ °\text{C} \\ 0 & \text{for } T_0 > 56\ °\text{C} \end{cases} \quad \text{(F31)}$$

Figure F7 plots Eq. (F30) as the final model variance with Eq. (F31) used in Eq. (F29) to produce the final log-variance as a function of $T_0$. Figure F8 compares the 1% and 99% percentiles of the ODR and final models for $\Delta RT_{arrest}$.

**Summary of Stochastic Model for $\Delta RT_{arrest}$**

The lognormal model for $\Delta RT_{arrest}$ is, therefore,

$$\overline{\Delta RT}_{arrest} = \mu(T_0) = 44.122 \exp(-0.005971 T_0); \quad T_0[°\text{C}]$$

$$\sigma_{\log}(T_0)_{rev} = \sqrt{\ln\left\{\exp\left[0.38998^2 + 2\ln(\mu(T_0))\right] - \text{var}\left(T_0\right)\right\} - 2\ln\left[\mu(T_0)\right]}$$

where

$$\text{var}(T_0) = \begin{cases} (12.778)^2 & \text{for } T_0 < -35.7\ °\text{C} \\ 99.905972 - 1.7748073 T_0 & \text{for } -35.7\ °\text{C} \le T_0 \le 56\ °\text{C} \\ 0 & \text{for } T_0 > 56\ °\text{C} \end{cases} \quad \text{(F32)}$$

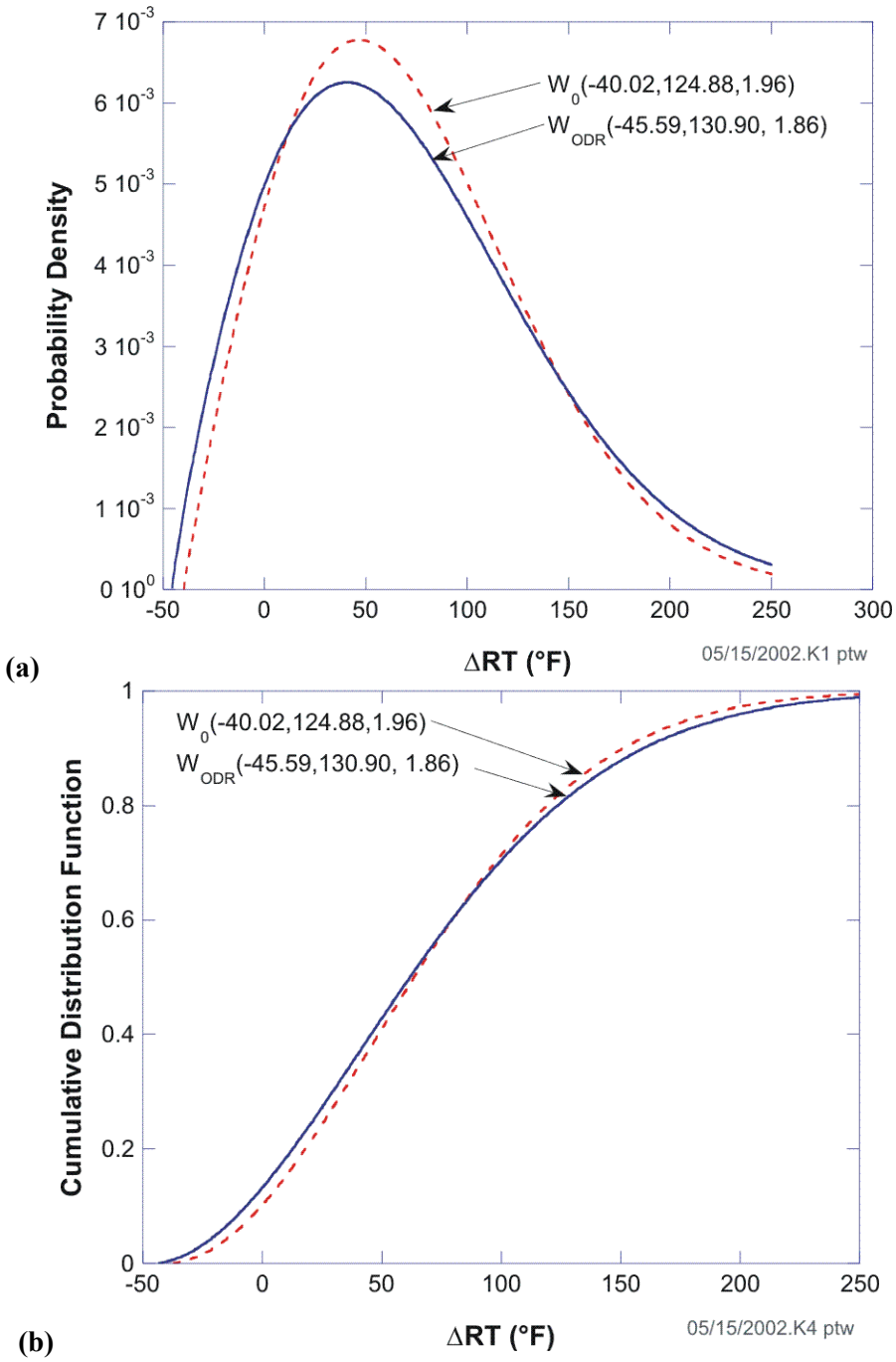


**Fig. F1. Comparison of the initial Weibull model, $W_0$, for $\Delta RT_{epistemic}$ with the ODR model: (a) probability density functions and (b) cumulative distribution functions.**

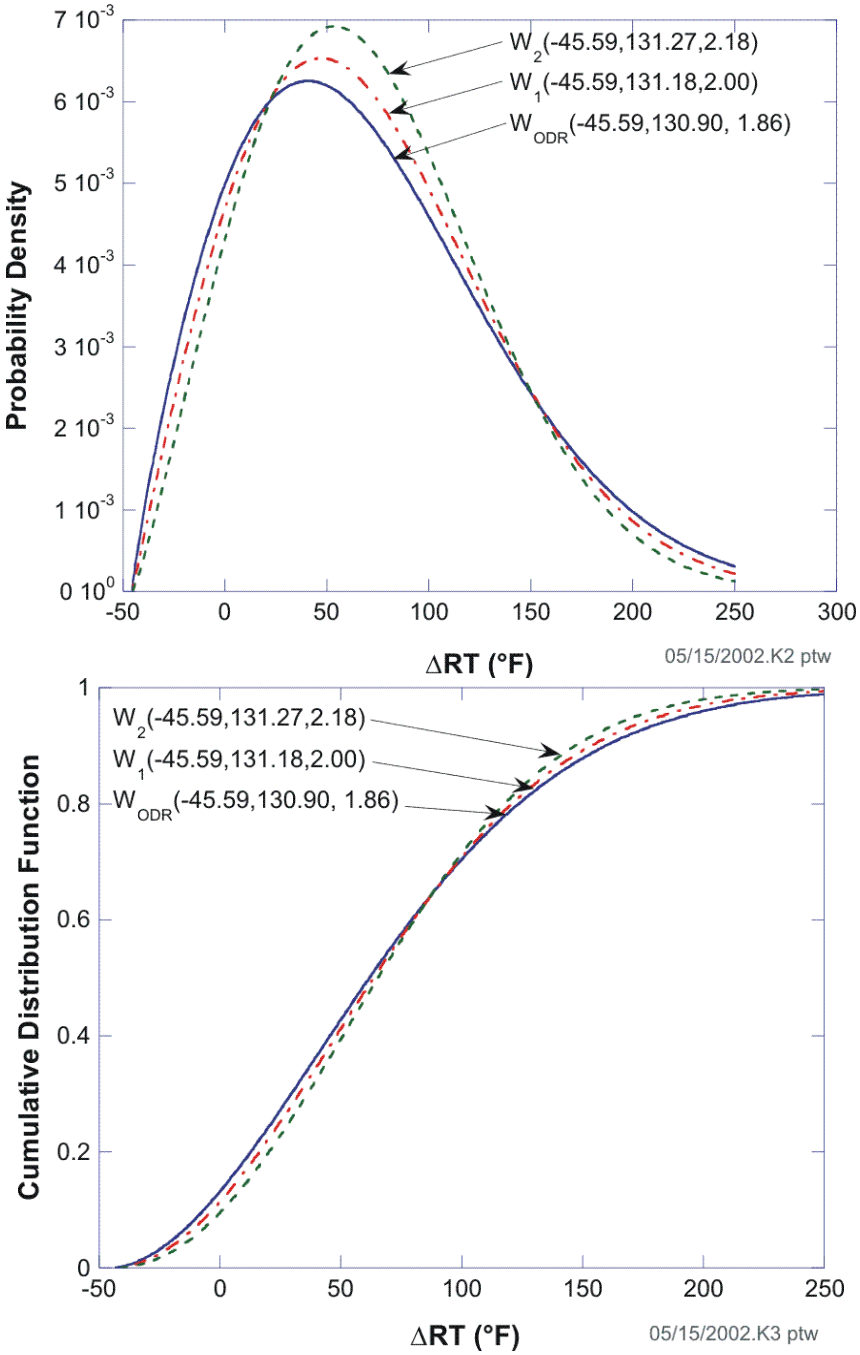


**Fig. F2. Comparison of ODR Weibull model, $W_{ODR}$, for $\Delta RT_{epistemic}$ with the models for Case 1 ($W_1$) and Case 2 ($W_2$): (a) probability density functions and (b) cumulative distribution functions.**

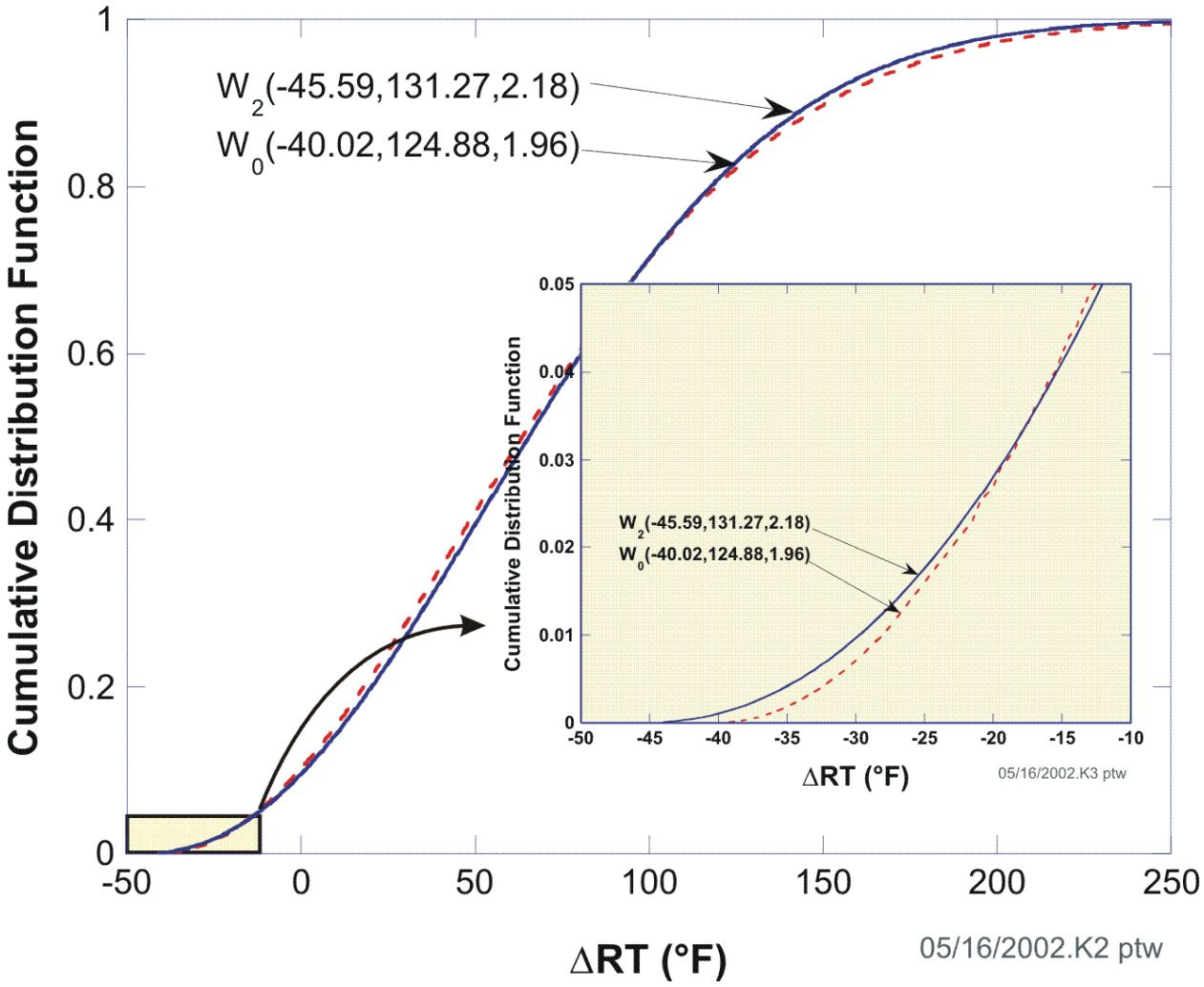


**Fig. F3. Comparison of initial model in FAVOR$^{EP}$, $W_0$, with Case 2, $W_2$.**

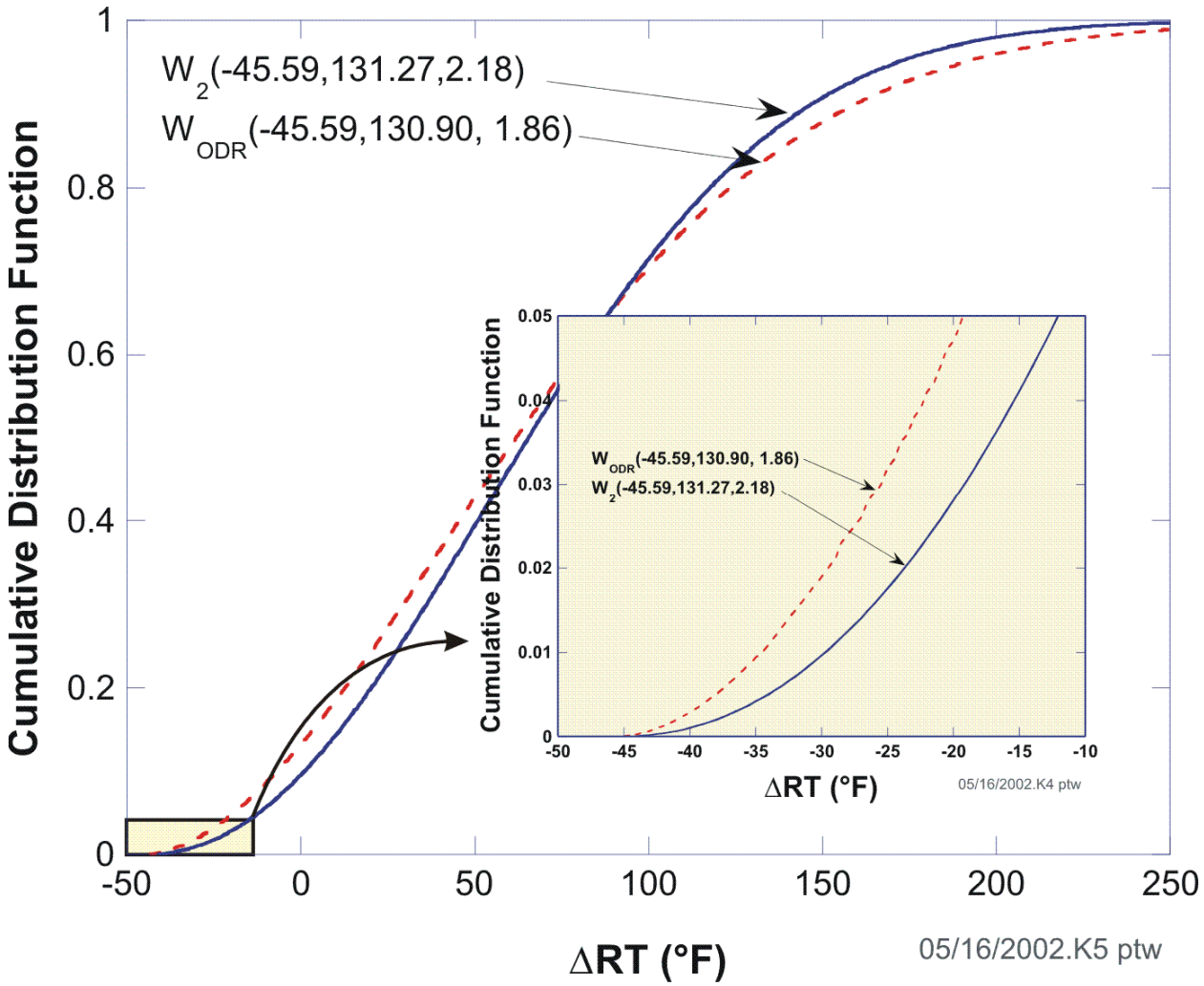


**Fig. F4. Comparison of ODR model, $W_{ODR}$, with Case 2, $W_2$.**

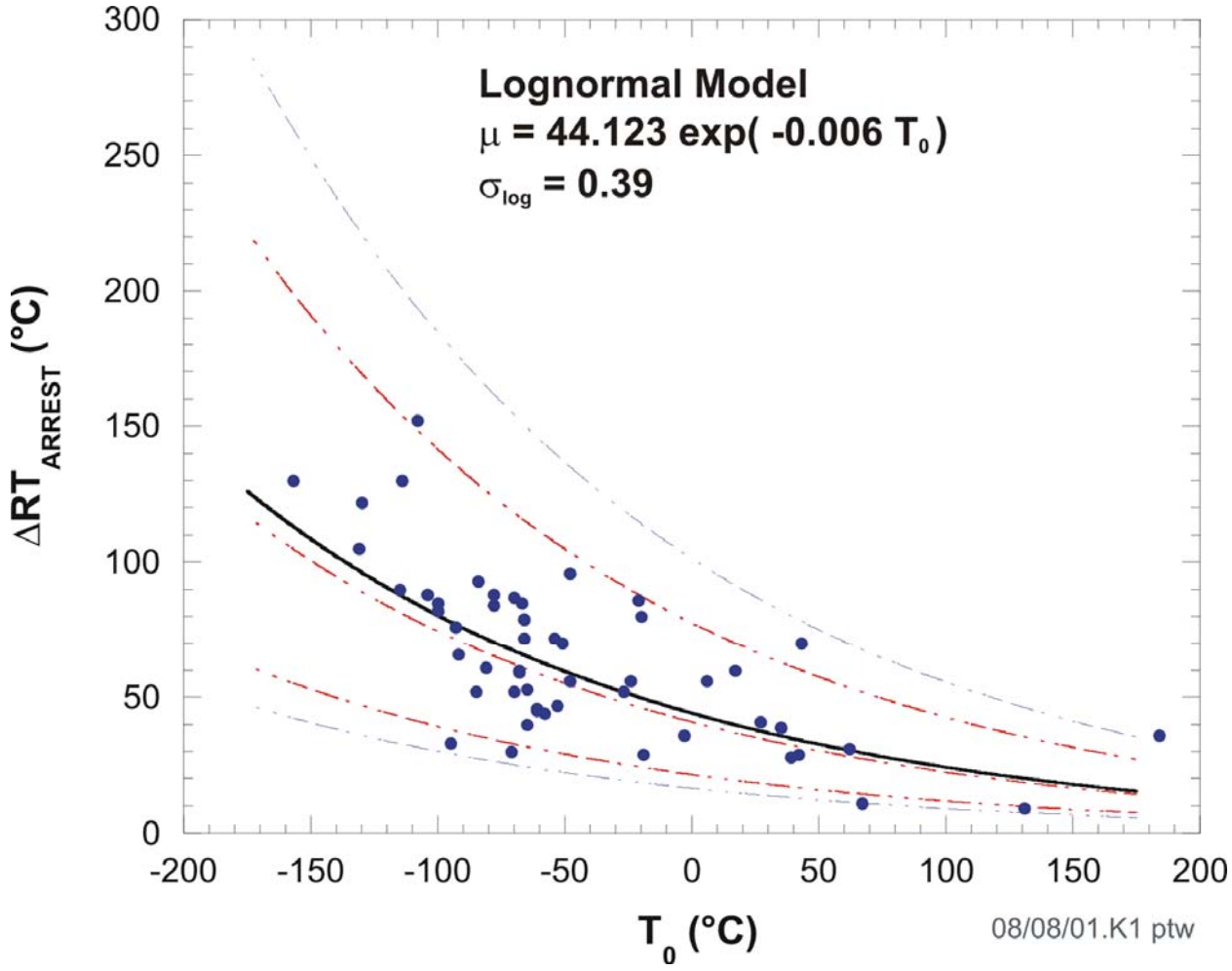


**Fig. F5. Data used to develop the lognormal statistical model for $\Delta RT_{arrest}$ as a function of $T_0$.**

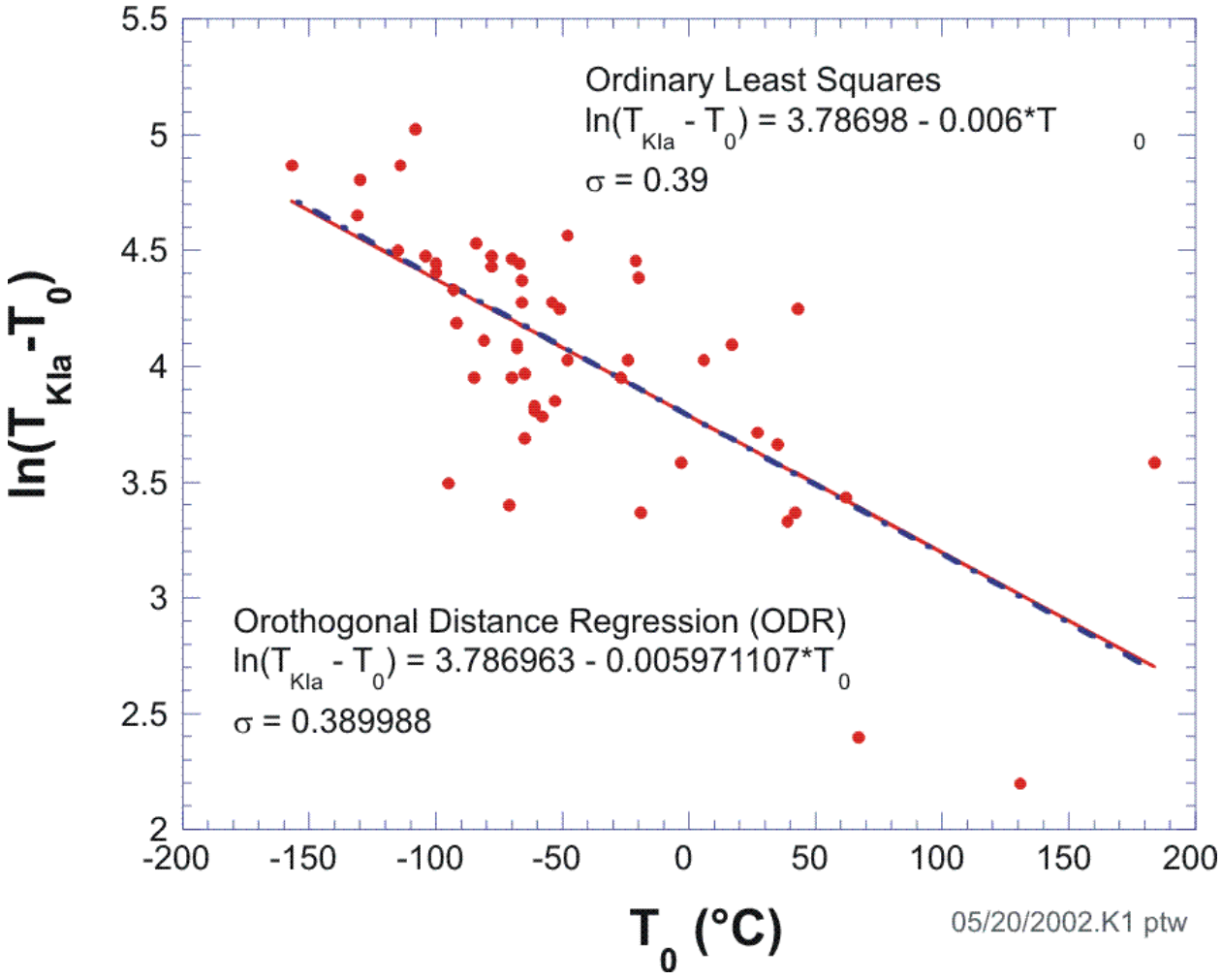


**Fig. F6. Model developed from ODR analysis of log-transformed data.**

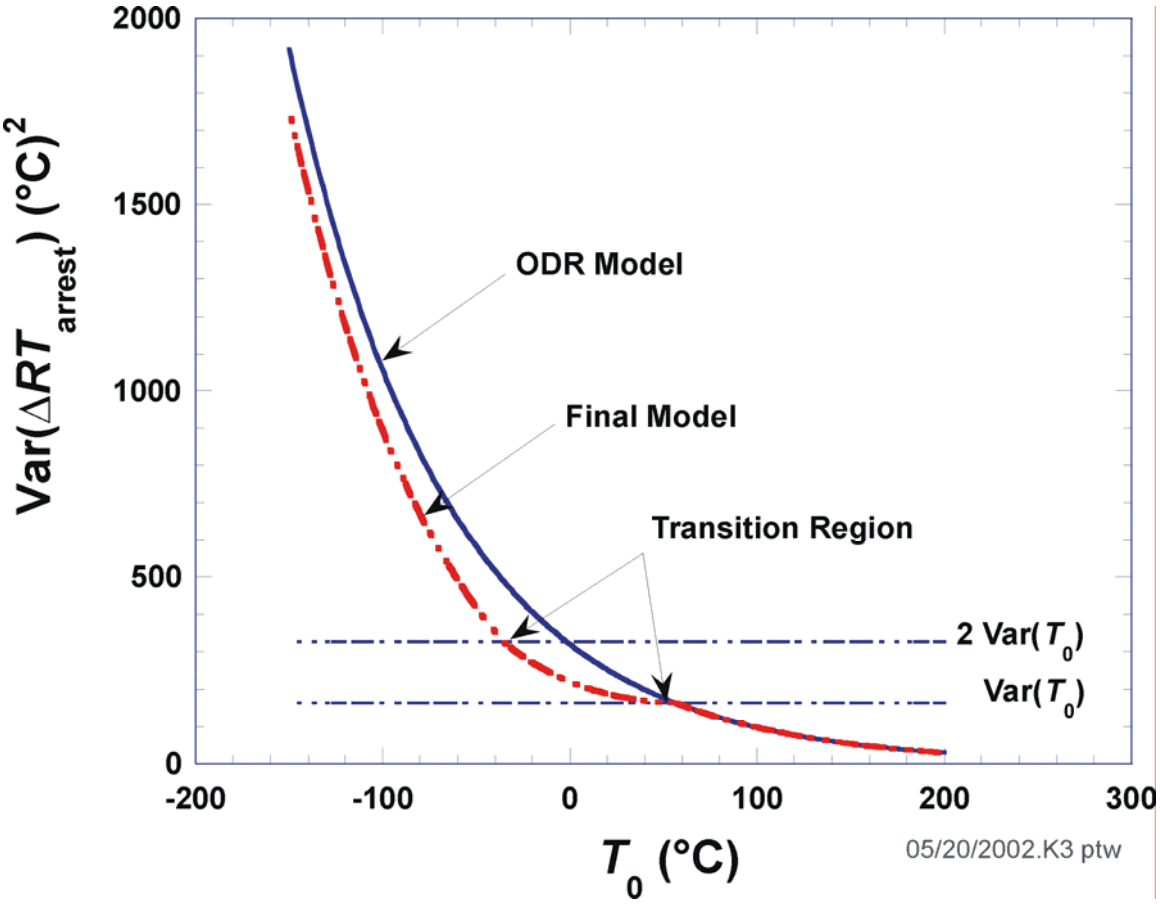


**Fig. F7. Variance of ODR model compared to final model.**

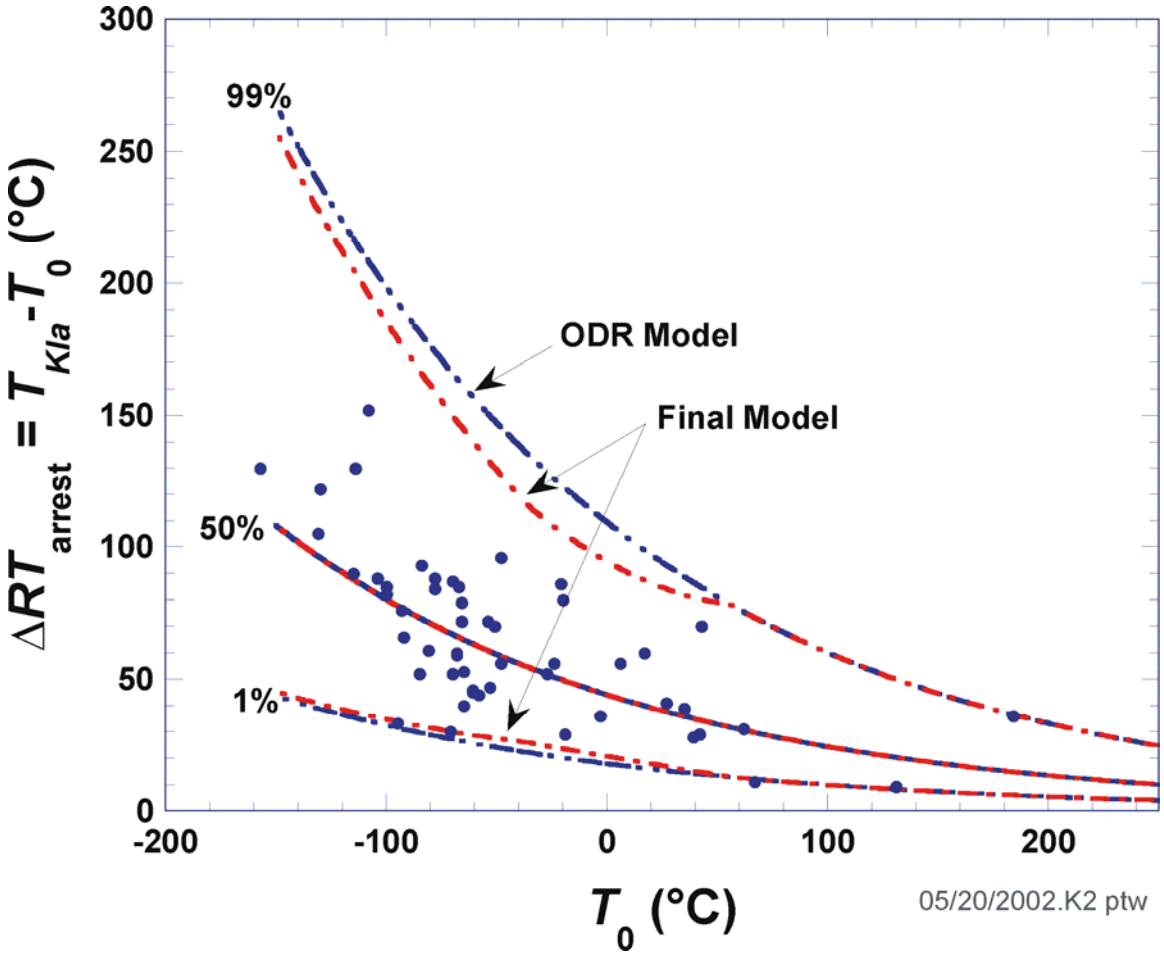


**Fig. F8. Comparison of ODR model with final model.**

REFERENCES

F1. P. T. Boggs, R. H. Byrd, J. E. Rogers, R. B. Schnabel, *User's Reference Guide for ODRPACK Version 2.01: Software for Weighted Orthogonal Distance Regression*, NISTIR 92-4834, National Institute of Standards and Technology, Gaithersburg, MD, 1992.

F2. P. T. Boggs and J. E. Rogers, "The Computation and Use of the Asymptotic Covariance Matrix for Measurement Error Models," Internal Report 89-4102, Applied and Computational Mathematics Division, National Institute of Standards and Technology, Gaithersburg, MD, 1990.